threshold photoelectron studies of the hydrogen halides and fluorine

Andrew James Cormack

A thesis presented for the degree of
Doctor of Philosophy in the
Faculty of Science at the
University of Edinburgh

1998

Acknowledgments

After four years in Edinburgh there are many people who need to be thanked. Firstly thanks to my first and second supervisors, Robert Donovan and Kenneth Lawley, who provided support, encouragement, and advice as and when required. The results in the following pages were collected solely at the Daresbury Laboratory with the help of many of the staff there. Andy Hopkirk, whose experimental expertise, and knowledge of places to find pieces of kit needed at all hours of the day, not to mention his ability to pick up the tab in the Whisky Society, made life at Daresbury almost a pleasure. Dave Fance and his team of technicians, who were always happy to make and modify kit at short notice, and to provide yet more kit when ours had broken down, helped to make prolonged spells at the synchrotron more bearable. John Flaherty pulled many strings with the Daresbury Workshops to keep all the modifications to the apparatus on track for beamtimes, and John Rowcroft, Peter Irvin, and Brian Rimmer, in the Drawing Offices at Manchester and Daresbury produced the drawings for the modifications and new apparatus built as part of the thesis. Andrew Yencha, with his unflinching determination towards achieving the best results possible and to using every available minute of beamtime to collect spectra, was a joy to work with. Especially as he preferred to work the night shift - only someone who has run experiments between 3 and 4 in the morning will understand how tiring this is. George King kept the spectrometer in fine fettle during the studies and also provided a rich seam of knowledge on ion optics, much of this will be invested in the new kit when it is built. Steven Henderson and Colin Pulham helped by preparing deuterium chloride and arranging a supply of deuterium fluoride. Robert Maier, for whom I acted as the incoming calls switchboard for over 3 years, has been pillaged for much help and advice on the technical aspects of the work and has always been willing to answer flurries of questions.

The room 6 dynasty is over and now the spiritual home of the laser group has been moved to room 5. However, the present inhabitants, Alison, Angela, Colin, and Michel, have still proven to be useful diversions from writing this thesis. Scott, Neil, and Trevor provided much needed excuses for trips to the pub, keeping my spirits high through dark days of data analysis. More importantly Scott gave many lifts to Uni., Neil provided many hours of irrelevant chat, and Trevor paid for too many rounds. The ZEKE group; Jon, Martin, David, and Neil; have been good pals over the years, thanks.

Finally, thanks to my family for all their support throughout my time in Edinburgh. After 25 years of learning it's now time to see if any of it has stuck.

Abstract

New results for the threshold ionisation of the molecules HF, DF, HCl, DCl, HBr, DBr, HI and F_2 have been recorded using threshold photoelectron spectroscopy (TPES) at resolutions down to 3 meV. The entire outer valence ionisation region has been studied for all of these molecules, and additionally, the inner valence region of the molecules not containing fluorine has been recorded. This represents a significant volume of consistent spectroscopic data for the halogen containing diatomic systems. The completeness of the study utilising both hydrogen isotopes has proven very useful for the in-depth analysis of the TPE spectra, allowing each system to be analysed by combining the data for both hydrogen isotopes. This has permitted the production of improved spectroscopic constants compared to previous TPE work.

In all study molecules, the TPE spectrum of the lowest electronic (X) state shows extended vibrational progressions due to the autoionisation of super-excited neutral (Rydberg) states, producing the molecular ion and a threshold electron.
The symmetry of the autoionising Rydberg states can be tentatively assigned from the position of enhancements in the TPE spectra. The assignments suggest that the Rydberg states that autoionise to produce threshold electrons do not have the same symmetry as the Rydberg states seen most strongly in photoabsorption and photoionisation spectra. The similarity between the recorded TPE spectra and fluorescence excitation spectra in the literature suggests the predominant autoionisation route leading to threshold electron production could be via repulsive intermediate states.

The first excited (A) ion state for the HX and DX species is well known to be predissociated for all systems except X=F. The TPE spectra of the predissociated vibrational levels in the HCl, DCl, HBr, and DBr systems show evidence of an additional ionisation mechanism that is not seen for non-resonant ionisation.
These additional mechanisms have been modeled as being due to a propensity for a large loss of rotational angular momentum from the ion core during the ionisation

process. It is suggested that these mechanisms involve the rotational autoionisation of dissociative Rydberg states into dissociative ion states accompanied by the ejection of a near threshold electron. The TPE spectrum of the A state of HI shows a previously unseen vibrational progression with a vibrational frequency that is much smaller than expected through comparison with HCl and HBr. Some elementary simulations show the A state of HI is well represented by an avoided crossing between two diabatic ion states.

The spectra for the inner valence regions of the HCl, DCl, HBr, DBr, and HI systems are approximately 500 times weaker than the outer valence region, whereas non-resonant ionisation studies using either high energy electrons or photons ($E > 500$ eV) show the inner and outer valence regions have approximately the same intensity. The reduction intensity of the inner valence region in the TPE spectra is probably due to a propensity for non-threshold autoionisation pathways of the excited neutral states in this region, yielding kinetic electrons and ions with outer valence electron configurations.

The continued development of the TPE apparatus and some designs for a new combined TPE and threshold photoelectron - photoion coincidence (TPEPICO) experiment are discussed. The TPE spectrometer can achieve 3 meV resolution and spectra of the X state of the HX and DX systems recorded at this resolution show evidence of partially resolved rotational structure. However, an increase in resolution to ~ 1 meV will be needed before the rotational structure can be compared to laser based zero kinetic energy (ZEKE) results.

Table of Contents

Chapter 1. Introduction

1.1 Introduction to the thesis

This thesis contains the results and analysis of high-resolution threshold photoelectron studies on some diatomic molecules, together with a description of some developments to the threshold photoelectron technique. The main molecules studied are the hydrogen and deuterium halides. These molecules have been and still are of great spectroscopic interest. Molecular fluorine has also been studied, and so threshold photoelectron spectra of all halogens (X_2), hydrogen halides (HX), and deuterium halides (DX), excluding deuterium iodide, have been studied at Edinburgh.

The thesis is organised as follows. Chapter 1 introduces the general background to the study of molecular ions. An introduction to the various spectroscopic techniques employed in these studies (including threshold photoelectron spectroscopy) is used to illustrate many of the features of molecular ionisation. The last section of Chapter 1 also introduces the reasons for studying the hydrogen halides and fluorine. Chapter 2 introduces the experimental considerations for threshold photoelectron spectroscopy, detailing the design and performance of the apparatus and the analysis methods for the results. Chapters 3-7 present, analyse, and discuss the threshold photoelectron spectra of the molecules under study. Each Chapter is devoted to a particular halogen atom. i.e. Chapter 3 for HF/DF, Chapter 4 for HCl/DCl, Chapter 5 for HBr/DBr, Chapter 6 for HI, and Chapter 7 for F_2. Every chapter contains an introduction to previous relevant work, the presentation and analysis of results, and the conclusion for the study. Chapter 8 is a short report of progress with the development of the threshold photoelectron apparatus. The existing apparatus (used for these studies) has been modified, and also a new threshold

photoelectron apparatus has been designed. Chapter 8 also includes some suggestions for future threshold photoelectron and threshold photoelectron-photoion coincidence studies. Finally, Chapter 9 concludes the thesis with a discussion of aspects of the threshold photoelectron studies which only become apparent when all of the results have been combined.

During the course of work for this thesis I have also participated in a short spell of research using ZEKE spectroscopy (see Section 1.2.6), however the results obtained are not reported in this thesis as they are not directly relevant to the main research topic of this work.

Finally, a few comments on the arrangement of the thesis. Figures referenced in the text are included as close as possible to the relevant text, whereas Tables are placed at the end of each Chapter. Reference numbering is continuous throughout with a single list given at the end of the thesis. The text and Figures have been prepared using Microsoft Word v.6, Microcal Origin v.3.73, and CorelDRAW v.3.

1.2 A review of molecular ionisation

The spectroscopic study of molecules is quite routine. Information on the electronic energy levels of molecules can normally be derived from the observation of allowed optical transitions using absorption and emission techniques. These observations have allowed the formulation of many simple rules governing the electronic structure of atoms and small molecules, for instance, the basic ideas of bonding and antibonding electronic orbitals and the arrangement of electrons within these orbitals (the electronic configuration).

The amount of information available on the electronic structure of small molecular ions is quite small compared to the wealth of spectroscopic data available on neutral species. This is mainly due to experimental difficulties in forming the molecular ions from the parent neutral. Historically, the two sources of information on the energetics of small molecular ions have been by electron impact ionisation or by the observation of ionic emission in electrical discharges. Electron impact ionisation (EI) gives a useful overview of the various accessible electronic states of molecular ions, however the technique is hampered by poor experimental resolution (~0.1 - 0.3 eV), which generally is not sufficient to fully resolve vibrational structure. Instead an entire band contour belonging to the electronic state is seen. However, useful information can still be extracted. Low resolution techniques including electron ionisation will be discussed later in the introduction. Although the emission spectroscopy of molecular ions is a much higher resolution technique, typically resolving extensive rotational structure in diatomic systems, it too suffers difficulties. Specifically, as only the energy differences between optically connected levels are observed it is impossible to determine the absolute energies of the upper and lower ion levels. Also, the technique cannot differentiate between emission lines from neutral levels, so unless the spectroscopy of the neutral molecule is well characterised the ionic transitions can be quite difficult to differentiate.

Emission and absorption studies form the backbone of knowledge about the various properties of electronic states in neutral molecules and ions. For instance, the combination of theoretical considerations for rotational angular momentum and the spectroscopic observation of many small molecules shows that the various angular momenta within a rotating molecule can couple together in different ways. These coupling schemes are called the Hund's coupling schemes, and underpin electronic spectroscopy. A typical molecule will have various contributions to its angular momentum: (1) the angular momentum of the nuclei (i.e. the overall rotational angular momentum - excluding nuclear spin), (2) the orbital angular momentum of the electrons within the molecule, and (3) the spin angular momentum of the electrons within the molecule. The different ways these three angular momenta couple to form a resultant total angular momentum are called the Hund's coupling cases and are shown schematically in Appendix C-1 and discussed briefly below. The cases are all idealised angular momentum coupling schemes and in general one particular scheme is most suitable for an electronic state, however it is not unknown for the most applicable coupling scheme in a particular electronic state to change even within a single vibronic band (see Herzberg [1]). In general, Hund's cases (a), (b), and (c) represent the angular momentum coupling of valence electronic levels where all electrons interact significantly with the nuclei. The electrons experience the electric field between the nuclei and the electron angular momenta tend to precess around it. Hund's cases (d) and (e) represent the coupling of a Rydberg electron to an ion core. Since the Rydberg electron is normally a large distance away from the nuclei it will no longer interact strongly with the electric dipole associated with the nuclei (the electric field from a dipole varies as $1/r^3$ [64], and only exists in heteronuclear diatomics), and instead the electron couples to the nuclear rotational angular momentum. Further details of the five Hund's cases are given in Appendix C and Herzberg [1], Lefebvre-Brion and Field [2], Atkins and Friedman [3], and Lefebvre-Brion [4].

In general, most transitions observed in spectroscopy obey the electric dipole selection rules. These rules impose stringent criteria on the transitions which are generally possible in absorption or emission spectroscopy. The selection rules vary

according to which Hund's coupling case is most applicable, however as an example the selection rules for Hund's case (a) coupling are included here.

Where $\Delta\Lambda$ and $\Delta\Sigma$ are the changes in orbital and spin angular momentum about the bond axis, $\Delta\Omega = |\Delta\Lambda + \Delta\Sigma|$ (i.e. the total electronic angular momentum about the

$$\Delta\Lambda = 0,\pm 1$$
$$\Delta S = 0$$
$$\Delta\Sigma = 0$$
$$\Delta J = 0,\pm 1$$
$$\Delta\Omega = 0,\pm 1$$
$$+ \longleftrightarrow + \quad \text{and} \quad - \longleftrightarrow -$$
$$g \longleftrightarrow u$$

Equation 1-1

bond axis), ΔJ is the change in total angular momentum of the system, ΔS is the change in spin multiplicity, g and u refer to the symmetry of the electronic wavefunction under inversion (in centro-symmetric molecules), and finally + and – refer to the symmetry of the electronic wavefunction under reflection in any plane containing the internuclear axis. + and – are only relevant for Σ states (i.e. where the orbital angular momentum Λ is zero).

1.2.1 Rydberg series extrapolation

The advent of continuum light sources in the vacuum ultra-violet (VUV) such as the Hopfield Continuum [5], and more recently Synchrotron Radiation [6], combined with a VUV spectrograph has allowed wavelength dependent studies of highly excited neutral states (Rydberg and ion-pair), and of ion states. Observation of Rydberg states can be useful in determining properties of the molecular ion. If a Rydberg series is well behaved then the series can be fitted to the Rydberg formula,

$$E_{n,l,\lambda} = I.P. - \frac{R_y}{(n-\delta_{l,\lambda})^2}$$

Equation 1-2

where n is the principal quantum number, l the orbital angular momentum, and λ the orbital angular momentum of the Rydberg electron about the molecular bond. $E_{n,l,\lambda}$ is the energy of a particular Rydberg transition, $I.P.$ is the ionisation energy of the Rydberg series, R_y is the Rydberg constant, and $\delta_{l,\lambda}$ is the quantum defect of the Rydberg series. It is difficult to determine the principal quantum number n for a Rydberg state (as it depends on the value of $\delta_{l,\lambda}$), so n-$\delta_{l,\lambda}$ is often given as n^*. For a well behaved Rydberg series $\delta_{l,\lambda}$ will remain essentially constant for increasing n. The relative photoabsorption cross-section of a Rydberg series as a function of principal quantum number n is also of importance in Rydberg spectroscopy. From quantum mechanical considerations it is possible to show that the oscillator strength for the transition to a Rydberg state with principal quantum number n varies as n^{*-3} in the limit of large n (Gallagher [7]), so in general the intensity of any observed valence $\rightarrow$ Rydberg transition will decrease towards the ion limit. This, combined with the separation between successive Rydberg states scaling as n^{*-3} [8], makes the observation of individual high-n Rydberg states very difficult. Although Rydberg extrapolation can be a very accurate means of determining ionisation potentials sometimes the Rydberg levels are quite perturbed making extrapolation to the ionisation potential impossible ($\delta_{l,\lambda} \rightarrow \delta_{n,l,\lambda}$ i.e. δ is an erratic function of n).

1.2.2 Photoionisation efficiency spectroscopy

The determination of accurate ionisation potentials is only possible by Rydberg extrapolation where the Rydberg series is well behaved. Detection of the ion signal with varying photon energy (photoionisation) is also a useful technique for the extraction of ionisation potentials. The selection rules for photoionisation are more relaxed than those for photoabsorption as the departing electron is capable of removing angular momentum in the ionisation process. A typical ionisation process can be represented as follows:

$$M + h\nu \rightarrow M^+ + e^-$$

Equation 1-3

For atoms the electric dipole selection rule is $\Delta l = \pm 1$ [9],[10] so the electron will depart with either $l+1$ or $l-1$ units of angular momentum (where l is the initial orbital angular momentum of the ejected electron). In molecules the combination of atomic orbitals to form molecular orbitals means that the electron wavefunctions are no longer atom-like and ejected electrons will leave with various angular momenta (*s, p, d, f,* ... waves). A final selection rule for molecular photoionisation is

$$\Delta S = \pm 1$$

Equation 1-4

where ΔS is the change in spin multiplicity in the photoionisation process. This selection rule arises purely from the removal of one electron. In summary the selection rules for photoionisation are much less stringent than photoabsorption. Essentially all ionising transitions where the ion state differs from the initial state by removal of a single electron are allowed, however the removal of more than one electron is formally forbidden.

The oscillator strength for a transition to a Rydberg series remains essentially constant below and above the ionisation limit (Gallagher [7]). So, in a basic photoionisation experiment where the ion yield is measured as a function of incident photon energy, the spectrum would be expected to show step-like features associated with each ionisation threshold. Such a spectrum is called a photoionisation efficiency (PIE) spectrum. Although experimental PIE spectra do exhibit simple step-like features they also contain many sharp features which cannot be associated with ionic levels. These resonance features occur both below and above the ionisation potential although they are most dominant above the I.P. Whereas the photoionisation cross-section varies only slowly with excess photon energy (as the oscillator strength varies only slowly above the ionisation potential) these extra features in the PIE spectrum

are sharp. So the sharp features are resonance effects where the ionisation process occurs through an intermediate state which has to be in resonance with the photoionisation wavelength. This process can be represented as

$$M + h\nu \xrightarrow{(photoabsorption)} M^* \xrightarrow{(autoionisation)} M^+ + e^-$$

Equation 1-5

where M^* is generally a Rydberg state, so the photoabsorption step will only occur at resonance. These autoionising Rydberg levels complicate the PIE spectrum by masking the true ion levels.

1.2.3 Photoionisation mass spectrometry

A further development in photoionisation experiments is photoionisation mass spectrometry. This is a general extension of the PIE technique where now the ionic fragments are mass-resolved allowing the parent molecular ion and ion fragments to be studied in parallel. The relevant ionisation processes are summarised as

$$(a) \quad AB + h\nu \longrightarrow AB^+ + e^- \quad \text{(monitor } AB^+ \text{ mass channel)}$$
$$(b) \quad AB + h\nu \longrightarrow A^+ + B + e^- \quad \text{(monitor } A^+ \text{ mass channel)}$$

Equation 1-6

Photoionisation mass spectrometry is very useful for determining the dissociation energies of molecular ion states and also, possibly more importantly, it can be used to determine the dissociation energy of neutral molecules. From Equation 1-6(b) it is clear that the onset of dissociative ionisation will coincide with the production of a zero energy electron, so the onset of ionic dissociation (ν_c) can be simply related to the ionisation potential of A ($I.P.$) and the dissociation energy of the AB neutral molecule (D_o) as shown in Equation 1-7.

The extraction of accurate and consistent ionisation potentials and dissociation energies from photoionisation mass spectroscopy and photoionisation efficiency

$$D_o = \nu_c - I.P.$$

Equation 1-7

studies have been discussed in detail by Guyon and Berkowitz [11], and a review of the use of photoionisation mass spectrometry and other techniques for the measurement of RH bond energies [12] clearly shows how photoionisation studies can be used to measure individual bond strengths in the neutral molecule.

1.2.4 Photoelectron spectroscopy

In the 1960's another form of ion spectroscopy was developed. Photoelectron Spectroscopy (PES) measures the kinetic energy distribution of electrons when a molecule is ionised by a high energy photon source. In most experiments the light source used is the HeI resonance emission line at 21.21 eV. The ionisation scheme is represented in Figure 1-1. Three electronic levels of a molecule (ε_1, ε_2, ε_3) are ionised with a fixed energy photon. The energies of the ejected electrons are then given by $h\nu-\varepsilon_1$, $h\nu-\varepsilon_2$, and $h\nu-\varepsilon_3$, as signified by the electron signal to the right of Figure 1-1. The electronic levels of the molecule (ε_1, ε_2, ε_3) are not the same as the binding energy of the electrons in Koopmans' Theorem (Equation 1-8) as Koopmans' Theorem takes no account of electron correlation effects which relax the energies of the spectator electrons upon ionisation.

$$I.P. = -\varepsilon_i$$

Equation 1-8

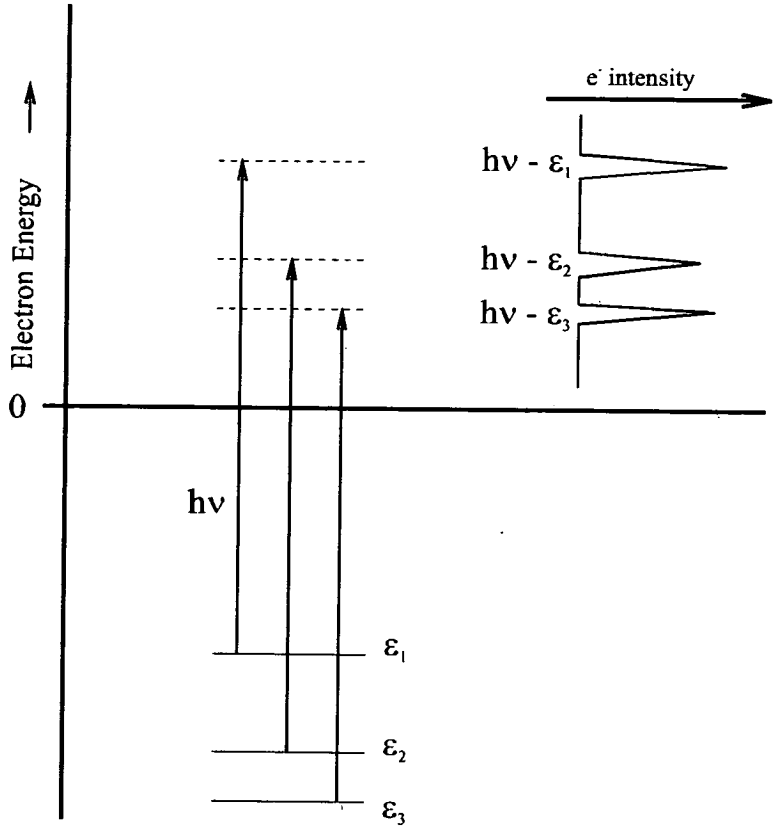

Figure 1-1 Schematic ionisation scheme for non-resonant ionisation (see text).

The energy of ejected electrons is measured using electrostatic analysers which either use a stopping voltage to measure the differential electron signal (retarding field type) or a deflection arrangement (deflection analysers). The most commonly used analyser is the 180 degree hemispherical deflection analyser as in general it produces the highest resolution spectra and also has good electron transmission characteristics. A schematic of the apparatus for a typical HeI PES experiment is shown in Figure 1-2. In operation the lens assembly close to the ionisation region is used to change the electron energies exiting the ionisation region so that they match the "pass energy" of the hemispherical analyser. Until quite recently the most accurate ionisation potentials of many small molecules were measured by conventional photoelectron spectroscopy (HeI PES and NeI PES). HeI photoelectron spectra has also proven a useful means of determining the equilibrium bondlengths of molecular ions where optical emission results are not available. The photoionisation probability for the transition from the lowest vibrational level of the

neutral molecule to various vibrational levels of the ion can be represented quantum mechanically by

$$P(v^+) = \left(\int \psi_{v^+} \psi_0 dr\right)^2$$

Equation 1-9

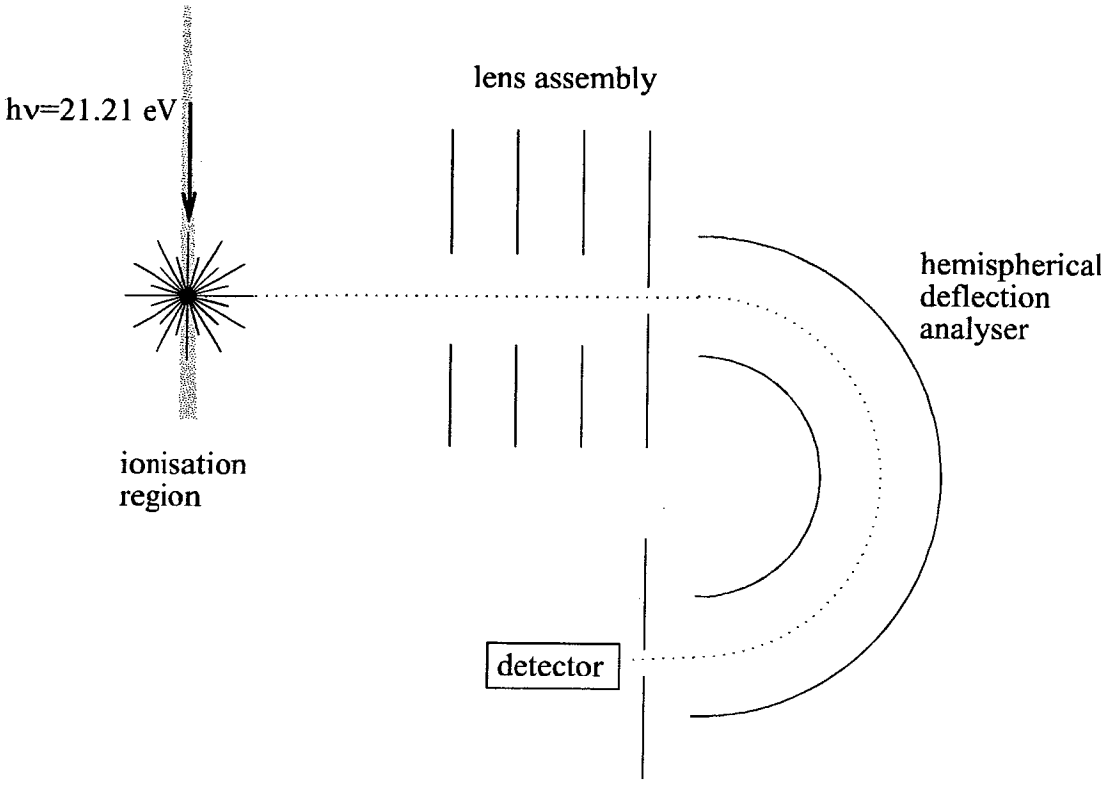

Figure 1-2 Schematic of apparatus for a HeI photoelectron experiment (see text).

assuming the Born-Oppenheimer approximation is valid [3] and that the purely electronic transmission moment is constant throughout the region of interest. Here ψ_{v+} and ψ_0 represent the vibrational wavefunctions of various ionic vibrational levels and the lowest neutral vibrational level. The vibrational distributions measured for an ion state can then be modeled using Franck-Condon calculations to establish the equilibrium bondlength of the ion state.

The effect of differing electronic potential energy curves on the final state vibrational intensity distributions is demonstrated in Figure 1-3. A single Morse potential has been used to simulate all potential energy curves, however in cases (a) and (c) the upper state potential has been displaced by 0.5 Å to shorter and longer *R*. A Franck-Condon simulation program [13] was then used to calculate the relative Franck-Condon factors to the upper state and the spectra immediately to the right of each upper state potential curve show the resultant vibrational distribution. The wavefunction for the lowest vibrational level of the lower state is also shown along with the vertical lines representing the Franck-Condon window (taken to be the classical turning points of the lower state vibrational wavefunction). The molecular constants used to generate the Morse curves and for the Franck-Condon calculations were typical for a hydrogen halide molecule (D_e=24000 cm^{-1}, ω_e=2000 cm^{-1}, and μ=1.0 a.m.u.). Clearly the number of observable vibrational levels is constrained by

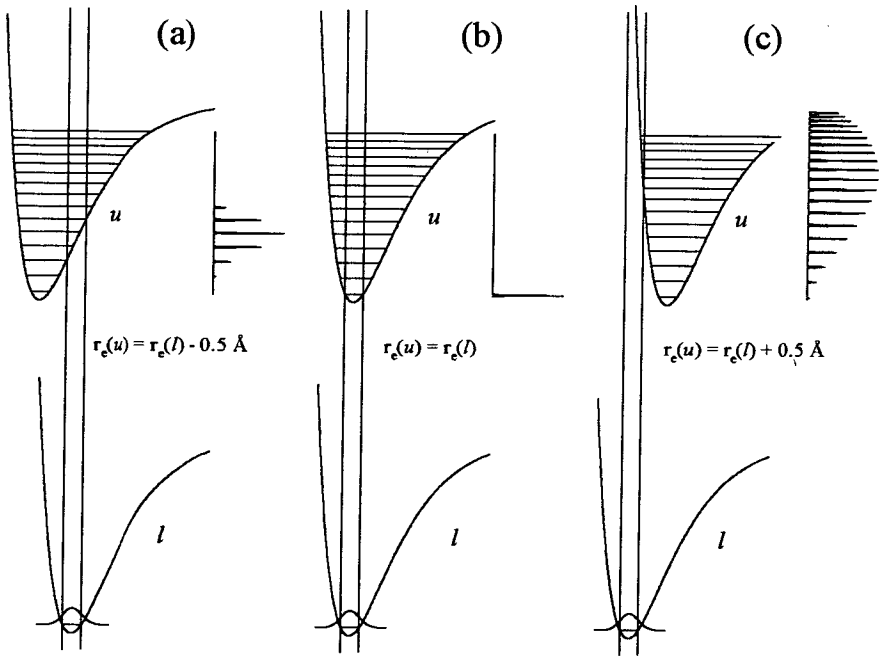

Figure 1-3 Franck-Condon simulations showing the change in vibrational distribution for different equilibrium internuclear distances. All potential curves are identical except for a change in the equilibrium internuclear distance.

the change in geometry between the two electronic states.

The majority of features seen in conventional photoelectron spectroscopy (HeI PES) can be explained within the Franck-Condon approximation, however when lower energy light sources are used, such as the NeI line at 16.848 eV or synchrotron radiation, the observed vibrational distributions show a marked departure from Franck-Condon behavior. Typically vibrational progressions are extended and the intensity of individual vibrational levels in the photoelectron spectrum are enhanced. These effects are due to the autoionisation of super-excited neutral states and give extra information not normally accessible in conventional (non-resonant) photoelectron spectroscopy. The electronic autoionisation of excited neutrals into a lower energy ion continuum has been modeled by Bardsley [14], and Smith [15],[16] using configuration interaction theory [17],[18] to discuss non-Franck-Condon behavior in the NeI excited photoelectron spectrum of O_2 [19] with qualitative success. Smith's calculations on ionisation of the X ($^2\Pi_g$) state of O_2 show that the final vibrational distribution can be ascribed to a combination of direct photoionisation and indirect autoionisation via a Rydberg state converging to the A ($^2\Pi_u$) state ion, where the vibrational distribution due to autoionisation is essentially the combined Franck-Condon factors for the process

$$AB_{v=0} \longrightarrow AB^{*}_{v'} \longrightarrow AB_{v^+}$$

Equation 1-10

Despite its unqualified success as a spectroscopic technique conventional photoelectron spectroscopy often suffers from one slight problem due to stray electric fields within the instrument. Stray electric fields (caused by surface charging of the spectrometer surfaces) generally cause the experimental spectra to be shifted in energy. However, recent advances (1994) in both HeI light sources and data collection techniques have now essentially overcome these difficulties so that a state-of-the-art conventional photoelectron experiment can now achieve experimental

resolutions as high as 2.5 meV (20 cm^{-1}) FWHM and absolute spectral positions accurate to less than ±0.5 meV (4 cm^{-1}) [20].

1.2.5 Threshold photoelectron spectroscopy

Threshold photoelectron spectroscopy is essentially an extension of the earlier photoionisation efficiency studies. As mentioned in section 1.2.2 photoionisation efficiency is an ideal method to determine the ionisation potentials of molecular ions. Only the monochromator wavelength is varied during an experiment so the technique does not suffer the same calibration problems as conventional photoelectron spectroscopy. However, the features associated with ionic levels in photoionisation efficiency spectra are often masked by intense autoionising features. But, since these

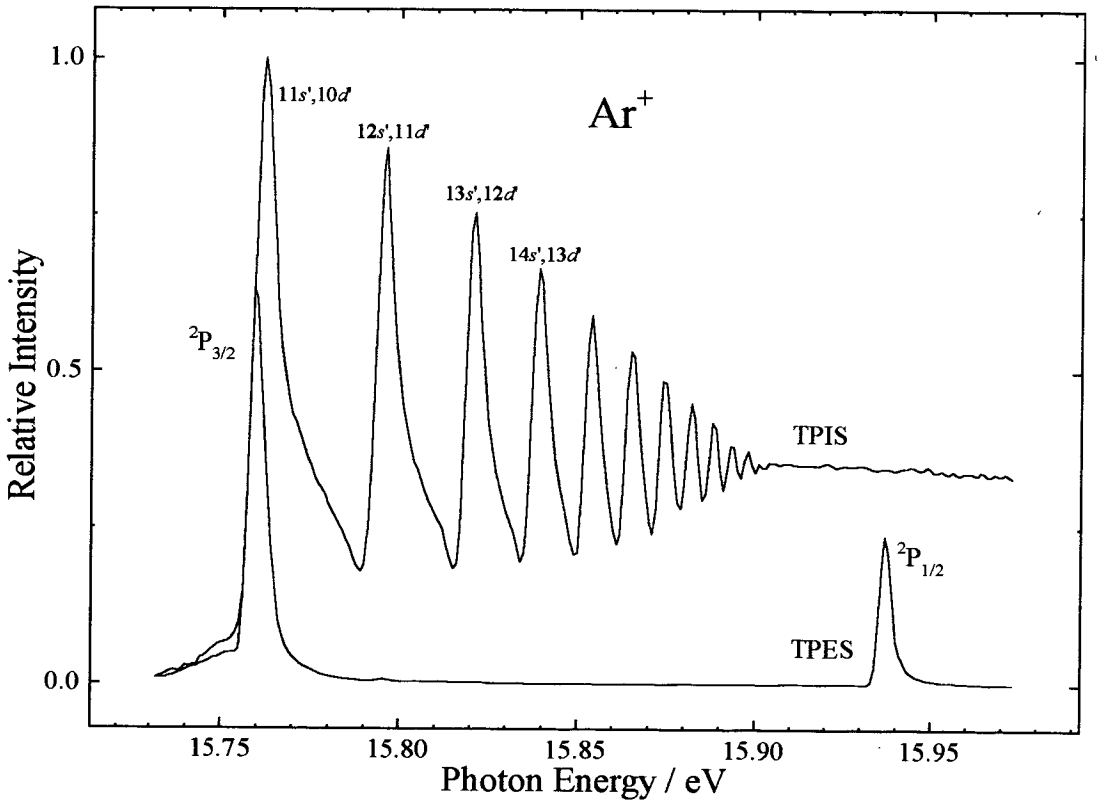

Figure 1-4 Threshold photoionisation and threshold photoelectron spectra of argon showing the suppression of the *ns'* and *nd'* Rydberg states converging on the Ar ($^2P_{1/2}$) ion core at 15.937 eV. (spectrum courtesy of G.C. King [21])

autoionising features do not correspond to an ionic level the autoionisation process must produce and electron with kinetic energy equal to the difference between the excited neutral level and the final ionic level. If only electrons with essentially zero kinetic energy are detected instead of all ions then only the ionic levels will be seen and autoionising resonances producing non-threshold electrons will suppressed. So threshold photoelectron spectroscopy promises the calibration stability of an optical experiment and the final state sensitivity of a photoelectron experiment. Figure 1-4 shows the threshold photoionisation spectrum (or PIE spectrum) and threshold photoelectron spectrum of argon [21] as a simple example of the difference between the two types of spectra. Figure 1-4 clearly shows that autoionising resonances that yield energetic electrons are effectively suppressed in TPES.

Historically threshold photoelectron experiments were performed using steradiancy analysers. A typical threshold electron spectrometer that uses the steradiancy technique is shown in Figure 1-5. Electrons ejected during the ionisation process are accelerated towards a metal plate with many small parallel holes. An electron ejected with initial energy E_0 will have kinetic energy $\mathbf{v}_o$ with components $\mathbf{v}_{o\perp}$ and $\mathbf{v}_{o\parallel}$. The electric field is homogeneous within the ionisation region so the velocity component $\mathbf{v}_{o\perp}$ will remain constant, however $\mathbf{v}_{o\parallel}$ increases due to the electric field. The actual transmission function of the analyser has been calculated by Spohr *et al.* [22], however the following condition must at least be met before an electron will pass through the grid

$$\frac{\mathbf{v}_\perp}{\mathbf{v}_\parallel} < \frac{d}{w}$$

Equation 1-11

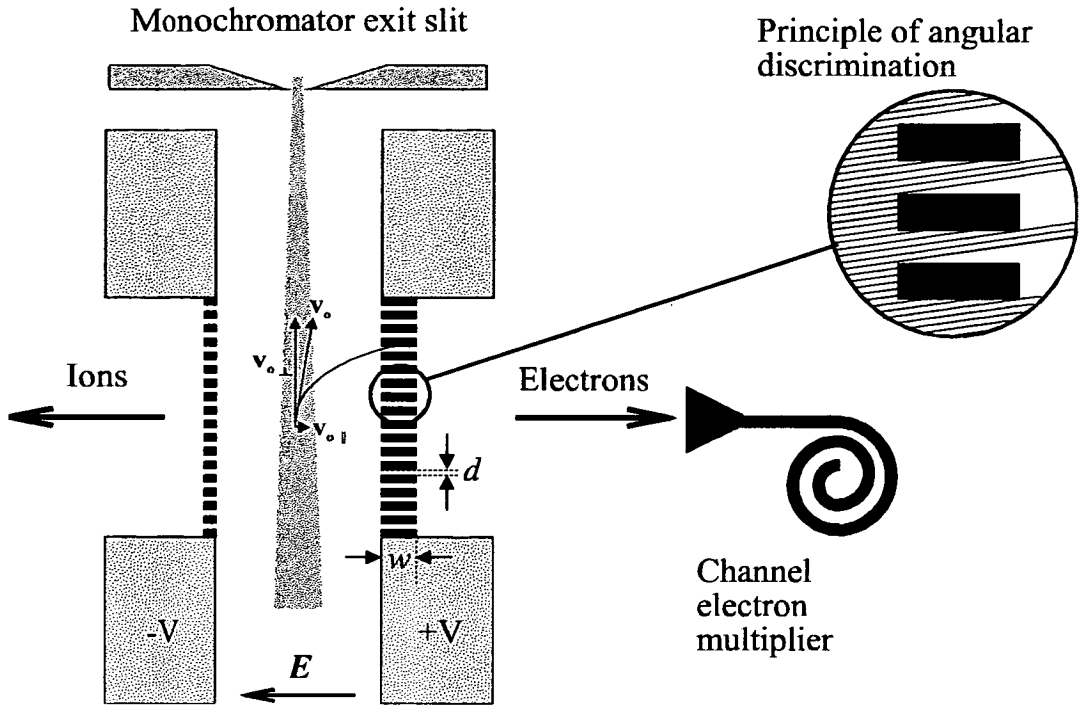

Figure 1-5 Schematic of the steradiancy analyser designed by Spohr *et al.* [22]. Electrons with high initial velocity components perpendicular to the electric field in the interaction region are selectively suppressed by the grid assembly whereas electrons with zero initial velocity component perpendicular to the electric field are transmitted with efficiency equal to the ratio ($A_h/(A_h+A_s)$), where A_h is the area of the holes, and A_s is the solid area.

where $\mathbf{v}_\perp$ and $\mathbf{v}_\parallel$ are the velocity components of the electron at the grid. These two velocity components are easily calculated to be $\mathbf{v}_\perp=\mathbf{v}_{o\perp}$, and $\mathbf{v}_\parallel = \sqrt{\mathbf{v}_{o\parallel}^2 + e\Delta V/m_e}$, where e is the charge on an electron, ΔV is the potential difference across the interaction region, and m_e is the mass of the electron. There are essentially two cases for Equation 1-11 that allow an electron through the grid. (1) the initial energy E_o of the electron is small so both $\mathbf{v}_{o\perp}$ and $\mathbf{v}_{o\parallel}$ are small, and (2) the initial energy E_o is larger, but $\mathbf{v}_{o\parallel}$ is much larger than $\mathbf{v}_{o\perp}$. In Case (1) true threshold electrons are collected however case (2) describes the situation where "hot" electrons which are ejected along the line of sight of the analyser are detected as threshold electrons. Threshold photoelectron and photoion studies by Guyon *et al.* [23] on HF, DF, and F_2 using the analyser described above produced spectra with 12 meV (~100 cm^{-1}) which

compares favourably with typical HeI photoelectron resolutions of 20-35 meV (160-280 cm^{-1}) [24],[25] for HF and F_2 until quite recently [26] (July 1994).

One of the most striking features of the threshold photoelectron spectrum of HF by Guyon *et al.* [23] is the extended vibrational progression seen in the X ($^2\Pi_i$) states of HF^+. The HeI [24] and HeII [26] photoelectron spectra show the Franck-Condon region extends from v^+=0-4, with v^+=0 vibrational level being the most intense (~3 times as intense as v^+=1 [26]), so the potential energy curves for HF and HF^+ are quite similar. However, the TPE spectrum clearly shows 12 vibrational levels [23], the highest 7 of which are not accessible in the Franck-Condon approximation. These additional levels must be populated indirectly via a two stage absorption / autoionisation process, where the super-excited intermediate level is probably a Rydberg state converging to the A ($^2\Sigma^+$) state of HF^+. The intensity distribution for these excited levels is quite erratic but does generally mirror the Franck-Condon profile of the ion state associated with the Rydberg state electronic core. The electronic autoionisation model of Bardsley and Smith [14],[15],[16] is difficult to apply to threshold photoelectron spectroscopy as the model takes no account of the energy difference between the autoionising state and the final ionic state. It essentially only considers the Franck-Condon overlap between the two states. However, in the framework of the Bardsley and Smith model of autoionisation [14],[15],[16], the total threshold photoelectron cross-section σ(E) can be represented as

$$\sigma(E) = \sigma_X \cdot \sum_{v^+=0}^{v^+_{max}} C(E - E_{v^+}) \cdot \left| \langle \psi_{v''} | \psi_{v^+} \rangle \right|^2 + \sigma_{Ryd} \cdot \left| \langle \psi_{v''} | \psi_{v_{Ryd}} \rangle \right|^2 \cdot \frac{\sum_{v^+=0}^{v^+_{max}} C(E - E_{v^+}) \cdot \left| \langle \psi_{v_{Ryd}} | \psi_{v^+} \rangle \right|^2}{\sum_{v^+=0}^{v^+_{max}} \left| \langle \psi_{v_{Ryd}} | \psi_{v^+} \rangle \right|^2}$$

Equation 1-12

where $\psi_{v''}$, $\psi_{v\ Ryd}$, and ψ_{v+} represent the neutral, Rydberg, and ion vibrational wavefunctions, and σ_x and σ_{Ryd} are the electronic transition probabilities for direct

ionisation and photoabsorption to the Rydberg state respectively. E is the photoexcitation energy and E_{v+} is the energy of the accessible vibrational levels of the ion. The function C represents the convolution function for the threshold electron analyser. In essence, Equation 1-12 states that the total threshold electron signal is the sum of all photoionisation and autoionisation contributions, convoluted with the detection function of the analyser. It should also be noted that Equation 1-12 takes no account of neutral dissociation channels which will reduce the autoionisation contribution or the Fano line profile of the intermediate Rydberg state. Finally, the expression is also adequate to represent vibrational autoionisation as this is simply the exchange of vibrational energy between nuclear motion and the Rydberg electron. An example of the features usually seen due to electronic autoionisation is shown in Figure 1-6. Morse curves have been generated using data for HCl/HCl^+ taken from Huber and Herzberg [27] to represent the X ($^1\Sigma^+$), X ($^2\Pi_{3/2}$), and a generic [A ($^2\Sigma^+$)] $nl\lambda$ $^1\Sigma$, $^1\Pi$ Rydberg state. The Rydberg state is assumed to have the same shape as the A ($^2\Sigma^+$) ion state, but lowered in energy. The Franck-Condon factors for photoionisation to the X ($^2\Pi_{3/2}$) ion state and for photoabsorption to the Rydberg state are shown in bold line to the left of the potential curves (labeled (a) and (b)). The vibrational levels are broader in the photoabsorption spectrum to simulate experimental results by Terwilliger and Smith [28] (the levels are broadened by a combination of configuration interaction with the X ($^2\Pi_i$) ion continuum [29], and by spin-orbit predissociation by dissociative states correlating to lower dissociation limits [29],[30].) Spectrum (c) in Figure 1-6 represents the contribution of the Rydberg state to the threshold photoelectron spectrum. As Equation 1-12 is quite complex spectrum (c) was calculated using Equation 1-13, which assumes that the relative Franck-Condon factor to the highest accessible vibrational level is constant with increasing v^+_{max}, that v^+_{max} is the only vibrational level within the convolution function of the analyser, and that there is no contribution from direct ionisation.

$$\sigma(E) = C\left(E - E_{v^+_{max}}\right) \cdot \sigma_{Ryd} \cdot \left|\left\langle \psi_{v''} \middle| \psi_{v_{Ryd}} \right\rangle\right|^2$$

Equation 1-13

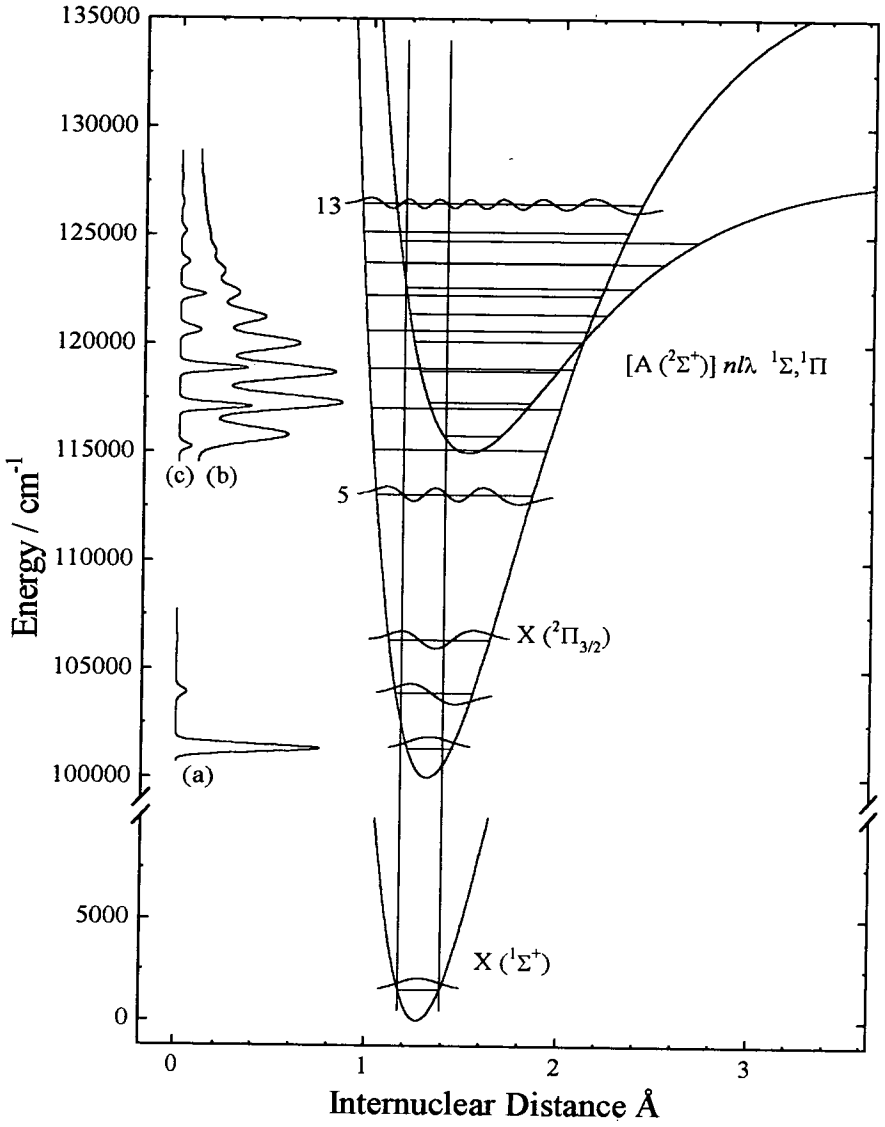

Figure 1-6 Simulated threshold photoelectron spectra showing the direct and indirect ionisation pathways for photoionisation and autoionisation. The potential energy curves are based on HCl/HCl$^+$ data from Huber and Herzberg [27], however the energy position of the curves is only approximate. Spectrum (a) represents the direct contribution to the TPE spectrum from the X ($^2\Pi_{3/2}$) state, (b) is the photoabsorption spectrum for the Rydberg state, and (c) represents the autoionisation contribution to the TPE spectrum.

Clearly the threshold photoelectron simulation due to autoionisation (spectrum (c)) resembles the photoabsorption (spectrum (b)) although the intensity distribution is different.

Threshold photoelectron studies on N_2O suggest there is another possible threshold autoionisation mechanism. In N_2O the X ($^1\Sigma^+$), X^+ ($^2\Pi$) and A^+ ($^2\Sigma^+$) ion states are all linear with similar bondlengths, so the Franck-Condon overlaps between the three states will be maximised for the lowest vibrational level as is seen in the HeI photoelectron spectrum [31]. However, in a threshold photoelectron study of the region between the X ($^2\Pi$) and A ($^2\Sigma^+$) states Baer *et al.* [32] found that threshold electrons were produced in the Franck-Condon gap region between the states where the Bardsley Smith model would predict no threshold electron signal. In these regions up to 3 eV of electronic energy was being converted into vibrational energy but the Franck-Condon factors between the excited Rydberg states and the X ($^2\Pi$) state could not be responsible. Guyon *et al.* [33],[34] have also shown that the threshold photoelectron and fluorescence excitation spectra of N_2O are essentially identical in the 840 - 760 Å (14.76 - 16.3 eV) region. From these observations Guyon *et al.* [33] proposed a second model for autoionisation in polyatomic molecules as shown in Figure 1-7. The photoabsorption step is to either a core-excited bound Rydberg state R_A or a repulsive state D. As the molecule dissociates it can either (1) autoionise to produce a kinetic electron, (2) dissociate to its products which then fluoresce, or (3) interact with high-n Rydberg states $R_X(n)$ associated with the X ionic state to convert the dissociative kinetic energy into vibrational energy. These high-n Rydberg states can then vibrationally autoionise to produce highly excited vibrational levels of the X state with an accompanying near-threshold electron. The model by Guyon *et al.* [33] seems a possible, if complicated, explanation for unexpected structure in threshold spectra.

Increasing the resolution of threshold photoelectron experiments is a constant challenge as increased resolution will reduce the number of autoionising features in the spectra and allow the study of heavier molecular systems. Experiments gradually evolved from steradiancy techniques using angular discrimination to time of flight techniques using pulsed light sources and a continuous extraction field. Synchrotron radiation sources can be operated in a pulsed mode where typically the light pulses are of 500 ps duration and occur every 300 ns. Electrons ejected in the ionisation pulse are accelerated towards a multichannel plate detector and arrive at different times according to their initial kinetic energy. The use of electronic time gating in the

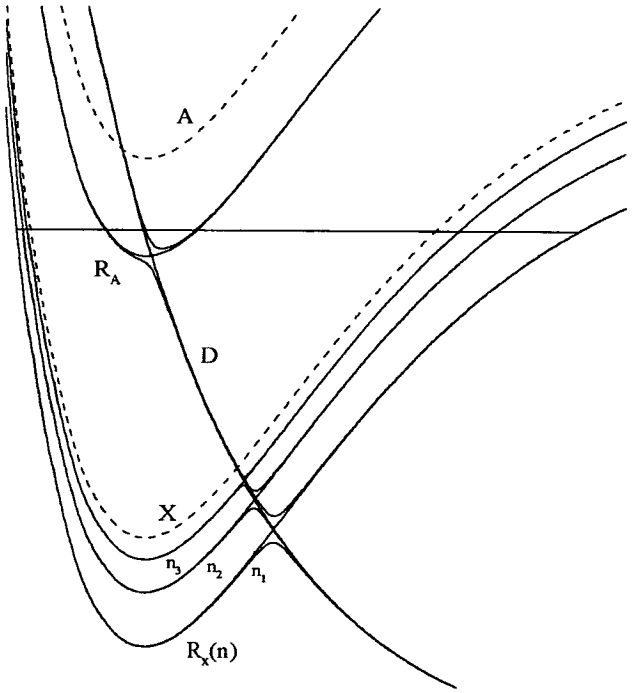

Figure 1-7 Schematic of the threshold ionisation mechanism proposed by Guyon *et al.* [33]. The Rydberg and ion states are represented by the same Morse potential. The electronic energy of Rydberg state R_A is converted into high vibrational levels of the X state by (1) predissociation of R_A by dissociative state D, (2) the interaction of D with vibrationally excited levels of high-*n* X Rydberg states, and (3) the vibrational autoionisation of these high-*n* Rydberg states to the X state of the ion. The net effect of the ionisation scheme is the transfer of a large amount of electronic energy into vibrational energy, so the ejected electron is close to threshold.

detection electronics allows only electrons with zero initial kinetic energy to be counted. An example of this technique is TPE studies of oxygen and N_2O by Guyon *et al.* [35] and Baer *et al.* [36] where the resolution of the photoelectron spectrometer was approximately 10 meV.

More recently the resolutions achievable in threshold photoelectron spectroscopy have increased considerably. In laser based (time-of-flight) TPE experiments the resolution achievable is of the order of 10 cm^{-1} [37] where the increase in resolution is mainly achieved from the narrower photon bandwidth. However, laser radiation sources are limited to relatively high photon wavelength compared to synchrotron sources so ionisation generally requires the absorption of more than one photon, and this can complicate the final spectra. The time-of-flight methods using synchrotron radiation require the synchrotron to operate in a pulsed mode [38],[36] which is not suitable for most synchrotron experiments. The penetrating field electron spectrometer [39],[40],[41] used in this work combines high collection efficiency (threshold electrons are collected over 4π steradians) with high resolution (down to 2 meV FWHM [42]) and operates without using time-of-flight techniques. This makes the spectrometer ideal for threshold photoelectron studies of molecular states not easily accessible by laser based techniques. The penetrating field electron spectrometer is discussed more fully in Chapter 2 and so will not be described here.

1.2.6 Zero kinetic energy photoelectron spectroscopy

The use of pulsed VUV sources such as radiation from a synchrotron operating in single bunch mode or pulsed laser systems allow electron spectra to be recorded by time of flight techniques. Figure 1-8 shows a schematic of the general principles involved in time of flight electron spectroscopy. A short duration light pulse (20 ns or faster) ionises gas molecules in the ionisation region. Ejected electrons gradually disperse according to their initial kinetic energies. At a later time an electric field is applied across the ionisation region and all remaining electrons are extracted down a time of flight tube towards the multichannel plate detector.

Electrons with initial velocities directly opposite to the flight tube arrive at the MCP detector first as they are accelerated most. An electronic gate is used to record only the threshold electrons from the time of flight spectrum. The resolution achievable with this technique is ideally equal to the photon bandwidth.

The unprecedented resolution of this technique was first shown in the Zero kinetic Energy (ZEKE) spectrum of NO, where individual rotational levels of the ion were resolved [43],[44] whereas previous conventional photoelectron studies resolved only vibrational structure [31]. The ionisation potential of NO had previously been derived from VUV absorption spectroscopy [45], however the ionisation potential obtained from ZEKE spectroscopy [43] was about 3 cm^{-1} lower than by Rydberg extrapolation [34]. This discrepancy was resolved as being due to the combination of stray electric fields in the interaction region and the dynamics of the ionisation process itself. Figure 1-9 shows the electronic potential energy diagram

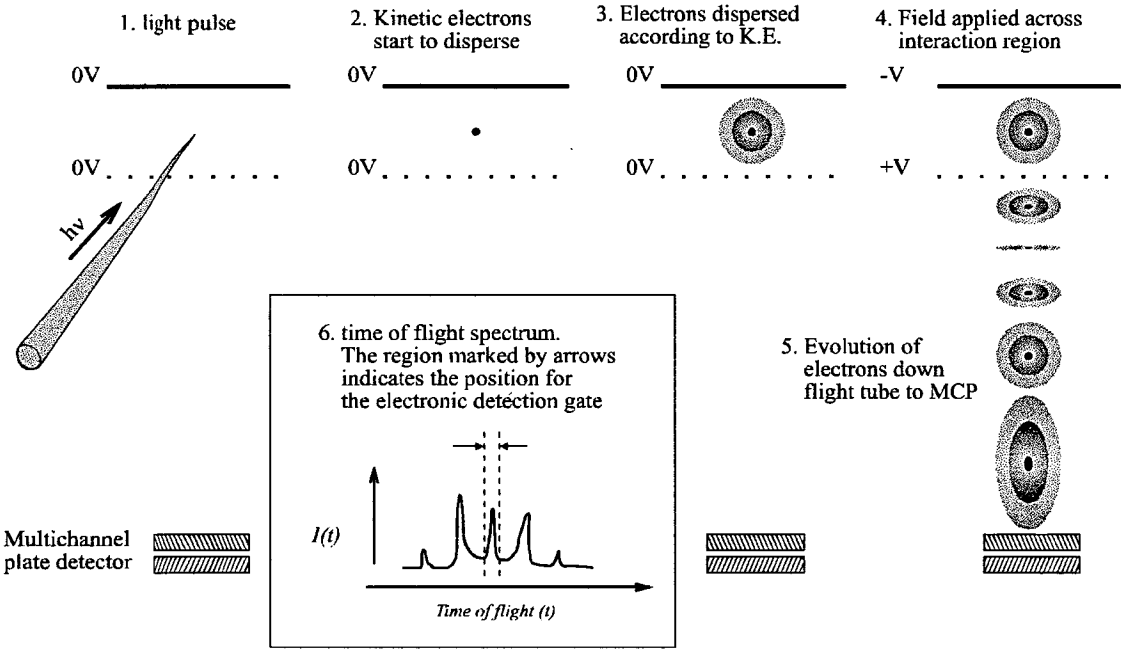

Figure 1-8 Schematic of a typical time resolved threshold photoelectron experiment. The numbering scheme in the figure represents the evolution of time with respect to the light pulse. Kinetic electrons are discriminated as they arrive at the multichannel plate detector at different times than the zero energy electrons.

for an electron under the electric field of an ion core. The Coulomb potential experienced by the electron when no external fields are present ($V_o(Z)$) is represented by the dotted curves. The modified Coulomb potential due to small stray fields (or a small applied d.c. field) is shown as the solid curves ($V_s(Z)$), and the modified Coulomb potential due to the application of a stronger delayed electric field ($V_d(Z)$) is shown as the dashed curves. A Rydberg series converging to the stray field ionisation potential is also shown. The shift in the ionisation energy due to the stray electric field is $\delta_s = c\sqrt{F_s}$ (i.e. the Stark effect),[7],[10], where F_s is the stray electric field and c is a constant. The depth of Rydberg states probed by the delayed ionisation pulse is given by $\delta_d = c\left(\sqrt{F_d} - \sqrt{F_s}\right)$, where F_d is the delayed ionisation pulse. In many ZEKE experiments a small d.c. electric field is applied to lower the ionisation potential in the same way as the stray field does. Measuring the ionisation potential as a function of the d.c. field allows extrapolation to the field free ionisation potential.

The d.c. fields used in ZEKE spectroscopy should also affect threshold photoelectron experiments, lowering the observed ionisation potential from that of the field free value. However, threshold photoelectron experiments are typically at lower resolution than the field ionisation shift as the extraction fields used in a d.c. threshold photoelectron experiment are typically 10 times smaller than those used in ZEKE spectroscopy. Also, the TPES work in this thesis uses a continuous extraction field, so no delayed field ionisation can take place. ZEKE-PFI and threshold photoelectron spectroscopy can be viewed as approaching the true ionisation potential from opposite sides. In TPES low energy electrons are collected and detected, whereas in ZEKE the detected electrons are produced by delayed field ionisation. So the ideal TPES and ZEKE experiments should yield the same results. A major driving force behind the need to increase resolution in TPES is to ensure that this is indeed the case.

Studies of pulsed field ionisation by Muller-Dethlefs *et al.* [43],[44] have shown that a typical ZEKE experiment only yields electrons within ~5 cm^{-1} of the field free ionisation limit. The principal quantum number for a Rydberg state within 5 cm^{-1} of the ionisation limit is greater than 150. Chupka [46] has shown that in a typical ZEKE experiment with stray electric fields, the lifetime of high-n Rydberg states should behave as $\tau(n) \propto n^x$, where x ranges somewhere between 4 and 5. When no electric fields present the lifetime varies as n^3 [7]. The increase in the lifetime of these high-n states is due to Stark mixing [46],[10] of the various nl Rydberg states. This process tends to create Rydberg states with high-n and high-l quantum numbers. The

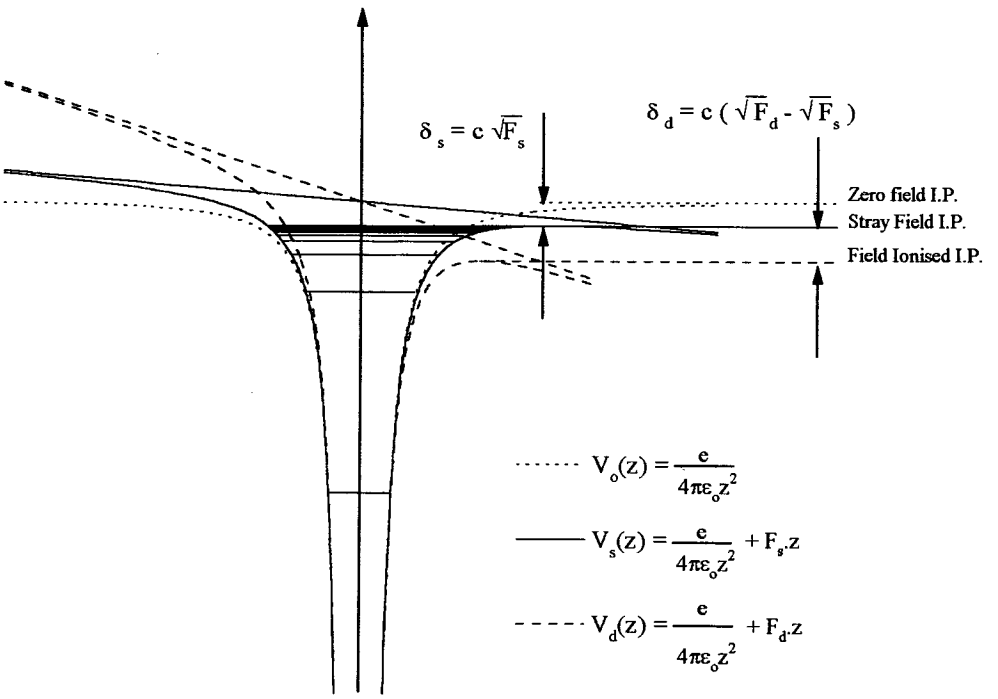

Figure 1-9 Potential energy diagram illustrating the field ionisation effect for high-n Rydberg states in atoms and molecules. The dotted curves represent the field free Coulomb potential ($V_o(Z)$). The solid curves mimic the modified Coulomb potential due to stray electric fields in the ionisation region, or an applied d.c. electric field ($V_s(Z)$). The dashed curves show the change in the Coulomb potential when a strong electric field is applied after a delay ($V_d(Z)$) . Rydberg states above the saddle point in $V_d(Z)$ are no longer bound and decay producing field ionised electrons. These electrons are detected as ZEKE electrons.

electron thus collides less frequently with the ion core and the states are therefore longer lived [46]. Vrakking and Lee [47],[48] have shown a $\tau(n) \propto n^{4.17}$ dependence for p series Rydberg states in NO confirming that Stark mixing is a dominant mechanism in ZEKE spectroscopy.

The use of ZEKE spectroscopy with pulsed synchrotron radiation is still in its infancy but looks promising. Currently spectral resolutions are limited by a combination of photoexcitation bandwidth and the high repetition rate of the synchrotron source. The repetition rate of the BESSY synchrotron radiation source is 4.8 MHz (208 ns between pulses) [49] whereas a typical laser based ZEKE experiment operates at 10 Hz [50] and the high repetition rate of synchrotron sources limits the time available for low energy electrons to disperse. Currently the highest resolution reported for a synchrotron ZEKE experiment is 35 cm^{-1} [51] so the technique is approaching the resolution of the penetrating field electron spectrometer. However, synchrotron ZEKE uses the synchrotron in *single bunch* or *gapped beam* mode which is often not suitable for other experimenters and has lower photon intensity, making data collection times longer.

1.2.7 High energy ionisation techniques

The resolving power ($\Delta R/R$) of many spectroscopic techniques is approximately constant for the variable R. For instance, even in an ideal threshold photoelectron experiment the spectral resolution decreases with decreasing excitation wavelength ($\Delta\lambda/\lambda$ = const.), and in conventional photoelectron experiments the highest resolution spectra are obtained when the excitation energy is close the ion internal energy as this minimises the energy of the ejected electron ($\Delta E/E$ = const.). However, excitation energies close to resonance can distort the observed spectrum as the electronic transition moment is unlikely to remain constant over the region of interest [52]. Excitation well away from resonance removes this problem and allows the true intensity of spectral features to be measured, however the resolution for these techniques is low. Generally, vibrational resolution is not achievable using high

energy excitation, however useful information can be extracted from the shape and intensity of the observed electronic bands. Typically a broad band (i.e. broader than the instrument linewidth) will indicate that the internuclear distance changes upon ionisation as would be expected from the Franck-Condon principle. The intensity of the various bands gives information on the probability of ionisation to each electronic state, and is often referred to as the *pole strength* or *spectroscopic factor* [53]. If the electrons within the molecule were truly independent each ionic state would give rise to a single peak in the spectrum and the pole strength for each state would be 1. However, electron motion will be correlated to some extent so that some relaxation will take place during the ionisation event which will result in a reduction in pole strength.

The removal of inner valence or core electrons results in large changes in the spectra from that of a single spectral peak for each electronic level. Typically many ionisation features are observed for the removal of an electron from a single molecular orbital. These features are normally spread over several eV of energy and so they are not attributable to one final ion state. Instead they are ascribed as the relaxation of molecular orbitals after creation of a hole in a deep lying orbital. These *shake-up* satellite states can be described as *2 hole - one particle* electron configurations, where the holes and particles refer to the change in the electron distribution compared to the lowest energy neutral state. i.e. a 2h-1p state will have two electrons removed from the initial configuration, one of which is excited into an unoccupied molecular orbital and the other is ejected to form the ion. Typically the excited electron will be in a Rydberg state converging to the doubly charged ion. As these 2h-1p states are not accessible within the independent electron approximation they are formed by electronic configuration interactions in either the initial state or the final state. Final state interactions are the most common and give rise to the complex multipole structure seen in the hydrogen halides [54],[55],[56] except for HF [57]. The electronic structure of the states formed during inner valence ionisation in the hydrogen halides is of interest both theoretically [58] and experimentally for the reasons above.

1.3 The hydrogen halides and fluorine

Previous studies on the halogens Cl_2, Br_2 [59], I_2 [60], and CF_4 [61] by the group have shown that the penetrating field threshold electron spectrometer is a useful and informative tool in the study of small molecular ions. It has also proven reliable and durable to chemical attack from quite aggressive gases. Molecular fluorine represents a significant challenge to any spectroscopic technique, however a study of F_2, combined with previous threshold photoelectron results, will create a complete set of results consistant spectra for the halogens. The hydrogen halides are also chemically aggressive molecules, so also represent a significant challenge to threshold photoelectron spectroscopy. The large rotational constants [27] for the HX and DX systems make them ideal test molecules for pushing the threshold photoelectron technique towards rotational resolution. From a molecular physics stand point the hydrogen halides should show similar characteristics to the noble gases, for instance argon and HCl are identical in the united atom approximation, so HCl and Ar should have similar gross spectroscopic features. However, the finer details of the spectra should be very different. For instance, energy transfer between the electronic and nuclear motions is possible in a molecule but not for an atom. The influence of these coupling processes on the spectroscopy and dynamics of simple molecular systems is of great interest.

The relative simplicity of the HX molecules should also make their threshold photoelectron spectra relatively simple to analyse, with a view to extracting information on electronic-vibronic energy coupling. For instance, there is very little information available on the preferred threshold ionisation dynamics of a molecule when electronic and vibrational energy exchange is involved. Assuming autoionisation occurs via a bound Rydberg state, it would be interesting to see if Rydberg states of particular symmetry are more dominant in threshold ionisation, and it may be possible to test the autoionisation models against a large class of consistent spectroscopic data. The combined analysis of the HX and DX spectra is also a useful

tool to check previous spectral assignments. Also, differences in the TPE spectra due to the different reduced mass of the isotopomers can be investigated.

In short, the TPE studies of the hydrogen and deuterium halides represent a unique opportunity to investigate threshold photoelectron phenomena to (1) attempt to understand more fully the ionisation mechanisms involved, (2) develop further the threshold photoelectron apparatus towards higher resolution and increased usability, and (3) use the non-specific ionisation pathways to increase the number of observed spectroscopic features in these molecules. The threshold photoelectron spectrum of fluorine also represents a significant challenge. Fluorine remains unstudied by ZEKE spectroscopy, effectively because of its toxicity and high ionisation potential. Also, attaining a high quality threshold photoelectron spectrum of fluorine may indicate spectroscopic regions where higher resolution ZEKE studies would be beneficial. Finally, and by no means least, the threshold photoelectron study of fluorine represents the completion of an ongoing program of research within the group.

Chapter 2. Experimental aspects

2.1 Daresbury Laboratory - The facility

The Daresbury Laboratory lies south of Daresbury village about 4 miles West of Warrington, in Cheshire. The village is famous as the birthplace of Lewis Carroll. The bedrock in the area is red sandstone which is very stable to seismic shock waves. The site itself has two facilities, the Nuclear Structure Facility, which conducted nuclear physics experiments using fast ion beams of energies up to 10 MeV, and the Synchrotron Radiation Source, or SRS, which was the first synchrotron radiation facility built solely to utilise the output radiation.

The Synchrotron Radiation Source consists of a linear electron accelerator (Linac), which accelerates a stream of electrons up to 12 MeV, a booster electron ring, which increases the electron energy to 0.6 GeV, and finally the storage ring itself. The storage ring consists of sixteen straight sections each separated by bending (dipole) magnets. Electrons are injected into the storage ring from the booster ring in short bursts at defined time intervals until the storage ring contains 160 bunches of electrons and a typical current of between 150 and 300 mA. Radio frequency radiation is used to accelerate the electrons around the storage ring and to ramp the electron energies up to 2 GeV. When an electric charge accelerates it emits radiation perpendicular to the accelerating direction, as described by electromagnetic theory [62],[63],[64]. So, light is emitted at each of the 16 bending magnets, and as the electrons are traveling at relativistic speeds most of the radiation is emitted as a narrow beam in the forward tangent to the electron orbit [62]. The electrons lose kinetic energy at each bend but this is replenished by R.F. radiation from the clystron. The entire synchrotron is timed so that each of the 160 packets of electrons is

separated by 2 nanoseconds and the orbital period of each packet is 320 nanoseconds. For the purposes of the experiments in this thesis the pseudo-continuous nature of the synchrotron light source can be neglected and the light source is considered continuous in time.

2.1.1 Beamline 3 and endstation 3.2

Usable radiation from the SRS extends from the infra-red to hard x-ray energy region. The position of the flux maximum is intimately related to the kinetic energy of the electrons in the storage ring and the power of the bending (dipole) magnets[a]. Synchrotron radiation produced at each bending magnet is transported to the experimenter (or user) via a beamline. Each beamline is optimised for a specific photon energy range of synchrotron radiation. Beamline 3 at the SRS is optimised for photon energies in the ultra violet to soft x-ray region (5-150 eV).

All the experimental results presented in this thesis were completed using endstation 3.2 at the SRS. This station is optimised for the high resolution study of gas phase samples where the required photon energy is between ~10 and 30 eV. The beamline has been characterised by Holland *et al.* [65] In essence, radiation from the storage ring is reflected by two silicon carbide mirrors before entering a 5 metre normal incidence monochromator (McPherson monochromator). The monochromator contains a concave diffraction grating with a line ruling of 1200 lines per inch. Light output from the monochromator enters a mirror box which deflects the light beam 20 degrees sideways using a gold coated mirror and focuses the light to the centre of the exit port on the mirror box. Finally, the experimental apparatus is attached to the mirror box.

The monochromator can be used with either of 2 gratings, however during the course of these experiments only the "high energy" grating was used. The photon

---

[a] see [62] for typical spectral output from synchrotron radiation sources and a general introduction to synchrotron radiation research, also, much more information on the SRS and Synchrotron Radiation itself is currently available at http://www.dl.ac.uk and Web pages within.

flux as a function of photon energy was measured during the course of this work and is presented in Figure 2-1. Usable output radiation from this grating extends from ~10 - 35 eV peaking at around 23 eV. The absolute photon flux was not measured, however the station characteristics have been reported by Holland *et al.* [65].

The synchrotron, beamline 3, and station 3.2 are all operated under high vacuum ($\leq 2\times10^{-9}$ mBar) for two reasons: firstly, the high vacuum conditions are necessary to maintain the circulating electron beam in the synchrotron for long periods (up to 24 hours), and secondly, station 3.2 is optimised for experiments in the vacuum ultra-violet (VUV) energy region where atmospheric oxygen and nitrogen

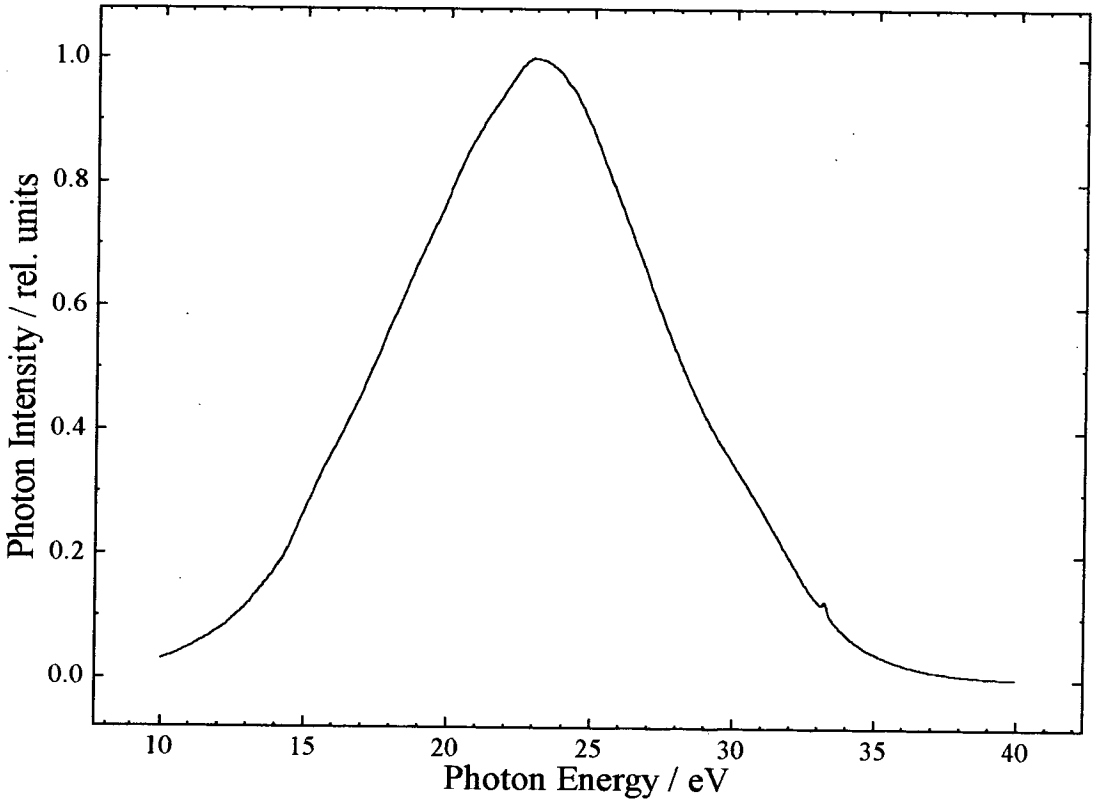

Figure 2-1 Relative photon intensity as a function of photon energy as measured from the output of station 3.2 using the high energy diffraction grating in December 1994. Measured using a stainless steel mesh as detector, the output current was amplified through a Keithley Electrometer and recorded using the standard grating scan / data acquisition program supplied by the Daresbury Laboratory.

strongly absorb radiation. This makes the study of gas molecules using photon energies greater than ~10 eV difficult to achieve as the sample gas pressures normally required in these studies are normally many orders of magnitude above $2x10^{-9}$ mBar (the background pressure in the experimental chamber is typically 1×10^{-4} mBar). For experiments below 10 eV it is normal to position a vacuum sealed lithium fluoride window between the experiment and the monochromator, however, the high energy transmission cut off for LiF is around 110 nm (11 eV), so a window is not suitable for energies in the 10-30 eV range. A windowless system using differential pumping must be used instead and is discussed below.

A glass capillary, ~300 mm long by 1mm bore, is positioned between the station mirror box and the experimental chamber as shown in Figure 2-2. A vacuum seal separates the two chambers except for the capillary bore. Synchrotron radiation then passes through the bore of the capillary into the experimental chamber. The normal working pressures for the experimental chamber, mirror box, and the monochromator, in typical experimental conditions, are shown in Figure 2-2. The integrity of the vacuum for the beamline and the storage ring is protected from unexpected pressure rises by electrical circuitry which closes a pneumatic gate valve between the mirror box and the monochromator if the pressure in the mirror box rises above $\sim1x10^{-6}$ mBar.

A schematic of the layout of the synchrotron, beamline 3, and station 3.2 detailing much of the above is shown in Figure 2-2. It should be noted that the absolute orientation of some of the components in this figure is not as drawn. The experimental chamber, mirror box, and the beam transfer mirror boxes are represented in plan view, the storage ring in a perspective view, and finally the monochromator is in side view, but drawn upside down. (the monochromator is vertically dispersing).

An indication of the scale of the facility is as follows: The storage ring is ~30 metres in diameter and the entrance slit of the monochromator is ~10 metres from the tangent to the storage ring. Endstation 3.2 is positioned about 1.5 metres above the building floor on a steel gantry and has floor-space similar to a small laboratory. The

entire synchrotron is housed in one large open-plan building where approximately 40 endstations attached to the storage ring can be in use at any given time. This has important safety implications, particularly for studies on hazardous gas samples, as many other experimenters in the vicinity are often unaware of the hazards involved in different experiments. This is the main reason for the use of minimal quantities of gas samples in these studies, as described later in this chapter.

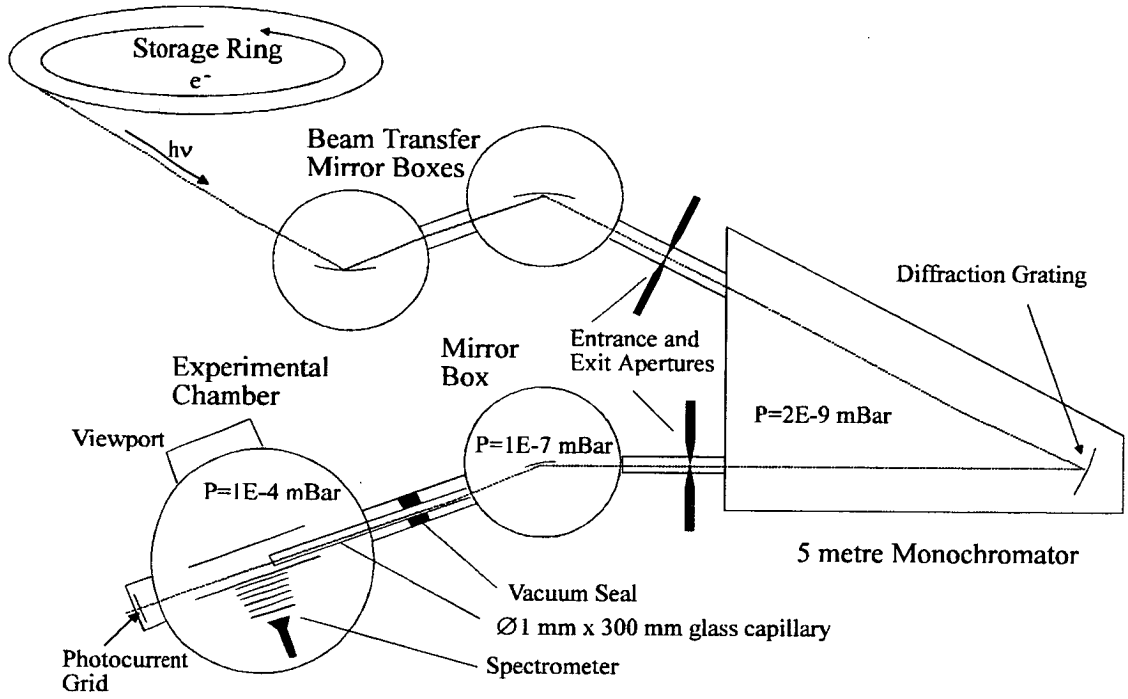

Figure 2-2 Schematic of the Synchrotron, Beamline 3, and Station 3.2 experimental layout for the Threshold Photoelectron experiments.

2.2 The experimental vacuum chamber and associated peripherals

Figure 2-3 shows a schematic of the apparatus used in the threshold photoelectron experiments at the Daresbury Laboratory. The vacuum line, or gas handling line, was constructed entirely of 1/4 inch stainless steel tubing using all metal Nupro valves from Swagelok [66]. A four litre stainless steel cylinder from Swagelok was fitted with a -1 to 2 Bar dial gauge, and a Baratron gauge was attached to the gas

handling line itself. Two *double* stainless steel needle valves from Swagelok (M series flow characteristics) were used to regulate the flow of gas into the experimental chamber. One needle valve controlled the flow of the study gas and the other controlled the argon calibration and tuning gas. The gas handling system was designed so that argon / experimental gas mixtures could be studied when desired without the need for pre-mixing. A Baratron gauge was used to monitor the inlet pressure to the chamber which was typically ~2 mBar during experiments.

Gas entering the chamber does so effusively though a 0.8 mm bore platinum capillary coated externally with colloidal graphite. The capillary is electrically isolated from the rest of the apparatus, and the electrical potential applied to the capillary can be adjusted from outside the chamber. The gas pressure inside the vacuum chamber was monitored using a Penning gauge[b], and gas purity and leak testing of the apparatus (including the gas handling line) was conducted using a Hal 100 quadrupole mass spectrometer (0-100 a.m.u.) manufactured by Hiden Analytical [67] and on loan from the Daresbury Laboratory.

Two layers of mu-metal shielding were employed to exclude the earth's magnetic field as is common in most electron spectrometers. (see for instance Baltzer *et al.* [73]) The electron spectrometer itself was mounted on an electrically isolated cradle. The position of the cradle was adjustable with respect to the chamber itself to allow accurate alignment of the spectrometer with the external ports to the chamber. A four inch diameter glass viewport was used to align the entire vacuum chamber assembly with the glass capillary. The capillary was fastened to the end of the beamline mirror box, and a flexible bellows sealed the chamber to the mirror box (see Figure 2-2). The tip of the capillary was positioned ~15 mm back from the exit line of the gas beam. The end of the glass capillary was coated with colloidal graphite to

---

[b] 3 penning gauges were fitted as the corrosive nature of the gases of interest results in the active lifetime of gauge filaments being typically 1 week.

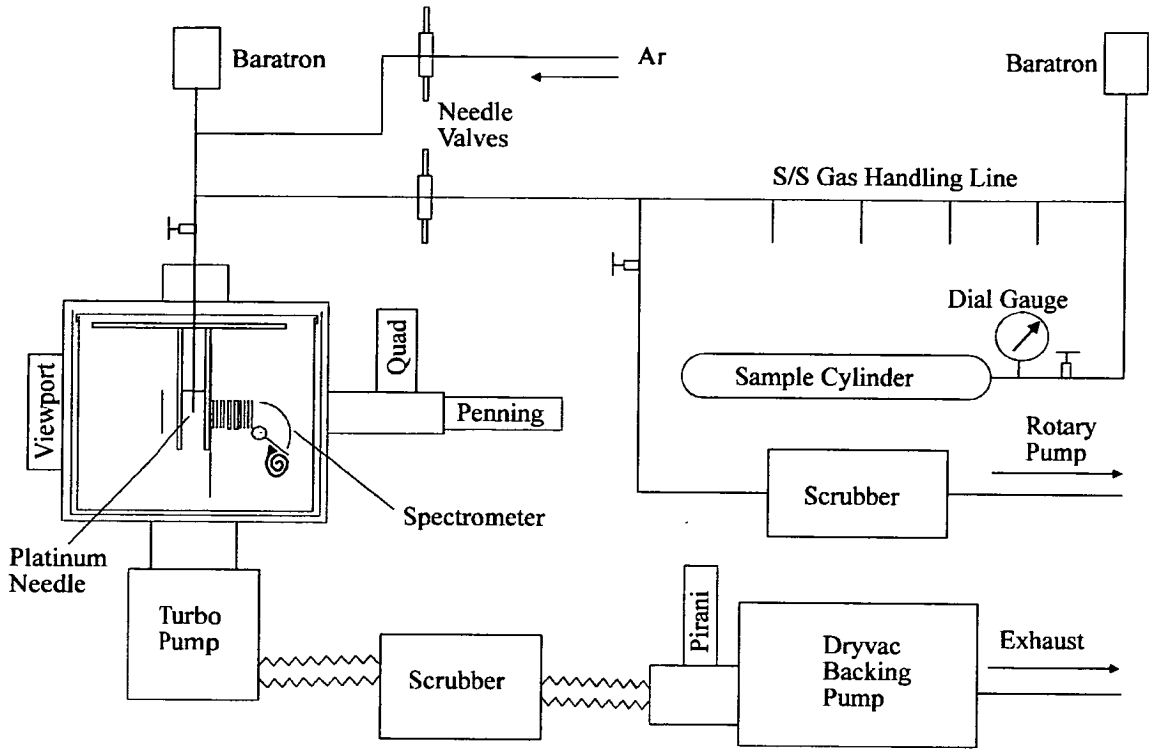

Figure 2-3 Schematic of the Experimental Chamber and associated peripheral apparatus for the Threshold Photoelectron Experiment. Radiation from the synchrotron enters from behind the plane of the page.

minimise stray (or patch) electric fields caused by electrical charging of the end surface of the capillary.

Flow of gas through the experiment was maintained using a Leybold 340M magnetic Bearing Turbo Pump, backed by a Leybold Dryvac 25B dry bearing Rotary pump [68]. Activated graphite filter canisters were fitted as shown in Figure 2-3 to remove the toxic and corrosive exhaust gases from the beamline exhaust system.

2.3 The threshold electron spectrometer and associated electronics

2.3.1 Overview of the Spectrometer

A schematic of the Threshold Electron Spectrometer used in this work is shown in Figure 2-4. The design is similar to the Penetrating Field Electron Spectrometer published by King *et al.* [69], and the later modified design for ion - electron or electron - electron coincidence studies by Hall *et al.* [70]. The

spectrometer used in these studies was originally built by Dr. A. Hopkirk, CLRC, Daresbury Laboratory in 1992 and has proven extremely robust; most of the components are unchanged from the original build. Essentially it consists of a Penetrating Field Extraction stage, two asymmetric lens stages with integral deflection assemblies, and a 127° cylindrical deflection analyser stage. Detection of the transmitted electrons is accomplished using a channeltron and single event counting electronics, all supplied by the Daresbury Laboratory. The lens elements are made from molybdenum allowing them to be thin yet robust while much of the support structure is aluminum, both materials are non-magnetic.

The electrostatic properties of the 127° cylindrical deflection analyser have been previously published [71],[72]. They show both analytically and experimentally that the best re-focusing of electrons entering a radial 1/r electrostatic field occurs at 127°17′, the reason why the 127° analyser is often used in electron spectrometry (it is also considerably easier to manufacture than a 180° hemispherical analyser). The electrostatic properties of the penetrating field region and the lens assembly are discussed in section 2.3.3.

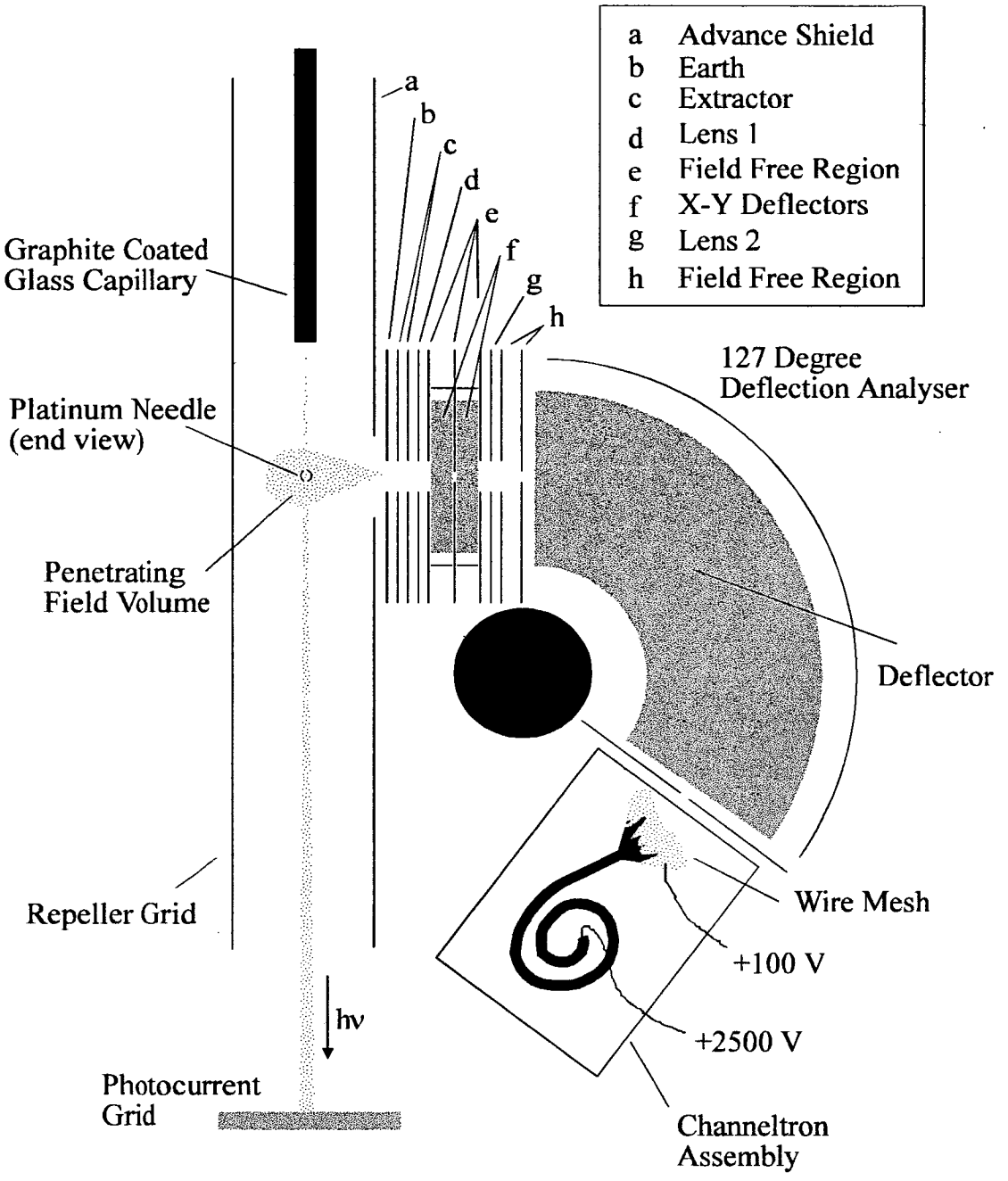

Figure 2-4 Schematic of the Penetrating Field Threshold Electron Spectrometer used in the current work shown in plan view. Support plates and insulating components have been omitted from the diagram. The lens elements have ∅5 mm holes while the three lens apertures are ∅1 mm. The linear lens assembly is ~50 mm long and the cylindrical defection analyser has a mean radius of 25.4 mm. The tip of the capillary was 15 mm back from the electron lens axis, the tip of the platinum needle was 2.5 mm above the electron lens axis, and the first lens element was 12.5 mm back from the photon beam axis.

2.3.2 Surface potentials : the problems and solutions.

Generally the electrical potential supplied to the bulk of a material will not be the same as the surface. The difference can be attributed to impurities on the surface which may make the surface slightly insulating allowing charge build-up and hence a potential difference to develop between the surface and the bulk. This development can take place over a period of hours or days as reported by Baltzer *et al.* [73] and is heavily dependent upon the gas to which the surface is exposed. One method to minimise these surface charge build-ups is to coat the electrode surface in colloidal graphite as in the work by Baltzer *et al.* [73], Gallagher and York [74], and Osborne *et al.* [75]. The first two papers ([73],[74]) also report the effect of radiation dosage on surface potentials, with Baltzer *et al.* [73] concluding that scattered light can have a large influence on the change of surface potentials over time.

Two conclusions can be drawn which are relevant in threshold electron spectroscopy. Firstly, coating of the spectrometer electrodes will decrease surface potential variations, and secondly, the surface potentials will drift over time, so the bulk electrode potentials will have to be re-optimised to compensate for this drift as discussed in section 2.4.

2.3.3 SIMION simulations of the electron lens assembly

The threshold electron spectrometer is not only highly efficient at detecting electrons close to zero energy but also has good suppression characteristics for non-threshold (or kinetic) electrons. SIMION v.4 [76] simulations presented in Figure 2-5 show the main features of the lens assembly for different electron initial energies. SIMION is an ion lens simulation program that allows the user to create electrodes in a X-Y array, and apply electrical potentials to these electrodes. The program then creates a potential array by using numerical solutions to Laplace's Equation ($\nabla^2\varphi = 0$ [64],[77] where φ is the electrostatic potential). Finally ion (or electron) trajectories can be calculated from the potential array using the classical equations of motion for charged particles in electric fields.

In the present simulation the electrodes were created in cylindrical mirrored symmetry to match that of the lens system. It should be noted that the platinum gas inlet needle and the glass capillary cannot be included in the simulation and these will act as a perturbation to the ion trajectories. However, the principles of operation of the spectrometer are most easily described by simulation.

Simulation (a) in Figure 2-5 shows the electron trajectories of a 1 meV electron in the lens system. The potentials on the electrodes have been optimised to maximise transmission of electrons with this energy while maintaining the extractor electrodes voltages to 10 V (see Figure 2-4 for position of the extractor electrodes). In all simulations the electrons are released mid-way between the repeller plate and the earth with only the polar angle between the lens axis and the initial direction of the electron allowed to vary (from 5° to 175° in 17° increments). By examining simulations (b) through (f) it is clear that fewer initial electron trajectories can successfully exit the lens system as the initial electron energy is increased.

The simulation also shows that the penetrating field electron extraction system is highly efficient, collecting threshold electrons over 4π steradians for electron energies below 10 meV. Simulation (a) also contains equi-potential contour lines within the penetrating field region, which indicate the rapid drop-off in electric field strength across the penetrating field region. Finally, it must be noted that even with 20 meV energy electrons some trajectories successfully exit the lens system, and hence the 127° cylindrical deflection analyser is used to suppress these energetic electrons from the final electron signal.

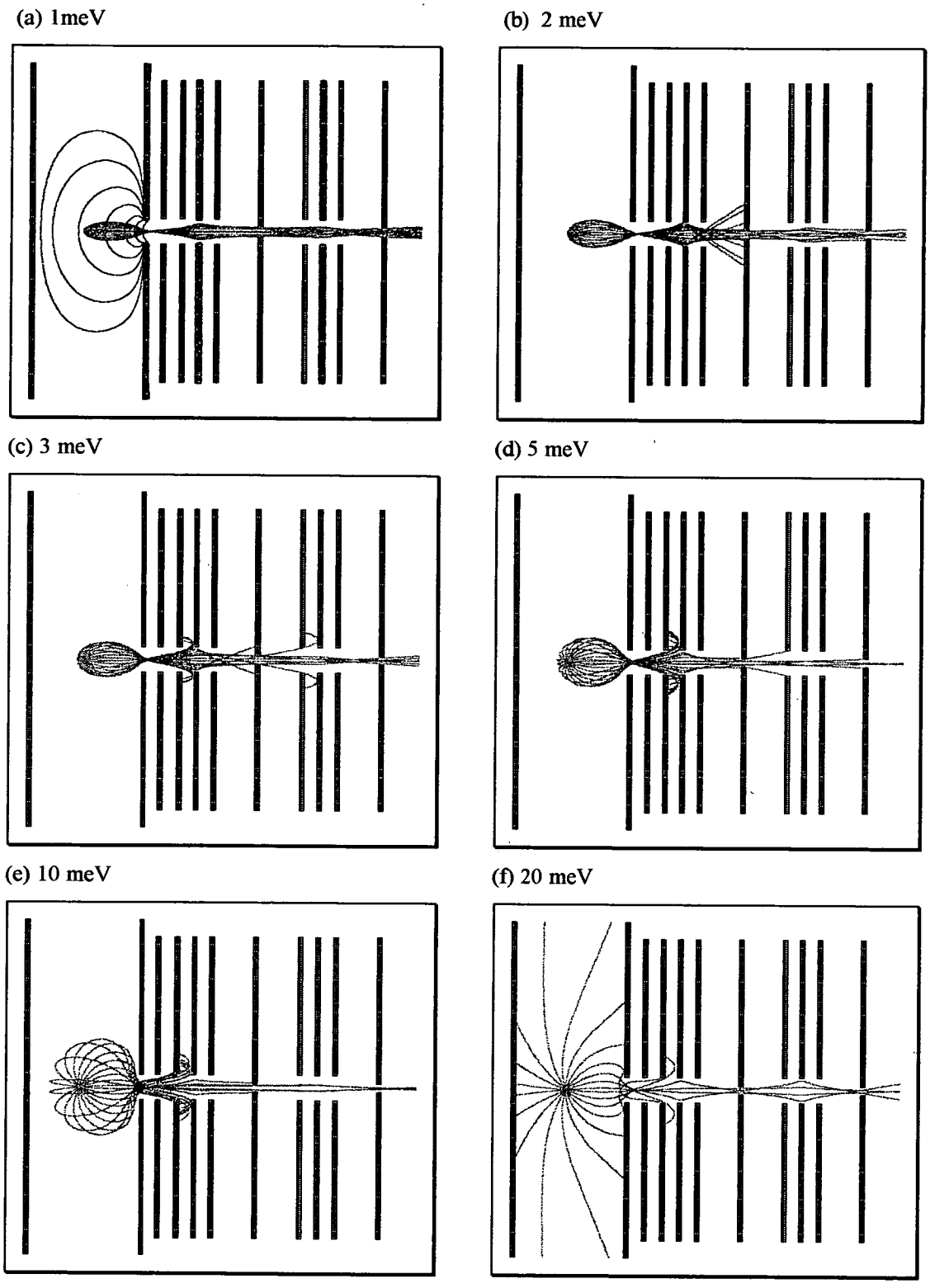

Figure 2-5 SIMION 4 simulations of the penetrating field electron spectrometer and the linear lens assembly. The text above each simulation indicates the initial electron kinetic energy. Simulation (a) also shows equi-potential contour lines for the penetrating field region, from left to right the space potentials of these lines are: 0.001, 0.003, 0.01, 0.03, 0.1, 0.3, and 1.0 volts.

2.3.4 Electrical power supplies and single event counting electronics

The main power supply to the apparatus was constructed by the electronics workshop at the Daresbury Laboratory to a design submitted by Dr. George King, University of Manchester, Department of Physics. The power supply is specifically designed to allow all the electrical potentials supplied to the various lens elements to be adjustable. All electrodes are supplied from a +100 V and -100 V DC reference within the power supply and the supply is constructed so that all potentials can be switched in sign (+ve to -ve and vice versa) allowing the spectrometer to be used to detect threshold cations when appropriate. Output voltages within the supply are designed to have a ripple / hum of less than 5 mV, which is necessary to achieve high resolutions with the spectrometer. Much of the detail of the wiring is not relevant for this thesis, however one feature of interest is the wiring arrangement for the X-Y deflector assemblies within the electron lens. These electrodes are wired using dual potentiometers which vary +v and -v from a variable reference voltage V, which is the potential supplied to the field free region (see Figure 2-4 for positions of electrodes). Although this wiring scheme is quite complex it is necessary for the effective operation of the spectrometer.

The electron detection electronics are shown schematically in Figure 2-6. Two high voltage power supplies (+100 V and +2500 V) are connected to the cone and signal parts of the channeltron. The +100 V potential is needed to accelerate electrons exiting the 127° cylindrical defection analyser into the channeltron. An electron cascade striking the signal end of the channeltron causes an instantaneous drop in voltage on the +2500V line. This voltage *spike* (typically ~25 mV and 10 ns duration) is transmitted through the capacitor to the Phillips preamplifier where it is amplified with a x50 gain. The preamplifier and capacitor circuitry, and associated noise filtering electronics, were constructed by the University of Manchester, Department of Physics. Output pulses from the preamplifier are further amplified by an Ortec amplifier (x2 gain) before being input to an Ortec constant fraction discriminator. This converts the spike shaped pulses to positive going square wave

pulses (~5 V, 0.5 μS duration). The constant fraction discriminator also discriminates against spurious pulses not related to the experiment (i.e. electrical noise within the building). These pulses tend to be smaller than the pulses arising from the channeltron and are simply discriminated using a variable discrimination level within the discriminator. The square wave pulses output from the discriminator are input to both a ratemeter and to the data acquisition electronics on the beamline (discussed below). The ratemeter is used to observe the electron signal, which is particularly important when the spectrometer is initially tuned to detect threshold electrons (see later).

The photon flux was measured in parallel with electron detection. An electrically biased stainless steel grid (wire mesh) was positioned within the vacuum chamber as shown in Figures 2-2 and 2-4. Photons striking the grid eject electrons

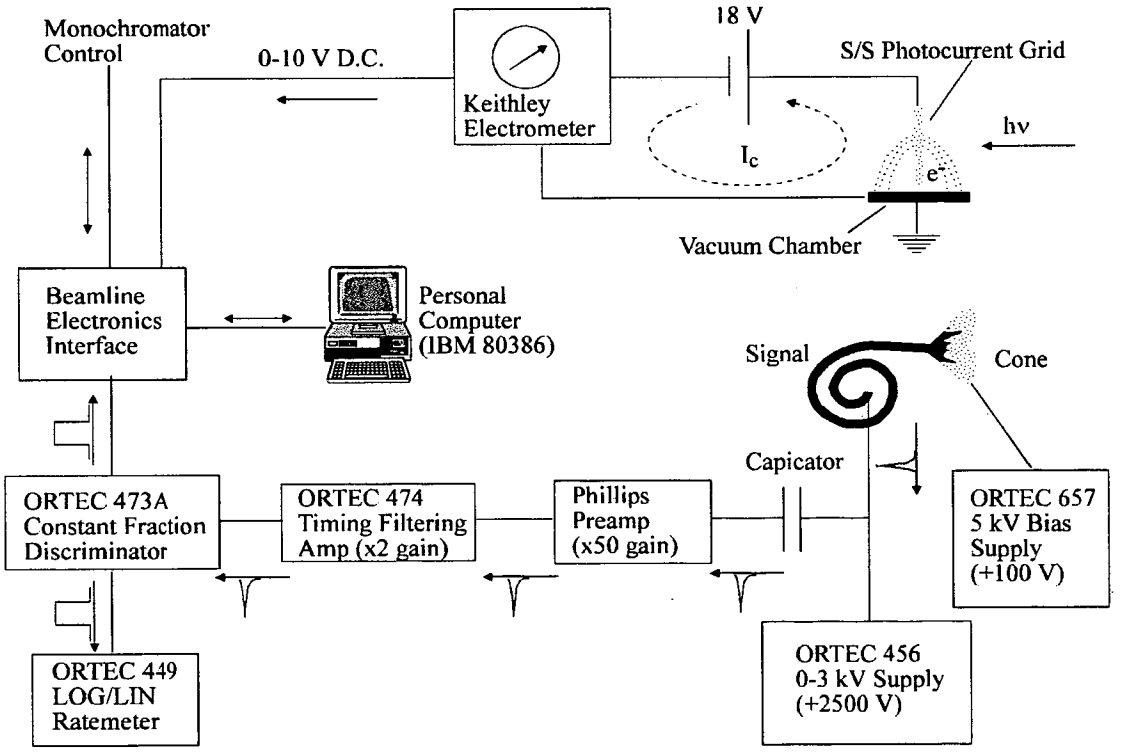

Figure 2-6 Schematic of the electron detection apparatus for the Threshold Photoelectron Experiment. The circuitry associated with the capacitor (high frequency noise filters etc.) was designed at the Manchester Physics Department. I_c represents the flow of conventional current in the photoelectric circuit.

according to the photoelectric effect [78] and are collected on the walls of the vacuum chamber. A Keithley electrometer supplied by the Daresbury Laboratory was used to convert this current to a 0-10 V DC signal which was output to the beamline control system. The analogue gauge on the electrometer was also utilised to tune the position of the mirrors in the beam transfer mirror boxes (see Figure 2-2) in order to maximise the monochromator output.

The beamline electronics interface consisted of standard data acquisition electronics supplied and maintained by the Daresbury Laboratory and permanently installed on station 3.2. Briefly, a NIM signal processing module and a standard CAMAC controller are interfaced to an IBM-PC. The PC controls the monochromator and the data acquisition using a standard data acquisition program, supplied and maintained by staff at the Daresbury Laboratory. The program allows up to four data channels to be recorded simultaneously and for the stepsize and stop duration of the monochromator to be varied [c]. The software only acquires data during periods whilst the monochromator drive is stationary. Spectra are plotted on the PC screen as the data points are accumulated and once a scan is complete data is saved to the PC hard disk in ASCII format.

2.4 Operation of the threshold electron spectrometer

The spectrometer is quite complex, in total there are 16 electrical potentials to be optimised. Also, the voltage supplied to an electrode will not in general be the same as the potential at the electrode surface. The difference between these two potentials is minimised by coating the electrodes with colloidal graphite as discussed in section 2.3.2. However, the surface potential varies with time and gas exposure, so threshold photoelectron experiments require continual monitoring of the performance of the spectrometer.

---

[c] the minimum stepsize was 0.5 meV and the minimum collection time duration used was 1 second.

2.4.1 Tuning the spectrometer to detect threshold electrons

Argon gas was leaked into the vacuum chamber until a pressure of $1x10^{-4}$ mBar was reached. The monochromator is positioned to 15.950 eV (~786.2 Å) with an output bandwidth of ~20 meV (1.0 Å) and then the voltages applied to the different spectrometer electrodes are gradually adjusted until an electron signal is detected. Next, the monochromator is gradually moved closer to 15.937 eV (in 1 meV steps), and the output resolution slowly reduced to ~ 2 meV (0.1 Å). After each change in either the monochromator position or resolution, the electrode potentials are re-optimised. This tuning scheme ensures that the final electrode potentials are optimised to detect true threshold electrons. A typical threshold photoelectron spectrum of argon recorded after the spectrometer has been optimised is shown in Figure 2-7. The relative intensity of the Ar^+ $^2P_{3/2}$ and $^2P_{1/2}$ peaks in a HeI

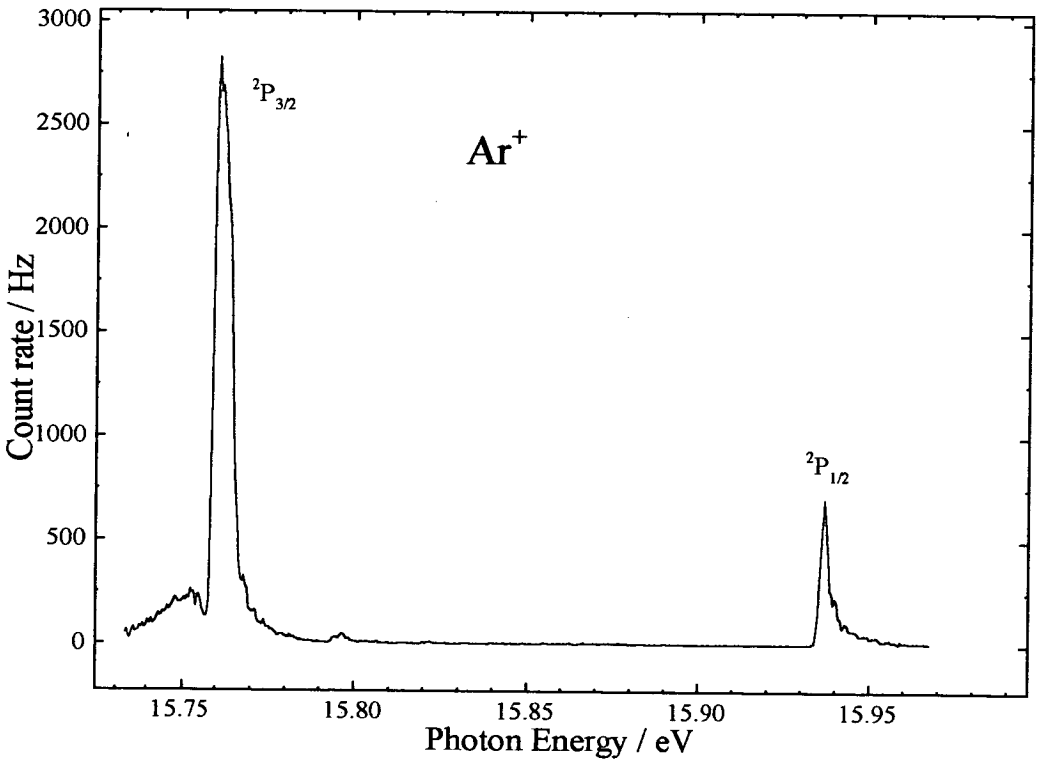

Figure 2-7 Threshold Photoelectron Spectrum of argon. The Ar^+ $^2P_{1/2}$ peak has a FWHM of 3 meV and the monochromator bandwidth was ~2 meV. Data points were collected at 0.5 meV intervals.

photoelectron spectrum is 2:1, here the intensity is ~5:1. This enhancement is due to autoionisation from the 11s′ Rydberg state (converging on the $Ar^+ {}^2P_{1/2}$ ion core) into the $Ar^+ {}^2P_{3/2}$ ion continuum as shown in Figure 1-4. The small peak at 15.797 eV is due to the 12s′ Rydberg state from the same series.

2.4.2 Collection of Threshold Photoelectron Spectra

The addition of corrosive gases like fluorine and hydrogen bromide to the vacuum system rapidly changes the surface chemistry of the spectrometer electrodes and hence the effective electrical potential of the surface. These gases are slowly added to the vacuum chamber in an excess of argon with the monochromator positioned on the $Ar^+ {}^2P_{3/2}$ line (15.759 eV). Changes to the surface potentials as the study gas is added are reflected by a drop in the threshold electron signal (for the argon gas) and can be quickly counteracted by adjusting the electrode potentials. The proportion of the study gas is then gradually increased in conjunction with a reduction in argon gas, ensuring that the total chamber pressure does not exceed 1×10^{-4} mBar. Data was normally collected using pure study gas [d], and after each study scan an argon scan was taken to ensure the performance of the spectrometer had not deteriorated during the study scan.

2.5 Gas sample preparations

Hydrogen gas is a common impurity for hydrogen halide gas samples and must be removed before studies. Hydrogen removal was achieved using a small stainless steel vacuum line constructed inside a fume hood in the Materials Science Laboratory at the Daresbury Laboratory. The vacuum line consisted of a small rotary pump and a Pirani gauge connected by stainless steel tubing, with connections for a 4 litre stainless steel cylinder (to be attached to the experiment) and the gas source (typically a corrosive gases lecture bottle). Normally the 4 litre cylinder was filled to below

---

[d] hydrogen iodide and fluorine were recorded as mixtures with argon gas

atmospheric pressure to ensure the safety risk in handling the gas on the beamline was negligible. Fluorine was an exception to this rule, it was prepared and used *in-situ* on the beamline as discussed in sections 2.5.1 and 7.2.

2.5.1 Hydrogen Fluoride

Hydrogen fluoride was purchased from Argo International [80] (340g, 98% purity, supplied in a corrosive gas lecture bottle) and was used by two different procedures during the course of experiments. The first procedure was identical to that on hydrogen bromide etc. in section 2.5.4. Alternatively, the cylinder underwent a freeze, pump, thaw cycle while attached to the experiment on the beamline, then the cylinder was kept cooled to 0°C and used as the gas reservoir for the experiment. This allowed a constant backing pressure to be used throughout all scans (~350 mBar). However, this also increases the quantity of toxic material on the beamline.

2.5.2 Deuterium Fluoride

Deuterium fluoride was prepared by Dr. D.R. Brown at the University of Oxford, Inorganic Chemistry Laboratory, on a fluorine compatible vacuum line. The gas was transported to the Daresbury Laboratory in a small (~50 cm^3) stainless steel cylinder. Approximately 22 grams were prepared and the purity was unknown, however no contaminants were found in the TPES spectrum (Chapter 3). The gas sample was purified and studied by the same two methods as hydrogen fluoride (section 2.5.1). The description of the preparation of deuterium fluoride is given in Appendix A as it does not seem to be well documented in the literature. The preparation notes are included from a report supplied by Dr. D.R. Brown.

2.5.3 Deuterium Chloride

Deuterium chloride was prepared in this department (University of Edinburgh, Department of Chemistry) by Dr. S.G.D. Henderson. The gas was produced from the low temperature reaction of Benzoyl Chloride with D_2O using a standard glass

vacuum line as described in reference [79]. The deuterium chloride was purified by low temperature distillation, then transferred to a corrosive gas lecture bottle for transport to the Daresbury Laboratory. The purity and quantity of DCl produced was not established, however, no hydrogen chloride was observed in the spectra (HCl is the most probable impurity via proton exchange). Final sample preparation was as described for hydrogen bromide etc. in section 2.5.4.

2.5.4 Hydrogen and Deuterium Bromide and Hydrogen Chloride

Hydrogen chloride and deuterium bromide were supplied by Argo International [80] (HCl 99% purity, DBr 99% D (^{2}H), both samples were supplied in corrosive gas lecture bottles). Hydrogen bromide was supplied by Linde [81] (HBr 99% purity, in corrosive gas lecture bottle). In all cases the lecture bottles underwent a freeze, pump, thaw cycle (as described in section 2.5.5) before a portion of the gas was transferred to the 4 litre stainless steel cylinder. A freeze, pump, thaw routine on the 4 litre cylinder was deemed unnecessary as no hydrogen gas was observed in the TPES spectrum.

2.5.5 Hydrogen Iodide

Hydrogen iodide was supplied by Argo Gases [80] (HI 98% purity, corrosive gases lecture bottle). Hydrogen iodide slowly decomposes back to its constituent elements at room temperature and also produces hydrogen as it reacts with the surface of its container. A pure hydrogen iodide sample was produced by freezing the lecture bottle under liquid nitrogen[c] then pumping away uncondensed gas with a rotary pump. The lecture bottle was then allowed to warm up to room temperature and a 4 litre stainless steel cylinder was filled to 1 Bar (absolute). The pressure in the cylinder fell as hydrogen iodide adsorbed onto, and probably reacted with, the cylinder walls. The cylinder was then evacuated and re-filled from the lecture bottle.

---

[c] the neck and inline valve on the lecture bottle are not immersed in the coolant, and instead are kept above 0°C using heat from fingers or a heat gun.

Any residual hydrogen was removed from the sample by freezing one end of the cylinder under liquid nitrogen and again pumping away any residual gas with the rotary pump.

2.5.6 Fluorine

Fluorine gas is highly toxic (and extremely oxidising) and must be handled with extreme caution. Bottled fluorine is supplied in gas cylinders at either 15 or 28 bar and at cylinder volumes of 10 litres or greater. This constitutes a large amount of fluorine available as an oxidising agent should any uncontrolled leakage occur. It was impossible to adequately contain a fluorine cylinder close to the beamline at the Daresbury Laboratory so another fluorine supply had to be sourced to meet safety requirements.

The fluorine supply chosen was a recently developed portable electrochemical fluorine generator leased from British Nuclear Fuels P.L.C. Electrogas Business. The "Fluorodec 30" electrochemical cell generates high purity (~99%) fluorine at ~8 mBar above ambient atmospheric pressure by electrolyzing a KF.2HF melt. Hydrogen fluoride impurity was removed from the fluorine stream using a sodium fluoride scrubber (leased with the electrochemical cell). Further details are discussed in Chapter 7.

2.6 Routine Data Analysis, Calibration, and Spectra Preparation

Typically two or more identical spectra for any particular energy region were collected. The argon calibration scans recorded before and after the spectra are checked to ensure the spectrometer functioned correctly for both study scans. The study spectra were first normalised to the incident photon intensity then equivalent study spectra were added to maximise the signal to noise ratio. All data manipulation was completed using Microcal Origin [82] and the LabTalk scripting language within Origin. The standard data acquisition program supplied by the Daresbury Laboratory could collect a maximum of 2000 data points per scan, so in order to collect closely

spaced data points over the large energy regions of interest, the spectra summed over small energy ranges were catenated to adjacent energy ranges. Energy and intensity matching of these ranges was completed using a spectral peak common to both ranges. Once the adjacent spectra were catenated the spectrum was calibrated. Threshold photoelectron spectra of the five rare gases (Helium, Neon, Argon, Krypton, and Xenon) were recorded and a graph of measured energy against accepted energy plotted. The Origin package allows easy fitting of a polynomial function to these five points [f]. The calibration curve can then be used to calibrate all spectra.

During the recording of some spectra it became evident that occasionally that some spectral feature was found to occur at different monochromator energies. This inconsistency has been traced to an intermittent fault in the control electronics of the beamline monochromator [g]. The intermittent discrepancy in the monochromator drive mechanism causes difficulties with spectral calibration as there is no way to ascertain which (if any) spectra of a given set will be calibrated incorrectly. As there is no possible strategy to combat this problem the following procedure was adopted.

After the spectra were summed and joined to produce the overall spectrum the x-axis translations made to individual spectra were noted. These were compared with the positions of the $Ar^+ {}^2P_{1/2}$ peaks from spectra recorded before and after the study gas (section 2.4.2) and a consensus for the exact positioning of spectra relative to a single argon scan was gained. In general there was a discrepancy between the energy of this single argon scan and the measured energy of the argon scan used in the calibration curve. The study spectrum was shifted to remove this discrepancy and then calibrated using the calibration curve from the rare gas data. This is normally sufficient to calibrate the spectra. However, during the course of the analysis work

---

[f] Origin uses the Levenberg Marquardt algorithm for non-linear least-squares fitting. It finds parameters of the model by minimising the chi-square values, see reference [82]

[g] The problem which was with the drive mechanism positioning register, has been noted by the Lab. and steps are now being taken to rectify it. (It affects all experiments on station 3.2 which require accurate scanning of the monochromator.)

there was sometimes a disagreement between the data presented in this thesis compared to the literature. This was particularly apparent in the work on hydrogen chloride (see Chapter 4). The discrepancy was alleviated by aligning the current work to agree with the literature. Details of when this procedure has been used will be given when relevant.

Chapter 3. Hydrogen and deuterium fluoride

3.1 Introduction

Figure 3-1 shows a schematic molecular orbital diagram for hydrogen and deuterium fluoride. Hydrogen fluoride is unique among the hydrogen halide series as the fluorine atom is the only halogen with an ionisation potential higher than the hydrogen atom (I.P. F ($^2P_{3/2}$) = 17.423 eV [183]; I.P. H ($^1S_0$)= 13.598 eV [223]). Electronic energy levels are modified compared to the lower members of the HX series (see Figure 4-1 for the M.O. diagram of HCl for comparison). From Figure 3-1 the ground state electron configuration of HF and DF can be written as $(2s\sigma)^2(2p\sigma)^2(2p\pi)^4$ and the state is labeled X ($^1\Sigma^+$). Removal of a $2p\pi$ electron leaves a $(2s\sigma)^2(2p\sigma)^2(2p\pi)^3$ electron configuration so the lowest electronic state of HF^+ is labeled X ($^2\Pi_i$), which is spin-orbit split, with Ω taking values 3/2 and 1/2. Removal of a $2p\sigma$ electron results in a $(2s\sigma)^2(2p\sigma)^1(2p\pi)^4$ electron configuration so the first excited state of HF^+ is labeled A ($^2\Sigma^+$). Ejection of a $2s\sigma$ electron would result in the formation of the B ($^2\Sigma^+$) state, however, the energy required is almost 40 eV (Brion *et*

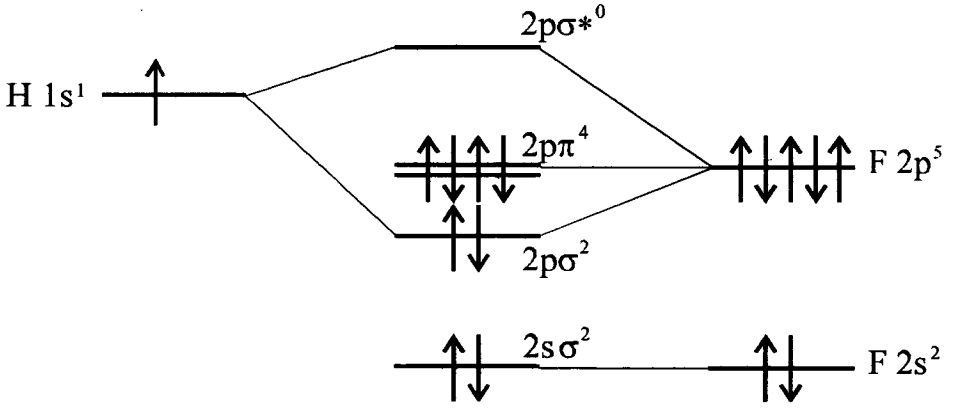

Figure 3-1 Molecular orbital diagram for hydrogen (and deuterium) fluoride.

al. [83]), which is too high to be probed in this work. However, the binary electron studies by Brion *et al.* [83] clearly show that both the X ($^2\Pi_i$) and A ($^2\Sigma^+$) states have nodal (or p type) symmetry whereas the B ($^2\Sigma^+$) state is non-nodal (or s type). This agrees with the molecular orbital picture in Figure 3-1, where both the X and A states are formed by the removal of an electron from a *p* type orbital whereas the B ($^2\Sigma^+$) state is formed by the removal of an electron from an *s* type orbital.

The most recently published and highest resolution conventional photoelectron experiment in the literature is by Edvardsson *et al.* [84]. Their work using HeII radiation (hν=40.814 eV) on HF^+ shows that five vibrational levels are accessible in the X ($^2\Pi_i$) state of the ion with the v=0 level being most intense (~3 times greater than v=1). The spectrum also shows the spin-orbit splitting in each vibrational level. A higher resolution spectrum using the NeI line at 16.848 eV and a spectrometer bandpass of 3.5 meV allowed the various rotational branches of the spin orbit split components of the X ($^2\Pi$) band origin to be assigned and compared to model calculations by Wang *et al.* [85]. Wang *et al.* [85] have calculated the final rotational distributions for ionisation to this vibrational level and the results are in reasonable agreement except for some small intensity variations. To date, the most accurate measurement of the ionisation potential of HF is 16.04633(10) eV, as reported by Mank *et al.* [86] from their ZEKE-PFI study of the X ($^2\Pi_i$) v^+=0,1 vibrational levels of HF. The intensity ratio of the spin-orbit components (Ω=3/2:1/2) in the origin band was ~8:1 in the ZEKE study, compared to ~1:1 in non-resonant ionisation [84]. Mank *et al.* [86] suggest this is due to the rapid spin-orbit autoionisation (and hence non-detection) of Rydberg levels with an X ($^2\Pi_{1/2}$) ion core.

Edvardsson *et al.* [84] also recorded a high resolution HeI photoelectron spectrum of the A ($^2\Sigma^+$) state of HF^+. The observed vibrational levels (v^+=0-3) are degraded to lower energy and show rotational structure which has been compared to the calculations of Wang *et al.* [85] for v^+=3. The calculated and measured spectra

are very similar except for slight intensity disparities in some rotational branches of the ion.

The rotationally resolved A ($^2\Sigma^+$) $\rightarrow$ X ($^2\Pi_i$) ion emission work by Gewurtz *et al.* [87] has yielded rotational constants for both electronic states and showed that the modified spin-orbit constant for the X ($^2\Pi$) state is negative (A=-0.040 eV). In their photofragment spectroscopy study of HF^+ Cosby *et al.* [98] have shown that the A ($^2\Sigma^+$) state of HF^+ is predissociated above v^+=3, N=3, where N is the ion rotational level. This predissociation has also been observed by Gewurtz *et al.* [87] where the next higher rotational level of HF^+ is absent in emission. The electronic structure of the ion states of HF^+ has been investigated using *ab initio* methods by Richards and Wilson [88], Julienne *et al.* [89], and Raftery and Richards [90]. Both Julienne *et al.* and Raftery and Richards calculate that the A ($^2\Sigma^+$) state electronic potential will have a small barrier at around 3 Å. From the combined results of Gewurtz *et al.* [87], Cosby *et al.* [98], Julienne *et al.* [89], and Raftery and Richards [90] it is clear that the predissociation does not involve another electronic state, instead it is caused by rotation, i.e. Herzberg's case III (see Herzberg p. 413 [165]).

The threshold photoelectron spectrum of HF and DF has been studied previously by Guyon *et al.* [91] at lower resolution (12 meV at the Kr^+ $^2P_{1/2}$ ion line) than the present study. 12 vibrational levels were observed in the X ($^2\Pi_i$) state and 4 in the A ($^2\Sigma^+$) state of HF. The extended vibrational progression in the X ($^2\Pi_i$) state is not present using non-resonant ionisation and thus is probably caused by the autoionisation of Rydberg states with an A ($^2\Sigma^+$) electronic core. Rydberg states converging to the A ($^2\Sigma^+$) state have been observed by Berkowitz *et al.* [92] in photoionisation studies on HF and DF. In DF, due to the increase in reduced mass, Guyon *et al.* [91] observed 5 vibrational levels in the A ($^2\Sigma^+$) state, however only the first 6 vibrational levels of the X ($^2\Pi_i$) state were observed. This was explained by a gradual desensitisation of the electron spectrometer from prolonged exposure to hydrogen fluoride.

A potential energy diagram for the X ($^1\Sigma^+$), X ($^2\Pi_i$), and A ($^2\Sigma^+$) states of HF and HF^+ is shown in Figure 3-2 showing the electronic states relevant to work in this Chapter. The X ($^1\Sigma^+$) state was modeled by a Morse potential using spectroscopic data from Huber and Herzberg [177] and Zemke *et al.* [93], and the X ($^2\Pi_i$) and A ($^2\Sigma^+$) states from work by Gewurtz *et al.* [87] and Cosby *et al.* [98]. The A ($^2\Sigma^+$) state has been calculated to have a small potential barrier at ~3 Å [89], however this has not been included in the potential energy diagram as the work by Cosby *et al.* [98]

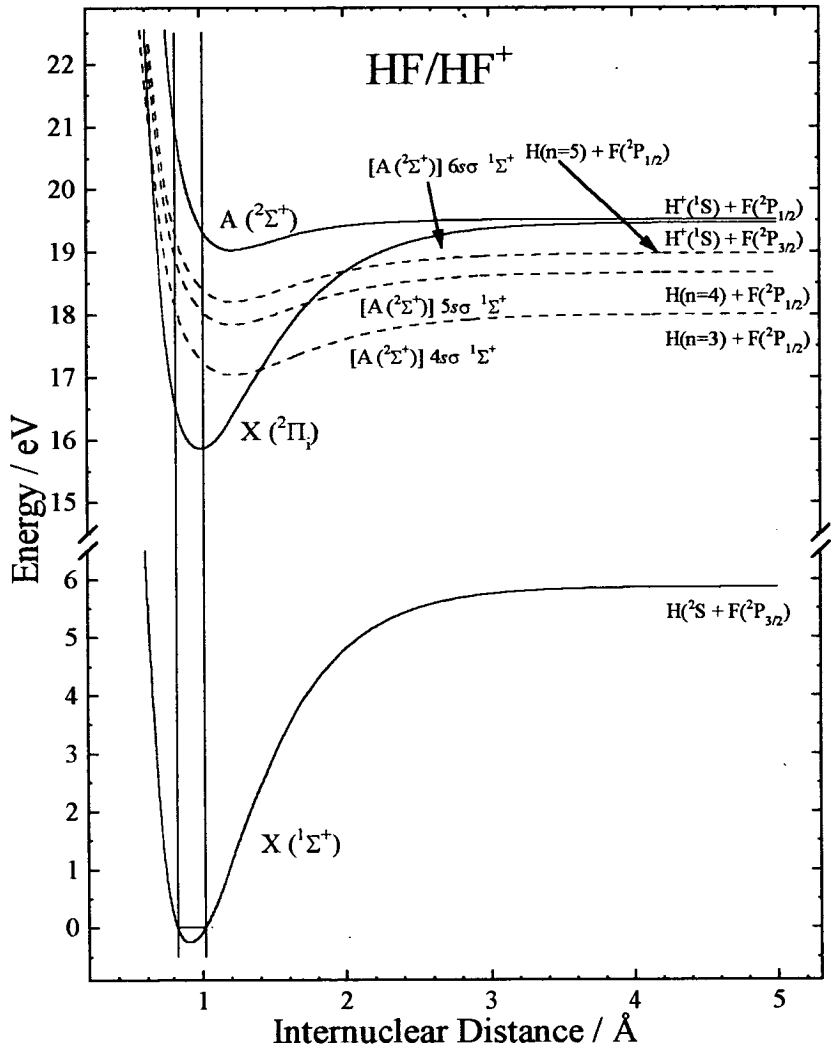

Figure 3-2 Potential energy diagram for the HF/HF^+ system showing the main ionic and neutral states involved in the results for this Chapter. (see text for details of potential energy curves)

suggests this barrier may only be due to the ion rotational energy. The [A $(^2\Sigma^+)$] $ns\sigma$ $^1\Sigma$ Rydberg states, where n=4-6, are simulated as follows. Berkowitz *et al.* [92] observed Rydberg states converging to the A $(^2\Sigma^+)$ state of HF^+ in a photoionisation experiment. The spectroscopic constants derived from a third order vibrational Dunham fit to their observations have been used to determine the depth of the three Rydberg states they observed. The dissociation limit for each of the three Rydberg states was calculated by combining the dissociation energy of the X $(^1\Sigma^+)$ state of HF from Zemke *et al.* [93] with the excitation energy to various Rydberg states of the hydrogen atom taken from Moore [223]. The equilibrium bondlength of the Rydberg states is assumed to be equal to that of the A $(^2\Sigma^+)$ state potential [87] and the vibrational frequency for the Morse curve was taken from Berkowitz *et al.* [92]. This type of potential energy construction has been used successfully by Yencha *et al.* [94] to model the lower energy [A $(^2\Sigma^+)$] $3s\sigma$ $^1\Sigma$ Rydberg state for their study of the ion-pair formation of HF and DF. It should be noted at this point that the Rydberg states observed by Berkowitz are probably the [A $(^2\Sigma^+)$] $nd\pi$ $^1\Pi$ series, where n=3-5, in common with assignments for HCl, DCl, HBr, and DBr (see Chapters 4 and 5). However, it would be expected that the Rydberg states of different symmetry would have similar potential energy curves.

This threshold photoelectron study of HF^+ and DF^+ was undertaken to improve the TPE work in the literature by Guyon *et al.* [91]. The increase in achievable resolution (up to 4 times higher) would allow a more detailed analysis of the TPE spectra. In particular there is the possibility that rotational structure could be resolved in the ion states which would allow a direct comparison of the ionisation dynamics of TPES with those of single photon ZEKE-PFI spectroscopy [86]. Also, a more detailed study of HF^+ and DF^+ could allow the Rydberg states involved in the autoionisation process to be identified. This study was undertaken as part of a systematic study of the hydrogen and deuterium halides by threshold photoelectron spectroscopy using the same spectrometer and monochromator assembly.

3.2 Special experimental details

Hydrogen fluoride is a highly toxic compound with can be extremely hazardous to health. The compound causes extremely painful skin and tissue burns which do not always occur immediately after exposure, and HF can also cause decalcification of bones [95],[96]. Extreme caution is required when HF or DF is handled. The spectra presented in this Chapter were recorded over 2 different study periods at the Daresbury Laboratory and, as detailed in sections 2.5.1 and 2.5.2, two different gas preparation methods were used. For both study periods the gases underwent a standard freeze - pump - thaw cycle to remove any hydrogen, however, during the first period only, the lecture bottle was connected to the gas vacuum line on the beamline (see Figure 2-3) and the lecture bottle maintained at ~0°C using an ice bath. The vapour pressure of HF at this temperature was 350 torr as measured on a capacitance manometer (Baratron) attached to the vacuum line. During the time between the two study periods safety regulations concerning gas handling operations were increased at the Daresbury Laboratory, so for the second study period a 4 litre stainless steel cylinder was used as the gas reservoir on the beamline. The cylinder was filled from the lecture bottle in a fumehood away from the beamline to ~650 torr, so that any gas leakage would be into the cylinder avoiding personnel exposure.

Calibration of the spectra was achieved as follows: Argon calibration scans adjacent to the high resolution spectra for the X ($^2\Pi_i$) v^+=0,1 levels of HF and DF were used to align the spectra with a calibration curve from measurements on the 5 rare gases (He, Ne, ...). After calibration using the rare gas curve the ionisation potentials of the X ($^2\Pi_{3/2}$) and A ($^2\Sigma^+$) states could be checked against the best literature values (Mank *et al.* [86], Wang *et al.* [85], and Guyon *et al.* [91]). The X ($^2\Pi_{3/2}$) ionisation limit agrees with the literature value within the experimental error, however the A ($^2\Sigma^+$) ionisation limit was found to be ~30 meV too high. Since the calibration of the McPherson monochromator used in this study is known to be unreliable (see Chapter 2) the present spectra were linearly adjusted to ensure the current A ($^2\Sigma^+$) state ionisation potential agreed with the literature while the X ($^2\Pi_{3/2}$)

ionisation limit was unchanged. Spectroscopic data from Huber and Herzberg [177], Mank *et al.* [86] and the isotope relations in Equation 4-1 (page 80) were used to cross-check the expected ionisation potentials of the X ($^2\Pi_{3/2}$) and A ($^2\Sigma^+$) states of DF which was calibrated using the same calibration formulae as HF.

3.3 Results and Discussion

Only the X ($^2\Pi_i$) and A ($^2\Sigma^+$) states of HF^+ and DF^+ were accessible for the current study as the B ($^2\Sigma^+$) state, or $(2s\sigma)^{-1}$ ionisation process, occurs at higher energy than the grating system in the McPherson monochromator can achieve. The results and discussion are split in two sections. Firstly the overall spectrum for the X ($^2\Pi_i$) and A ($^2\Sigma^+$) states is described and analysed, then a higher resolution study of the two lowest vibrational levels of the X ($^2\Pi_i$) state is discussed.

3.3.1 The threshold photoelectron spectra of the X ($^2\Pi_i$) and A ($^2\Sigma^+$) states of hydrogen and deuterium fluoride

Figure 3-3 shows the threshold photoelectron spectra of hydrogen and deuterium fluoride for the entire region of study. Details of the various sub-spectra that construct the overall spectra are as follows: (a) HF. from 15.92 - 17.710 eV, then from 17.711 - 19.009 eV, and finally from 19.010 - 20.794 eV, all with 1 meV stepsize. For each range 3 spectra were recorded at better than 7.0 meV resolution (as measured on the Ar^+ ($^2P_{3/2}$) ion line at 15.759 eV in adjacent argon calibration scans). (b) DF. from 15.933 - 17.845 eV, 2 spectra, 1 meV stepsize and 6 meV resolution; from 17.846 - 19.806 eV, 4 spectra, 1 meV stepsize and 6 meV resolution. For DF the resolution was measured from adjacent argon scans at the Ar^+ ($^2P_{1/2}$) ionisation line. The Ar^+ ($^2P_{3/2}$) line is broadened in the TPES spectra due to the autoionising Ar $11s'$ Rydberg state (converging to the higher energy Ar^+ ($^2P_{1/2}$) ion core). Typically this broadening is ~1 meV so both the spectra of HF and DF in Figure 3-3 will have essentially the same experimental resolution of 6 meV FWHM.

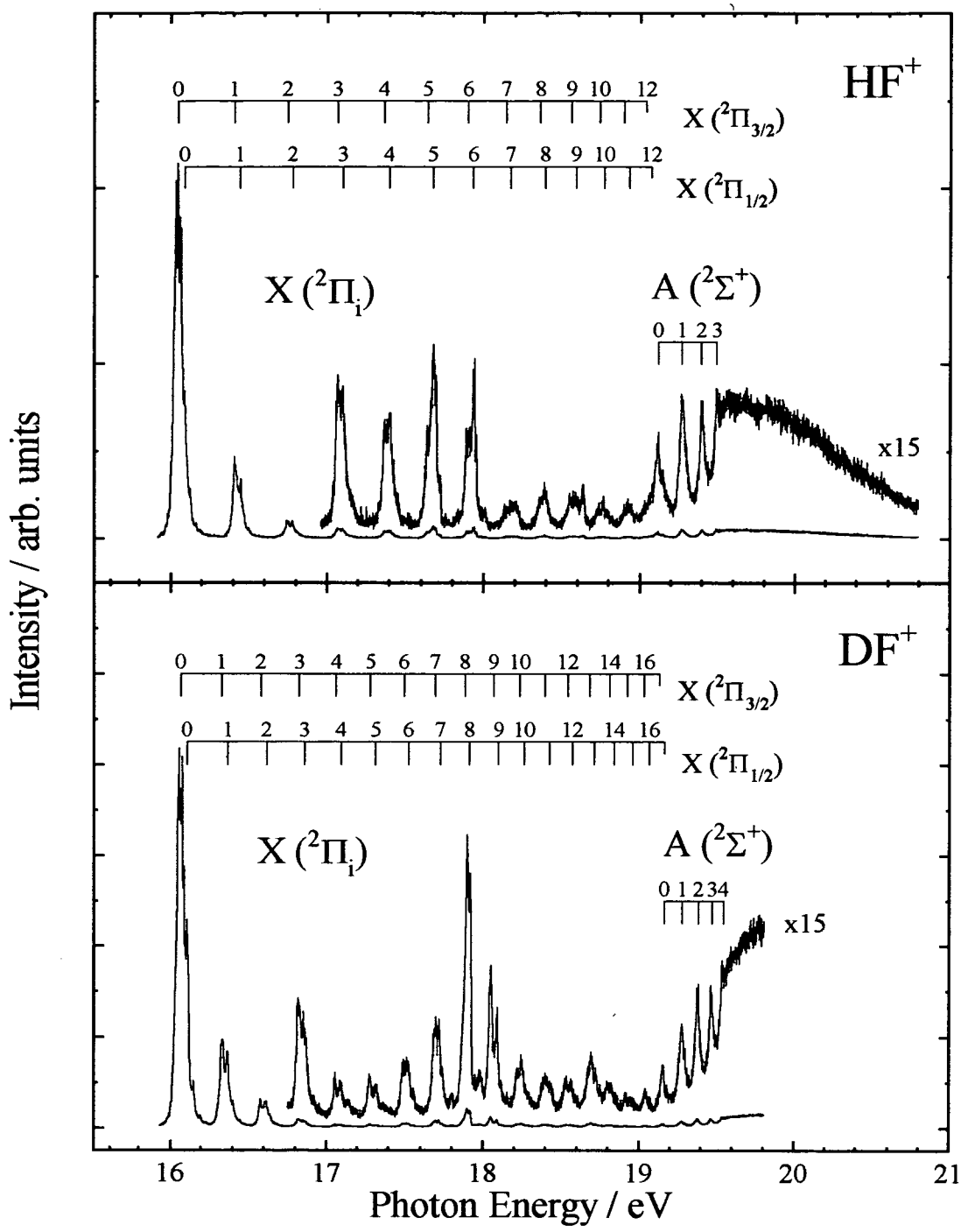

Figure 3-3 Threshold photoelectron spectrum of the outer valence ionisation region of hydrogen and deuterium fluoride showing the X ($^2\Pi_i$) and A ($^2\Sigma^+$) states of the molecular ion. (See text for spectral resolution and discussion of spectral features.)

The upper panel of Figure 3-3 clearly shows extensive vibrational structure due to the X ($^2\Pi_i$) and A ($^2\Sigma^+$) states of HF^+. The spectral features are very similar to the previous work on this energy region by Guyon *et al.* [91], however there is a 100% improvement in the experimental resolution in the present work. Although the spectral features are more highly resolved in the results presented here the vibrational levels are still quite broad due to a combination of the large rotational constants for the X ($^2\Pi_i$) and A ($^2\Sigma^+$) states of HF^+ [177], and the small spin orbit separation within the X ($^2\Pi_i$) states [87],[177]. Full length ticks in upper and lower panels of Figure 3-3 mark the measured position of the vibrational levels of HF^+ and DF^+ while half length ticks are positioned by extrapolating the Dunham fit to the data as discussed below. The X ($^2\Pi_{3/2}$) state of HF^+ clearly shows 12 vibrational levels before the onset of the A ($^2\Sigma^+$) state dominates the spectrum at higher energy. These vibrational levels have been combined with the 16 observed levels for the X ($^2\Pi_{3/2}$) state of DF^+ and fitted to the second order Dunham expression shown in Equation 4-1 (page 80) to determine the spectroscopic constants for the state. This combined analysis was also completed for the X ($^2\Pi_{1/2}$) and A ($^2\Sigma^+$) states of HF^+ and DF^+. The experimental vibrational peak positions for the X ($^2\Pi_i$) states of HF^+ are given in Table 3-1, for the X ($^2\Pi_i$) states of DF^+ in Table 3-2, and for the A ($^2\Sigma^+$) state of both HF^+ and DF^+ in Table 3-3. Also, the results of the second order Dunham analysis using the experimental peak positions are given in Table 3-4 along with relevant literature values. There is good agreement between the current results and the work in the literature for the ionisation potential of the X ($^2\Pi_{3/2}$) state (the A ($^2\Sigma^+$) state I.P. was fixed to the literature value). The slight discrepancies in the derived vibrational constants will be due to (a) differences in the dimensionality of the Dunham fit, (b) the relatively broad vibrational structure in the present work, and (c) the number of vibrational levels included in the vibrational analysis. (c) is particularly relevant in the vibrational analysis of the X ($^2\Pi_i$) state, where the vibrational constants from the emission work by Gewurtz *et al.* [87] are calculated from the observation of the v^+=0,1,2 levels only, whereas the current fitting work includes the vibrational positions of 30 vibrational levels. In this regard it should be noted that the

conventional photoelectron results by Edvardsson *et al.* [84] only include data from the first 5 vibrational levels also, so the vibrational constants for the X ($^2\Pi_i$) state can only really be compared with the previous threshold results from Guyon *et al.* [91]. From Table 3-4 it is clear that there is a slight discrepancy between the harmonic frequencies for the X ($^2\Pi_i$) states of HF^+ and DF^+, however it should be noted that Guyon *et al.* [91] did not undertake a combined isotopic analysis and that there is some discrepancy between vibronic frequency of the two isotopomers in that work. Also the X ($^2\Pi_i$) state vibrational constants for DF^+ derived by Guyon *et al.* [91] only include vibrational data for the first 6 vibrational levels, Guyon *et al.* [91] speculated this was due to a gradual desensitisation of the apparatus due to prolonged exposure of HF.

As previously mentioned the Franck-Condon region for the X ($^2\Pi_i$) state of HF covers from v^+=0-4 only [84],[97], so the extended vibrational progression is probably due to the autoionisation of excited neutral states lying between ~17-19 eV. As the B ($^2\Sigma^+$) state of HF^+ occurs at ~40 eV [83], any Rydberg states with an B ($^2\Sigma^+$) *nl*λ electron configuration will certainly lie to higher energy and would not autoionise to give threshold electrons at ~18 eV. Instead, bound Rydberg states with an A ($^2\Sigma^+$) *nl*λ electron configuration or repulsive neutral states are probably responsible for the autoionising structure. It is desirable to assign the autoionising Rydberg levels seen (indirectly) in the threshold photoelectron spectrum. No photoabsorption results have been found in the literature for this energy region in HF or DF, however the mass resolved photoionisation study of HF and DF by Berkowitz *et al.* [92] reported vibrational structure arising from a series of Rydberg states converging to the A ($^2\Sigma^+$) state in both HF and DF with effective quantum numbers, n^*, equal to 2.927, 3.905, and 4.910. Analysis of photoabsorption and photoionisation work in HCl and HBr by Lefebvre Brion *et al.* [116],[136] showed that the most prominent Rydberg series seen in photoabsorption and photoionisation studies is of A ($^2\Sigma^+$) *ndπ* $^1\Pi$ symmetry with effective quantum numbers of 2.79 (HCl) and 2.74 (HBr) [143]. It therefore seems likely that the vibrational structure observed in the HF^+ and DF^+ mass channels

by Berkowitz *et al.* [92] belongs to the same Rydberg series (A $(^2\Sigma^+)$ $nd\pi$ $^1\Pi$). It would seem likely that the Rydberg states seen in photoionisation were acting as neutral intermediate states in the threshold photoelectron spectrum. However from Berkowitz *et al.* [92] the lowest assigned Rydberg level for DF^+ occurs at 17.589 eV whereas the TPE signal is enhanced by autoionisation from $v^+=5$ (at ~17.3 eV) upwards (see Figure 3-3). So, it seems likely that the Rydberg structure seen in photoionisation is not directly related to the autoionising enhancements in the threshold photoelectron spectrum. From the results and analysis of HCl (Chapter 4) two possible Rydberg series were identified as candidates for threshold electron production (the A $(^2\Sigma^+)$ $ns\sigma$ $^1\Sigma$ and the A $(^2\Sigma^+)$ $nd\sigma$ $^1\Sigma$). Of these the two the A $(^2\Sigma^+)$ $ns\sigma$ $^1\Sigma$ Rydberg series was chosen as the most likely from its energy position and also from its prominence in ion-pair formation (see section 4.3.2). It seems likely that the same Rydberg series enhances the higher vibrational levels of the TPE spectra of HF^+ and DF^+.

The A $(^2\Sigma^+)$ state of HF^+ and DF^+ is quite different from the other members of the hydrogen halide series. In HCl and HBr the A $(^2\Sigma^+)$ state is predissociated by a repulsive $^4\Pi$ state (see Chapters 4 and 5) however, in HF the arrangement of the electronic states is different because fluorine has a higher ionisation potential than hydrogen, so the A $(^2\Sigma^+)$ state is not predissociated in the same way as the lower member of the HX series. The A $(^2\Sigma^+) \rightarrow$ X $(^2\Pi_i)$ emission work by Gewurtz *et al.* [87] and the photofragment spectroscopy of HF^+ by Cosby *et al.* [98] has shown that the X $(^2\Pi_i)$ state of HF^+ dissociates to $[H^+ + F\ (^2P_{3/2})]$ products whereas the A $(^2\Sigma^+)$ state dissociates to the spin-orbit excited $[H^+ + F\ (^2P_{1/2})]$ limit. The A $(^2\Sigma^+)$ state has a much smaller dissociation limit than the X $(^2\Pi_i)$ state and, as can be seen from the Dunham vibrational parameters in Table 3-4, the potential well is very anharmonic. In fact only the first three vibrational levels of the A $(^2\Sigma^+)$ state are truly bound, with the $v^+=3$ level existing as a shape resonance. The TPE spectrum for the A $(^2\Sigma^+)$ state of HF can be compared with the *ab initio* configuration interaction calculations by Cacelli [99]. Good agreement is found showing that the TPE spectrum of HF is not

strongly influenced by autoionisation features unlike the X ($^2\Pi_i$) state. The comparison also shows that vibrational autoionisation is not an effective ionisation pathway in this region (as vibrational autoionisation would enhance the intensity of the lowest vibrational levels).

3.3.2 Threshold photoelectron spectroscopy of the X ($^2\Pi_i$) v^+=0,1 vibrational levels of hydrogen and deuterium fluoride

Figure 3-4 shows the threshold photoelectron spectrum of HF^+ and DF^+ from ~15.9 to 16.5 eV. Details of the sub-spectra are as follows: (a) HF: from 15.900 - 16.242 eV, 0.5 meV stepsize, 3 meV resolution, 5 spectra; from 16.2425 - 16.3455 eV, 0.5 meV stepsize, 3 meV resolution, 1 spectrum; from 16.346 - 16.525 eV, 1 meV stepsize, 4 meV resolution, 7 spectra. (b) DF: from 15.890 - 16.230 eV, 0.5 meV stepsize, 3.5 meV resolution, 5 spectra; from 16.2305 - 16.530 eV, 0.5 meV stepsize, 3.5 meV resolution, 6 spectra. The resolution was measured from the width of the Ar^+ ($^2P_{1/2}$) line at 15.937 eV on adjacent argon calibration scans. The relative intensity of the two vibrational levels in the HF^+ and DF^+ spectra was fixed using single scans covering both vibrational levels recorded with 1 meV stepsize. These scans also served to correct any problems with the spectral calibration between the two sets of sub-spectra (see Chapter 2 for details of calibration problems).

This energy region has been the subject of a recent ZEKE-PFI study on HF^+ by Mank *et al.* [86] where the rotational lines for v^+=0 and 1 in both spin-orbit components were clearly resolved. Mank *et al.* [86] noted a large disparity in the intensity of equivalent rotational lines for the different spin-orbit components. The Ω=3/2 component was ~8 times more intense than the Ω=1/2 component for the v^+=0 vibrational level, and ~4 times more intense for the v^+=1 level. For direct photoionisation the ratio should be ~1 [85]. A similar enhancement in the Ω=3/2 spin-orbit component was also observed in the previous TPE spectrum by Guyon *et al.* [91] where only rotational band contours are seen. The enhancement of the lower energy spin-orbit component is seen in the current threshold photoelectron spectrum, however it is not feasible to measure the intensity ratio of the two components. It

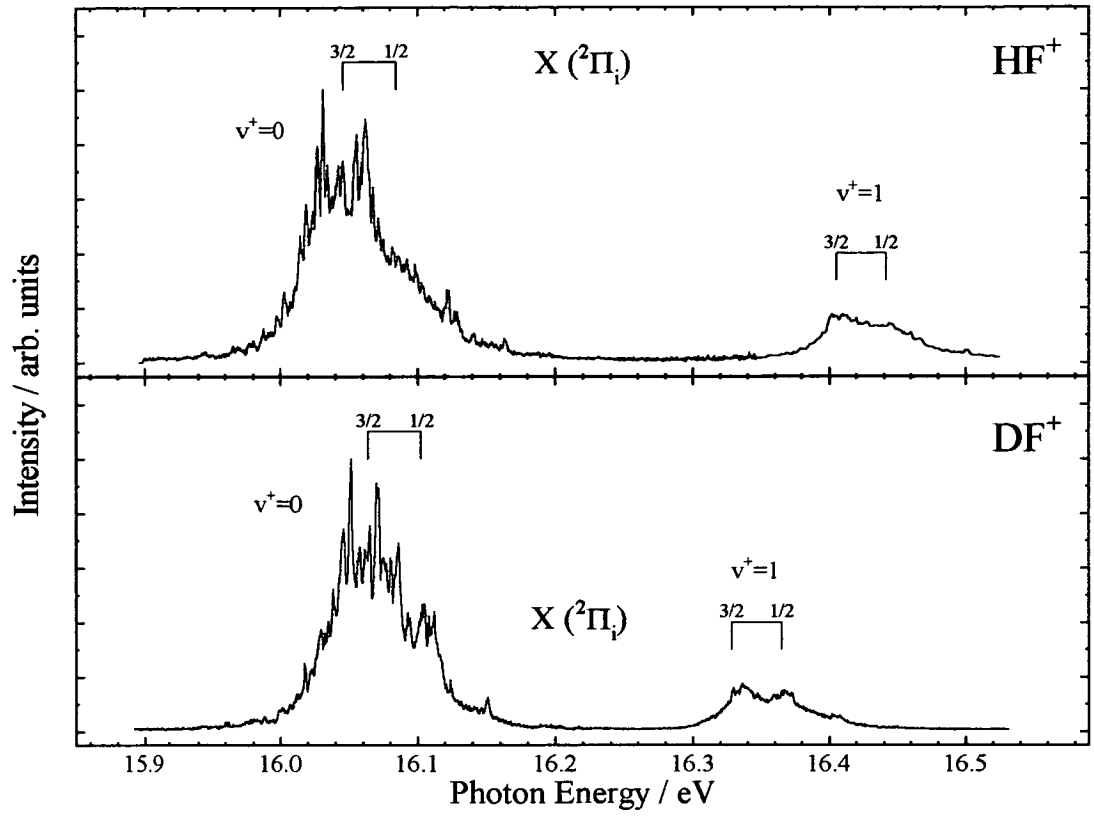

Figure 3-4 Threshold photoelectron spectra of the first two vibrational levels of the X ($^2\Pi_i$) state of HF^+ and DF^+. The resolution of the spectra is <3meV as measured on the Ar^+ ($^2P_{1/2}$) ionisation line at 15.937 eV. The position for the rotational origins for each vibrational level is taken from the vibrational fit.

seems likely that the intensity of the lower energy spin-orbit component is enhanced by spin-orbit autoionisation, where energy stored in the electronic coupling of the Rydberg electron to the ionic core is used to ionise the Rydberg electron.

The extensive structure between the $v^+=0$ levels of HF^+ and DF^+ is due to partially resolved individual rotational lines in the TPE spectrum. Although it is possible to tentatively assign some of the rotational lines using the ZEKE-PFI measurements by Mank *et al.* [86] the assignments are very dubious so have not been included in the analysis. A higher resolution spectrum will be needed before the position and intensity of individual rotational lines can be measured. The spectra shown in Figure 3-4 represent the best resolution currently achievable using the McPherson monochromator at the Daresbury Laboratory and a penetrating field

electron spectrometer. The photoionisation simulations by Wang *et al.* [85] suggest an experimental resolution of 1 meV (8 cm^{-1}) will be necessary before individual rotational lines are clearly resolvable in the TPE spectrum. This resolution should be achievable simply by coupling the current electron spectrometer to a higher resolution monochromator such as The Molecular Dynamics Beamline at the Advanced Light Source, Berkeley, California. This would allow a direct comparison between the rotational line strengths in threshold photoelectron spectroscopy and ZEKE-PFI spectroscopy.

3.4 Conclusions for the threshold photoelectron spectrum of hydrogen and deuterium fluoride

New experimental data and analysis for the X ($^2\Pi_i$) and A ($^2\Sigma^+$) states of HF^+ and DF^+ is presented and discussed. The threshold photoelectron spectra show extended vibrational progressions in both spin-orbit components of the X ($^2\Pi_i$) state that terminate at the onset of ionisation to the A ($^2\Sigma^+$) state. The measured vibrational peak positions for the X ($^2\Pi_{3/2}$), X ($^2\Pi_{1/2}$), and A ($^2\Sigma^+$) states of HF^+ and DF^+ have been combined and analysed to produce new spectroscopic constants for the 3 states. The new spectroscopic constants are in general agreement with previous work. The adiabatic ionisation potential of HF^+ is found to agree (within the present experimental error) with the high resolution ZEKE-PFI and NeI PES experiments [86],[84]. High resolution (<3.5 meV) spectra of the lowest two vibrational levels of the X ($^2\Pi_i$) state of HF^+ and DF^+ show evidence of rotational structure, however the current experimental resolution is not high enough for the rotational lines to be assigned. A repeat of the current study at higher resolution would allow a comparison of the ionisation dynamics in threshold photoelectron spectroscopy with conventional (non-resonant) photoelectron spectroscopy and ZEKE spectroscopy.

Tables of results for hydrogen and deuterium fluoride

Table 3-1 Observed and calculated vibrational band head positions (in eV) for the transitions: $e + HF^+ (X\ ^2\Pi_i,\ v') \leftarrow HF (X\ ^1\Sigma^+, v''=0)$

	$X\ ^2\Pi_{3/2}$		$X\ ^2\Pi_{1/2}$	
v′	meas [a]	calc	meas [a]	calc
0	16.045	16.046	16.085	16.084
1	16.406	16.405	16.442	16.442
2	16.745	16.745	16.779	16.779
3	17.064	17.064	17.098	17.097
4	17.365	17.364	17.397	17.396
5	17.643	17.643	17.675	17.674
6	17.903	17.903	17.933	17.933
7	18.142	18.142	18.173	18.172
8	18.361	18.361	18.391	18.392
9	18.560	18.561	18.591	18.591
10	18.740	18.740	18.771	18.771
11	18.899	18.899	18.931	18.931
12		19.038		19.071

[a] ±0.001 eV

Table 3-2 Observed and calculated vibrational band head positions (in eV) for the transitions: $e + DF^+ (X\ ^2\Pi_i),\ v') \leftarrow DF\ (X\ ^1\Sigma^+),\ v''=0)$

	$X\ (^2\Pi_{3/2})$		$X\ (^2\Pi_{1/2})$	
v'	meas [a]	calc	meas [a]	calc
0	16.064	16.064	16.102	16.103
1	16.329	16.329	16.365	16.366
2	16.582	16.583	16.618	16.618
3	16.825	16.826	16.860	16.861
4	17.059	17.059	17.092	17.092
5	17.281	17.281	17.315	17.314
6	17.494	17.493	17.524	17.525
7	17.695	17.695	17.725	17.726
8	17.886	17.886	17.917	17.916
9	18.065	18.066	18.096	18.096
10	18.235	18.236	18.266	18.266
11	18.396	18.395	18.426	18.425
12	18.543	18.544	18.574	18.574
13	18.681	18.682	18.713	18.713
14	18.811	18.810	18.841	18.841
15	18.927	18.927	18.959	18.959
16	19.034	19.034	19.067	19.067
17		19.130		19.164

[a] ±0.001 eV

Table 3-3 Observed and calculated vibrational band head positions (in eV) for the transitions: $e + HF^+ (A\ ^2\Sigma^+),\ v') \leftarrow HF\ (X\ ^1\Sigma^+),\ v''=0)$ and $e + DF^+ (A\ ^2\Sigma^+),\ v') \leftarrow DF\ (X\ ^1\Sigma^+),\ v''=0)$

	$HF^+\ A\ (^2\Sigma^+)$		$DF^+\ A\ (^2\Sigma^+)$	
v'	meas [a]	calc	meas [a]	calc
0	19.117	19.117	19.163	19.163
1	19.271	19.270	19.280	19.280
2	19.397	19.396	19.381	19.382
3	19.495	19.494	19.469	19.470
4			19.542	19.543

[a] ±0.001 eV

Table 3-4 Summary of spectroscopic constants (in eV) derived from the analysis of the HF and DF TPES spectra for the outer valence region presented in this Chapter, with some relevant literature values included for comparison.

State	ionisation energy	ω_e	$\omega_e x_e / 10^{-3}$	Ref.
$HF^+ X (^2\Pi_{3/2})$	16.045 [a]	0.37961(14)	-10.02(1)	this work
	16.04633(12)			[86]
	16.0460	0.38137	-10.6	[84]
	16.046			[85]
	16.039	0.3789	-9.86	[91]
		0.3831702	-11.034	[87]
$HF^+ X (^2\Pi_{1/2})$	16.085 [a]	0.37726(13)	-9.87(1)	this work
	16.0823	0.38137	-10.6	[84]
	16.076	0.3789	-9.86	[91]
		0.3831702	-11.034	[87]
$HF^+ A (^2\Sigma^+)$	19.117 [a]	0.1809(10)	-13.77(24)	this work
	19.1154	0.18593 [b]	-11.0 [b]	[84]
	19.116			[85]
	19.118	0.1934	-15.5	[91]
		0.1854886 [c]	-10.963 [c]	[87]
$DF^+ X (^2\Pi_{3/2})$	16.064 [a]	0.27505(10)	-7.260(8)	this work
	16.058	0.2789	-5.68	[91]
$DF^+ X (^2\Pi_{1/2})$	16.102 [a]	0.27335(9)	-7.153(7)	this work
	16.090	0.2789	-5.68	[91]
$DF^+ A (^2\Sigma^+)$	19.163 [a]	0.1311(7)	-9.98(18)	this work
	19.162	0.1339	-6.8	[91]

[a] ±0.001 eV
[b] $\omega_e y_e = -9.05\times10^{-4}$ (3rd order Dunham fit used in Ref. [84])
[c] $\omega_e y_e = -9.086\times10^{-4}$ (3rd order Dunham fit used in Ref. [87])

Chapter 4. Hydrogen and deuterium chloride

4.1 Introduction

The valence states of HCl^+ and DCl^+ have been well studied in the past. This is to be expected of such simple molecules which are also chemically important. A molecular orbital diagram of hydrogen chloride is given in Figure 4-1. From the diagram it would be expected that removal of a $3p\pi$ electron will produce the X ($^2\Pi_i$) state of the ion which should be spin-orbit split in common with the lowest ion state for the entire hydrogen halide series. Ejection of a $3p\sigma$ electron will produce the A ($^2\Sigma^+$) state. Removal of a $3s\sigma$ electron from hydrogen chloride results in the production of more than one final ion state through final state configuration interactions, in common with hydrogen bromide and iodide.

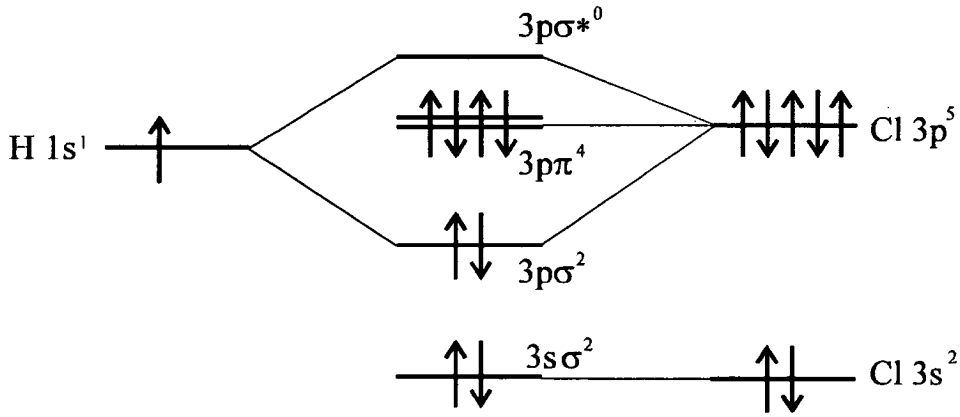

Figure 4-1 Molecular orbital diagram for the valence electron levels of hydrogen chloride

In a recent special volume of J. Electron. Spect. Rel. Phenom., dedicated to the memory of Professor W.C. Price., Edvardsson *et al.* [100] reported high resolution (~3 meV) Ultra-violet photoelectron spectra (HeI and NeI PES) of HF and

HCl. The HF section of that paper is of relevance in Chapter 3 of this thesis however their results for HCl are important here. The HeI photoelecton spectrum of HCl for the X ($^2\Pi_i$) state shows only 3 vibrational levels, with the ratio of $v^+=0$ to $v^+=1$ approximately 14:1. So, the X ($^1\Sigma^+$) and X ($^2\Pi_i$) potential curves are very similar confirming the non-bonding nature of the $3p\pi$ electrons.

Ionisation to the A ($^2\Sigma^+$) state leads to a long vibrational progression showing 15 vibrational peaks. The resolution of the spectrum is high enough to show that vibrational levels $v^+=0$-7 and $v^+=11$-13 show rotational structure which is well resolved in the *P rotational branch* ($\Delta N=-1$), but the levels $v^+=8$-10 show no rotational structure. In common with HBr and HI, there seems to be state mixing between repulsive states correlating to the [H (^2S) + Cl^+ (^3P_j)] dissociation limit and the A ($^2\Sigma^+$) state. Ab-initio calculations by Raftery and Richards [101] and Pradhan *et al.* [102] have shown that three repulsive states ($^4\Sigma^-$,$^2\Sigma^-$,$^4\Pi$) cross the A ($^2\Sigma^+$) state, with the spin-orbit coupling between the A ($^2\Sigma^+$) state and the $^4\Pi$ being the strongest. These two states are calculated to cross between $v^+=7$ and $v^+=8$ and Raftery and Richards estimated that the maximum broadening in the A ($^2\Sigma^+$) vibrational levels would be ~5 meV. This is in quite good agreement with the work by Edvardsson *et al.* [100] where they calculate a rotational line broadening of ~10 meV is required to simulate their spectra for the $v^+=8$-10 levels.

Yencha *et al.* [103] reported the threshold photoelectron spectrum of hydrogen chloride up to 40 eV at a relatively low resolution of between 50 and 70 meV. This study was completed in conjunction with a TPEsCO study of HCl [104]. In the study by Yencha *et al.* [103] vibrational levels in the X ($^2\Pi_i$) state from $v^+=0$-14 were recorded before the onset of the A ($^2\Sigma^+$) state levels. The vibrational levels from $v^+=3$-14 are outside the Franck-Condon region from the X ($^1\Sigma^+$) state and seem to be populated through resonant autoionisation from Rydberg levels converging to the A ($^2\Sigma^+$) state. The intermediate levels were assigned to the [A ($^2\Sigma^+$)] $ns\sigma$ $^1\Sigma$ Rydberg

series, where n=4-6. These states autoionise into high vibrational levels of the X ($^2\Pi_i$) state yielding a threshold electron.

Yencha *et al.* [103] also found the structures in the A ($^2\Sigma^+$) state are essentially the same as the in previous photoelectron spectra in the literature [105],[106],[107], suggesting autoionising processes producing threshold electrons are not important in this region. They also noted that levels v^+=7-10 were broadened in the threshold photoelectron spectrum, the broadening was significantly greater than seen in the work by Edvardsson *et al.* [100], suggesting that some additional vibrational line broadening mechanism occurs in threshold photoelectron spectroscopy. Yencha *et al.* [103] speculated some of the peak broadening was due to the autoionisation of repulsive Rydberg levels into repulsive ion levels (and so yielding a threshold electron).

Frohlich *et al.* [108] have also reported the threshold photoelectron spectrum of the X ($^2\Pi_i$) states of HCl^+. The spectrum has a resolution of 8 meV and ranges from v^+=0 to 14. Frohlich *et al.* found that population of the v^+= 3-5 vibrational levels occurred via autoionisation of the [A ($^2\Sigma^+$)] $4p\pi$ $^1\Pi$ Rydberg state, and that the v^+=7-14 levels were accessed via autoionisation of the [A ($^2\Sigma^+$)] $nd\pi$ $^1\Pi$ Rydberg series, where n = 3 and 4.

The $(3s\sigma)^{-1}$ ionisation region yields many different states through final state electron correlations and many of these states were assigned to a "main band" $(3s\sigma)^{-1}$ state and several *two hole - one particle* satellite states with typical configurations of the type $[(3p\sigma)^1(3p\pi)^3\ nl(\sigma,\pi)]$, and $[(3p\pi)^2\ nl(\sigma,\pi)]$. The $(3s\sigma)^{-1}$ region of HCl has also been studied by Svensson *et al.* [109] and by Adam [110] where 11 features between 23 and 51 eV were noted and discussed. von Niessen *et al.* [159] have investigated the ionisation processes for the inner valence region using many-body Green's-function calculations and these calculations show that the many states formed from $(3s\sigma)^{-1}$ ionisation cannot be represented by one single electronic configuration.

This is common for the inner valence ionisation of atoms and small molecules as reviewed by Cederbaum *et al.* [158].

Natalis *et al.* [111] reported studies of autoionisation in hydrogen and deuterium chloride using the NeI lamp double lines at 73.6 and 74.4 nm (16.845 and 16.645 eV). Using this technique they were able to resolve 14 vibrational levels in the X ($^2\Pi_i$) state of HCl and 19 in the deuterium isotope. As the Franck-Condon region only extends up to $v^+=2$ for the X ($^2\Pi_i$) state the extended vibrational progression is attributed to autoionisation of a state of unknown character into the X ($^2\Pi_i$) ion state. The intensity of the various ion vibrational levels seemed to agree with the model by Smith [112] which essentially models the final vibrational level intensity as the product of two Franck-Condon Factors, the first from the X ($^1\Sigma^+$) to the intermediate state, Y, and the second from Y to the final ion state [X ($^2\Pi_i$), v^+]. Natalis *et al.* [111] concluded that the unknown state Y was probably a doubly excited mixed valence-Rydberg state of $(3p\sigma)^2(3p\pi)^2(3p\sigma^*)^1$ ($ns\sigma$ or $np\pi$) configuration. They discounted singly excited states following in-depth energy and intensity considerations of their spectra.

Another electron spectroscopic publication worthy of note is the work by Frohlich *et al.* [113] on threshold photoionisation in HCl at 8 meV resolution. This study concerns the energy region between the two X ($^2\Pi_i$) ion origins, where the intensity of the threshold electron signal is ~2-3 times greater in the lower energy X ($^2\Pi_{3/2}$) band. Frohlich *et al.* [113] were able to simulate their threshold spectrum by considering both direct ionisation and autoionisation contributions. They noted that the autoionisation contribution occurred with high rotational transfer and this could be explained as the result of a change from Hund's case (a) to Hund's case (e) or (e') coupling.

Additionally there are a few other publications to be quickly mentioned in this introduction. Firstly, the single photon ZEKE photoelectron study of HCl by Tonkyn *et al.* [114] shows the rotationally resolved spectra for the X ($^2\Pi_i$) origin bands. The

resolution of this study is 0.7 cm^{-1} (<0.1 meV) which is much higher than can currently be achieved by the threshold technique. However, Tonkyn *et al.* [114] also recorded a laser TPES spectrum and this spectrum was used in the calibration of the results presented in this chapter (see section 4.2).

The rotationally resolved A ($^2\Sigma^+$) → X ($^2\Pi_i$) emission spectrum of HCl and DCl has been well studied by Sheasley and Mathews [115] and this has allowed accurate vibrational and rotational constants to be derived covering A ($^2\Sigma^+$) v'=0-7 and X ($^2\Pi_i$) v''=0-3. Also, Terwilliger and Smith [171] have reported absorption work on HCl from 1000 to 700 Å (12.4 - 17.7 eV) and assigned the observed Rydberg series. However, more recent work by Lefebvre-Brion *et al.* [116],[117], has resulted in a re-assignment of the Rydberg series. Frohlich and Glass-Maujean [118] have also reported the absolute photoabsorption, photodissociation, and photoionisation cross sections of HCl from 980 - 720 Å (12.52 - 17.71 eV) and their analysis of the photoabsorption and photoionisation spectra is in agreement with Lefebvre-Brion *et al.* [116],[117].

A potential energy diagram which summarises the main features of the electronic states involved in outer valence ionisation is given in Figure 4-2 to aid the discussion of results in this Chapter. The data for the X ($^1\Sigma^+$), X ($^2\Pi_i$), and A ($^2\Sigma^+$) states comes from Yencha *et al.* [173] and Huber and Herzberg [177]. The two Rydberg levels (shown as dashed lines in the Figure) are positioned by duplicating the A ($^2\Sigma^+$) state ion potential at lower energy and are assigned from analysis later in this chapter. These states are positioned in energy to account for the autoionising structure for DCl shown in Figure 4-4. Finally, the $^4\Pi$ state was positioned and scaled such that it crossed the A ($^2\Sigma^+$) state between the classical turning points of the v^+=7 and 8 vibrational levels.

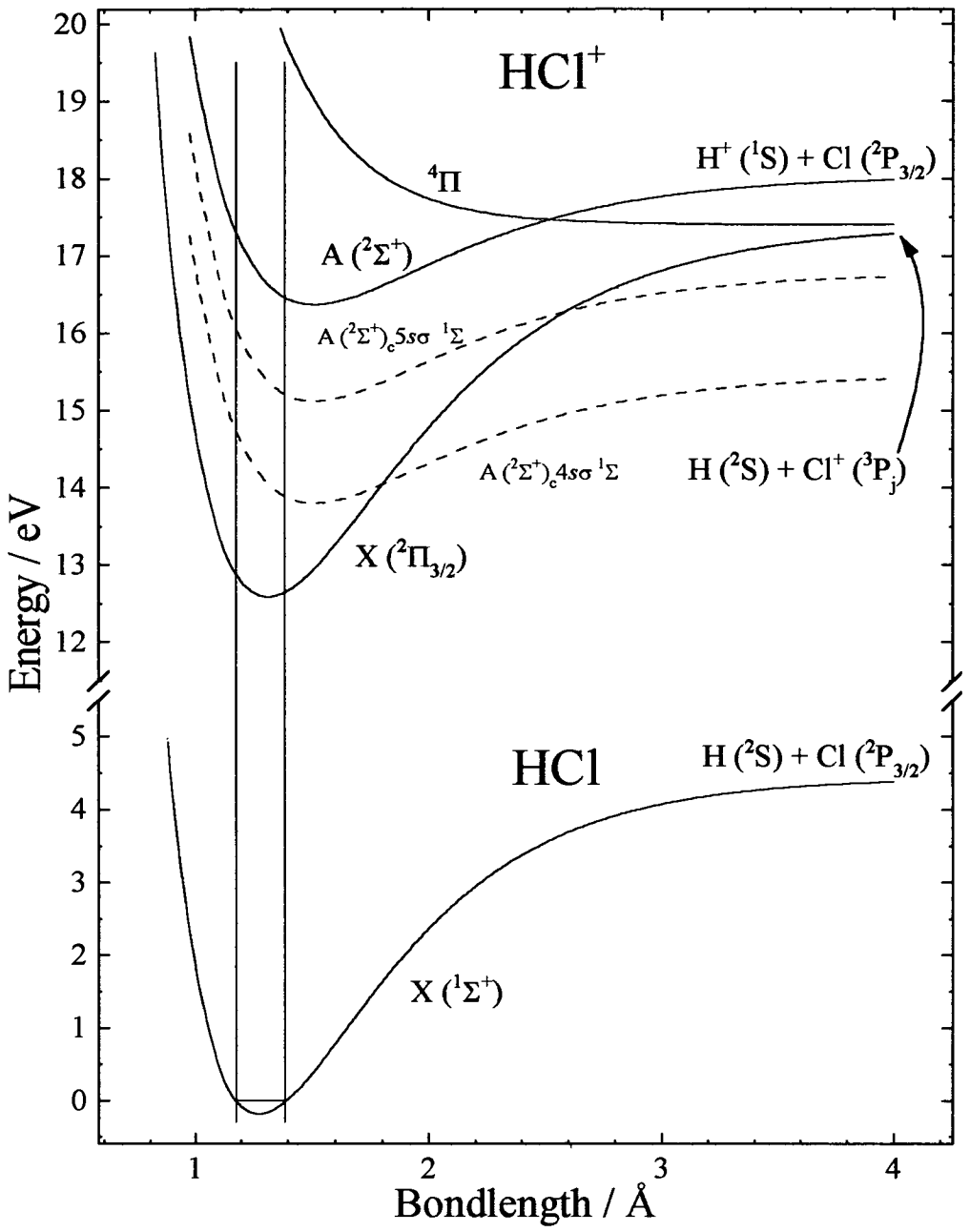

Figure 4-2 Potential energy diagram for the relevant electronic states of HCl in the outer valence ionisation region. Data used to construct the diagram has been taken from [173],[177],[223]

The present study of the threshold photoelectron spectrum of hydrogen chloride was undertaken to investigate the effect of the large improvement in incident photon resolution on the threshold photoelectron spectrum. It was also hoped that the inclusion of the deuterium isotope in the study would aid assignment of the $(3s\sigma)^{-1}$

ionisation states and the broadening mechanism occurring for the predissociated levels of the A ($^2\Sigma^+$) state.

4.2 Special experimental details

General details for the experiment are discussed in Chapter 2 and specific details of gas sample preparations are contained in section 2.5. Calibration of the spectra described in this chapter has proven difficult. The poor wavelength reproducibility of the McPherson monochromator at the Daresbury Laboratory resulted in the need to calibrate the spectra using secondary standards from the literature. Firstly, spectra were normalised and calibrated using the rare gas calibration curve (see section 2.6 for details) and the resultant adiabatic ionisation potentials for the X ($^2\Pi_{3/2}$) and the A ($^2\Sigma^+$) states were compared to the literature. For the X ($^2\Pi_{3/2}$) ionisation limit the rotationally resolved work by Tonkyn *et al.* [114] was used: in particular, Figure 4 in that paper shows a laser TPES spectrum of HCl which is at intermediate resolution to their PFI-ZEKE work and this threshold photoelectron work. By relating the rotational band shapes in Figure 4 (Tonkyn *et al.* [114]) to Figures 4-4 and 4-6 (this Chapter) it is possible to calibrate the X ($^2\Pi_{3/2}$) origin band in the current work. The A ($^2\Sigma^+$) state ionisation potential was found to be 8 meV higher than that found by Edvardsson *et al.* [100] so the A ($^2\Sigma^+$) state band origin was calibrated from the HeI PES work by Edvardsson *et al.* [100]. A linear correction function was used to align the present work with Edvardsson *et al.*.

The DCl spectrum was calibrated using the same procedure as for HCl and the consistency of the calibration between the two isotopomers was cross-checked using a spectrum obtained from an HCl/DCl mixture (not shown). The spectra presented in this chapter have been recorded at various experimental resolutions, further details are given when relevant. Resolutions are quoted as the FWHM for the Ar^+ $^2P_{1/2}$ ionisation line measured from calibration scans adjacent to the study scans.

4.3 Results and discussion

4.3.1 Overview of the valence threshold photoelectron spectrum of hydrogen chloride

The threshold photoelectron spectra of hydrogen and deuterium chloride over the current region of study are shown in Figure 4-3. For HCl^+ sub-spectra were recorded and catenated as follows: from 12.526 to 18.216 eV, 2 meV steps at 6.0 meV resolution: from 18.216 to 29.964 eV, 10 meV steps at 17.5 meV resolution: from 29.964 to 35.461 eV, 20 meV steps at 22.5 meV resolution. For DCl^+ the spectrum is made up as follows: from 12.526 to 18.018 eV, 2 meV steps at 6.6 meV resolution: from 18.018 to 33.95 eV, 10 meV steps at 18.5 meV resolution. The spectra in Figure 4-3 are quite similar, as would be expected for molecules which have essentially identical electronic structure. Clearly, by far the greatest signal intensity is seen in the Franck-Condon region of the X ($^2\Pi_i$) states. This seems to be a common feature of all the threshold photoelectron studies of the hydrogen halides presented in this thesis. The $(3s\sigma)^{-1}$ region is very weak compared to the outer valence region and this suggests that the probability of producing a threshold electron in what is generally a correlated two electron process is quite small.

The ionisation of the inner valence and outer valence regions are quite different. So it is easiest to discuss each section separately in more detail. Results and discussion of the outer valence region follow directly, and the inner valence region concludes the chapter.

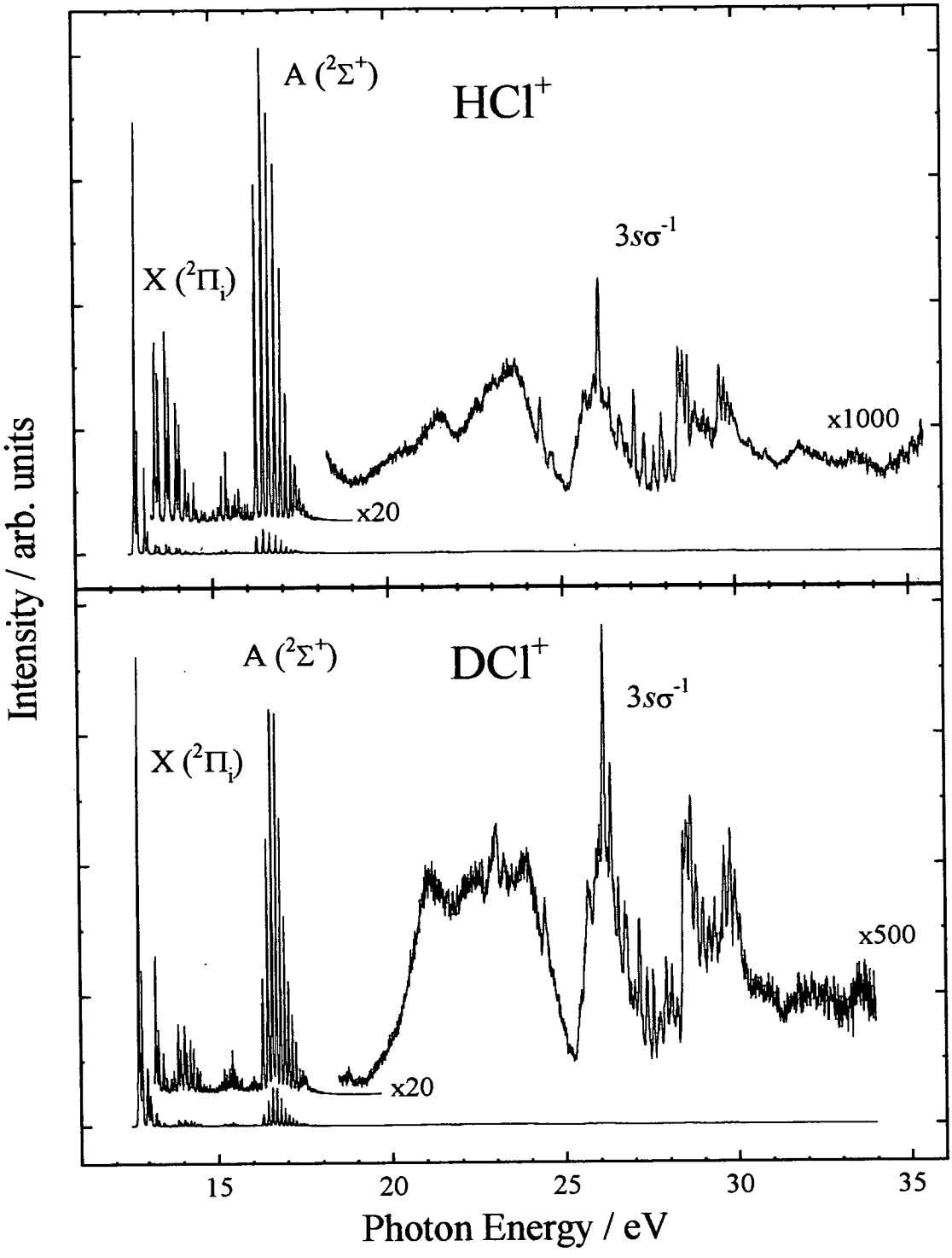

Figure 4-3 The complete threshold photoelectron spectra of hydrogen and deuterium chloride up to ~35 eV showing the X ($^2\Pi_i$), A ($^2\Sigma^+$), and $(3s\sigma)^{-1}$ ionisation regions. These spectra were produced by catenating sub-spectra as discussed in section 4.3.1.

4.3.2 The outer valence region of hydrogen and deuterium chloride

The threshold photoelectron spectra of hydrogen and deuterium chloride, for outer valence ionisation, are shown Figure 4-4. The Figure is an expanded view of Figure 4-3, and the resolution has already been quoted in section 4.3.1. Returning to Figure 4-4, most of the threshold photoelectron intensity occurs in the region of the origin of the X ($^2\Pi_i$) vibrational band. For both molecules the Ω=3/2 component is more intense than the higher energy Ω=1/2 component, suggesting the Ω=3/2 level is enhanced via spin-orbit autoionisation from Rydberg levels converging to the Ω=1/2 ion state.

The higher vibrational levels ($v^+>2$) of the X ($^2\Pi_i$) state are outside the Franck-Condon region and therefore must be accessed indirectly via autoionising neutral levels. Closer examination of the spectrum for deuterium chloride (Figure 4-4) shows that the vibrational intensities have a similar shape and energy spread to the A ($^2\Sigma^+$) state and so it is likely that Rydberg levels converging to the A ($^2\Sigma^+$) state act as intermediate states, autoionising to high vibrational levels of the X ($^2\Pi_i$) state.

The A ($^2\Sigma^+$) shows a vibrational intensity distribution which is essentially identical to that of the HeI photoelectron spectrum. In both spectra vibrational levels of the A ($^2\Sigma^+$) state which are predissociated are marked by a half-length tick. (see section 4.3.2.(a) for more details)

The peak positions of the vibrational progressions for both X ($^2\Pi_i$) states, and A ($^2\Sigma^+$) state, of HCl and DCl are given in Tables 5-1, 5-2, and 5-3. The measured peak positions have been fitted using a third order Dunham expression (described below) and the fitted peak positions are given beside the measured position. A ($^2\Sigma^+$) state peaks which show evidence of predissociation have not been included in the fit procedure.

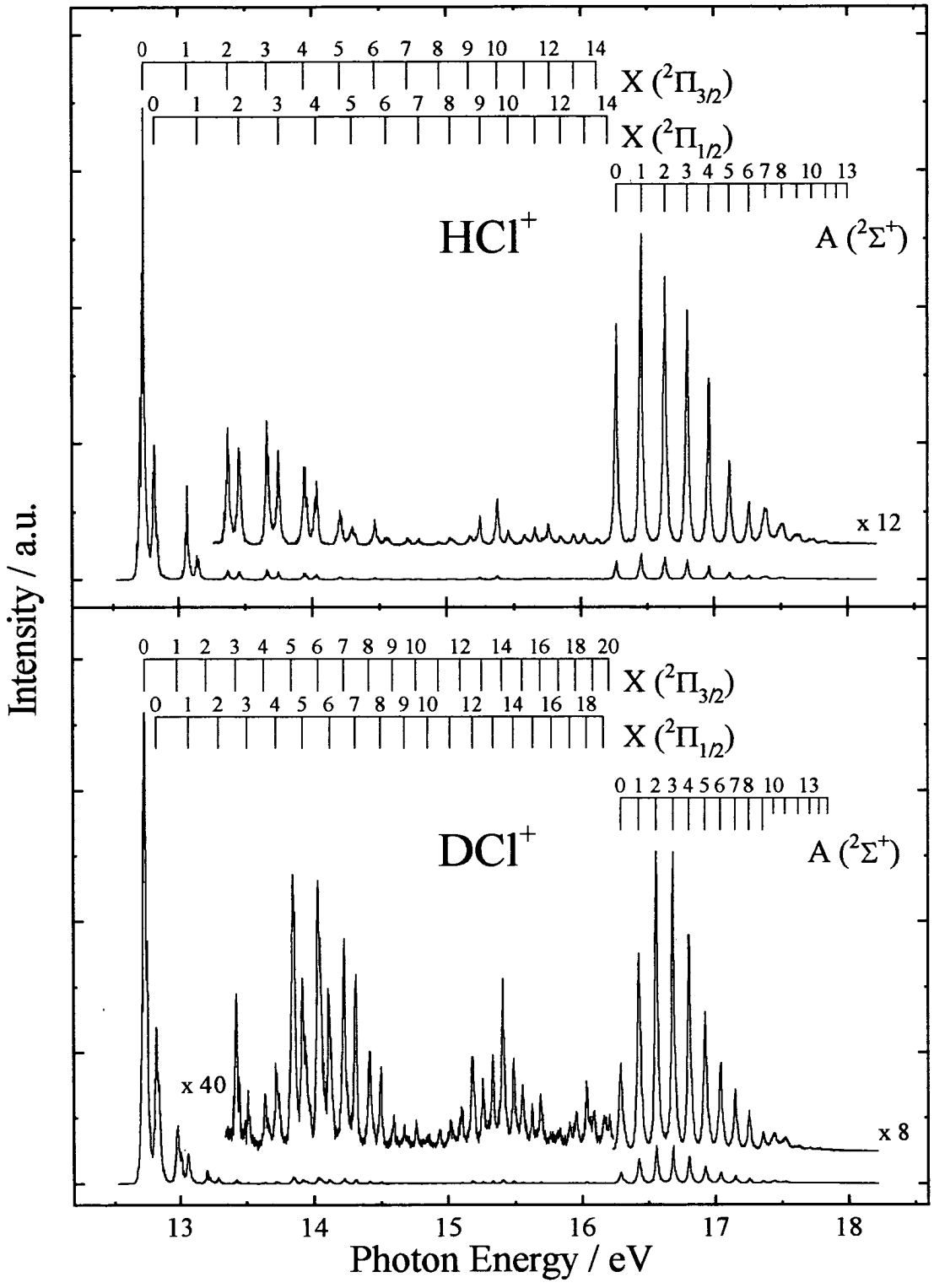

Figure 4-4 Threshold photoelectron spectra of the outer valence ionisation region of hydrogen and deuterium chloride. Vibrational levels of the X ($^2\Pi_i$) and A ($^2\Sigma^+$) states are marked by the ladders. Levels marked by half-length ticks were not used in the vibrational fitting procedure. The resolution for the spectra is given in section 4.3.1.

In the Born-Oppenheimer approximation, the electronic potential energy curves will be independent of the nuclear mass, so the vibrational peak positions for both HCl and DCl can be fitted to a single vibrational Dunham expression as in Equation 4-1 [165],[119],[120].

$$G^i(v') = \sum_n Y_{n,0}\left[\rho_i\left(v' + \tfrac{1}{2}\right)\right]^n$$

Equation 4-1

Where $G^i(v')$ is the vibrational term value for vibrational level v', $Y_{n,0}$ is the Dunham parameter, and $\rho_i = \sqrt{\mu(\mathbf{HCl})/\mu_i}$,[119],[165], where μ_i is the reduced mass of either HCl or DCl. Spectroscopic constants derived using Equation 4-1 for the X ($^2\Pi_i$) states and the A ($^2\Sigma^+$) state of HCl and DCl are given in Table 4-4. A selection of spectroscopic parameters for the various electronic states, taken from the literature, is also included in Table 4-4. There is good agreement between most of the results, however, many of the constants cannot be directly compared as the dimensionality of the fit is different.

The resolution of the current work is slightly higher than Frohlich *et al.* [108], however, the spectra are very similar. Comparison of the spectrum for HCl (Figure 4-4) with the threshold photoelectron spectrum by Yencha *et al.* [103] shows that the spectral features are now more clearly resolved, as would be expected from the higher resolution of this work. However, since both experiments were undertaken at room temperature the width of the vibrational bands are much greater than the experimental resolution through thermalisation of the initial X ($^1\Sigma^+$) state.

The Rydberg levels converging to the A ($^2\Sigma^+$) state that autoionise into high vibrational levels of the X ($^2\Pi_i$) state can be assigned from the vacuum ultra-violet absorption work by Terwilliger and Smith [171],[121]; the combined photoionisation cross section measurements and *ab initio* multichannel quantum defect theory calculations by Lefebvre-Brion *et al.* [116],[117]; and the photabsorption,

photoionisation and photodissociation work by Frohlich and Glass-Maujean [118]. Frohlich *et al.* [108] assigned the majority of the autoionising structure to the $4d\pi$ and $5d\pi$ Rydberg states converging to the A ($^2\Sigma^+$) state from their threshold photoelectron study of HCl. These assignments can be cross checked using the DCl^+ spectrum in the present work. In Figure 4-4, there is clearly an enhancement in the X ($^2\Pi_i$) vibrational levels of DCl^+ between 13.6 and 14.5 eV. This occurs at the same energy as an absorption band assigned to the [A ($^2\Sigma^+$)] $4p(\sigma,\pi)$ *p*-complex, (with $n^* = 2.31$) as assigned by Terwilliger and Smith [122 (series II)],[171] which was later confirmed as a $4p\pi$ Rydberg state by Lefebvre-Brion *et al.* [116][h] and Lefebvre-Brion and Keller [117]. Lefebvre-Brion *et al.* [116] also calculated that another Rydberg state ($3d\sigma$) occurred very close to the $4p\pi$, however this level was not seen in their photoionisation studies, suggesting the level is strongly predissociated. The predissociative nature of the $3d\sigma$ state has been confirmed by *ab initio* multichannel quantum defect theory (MQDT) calculations by Lefebvre-Brion and Keller [117], and has been observed in photodissociation studies by Frohlich and Glass-Maujean [118].

The calculated first vibrational level of the next member of the $np\pi$ Rydberg series (15.03 eV, n=4) coincides with the onset of the second lobe of intensity in the DCl spectrum so the Rydberg series which is most prevalent in the threshold photoelectron spectrum of DCl^+ is assigned as the $(2s\sigma)^2(2p\sigma)^1(2p\pi)^4$, $np\pi$ $^1\Pi$ series, where n = 4-5. Using the absorption spectrum by Terwilliger and Smith [171] with the electronic state assignments by Lefebvre-Brion *et al.* [116], the $(2p\sigma)^1(2p\pi)^4$ $3d\pi$ $^1\Pi$ Rydberg state occurs between ~850 and 800 Å (14.6 - 15.5 eV). The DCl^+ threshold photoelectron spectrum shows only weak vibrational structure in this energy range. This shows that the $3d\pi$ Rydberg state does not autoionise producing threshold electrons (significantly).

---

[h] In [116] the Rydberg is assigned as the $3p\pi$ state. This is corrected in [117] to the $4p\pi$ Rydberg state.

The DCl^+ spectrum suggests the Rydberg series seen (indirectly) in the threshold photoelectron spectrum has [A $(^2\Sigma^+)$] $np\pi$ $^1\Pi$ symmetry. However, this assignment does not seem to hold for HCl^+. A close examination of the first three vibrational levels of the X $(^2\Pi_i)$ state of HCl shows that the ratio of the spin-orbit components is quite different for $v^+=2$ compared to the first two vibrational levels, suggesting that the $\Omega=1/2$ component of the $v^+=2$ vibrational level is enhanced by electronic autoionisation. The lowest vibrational level of the $4p\pi$ Rydberg state occurs at 13.71 eV in HCl [118] which is too high in energy to enhance the $v^+=2$ level of the ion at 13.454 eV. This suggests that the Rydberg series active in threshold photoelectron production is of different symmetry. Lefebvre-Brion and Keller [117] have published VUV fluorescence excitation spectra of HCl and DCl in the region 920 - 760 Å (13.48 - 14.41 eV) where two Rydberg states have been assigned as the [A $(^2\Sigma^+)$] $4s\sigma$ $^1\Sigma$ state and the [A $(^2\Sigma^+)$] $3d\sigma$ $^1\Sigma$ state. As both the VUV fluorescence excitation and TPE spectra for HCl are enhanced at lower energy than the corresponding DCl spectra it seems possible that the same Rydberg states may be involved in both processes. Yencha *et al.* [152] have suggested that the [A $(^2\Sigma^+)$] $ns\sigma$ $^1\Sigma$ Rydberg states are the predominant intermediate states involved in ion-pair formation in HCl and DCl and in a different paper Yencha *et al.* [103] assigned the autoionising structure in the threshold photoelectron spectrum to the [A $(^2\Sigma^+)$] $ns\sigma$ $^1\Sigma$ Rydberg series. While it is impossible to rule out the [A $(^2\Sigma^+)$] $nd\sigma$ $^1\Sigma$ Rydberg series as possible intermediate states without further work, it seems most likely that the extended vibrational progression in the threshold photoelectron spectra of HCl and DCl arises from the electronic autoionisation of the [A $(^2\Sigma^+)$] $ns\sigma$ $^1\Sigma$ Rydberg series, where n=5-7. Certainly the most intense Rydberg series observed in photoabsorption and photoionisation ([A $(^2\Sigma^+)$] $np\pi$ $^1\Pi$, and [A $(^2\Sigma^+)$] $nd\pi$ $^1\Pi$) do not seem to contribute to the threshold photoelectron spectrum.

4.3.2.*(a) Detail of the 17.2 to 18.1 eV regions in hydrogen and deuterium chloride*

The predissociative nature of the A ($^2\Sigma^+$) state at higher vibrational levels has already been noted in this chapter, however with these new results and the work by Edvardsson *et al.* [100] it is possible to compare spectra at similar resolution. Figure 4-5 shows the threshold photoelectron spectra of HCl and DCl from 17.2 to 18.1 eV accompanied by the high resolution HeI PES work on HCl by Edvardsson *et al.* [123], and some simulations of the TPE vibrational levels. The resolution of the TPE spectra is included in the figure caption. From panel (a) in Figure 4-5 it is clear that the features of the HCl TPES spectrum are very different from those of the HeI PES spectrum. In particular, the TPES vibrational progression is shorter and the vibrational levels much broader than the HeI PES progression.

The HCl TPES v^+=6 peak has quite similar shape to the HeI PES v^+=7 peak suggesting that rotational autoionisation does not play a dominant part in the ionisation process for non-predissociated levels. However, comparing the HCl v^+=7 peaks for the two spectra shows that in TPES the level has been broadened to lower energy. This seems to be a consistent effect for the v^+=7-13 peaks in TPES spectra. That there is such a strong broadening in the v^+=7 TPES peak is quite remarkable, and possibly more remarkable is that the broadening takes place entirely to lower energy. This broadening of the v^+=7 peak seems in common with the absence of emission data from this level by Sheasley and Mathews [115]. The rotational structure on the lower energy side of the HeI PES v^+=7 peak is assigned to the *P branch* transitions (i.e. $\Delta N = -1$, see Edvardsson *et al.*[100]) and this suggests that the ionisation scheme has a propensity towards negative changes in total angular momentum (i.e. $\Delta N = -1,-2,...$). It would be worthwhile to attempt to simulate the rotational angular momentum changes that are needed to obtain the observed spectral profiles in HCl and DCl. Edvardsson *et al.* [100] successfully modeled the rotational profile of the vibrational levels of the A ($^2\Sigma^+$) state of HCl using only a Boltzmann distribution for the initial state and adjustable parameters for the rotational branching ratios to the ion. Panels (b) and (c) of Figure 4-5 show the results of a similar fitting

procedure on the present TPE spectra. The LabTalk script in Appendix E was used for the simulations. The weighting factors for the various rotational branches ($\Delta N = -5$ to $+5$) for the fits to each vibrational level are given in Table 4-5. The validity of the fit expression has been checked by fitting the non-predissociated $v^+=6$ level of HCl, and the position and intensity of the rotational structure on the lower energy side of the peak are well reproduced (panel (b) in Figure 4-5). The fit procedure works well for all of the HCl vibrational levels, with most of the rotational contours accounted for, however the high background between $v^+ = 7$ and $v^+ = 8$ cannot be accounted for with the model unless even larger changes in rotational momentum (ΔN) are allowed. From the fitted intensity data in Table 4-5 it is clear that there must be additional ionisation pathways available as the intensity of $v^+=7$ and $v^+=8$ is greater than $v^+=6$. Table 4-5 also shows that there is a propensity for $\Delta N < 0$ as expected from the shape of the vibrational levels. The relative branching ratios have been normalised to the R branch in common with the fits on the HeI PES spectrum by Edvardsson *et al.* [100].

The fits to the DCl vibrational levels (panel (c)) are not as good. Vibrational levels $v^+ = 8$ and $v^+ = 9$ are well represented by the fit but the higher vibrational levels are broader than the fit parameters allow. The number of rotational branches could be increased to produce a better result, however it is uncertain whether this is physically applicable. For instance, an L branch corresponds to $\Delta N = -5$, which is already a large change in angular momentum.

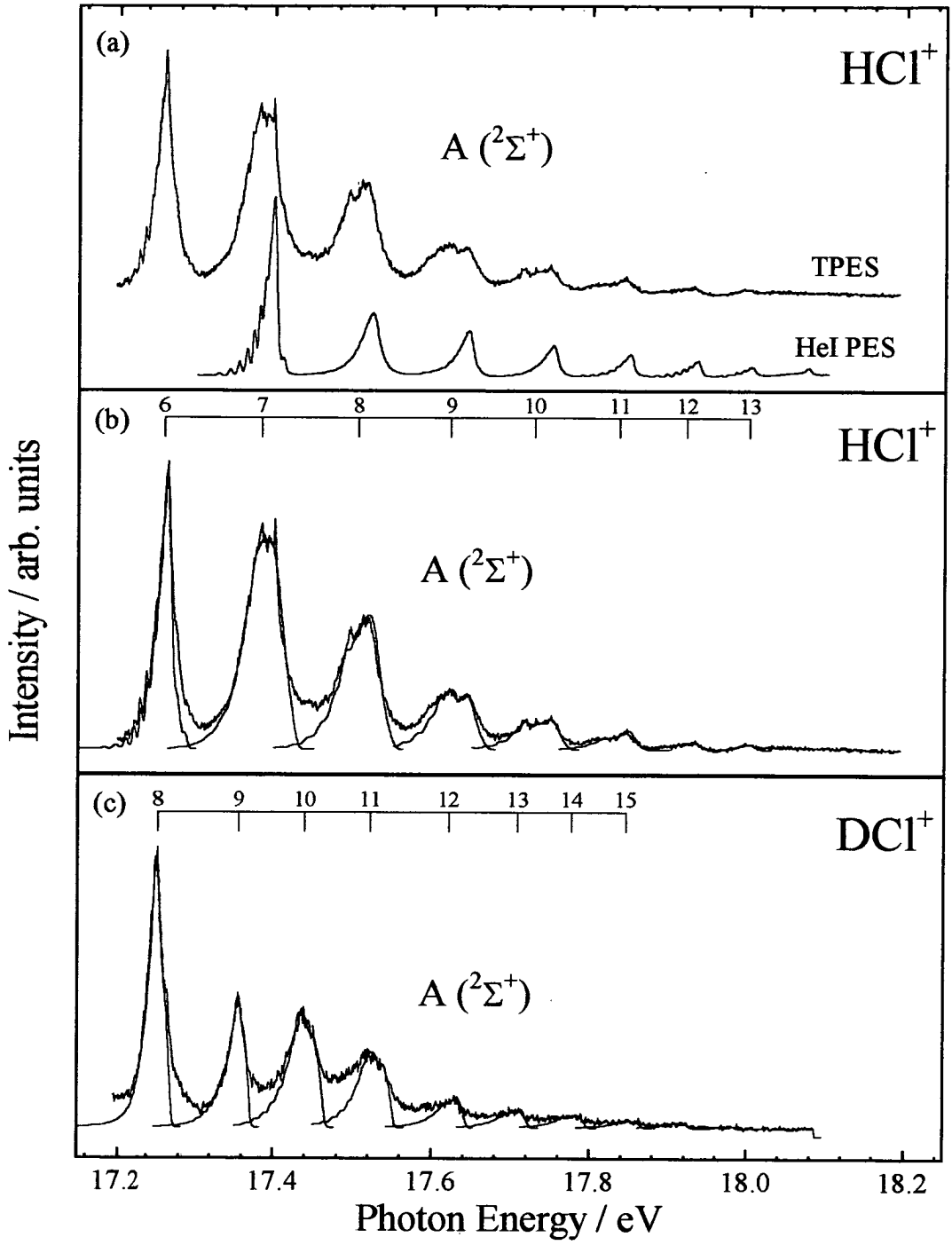

Figure 4-5 Threshold photoelectron spectrum of the predissociated levels of the A ($^2\Sigma^+$) state of HCl and DCl. Panel (a) shows the HeI PES spectrum by Edvardsson *et al.* [100] for comparison. Panels (b) and (c) show the TPE spectra accompanied by rotational band contour simulations for the various vibrational levels (see text). The resolution of the spectrum is 7.2 meV at 17.5 eV, $\Delta E/E = 4.13\times10^{-4}$ for HCl, and 4.8 meV at 17.5 eV, $\Delta E/E = 2.756\times10^{-4}$ for DCl.

From the fit work it can be concluded that there seems to be a large propensity for negative changes in rotational angular momentum during autoionisation to a predissociated ion state, however the mechanism for this autoionisation process is unclear. It does not occur in the HeI PES spectrum and so is probably a resonant effect. It is possible that the extra structure on the lower energy side of the peak is caused by the rotational autoionisation of dissociative Rydberg states into the $^4\Pi$, $^2\Sigma^-$, $^4\Sigma^-$ dissociative ion states (Raftery and Richards [101]), however simulation of this type of effect is well beyond the scope of this thesis.

4.3.2.*(b)* *High resolution study of the X ($^2\Pi_i$) v^+=0,1 levels of hydrogen and deuterium chloride.*

Figure 4-6 shows the high resolution threshold photoelectron spectrum of hydrogen and deuterium chloride at a resolution of ~3 meV. This resolution allows rotational structure to be partially resolved. The general features of the spectrum for HCl are similar to the previous lower resolution (~8 meV) threshold photoelectron study over part of this region by Frohlich *et al.* [113]. Frohlich *et al.* were able to simulate the features in the HCl origin band by assuming the X ($^2\Pi_{1/2}$) band is due entirely to direct ionisation and that the X ($^2\Pi_{3/2}$) bandshape resulted from a combination of direct ionisation and spin-orbit autoionisation from Rydberg levels converging to the X ($^2\Pi_{1/2}$) ion.

The extensive structure for the X ($^2\Pi_{3/2}$) origin band of HCl is quite similar to the laser TPES spectrum by Tonkyn *et al.* [114, (Fig. 4)], however the work by Tonkyn *et al.* is at higher resolution. This spectrum was collected with the idea of comparing the final ion rotational distributions in the PFI-ZEKE spectra (Tonkyn *et al.*) with that of high resolution TPES, however the resolution is not high enough to fully analyse the spectrum unambiguously. So, a comparison of the results for the two techniques awaits higher quality results. The Advanced Light Source at Berkeley

can now achieve sub-meV resolution in this energy range, and a new study would seem advantageous.

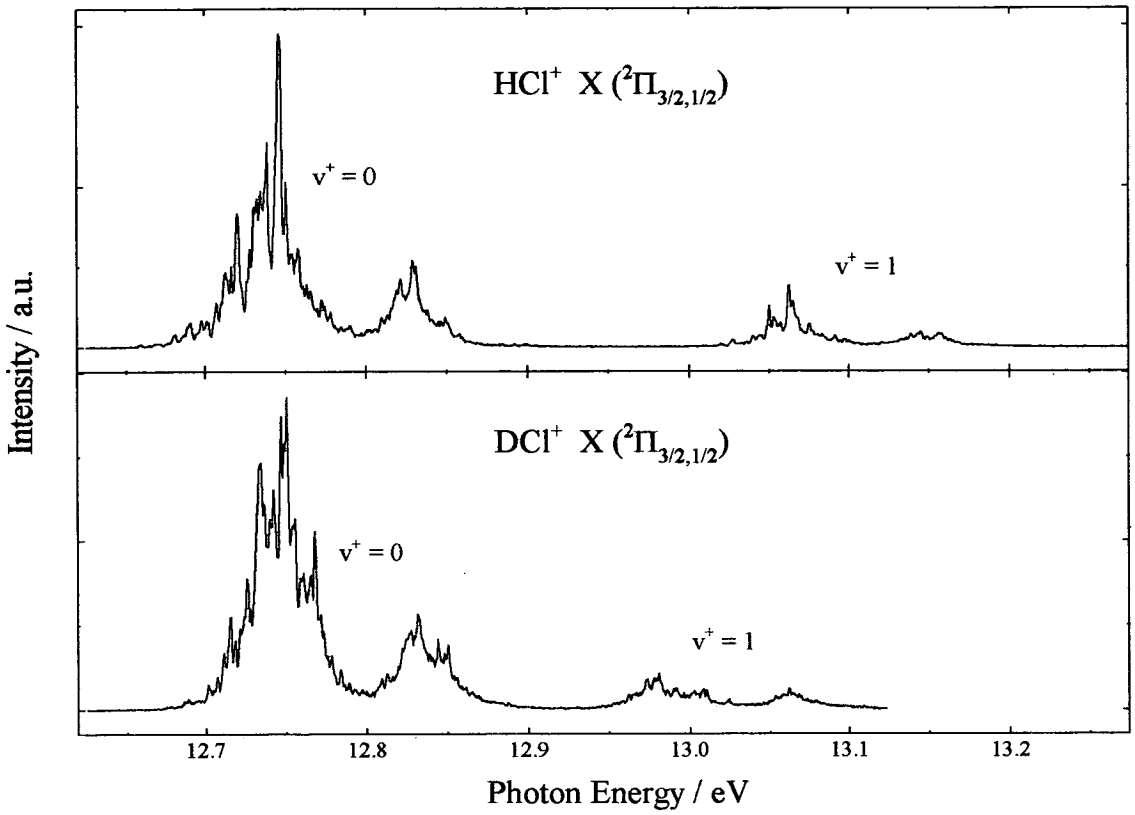

Figure 4-6 Threshold photoelectron spectrum of the X ($^2\Pi_i$) v^+=0,1 levels of hydrogen and deuterium chloride showing extensive rotational band structure. (the resolution for the spectra is given in 4.2) The relative intensity of the 3/2 to 1/2 components is enhanced by the spin-orbit autoionisation of Rydberg levels converging to the higher spin-orbit component. In both spectra the resolution is ≤ 3 meV.

4.3.3 The inner valence ionisation region of hydrogen and deuterium chloride

Figure 4-7 shows the threshold photoelectron spectrum of hydrogen and deuterium chloride up to ~35 eV. The resolution of the spectra is given in the figure caption. The DCl spectrum terminates at 34 eV as the signal to noise ratio is very poor. This is entirely due to the low photon flux in this energy as can be seen from the measured synchrotron output in Figure 2-1. As mentioned previously this region has been studied for HCl by Yencha *et al.* [103], by Adam *et al.* [110],[124], and by

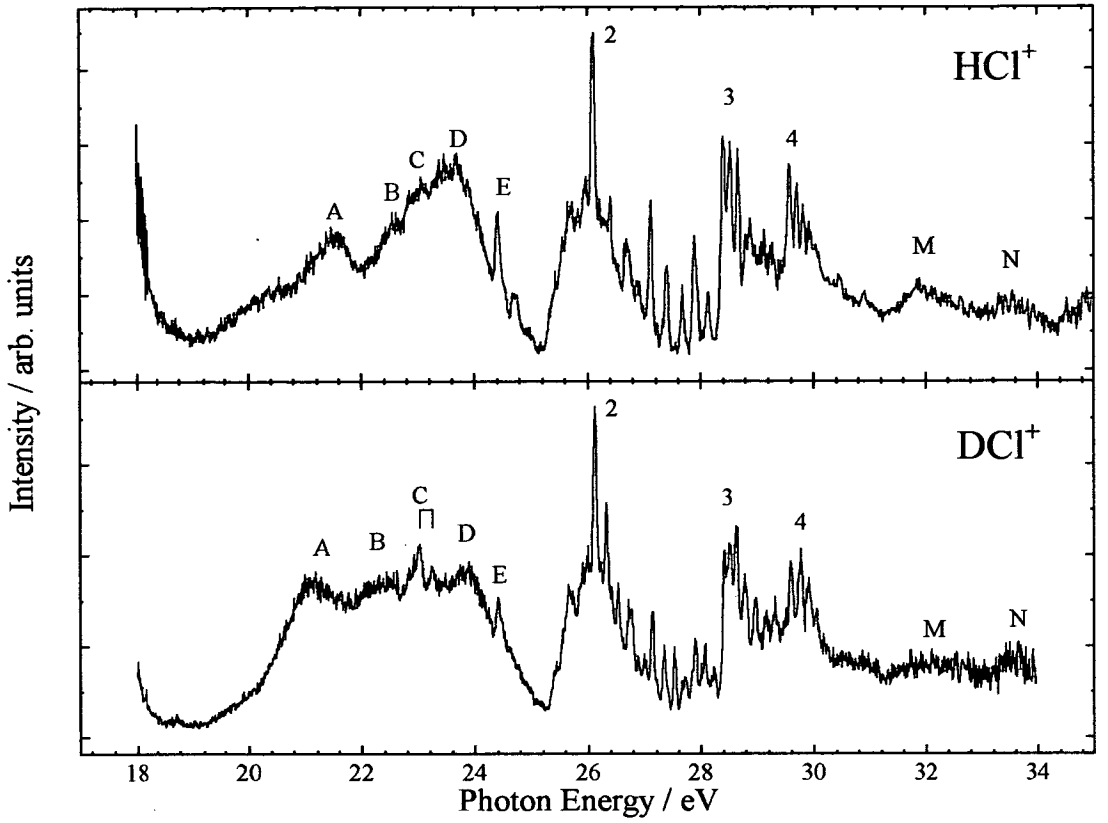

Figure 4-7 Overview of the TPE spectrum of hydrogen and deuterium chloride for the inner valence ionisation region. The resolution for the HCl trace is 45 meV at 26 eV, $\Delta E/E=1.74\times10^{-3}$, and 48 meV at 26 eV, $\Delta E/E=1.84\times10^{-3}$ for the DCl spectrum.

Svensson *et al.* [109]. In Figure 4-7 a combination of numbering and lettering is used to identify spectral features. The lettering corresponds to the labeling system adopted by Yencha *et al.* [103] and the numbering corresponds to the bands identified by Adam *et al.* [110],[124] and Svensson *et al.* [109].

Yencha *et al.* [103] assigned labels A though D as ionisation to repulsive ion states. Line E must be a bound state due to the sharpness of its features, Yencha *et al.* described it as most likely to be initial absorption to a Rydberg level converging to the $4s\sigma^{-1}$ ionisation limit followed by autoionisation into the dissociative continuum of State D. This ionisation scheme has been seen for Rydberg levels converging to the B ($^2\Sigma_g^+$) state of fluorine that autoionise into the repulsive continua of either the X ($^2\Pi_{g,i}$) or A ($^2\Pi_{u,i}$) states of F_2 (see section 7.3.4, Figure 7-9) where the structure of the intermediate Rydberg level is clearly seen on a featureless continuum. The

positions of the band maxima are given in Table 4-6. In DCl there seems to be a short vibrational progression for band C. It may be that this progression is due to another intermediate Rydberg level as in the case of band E, and the continuum signal labeled C in the HCl trace is hidden below this signal.

Labels M and N again correspond to the labeling by Yencha *et al.* [103] and are discussed more fully in that paper. The region of the spectrum containing peaks 2, 3, and 4 is shown in Figure 4-8.

4.3.3.*(a)* *The threshold photoelectron spectrum of hydrogen and deuterium chloride from 23.5 to 31.2 eV*

Figure 4-8 shows the observed vibrational progressions for inner valence ionisation seen in this study. The features of both traces in this figure are quite similar as would be expected where the electronic states are identical. Various vibrational progressions are labeled to correspond with the work by Yencha *et al.* [103] (E,F,G,H,K,L,M,N) while different progressions to those found by Yencha *et al.* are labeled #,*,Q,R. The positions for the various peaks observed for both HCl and DCl are given in Table 4-6. The peak positions for HCl from the present work seem to be consistently 50 to 70 meV below the results for Yencha *et al.* [103], which are also included in the table. This may point to a calibration problem in the present data as the results by Yencha *et al.* correspond relatively well to the results by Wills *et al.* [125], the discrepancy almost certainly lies in the poor performance of the monochromator on Beamline 3.2 at the Daresbury Laboratory (see Chapter 2 for discussion).

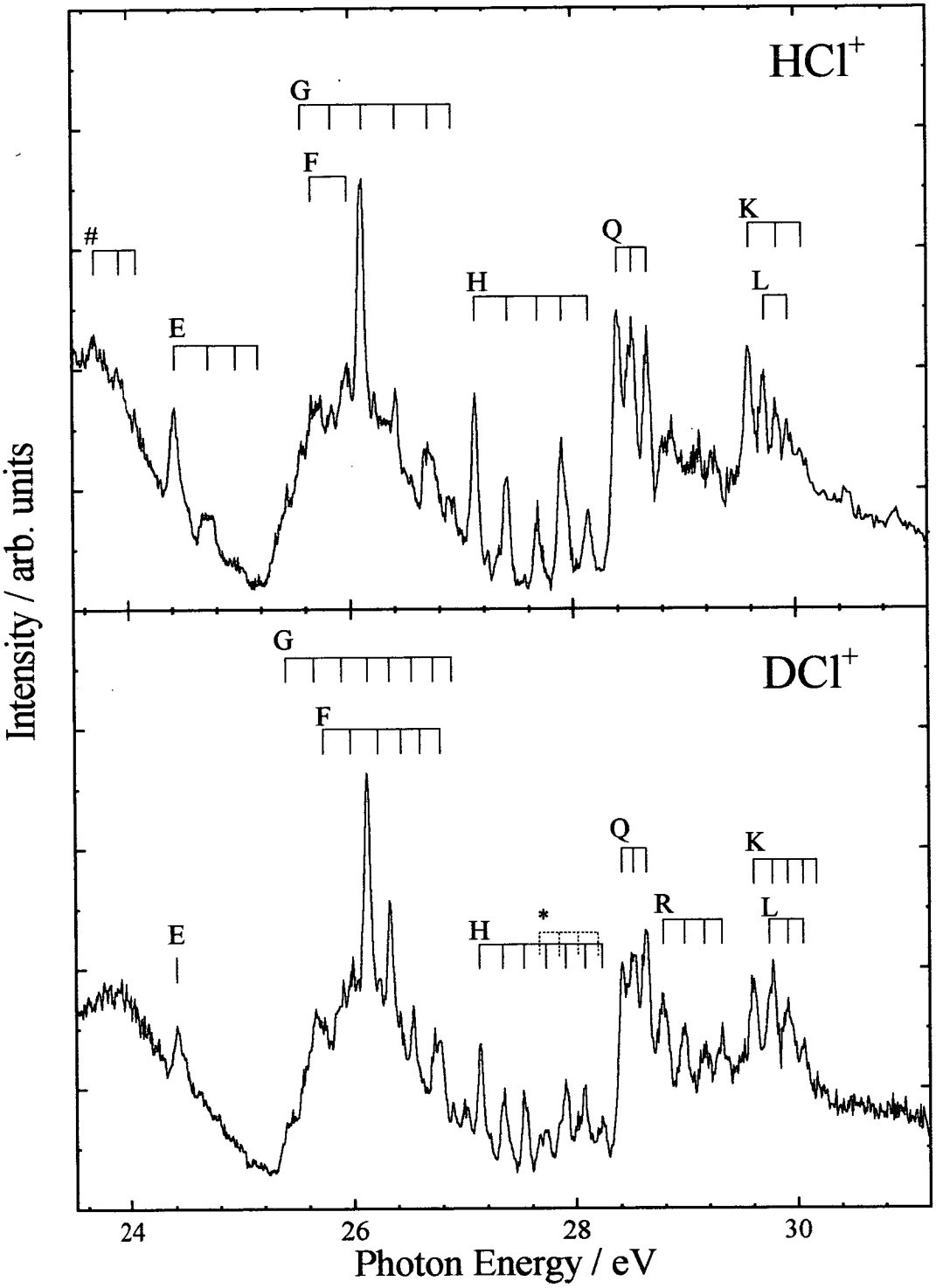

Figure 4-8 The threshold photoelectron spectrum of hydrogen and deuterium chloride from 23.5 to 31.2 eV which probable vibrational progressions assigned. The resolution for the spectra in this figure is as detailed in Figure 4-7.

Starting at lowest energy in the HCl trace the band marked # consists of 3 weak levels lying on the continuum structure of the state labeled D in Figure 4-7. This progression is probably formed in the same way as the E state, namely the structure is that of a bound Rydberg level converging to one of the ion states which then autoionises into the D state continuum. This weak structure was not observed by Yencha *et al.* [103] however, it was observed by Wills *et al.* [125] and was associated with the ion state at 26.15 eV. As three vibrational levels are observed in # it seems likely that the Rydberg level is shifted to larger bondlength than the neutral. There does not seem to be any evidence of this state in the DCl spectrum at current signal to noise levels.

For the E state itself 4 levels are observed in HCl whereas only one is seen in DCl, there are possibly further levels in DCl, however the signal to noise ratio is not high enough to decipher further levels. As with state # it seems likely that potential minimum of the Rydberg state is moved to larger bondlength.

The G and F states are quite similar to the assignments by Yencha *et al.* [103] in HCl, both of these levels show a degree of vibrational excitation. This suggests the geometry of these states are quite different from the ground state of the neutral, or that the extended vibrational progressions are due to autoionising levels. It seems likely that the first case is most prevalent.

State H seems to form a single progression in both spectra, however in the DCl trace a further state marked with an asterisk (*) could possibly be present. Only four vibrational levels can be identified however the spacing between these levels is very similar to the highest four levels in the H state. It is possible that the state labeled H is in fact two states: thus, in DCl the last four levels and the state marked * could be two spin-orbit split states, and the first three levels of H could belong to a different state. The variation of intensity of the seven observed levels in state H for DCl supports this idea as there seems to be two *lobes* of intensity with a minimum at peak 4. However, there is no evidence for two spin-orbit states in HCl, and although

the intensity distributions are again similar to DCl it cannot be clarified whether H is in fact really two (or three) states, from this work.

States Q and R are assigned differently by Yencha *et al.* [103]. They assigned these states as two intermeshed states I and J with twice the vibrational spacing of states Q and R. Whilst the I,J assignment has benefits it does not adequately describe the spectrum for DCl where the I,J assignment results in erratic vibrational spacings for the higher levels. So two new states are assigned as Q and R. The region corresponding to R in DCl cannot be assigned in HCl as the signal to noise ratio is too poor to discern vibrational features and is left unassigned. The spacing between the three peaks in band Q increases with peak number for both molecules, it may be that these three peaks correspond to ionisation to different ion states where the ionisation is exclusively vertical.

Band systems K and L in HCl are as assigned by Yencha *et al.* [103]. In DCl the spacing between adjacent vibrational levels almost matches that of the spacing between the two bands giving rise to broader peaks. The shape of the band in DCl also differs to that of HCl due to the overlap of the two states. As the vibrational spacings for both states are very similar it seems likely that these states arise from spin-orbit components with the same electronic structure.

From the results of the Green's-function calculations on HCl by von Niessen *et al.* [126] it can be seen that most of the inner valence ionisation states of HCl cannot be represented by one single electron configuration. However, the calculations by von Niessen *et al.* predict 5 states at 23.28, 25.88, 27.94, 29.34, and 30.53 eV[i]. It is possible these correspond to the following: (1) 23.28 eV - the two peaks labeled C in DCl (Figure 4-7), (2) 25.88 eV - states F and G in Figure 4-8, (3) 27.94 eV - band H in the same figure, however see the description of band H above. (4) 29.34 eV -

---

[i] Basis J in [126] Table VII, further states also exist at higher energy.

possibly band R in DCl and the equivalent region in HCl, or possibly band Q in both spectra. (5) 30.53 eV - states K and L.

Finally, from the various electron configurations which give rise to the five bands calculated by von Niessen *et al.* [126] the following is noted. Bands 2,4, and 5 of the five mentioned above have significant contributions from $(\pi^2)n\delta$ *two hole one particle* (2h-1p) states. These states are likely to exhibit some spin-orbit interactions, which would agree with the assignments to bands F,G, and to bands K,L. (2 and 5 from von Niessen *et al.*), but not the assignment of band R to band 4 as there does not seem to be any evidence for multiple spin states in band R. By noting that the start of band K is at 29.58 eV in HCl as opposed to 30.47 eV as calculated by von Niessen *et al.* [126] for band 5 (0.89 eV lower) one could assume that band 4 would also be ~ 0.89 eV lower in the threshold spectrum, i.e. at 28.38 eV. Band Q starts at 28.40 eV which seems to correspond to this energy. Thus it seems possible that band Q comprises of at least two spin-orbit sub-states instead of a single vibrational progression, explaining why the spacing between the levels assigned to Q increase towards higher energy.

In summary this work has identified some new electronic states with vibrational structure in the inner valence ionisation region of hydrogen and deuterium chloride. The results and assignments are in general very similar to those obtained by Yencha *et al.* [103], however some of the assignments have been changed as a result of the combined analysis of the spectra for the hydrogen and deuterium isotopes. The full classification of the states in this region awaits both a more highly resolved spectrum and more detailed calculations on the electronic nature of the states.

4.4 Conclusions for the threshold photoelectron spectrum of hydrogen and deuterium chloride

The threshold photoelectron spectra of hydrogen and deuterium chloride up to ~35 eV are complex. Taking an overall view it is clear that most of the threshold photoelectron signal lies in the lowest X ($^2\Pi_i$) state in common with HF/DF,

HBr/DBr, and HI presented in this thesis. Inner valence ionisation does not obey the independent electron approximation and a large number of mixed configuration states are found instead.

Extended (weak) vibrational progressions are found in the X ($^2\Pi_i$) state of both hydrogen and deuterium chloride. These progressions are assigned as due to autoionisation from the $ns\sigma$ $^1\Sigma$ (n=4-6) Rydberg series. The Rydberg assignments agree with the assignments in the threshold photoelectron experiment by Yencha *et al.* [103], however it is also possible that the $nd\sigma$ $^1\Sigma$ (n=3-5) Rydberg series could also be involved in threshold photoelectron production. The vibrational progressions for the X ($^2\Pi_i$) state have generated accurate third order Dunham coefficients fitted over approximately 75% of the potential well.

The predissociated levels of the A ($^2\Sigma^+$) state ($v^+\geq7$) are seen to be extensively broadened in the present study. When the HCl spectrum for this region is compared to a high resolution HeI PES spectrum of HCl the broadening is found to occur only to lower energy. Simulation of the TPE spectra shows that there is a propensity for negative changes in rotational angular momentum during the ionisation event (ΔN=-1,-2,...), however the mechanism through which this occurs is presently not understood.

A high resolution study of the X ($^2\Pi_i$) v^+=0,1 bands shows that the intensity of the X ($^2\Pi_{3/2}$) levels are increased through spin-orbit autoionisation from the corresponding vibrational level of the X ($^2\Pi_{1/2}$) state. As this has already been studied no simulations were attempted, a more fully resolved spectrum and a cooled gas beam would be advantageous for future studies in this energy region.

The $(3s\sigma)^{-1}$ ionisation region is extremely complex. Much of the new analysis follows the previous threshold photoelectron work on HCl, however some new assignments have been made. In particular a Rydberg state noted as missing in the previous threshold photoelectron work has been assigned. Also extensive use of the

deuterium chloride isotope results for this region has allowed some possible re-assignments of bands in this region.

Further work at higher resolution would be useful for a better understanding of the results presented in this thesis. The use of the molecular dynamics beamline at the Advanced Light Source (Berkeley) [127] to study the origin and first excited vibrational levels of the X ($^2\Pi_i$) band of HCl and DCl at higher resolution [128] would resolve much of the rotational structure in this region. A high resolution study of the A ($^2\Sigma^+$) state could also be useful and aid understanding of the vibrational level broadening in the predissociated levels.

4.5 Tables of results for hydrogen and deuterium chloride

Table 4-1 Observed and calculated vibrational band head positions (in eV) for the transitions: $e + HCl^+ (X\ (^2\Pi_i),\ v') \leftarrow HCl\ (X\ (^1\Sigma^+),\ v''=0)$

	HCl X ($^2\Pi_{3/2}$)		HCl X ($^2\Pi_{1/2}$)	
v′	obs[a]	calc	obs[a]	calc
0	12.745	12.744	12.830	12.829
1	13.062	13.062	13.147	13.148
2	13.367	13.367	13.454	13.453
3	13.660	13.660	13.746	13.746
4	13.939	13.940	14.026	14.026
5	14.207	14.208	14.294	14.294
6	14.463	14.464	14.550	14.549
7	14.708	14.708	14.794	14.794
8	14.941	14.941	15.027	15.026
9	15.163	15.164	15.248	15.248
10	15.376	15.376	15.458	15.459
11	15.577	15.577	15.659	15.660
12	15.768	15.768	15.850	15.850
13	15.950	15.950	16.031	16.031
14	16.122	16.123	16.202	16.203

[a] ± 0.002 eV

Table 4-2 Observed and calculated vibrational band head positions (in eV) for the transitions: $e + DCl^+ (X\ ^2\Pi_i,\ v') \leftarrow DCl\ (X\ ^1\Sigma^+,\ v''=0)$

	DCl X ($^2\Pi_{3/2}$)		DCl X ($^2\Pi_{1/2}$)	
v′	obs[a]	calc	obs[a]	calc
0	12.749	12.749	12.834	12.834
1	12.980	12.980	13.066	13.066
2	13.205	13.204	13.289	13.290
3	13.421	13.422	13.507	13.507
4	13.633	13.632	13.719	13.718
5	13.838	13.837	13.923	13.923
6	14.036	14.035	14.120	14.121
7	14.228	14.227	14.312	14.313
8	14.413	14.412	14.498	14.498
9	14.592	14.592	14.678	14.678
10	14.765	14.766	14.851	14.851
11	14.934	14.934	15.019	15.019
12	15.097	15.097	15.181	15.181
13	15.254	15.253	15.337	15.338
14	15.406	15.405	15.489	15.489
15	15.552	15.551	15.634	15.634
16	15.692	15.692	15.776	15.775
17	15.828	15.828	15.911	15.910
18	15.958	15.959	16.040	16.040
19	16.086	16.085	16.166	16.166
20	16.207	16.206		

[a] ± 0.002 eV

Table 4-3 Observed and calculated vibrational band head positions (in eV) for the transitions: $e + HCl^+ (A\ ^2\Sigma^+,\ v') \leftarrow HCl (X\ ^1\Sigma^+,\ v''=0)$ and $e + DCl^+ (A\ ^2\Sigma^+,\ v') \leftarrow DCl (X\ ^1\Sigma^+,\ v''=0)$

	HCl A $(^2\Sigma^+)$		DCl A $(^2\Sigma^+)$	
v′	obs[a]	calc[b]	obs[a]	calc[b]
0	16.270	16.269	16.293	16.294
1	16.456	16.454	16.427	16.428
2	16.632	16.631	16.557	16.558
3	16.799	16.800	16.683	16.684
4	16.961	16.961	16.805	16.806
5	17.115	17.115	16.924	16.924
6	17.260	17.261	17.038	17.038
7	17.384[c]		17.148	17.148
8	17.506[c]		17.254	17.254
9	17.622[c]		17.355	17.356
10	17.728[c]		17.439[c]	
11	17.836[c]		17.522[c]	
12	17.921[c]		17.621[c]	
13	18.001[c]		17.708[c]	
14			17.776[c]	
15			17.845[c]	

[a] ±0.002 eV

[b] only measured values adjacent to fit values used as data for fit

[c] taken as the top of the predissociated peak

Table 4-4 Summary of spectroscopic constants (in eV) derived from the analysis of the HCl and DCl TPES spectra presented in this chapter in comparison with some of the relevant literature.

State	ionisation energy	ω_e	$\omega_e x_e$ /10^{-3}	$\omega_e y_e$ /10^{-5}	Ref.
HCl^+ X ($^2\Pi_{3/2}$)	12.745(2) [e]	0.3316(3)	-6.76(4)	5.15(19)	this work [d]
	12.747(2)	0.33178(4)	-6.732(24)	4.9(5)	[108][f]
	12.7447	0.3316	-6.84		[100][a]
	12.747(2)	0.3309(24)	-6.07		[111][a]
	12.75(1)				[103]
	12.7459(2)				[114][b]
		0.3314(8)	-6.45(74)		[115][a,c]
HCl^+ X ($^2\Pi_{1/2}$)	12.830(2) [e]	0.3322(2)	-6.85(4)	5.25(18)	this work [d]
	12.83(1)				[103]
	12.8282(2)				[114][b]
HCl^+ A ($^2\Sigma^+$)	16.270(2) [e]	0.1924(5)	-3.88(6)		this work [d]
	16.270	0.1942	-3.68	4.71	[100]
	16.265(3)	0.1959(24)	-4.33		[111]
	16.27(1)				[103]
		0.1991	-4.99		[115][c]
DCl^+ X ($^2\Pi_{3/2}$)	12.749(2) [e]	0.2378(4)	-3.49(4)	1.93(13)	this work [d]
	12.752(2)	0.2389(24)	-3.22		[111][a]
		0.2378(6)	-3.34(37)		[115][a,c]
DCl^+ X ($^2\Pi_{1/2}$)	12.834(2) [e]	0.2367(8)	-3.29(9)	1.00(27)	this work [d]
DCl^+ A ($^2\Sigma^+$)	16.293(2) [e]	0.1379(3)	-1.99(3)		this work [d]
	16.291(3)	0.1416(24)	-2.23		[111]
		0.1428	-2.529		[115][c]

[a] fine structure constants for the Ω = 3/2 and 1/2 components are not derived.
[b] HCl X ($^1\Sigma^+$), J''=0 → HCl^+ (X ($^2\Pi_i$), J^+=3/2
[c] constants for the ^{35}Cl isotope
[d] calculated from the analysis of the combined HCl and DCl vibrational data
[e] from the measured v′=0 peak positions
[f] using combined analysis with ref. [129]

Table 4-5 Fit parameters for the predissociated levels of the A ($^2\Sigma^+$) state of HCl and DCl The fitted peaks are shown in Figure 4-5.

	HCl A ($^2\Sigma^+$) v^+ =							
	6	7	8	9	10	11	12	13
Intensity [e]	1.000	1.930	1.213	0.572	0.300	0.144	0.054	0.026
Term Energy /eV	17.2657	17.3995	17.5267	17.647	17.7358	17.8506	17.935	18.005
$\overline{B}$ / eV [c]	6.5E-4	6.472E-4	6.075E-4	5.703E-4	5.33E-4	4.959E-4	4.587E-4	4.215E-4
FWHM / eV	0.0055	0.011	0.011	0.011	0.011	0.011	0.011	0.011
Branches	Relative branching ratio [d]							
L ($\Delta N = -5$)	0	1.2	3.2	3.2	5.6	2.4	1.6	0
M ($\Delta N = -4$)	0	2.2	2.4	5	2.6	2	2	0
N ($\Delta N = -3$)	0.08	2.4	1.6	1.2	1.2	0.4	1.4	0.16
O ($\Delta N = -2$)	0.03	1.4	1.2	0.8	0.8	0.4	0.6	0.08
P [a] ($\Delta N = -1$)	0.75	1	1.2	1	1	1	1.2	1.32
Q [a] ($\Delta N = 0$)	0.04	0.08	0.08	0.08	0.08	0.08	0.08	0.08
R [a] ($\Delta N = 1$)	1	1	1	1	1	1	1	1
S [b] ($\Delta N = 2$)	0.2	0.8	0.6	0.6	0.6	0.6	0.6	0.6
T [b] ($\Delta N = 3$)	0.15	0.6	0.4	0.4	0.4	0.4	0.4	0.4
U [b] ($\Delta N = 4$)	0.05	0.4	0.2	0.2	0.2	0.2	0.2	0.2

	DCl A ($^2\Sigma^+$) v^+ =							
	8	9	10	11	12	13	14	15
Intensity [e]	1	0.576	0.772	0.514	0.171	0.103	0.076	0.043
Term Energy /eV	17.254	17.356	17.451	17.54	17.632	18.712	17.786	17.858
$\overline{B}$ / eV [c]	3.531E-4	3.394E-4	3.254E-4	3.114E-4	2.956E-4	2.808E-4	2.666E-4	2.51E-4
FWHM / eV	0.006	0.006	0.006	0.006	0.006	0.006	0.006	0.006
Branches	Relative branching ratio [d]							
L ($\Delta N = -5$)	0.1	0.4	3	3.2	1.6	2	2.2	2.2
M ($\Delta N = -4$)	0.1	0.4	3.2	3.2	1.6	2	2.2	2.2
N ($\Delta N = -3$)	0.16	0.3	3	3	1.6	2	2.2	2.2
O ($\Delta N = -2$)	0.03	0.2	0.4	0.33	0.4	0.4	0.4	0.4
P [a] ($\Delta N = -1$)	0.75	0.6	1.2	1.2	1.2	1.2	1.2	1.2
Q [a] ($\Delta N = 0$)	0.04	0.04	0.08	0.07	0.08	0.08	0.08	0.08
R [a] ($\Delta N = 1$)	1	1	1	1	1	1	1	1
S [b] ($\Delta N = 2$)	0.4	0.5	0.8	0.83	1	1	1	1
T [b] ($\Delta N = 3$)	0.4	0.5	0.8	0.83	1	1	1	1
U [b] ($\Delta N = 4$)	0.4	0.6	8	0.83	1	1	1	1

[a] These branches are strongly overlapped so only the P and R branch intensities were varied

[b] Branches form band heads, however they are overlapped by the P,Q,R branches due to the large rotational constants.

[c] From Edvardsson *et al.* [100] (isotope relations used to derive $\overline{B}_{DCl}$)

[d] Normalised to the R branch

[e] Intensity of the fitted peak

Table 4-6 Table of peak positions (in eV) for the inner valence ionisation region of hydrogen and deuterium chloride.

	HCl^+		DCl^+
Band system	present work [a]	previous work [103]	present work [a]
A	21.57 [e]	21.63	21.15 [e]
B	22.61 [e]	22.73	22.33 [e]
C	23.11 [e]	23.20	23.04
			23.25
D	23.68 [e]	23.69	23.90 [e]
E	24.42	24.47	24.41
	24.73	24.76	
	24.98	25.02	
	25.18		
F		25.48	
	25.66	25.73	25.74
	25.98	26.01	25.99
			26.23
			26.44
			26.61
			26.78
G	25.57	25.62	25.41
	25.84	25.91	25.66
	26.12	26.16	25.91
	26.42	26.46	26.14
	26.71	26.75	26.34
	26.91	26.96	26.54
			26.73
			26.89
H	27.12	27.19	27.13
	27.41	27.47	27.34
	27.68	27.74	27.53
	27.90	27.97	27.73
	28.14	28.21	27.91
			28.08
			28.24
K	29.58	29.66	29.61

	29.83	29.90	29.77
	30.06	30.12	29.92
			30.05
			30.17
L	29.72	29.79	29.744
	29.93	30.00	29.914
			30.053
Q	28.40	28.48 [b]	28.42
	28.53	28.60 [c]	28.52
	28.67	28.74 [d]	28.64
R			28.79
			28.98
			29.16
			29.32
# [f]	23.69		
	23.91		
	24.09		
* [g]			27.67
			27.85
			28.02
			28.20
M	31.90	31.99	32.08
N	33.57	33.37	33.64

[a] ± 0.01 eV
[b] assigned to Band I level 1
[c] assigned to Band J level 1
[d] assigned to Band I level 2
[e] Band maximum, no discernible vibrational structure
[f] weak progression on state D continuum
[g] possible progression (see text)

Chapter 5. Hydrogen and deuterium bromide

5.1 Introduction

Figure 5-1 shows a schematic of the valence electronic structure of hydrogen and deuterium bromide. The diagram is essentially the same as the other members of the hydrogen halide series. Ionisation of an essentially non-bonding $4p\pi$ electron gives rise to the X ($^2\Pi_i$) ion state, which will be spin-orbit split. Removal of a $4p\sigma$ electron results in the formation of the A ($^2\Sigma^+$) state, and removal of a $4s\sigma$ electron would be expected to result in the formation of the B ($^2\Sigma^+$) state, however, in reality many electronic states are formed through electron correlation.

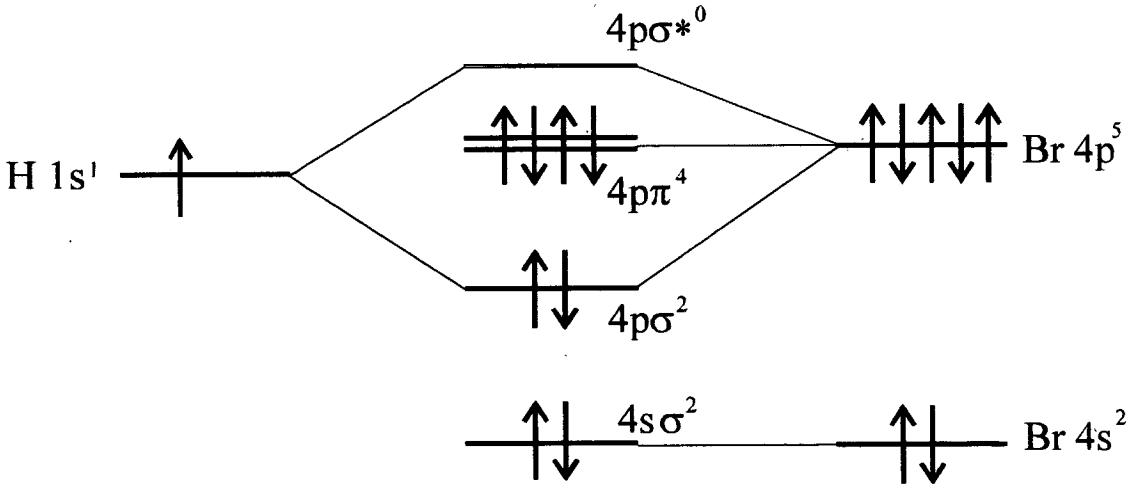

Figure 5-1 Molecular orbital diagram for hydrogen and deuterium bromide.

The previous literature on the ion and excited neutral states of hydrogen and deuterium bromide is quite sizable and only the most relevant work will be referenced in this introduction. The outer valence ionisation region (X ($^2\Pi_i$) and A ($^2\Sigma^+$) states) has been thoroughly studied in past. In HeI work by Lempka *et al.* [130] and Yencha *et al.* [131] only the X ($^2\Pi_i$) state v^+=0-2 vibrational levels are observed, with the

intensity ratio of v^+=0:v^+=1 being 100:6, so the shape of the HBr X ($^1\Sigma^+$) and HBr^+ X ($^2\Pi_i$) states are very similar. The A ($^2\Sigma^+$) → X ($^2\Pi_i$) fluorescence work by Haugh and Bayes [132] and Barrow and Caunt [133] has produced accurate rotational constants for the A ($^2\Sigma^+$) and X ($^2\Pi_i$) states of HBr^+ and DBr^+. However, fluorescence is only observed from v^+=0,1 and v^+=0,1,2 levels of the A ($^2\Sigma^+$) state in HBr^+ and DBr^+ respectively, whereas the Franck-Condon region for the A ($^2\Sigma^+$) state, starting from v''=0 of the ground state, covers many more vibrational levels as shown by HeI photoelectron spectroscopy [130],[131],[134]. A recent PFI-ZEKE photoelectron study by Mank *et al.* [135] of the v^+=1-3 vibrational levels of the A ($^2\Sigma^+$) state of HBr showed that vibrational levels v^+=1-2 show clear rotational structure while the v^+=3 level is structureless, with essentially a Gaussian peakshape. The predissociating state that causes the loss of both fluorescence and rotationally resolved ZEKE spectra for higher vibrational levels of the A ($^2\Sigma^+$) state was originally assigned as a $^4\Pi$ state [130], however, in their MRD-CI calculation on HBr^+ and DBr^+, Banichevich *et al.* [186] have calculated that three repulsive states ($^4\Sigma^-$,$^2\Sigma^-$,$^4\Pi$) are involved in the spin-orbit predissociation of the A ($^2\Sigma^+$).

Baltzer *et al.* [134] have studied the A ($^2\Sigma^+$) state of HBr^+ using HeI photoelecton spectroscopy at high resolution (4-5 meV). This resolution is sufficient to resolve rotational structure in some vibrational levels (v^+=0-3 and 11-13). The rotational constant for the A ($^2\Sigma^+$) state is smaller than for the X ($^1\Sigma^+$) state [B_e(A ($^2\Sigma^+$))=5.97 cm^{-1}, B_e(X ($^1\Sigma^+$))=8.46 cm^{-1}] [177], so vibrational levels are degraded towards lower energy. The rotational structure associated with the vibrational levels was modeled as involving transitions for different ΔN and assuming that the final state rotational populations are governed only by the initial state Boltzmann distribution. (ΔN is the change in rotational angular momentum in the transition from the initial rotational level of the neutral molecule to the total angular momentum of the ion and electron pair)

The energy region between the vibrational origins of the X ($^2\Pi$), Ω=3/2 and 1/2 sub-states has been of much experimental and theoretical interest. In HBr^+ the

spin-orbit splitting is very close to the vibrational spacing (A=–0.328 eV, ω_e=0.302 eV) [177], so three main autoionisation routes are possible. They are: (1) [X ($^2\Pi_{1/2}$) v^+=0] *nl*λ → X ($^2\Pi_{3/2}$) v^+=0 (pure spin-orbit autoionisation), (2) [X ($^2\Pi_{1/2}$) v^+=1] *nl*λ → X ($^2\Pi_{3/2}$) v^+=0 (combined spin-orbit and vibrational autoionisation), and (3) [X ($^2\Pi_{3/2}$) v^+=1] *nl*λ → X ($^2\Pi_{3/2}$) v^+=0 (pure vibrational autoionisation). Lefebvre-Brion *et al.* [136] reported the results of high resolution photoionisation experiments and multichannel quantum defect theory (MQDT) calculations between the HBr^+ X $^2\Pi_{3/2}$ and $^2\Pi_{1/2}$ ionic limits and found that all three ionisation channels are involved in the photoionisation spectrum. Ruscic and Berkowitz [137] have studied the photoionisation of room temperature HBr^+ in the region below the adiabatic ionisation potential. Their work shows that the rotational peaks in their spectra can be ascribed to rotational autoionisation where changes in rotational angular momentum, ΔN, are predominantly negative, taking values down to ΔN =–3. ZEKE-PFI studies by Wales *et al.* [138] and Irrgang *et al.* [139], have determined the ionisation potential of HBr^+ as 94098.9±1 cm^{-1} (11.6667 eV) [138]. Wales *et al.* [138] and Irrgang *et al.* [140] have also shown that Rydberg states converging to ionic limits in this region evolve from Hund's case (c) to Hund's case (e) coupling for increasing principal quantum number *n* (Aspects of Hund's case (e) coupling have been discussed for a $^2\Pi$ electronic core by Lefebvre-Brion *et al.* [141])

Rydberg states with an A ($^2\Sigma^+$) ion core have also been observed. Terwilliger and Smith [142],[143] observed the HBr and DBr absorption spectra from 1000 - 800 Å (12.4 - 15.5 eV) and identified two dominant Rydberg series. Dehmer and Chupka [144] also observed the same two series in photoionisation experiments. Lefebvre-Brion *et al.* [145] have shown that these Rydberg series can be assigned as having [A ($^2\Sigma^+$)] *np*π, *nd*π $^1\Pi$ symmetry. The spin-resolved photoelectron study of HBr by Salzmann *et al.* [146] uses the Rydberg states assigned by Lefebvre-Brion *et al.* [145] to investigate the spin polarisation effects in the same energy region. Finally, electron energy loss spectra have been reported by England *et al.* [147] which also show structure due to Rydberg states with an [A ($^2\Sigma^+$)] *nl*λ electronic configuration.

The inner valence $(4s\sigma)^{-1}$ ionisation region has also been the subject of previous study. Adam *et al.* [148] have published results and an analysis for the photoelectron spectra of HBr and DBr over the inner valence region. The X ($^2\Pi_i$), A ($^2\Sigma^+$), and $(4s\sigma)^{-1}$ states are of similar intensity in the XPS photoelectron spectrum (hν=1487 eV), however Adam *et al.* [148] observed at least 7 different electronic states lying between 20 and 32 eV corresponding to $(4s\sigma)^{-1}$ ionisation. The most intense peak occurred at 24.58 eV and was assigned to the "main band" $(4s\sigma)^{-1}$ ionisation, whereas the other states are assigned as "shake up" states which generally have a $(4s\sigma)^2(4p\sigma)^2(4p\pi)^2$ $nl\lambda$ electron configuration. Brion *et al.* [149] also report photoabsorption and photoionisation studies on HBr. This work concerns the measurement of the absolute photoabsorption and photoionisation cross section of HBr in the region from 10 to 100 eV. Their results also show the complex ionisation features attributable to $(4s\sigma)^{-1}$ ionisation, and also the various decay products for the X ($^2\Pi_i$), A ($^2\Sigma^+$), and "B ($^2\Sigma^+$)" ($(4s\sigma)^{-1}$) ion states. The Auger electron study of HBr by Wannberg *et al.* [150] has observed three (bound) doubly ionised states of HBr^{2+} between 32.5 and 35.5 eV. The valence electronic configuration of these states is also $(4s\sigma)^2(4p\sigma)^2(4p\pi)^2$, so the observations by Adam *et al.* [148] and Wannberg *et al.* [150] are closely related.

Currently, there are no threshold photoelectron spectra for the entire valence region of hydrogen or deuterium bromide in the literature. However, the isotopomers have been well studied by other methods as discussed in this introduction. This study was undertaken to record the threshold photoelectron spectrum of HBr and DBr from the onset of ionisation up to 31 eV. The spectra recorded can then be contrasted with the other hydrogen halide molecules reported in this thesis. Finally, Figure 5-2 shows a potential energy diagram of most of the electronic states observed in previous work which are of relevance to this Chapter to help visualise the results presented later.

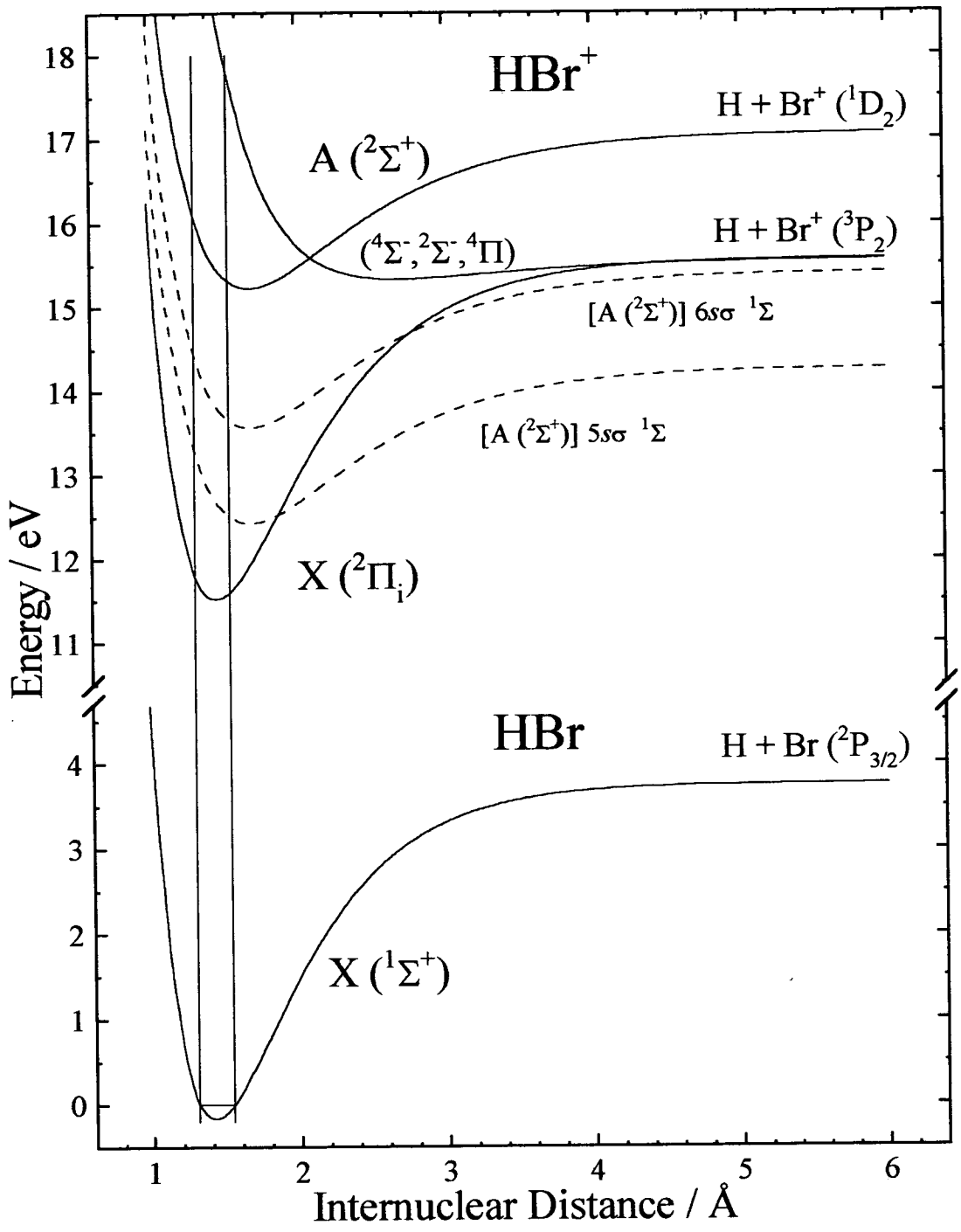

Figure 5-2 Simplified potential energy diagram for HBr/HBr$^+$. Data used to construct the diagram comes from Huber and Herzberg [177] and Yencha *et al.* [131]. The dashed curves indicate the approximate position of Rydberg states converging to the A ($^2\Sigma^+$) state which give rise to the threshold photoelectron spectra presented later in this Chapter. The $^4\Sigma^-$,$^2\Sigma^-$,$^4\Pi$ states are represented by one curve only, a more accurate representation of this energy region is given by Yencha *et al.* [131]

5.2 Special experimental details

Experimental details concerning the preparation and purification of the gas samples and normal data collection methods are given in sections 2.5.4 and 2.4.2. The HBr and DBr spectra presented in this Chapter was collected during different visits to the synchrotron. During the break between two periods of study the diffraction grating in the McPherson Monochromator was changed, so the calibration curves for the two isotopes are different. Since the HCl and DCl spectra were prone to calibration problems (see section 4.2) the calibration of the results for this Chapter needs to be discussed. The calibration of the present work has been compared to previous literature for the X ($^2\Pi_i$) and A ($^2\Sigma^+$) states, however the calibration for the $(4s\sigma)^{-1}$ energy region cannot be compared with previous literature at a comparable resolution. However, the current HBr and DBr spectra were calibrated separately using different calibration data, but the peak assignments and positions in the inner valence region seem to be consistent between the isotopes (within the experimental resolution) showing that the calibration of the inner valence region is reliable.

5.3 Results and Discussion

5.3.1 Overview of the valence region

Figure 5-3 shows the threshold photoelectron spectrum of hydrogen and deuterium bromide from 11.5 to 31.5 eV. The spectra presented in the Figure comprise of multiple sub-spectra detailed as follows. (1) HBr spectrum: from 11.5 to 13.404 eV, four spectra at 1 meV stepsize and 6 eV resolution; from 13.405 to 15.222 eV, and from 15.223 to 16.905 eV, two sets of 3 spectra at 1 meV stepsize and 6 meV resolution; from 16.905 to 31.5 eV, 8 spectra at 10 meV stepsize and 13 meV resolution. (2) DBr spectrum: from 11.55 to 15.226 eV, three spectra at 2 meV stepsize and 6 meV resolution; from 15.227 to 16.945V, three spectra at 1 meV stepsize and 5 meV resolution; from 16.953 to 31.515 eV, 10 meV stepsize and 12 meV resolution. All resolutions are taken from argon calibration scans adjacent to study scans and are quoted at the Ar ($^2P_{3/2}$) ionisation line (15.759 eV).

The three main features in Figure 5-3 can be assigned to the $(4p\pi)^{-1}$ [X $(^2\Pi_i)$], $(4p\sigma)^{-1}$ [A $(^2\Sigma^+)$], and $(4s\sigma)^{-1}$ states of hydrogen and deuterium bromide. The relative intensity of the three band systems varies widely, with the inner valence $(4s\sigma)^{-1}$ ionisation feature being almost 100 times less intense than the X $(^2\Pi_i)$ and A $(^2\Sigma^+)$ states. This marked trend towards lower spectral intensities for the higher energy band systems is also seen in HCl, DCl, and HI (see Chapters 4 and 6) but is not generally found in studies using non-resonant ionisation [148],[110],[124]. The ionisation of inner valence or core electrons often leads to multiple final ion states due to electron correlation effects during the ionisation process. It is possible that the probability of producing a threshold electron (within the bandpass of the spectrometer) is quite small in a correlated multi-electron process, explaining the loss of signal intensity for inner valence ionisation.

A small amount of hydrogen (H_2/D_2) impurity is seen in the spectra at around 16.5 eV even after thorough gas preparations. However, since hydrogen has only one bound electronic state in the region of study the very small trace impurity can be neglected.

As the dynamics and spectroscopy of the outer valence $(4p\pi)^{-1}$ and $(4p\sigma)^{-1}$ differ from $(4s\sigma)^{-1}$ inner valence ionisation it is useful to discuss the two regions separately. Section 5.3.2 presents and discusses results for the outer valence region and Section 5.3.3 concludes experimental results for this Chapter.

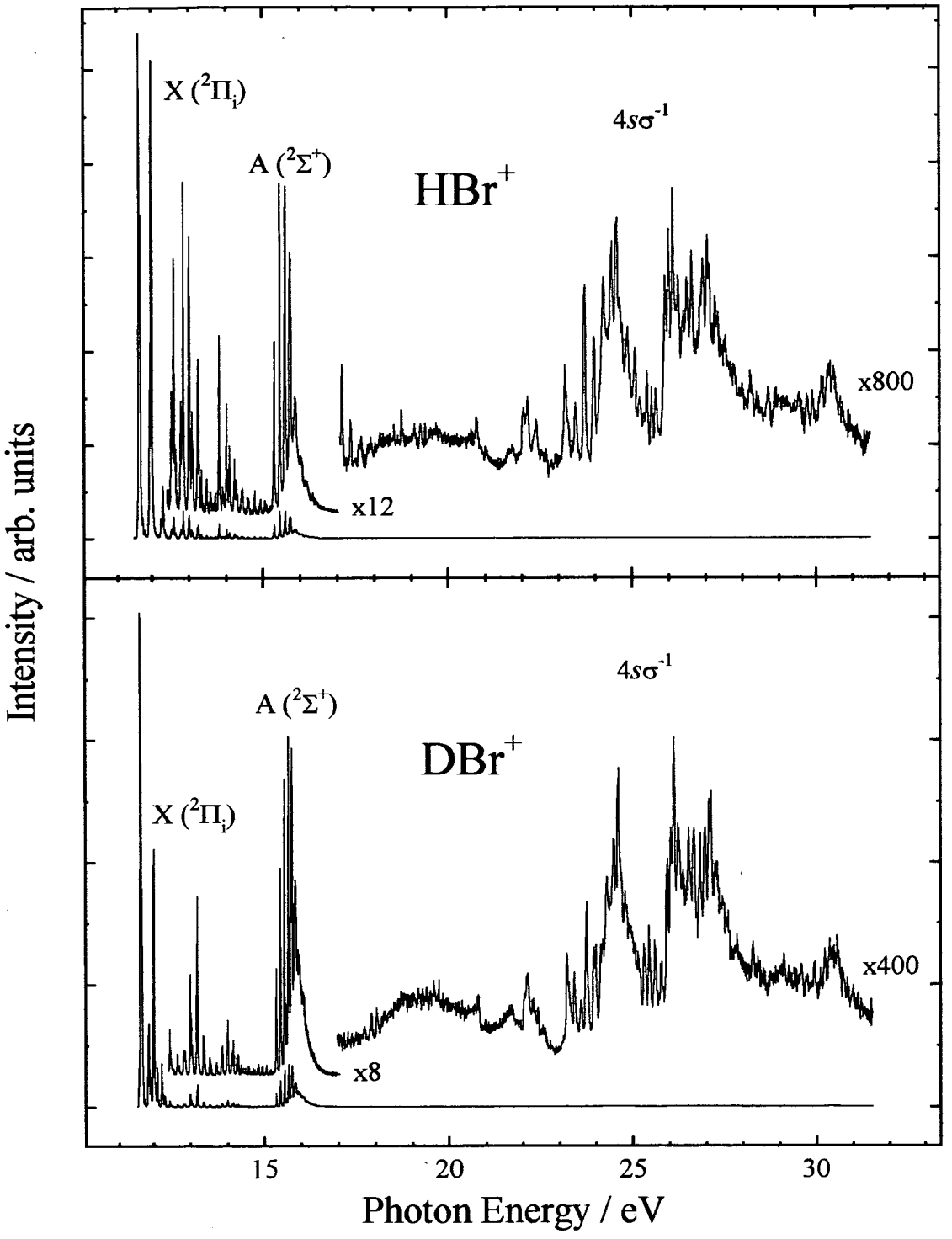

Figure 5-3 Threshold photoelectron spectrum of hydrogen and deuterium bromide for the entire study region showing the three ionisation regions. The spectra are comprised of many data scans, further details are given in section 5.3.1

5.3.2 Threshold photoelecton spectroscopy of the outer valence region of hydrogen and deuterium bromide

The threshold photoelectron spectra of hydrogen and deuterium bromide from the onset of ionisation to 17.0 eV are shown in Figure 5-4. The resolution of the spectra in Figure 5-4 is the same as for Figure 5-3. Both spectra exhibit extensive vibrational structure in the X ($^2\Pi_i$) state that stops at the onset energy of the A ($^2\Sigma^+$) state. As only the v^+=0-2 levels of the X ($^2\Pi_i$) state have appreciable Franck-Condon factors the higher vibrational levels must be accessed through the autoionisation of super-excited neutral states. The A ($^2\Sigma^+$) state of HBr shows similar structure to previous HeI photoelectron studies [151],[131], where vibrational levels above v^+=2 are extensively broadened by predissociation [186].

The vibrational levels marked with a full length tick in Figure 5-4 have been used to determine vibrational constants for HBr and DBr. A third order vibrational Dunham expression was required to accurately represent the experimental data for the two spin-orbit components of the X ($^2\Pi_i$) state, however for the A ($^2\Sigma^+$) state a second order vibrational Dunham expression was sufficient. For all analyses the experimental data of both isotopomers has been combined and the data fitted using Equation 4-1 (page 80). The measured and fitted peak positions for the X ($^2\Pi_i$) state of HBr^+ is given in Table 5-1, for the X ($^2\Pi_i$) state of DBr^+ in Table 5-2, and for the A ($^2\Sigma^+$) state of both HBr^+ and DBr^+ in Table 5-3. The derived spectroscopic constants from the vibrational data are shown in Table 5-4, also included in the table are comparable spectroscopic constants from the literature. The positions of vibrational levels of the A ($^2\Sigma^+$) state marked with a half length tick were determined from a fit of multiple Gaussian peaks to the spectrum. The Origin 3.5 Peak Fitting Module was used for the Gaussian fit work [82]. Results of the fitting procedure are presented and discussed in Section 5.3.2.(a).

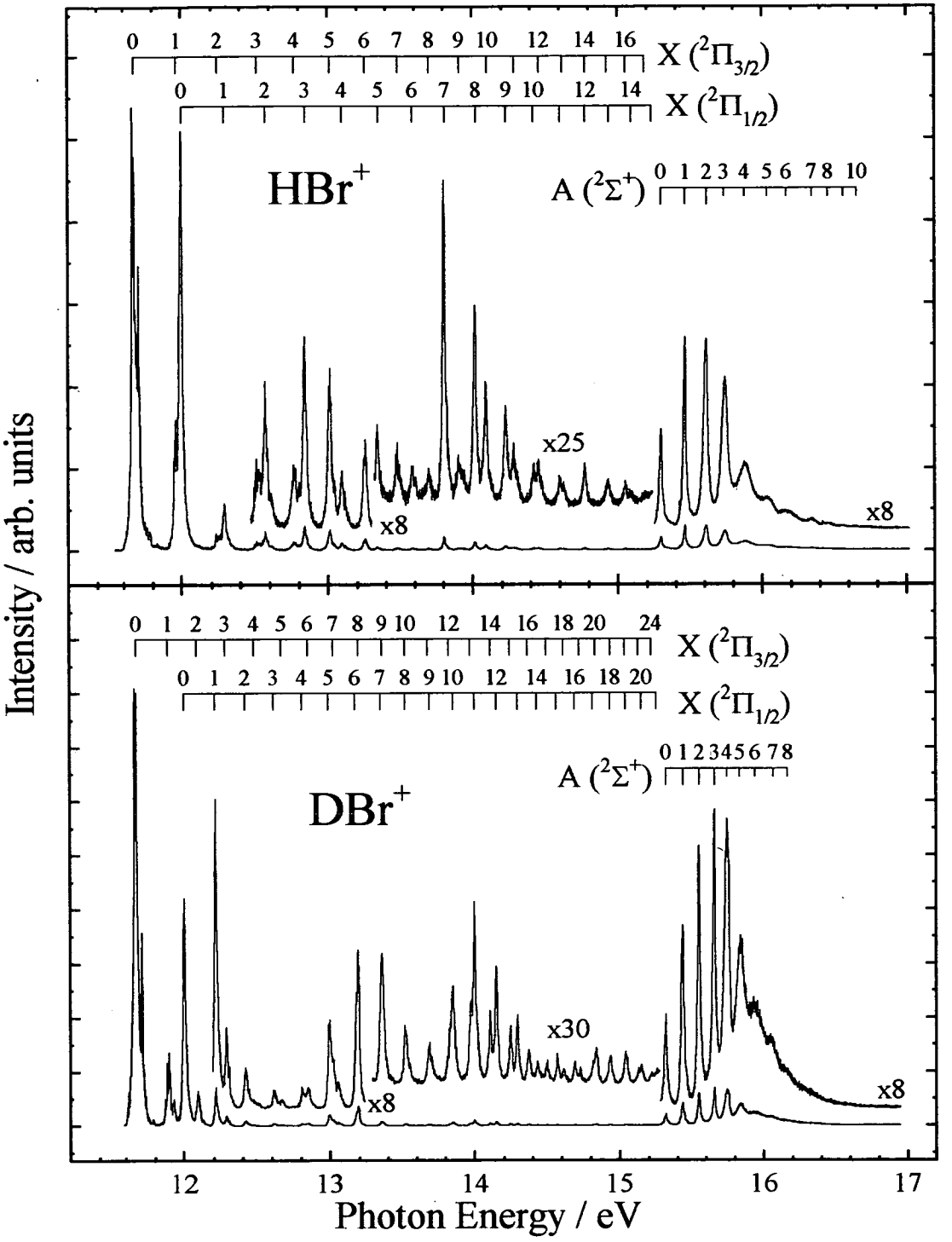

Figure 5-4 Threshold photoelectron spectra of hydrogen and deuterium bromide for the outer valence region. Both isotopomers show extended vibrational structure in the X ($^2\Pi_i$) state which is attributed to autoionising Rydberg states with an A ($^2\Sigma^+$) state electronic core.

Vibrational levels $v^+=2$ and higher of the X ($^2\Pi_i$) state of HBr are not accessible by a simple one-step Franck-Condon allowed process, instead these vibrational levels are accessed via a two step process involving an intermediate Rydberg state. The assignment of these intermediate Rydberg states can be attempted using the photoabsorption and photoionisation work by Terwilliger and Smith [143], Dehmer and Chupka [144], Lefebvre-Brion *et al.* [145], and by comparison to the assignments for hydrogen and deuterium chloride in Chapter 4. Initial assignments for HCl and DCl in Chapter 4 suggested that the autoionising Rydberg states belong to the A ($^2\Sigma^+$) $np\pi$ $^1\Pi$ series, where n=3-5. However, the lowest $4p\pi$ Rydberg state could not enhance the X ($^2\Pi_i$) $v^+=2$ level as the ion level lies to lower energy than the Rydberg state, so autoionising Rydberg series for HCl and DCl were assigned as the $ns\sigma$ series, where n=4-6. These Rydberg states are prominent in the dissociative ion-pair formation in HCl and DCl (see Yencha *et al.* [152]) and are also active in photodissociation in this energy range as shown by Frohlich and Glass-Maujean [118]. The similarity between the photodissociation (fluorescence excitation) spectrum and the threshold photoelectron spectrum has been shown for N_2O by Guyon *et al.* [153] and it seems quite likely that the same Rydberg states involved in photodissociation are also involved in threshold electron production in this work. So the underlying Rydberg structure in the non Franck-Condon region of the X ($^2\Pi_i$) state is assigned to the A ($^2\Sigma^+$) $ns\sigma$ $^1\Sigma$ Rydberg series, where n=5-7.

5.3.2.*(a)* *The TPE spectra of the A ($^2\Sigma^+$) state of hydrogen and deuterium bromide*

Figure 5-5 shows the threshold photoelectron spectra of hydrogen and deuterium bromide from 15 to 17 eV and a previously published HeI photoelectron spectrum of HBr by Yencha *et al.* [131]. Details of the resolution for the spectra are as follows: (1) HBr: 2 complete spectra from 15 to 17 eV with 2 additional spectra from 15.8 eV to 17 eV all combined (with intensity scaling), 2 meV stepsize, 5 meV resolution. (2) DBr: 3 spectra from 15 to 17 eV, 2 meV stepsize, 5 meV resolution. Resolution is quoted from adjacent argon calibration scans and measured on the Ar

($^2P_{1/2}$) ionisation line at 15.937 eV. The HeI photoelectron spectrum has a resolution of 20 meV as quoted from Yencha *et al.* [131]. From panel (a) in Figure 5-5 it is clear that the peak positions for predissociated levels ($v^+ \geq 2$) of the A ($^2\Sigma^+$) state of HBr^+ occur at different positions in the HeI PES and TPES spectra. This has also been observed for the current work on HCl and DCl (see Chapter 4). The fluorescence excitation work by Haugh and Bayes [132] reported that emission from vibrational levels higher than $v^+=1$ in HBr and $v^+=2$ in DBr could not be observed. From panel (a) in Figure 5-5 it is clear that the TPES and HeI PES spectra begin to differ at $v^+=2$, with an increase in the background intensity between vibrational peaks and a broadening of each vibrational peak towards lower energy. It is also clear that the vibrational levels from $v^+=4$-7 also have increased intensity as compared with the HeI PES spectrum in panel (a).

The broadening for the TPES vibrational levels has already been observed in the predissociative region of the A ($^2\Sigma^+$) state of HCl^+ (see Section 4.3.2(a)) where it was modeled as a propensity for large (negative) changes of total angular momentum in the threshold ionisation process. However, in their high resolution HeI PES study of this energy region in HBr, Baltzer *et al.* [134] were unable to simulate the heavily predissociated vibrational levels ($v^+=5$-9) using the "ΔN" model, so extending the model does not seem applicable here. Instead, the vibrational structure in HBr and DBr has been fitted to a combination of Lorentzian and Gaussian functions as shown in panels (b) and (c) of Figure 5-5. For fitting purposes vibrational levels $v^+=0$-2 in HBr and $v^+=0$-3 in DBr have been modeled using Lorentzian functions whereas higher vibrational levels have been fitted to Gaussian functions. Fitting was achieved using the Origin 3.5 Peak Fitting Module [82] which allowed all peaks to be fitted simultaneously. Numerical results of the fit procedure are given in Table 5-5. Also included in panels (b) and (c) of Figure 5-5 are the residuals from the fit process which clearly show the fit data are an accurate representation of the results.

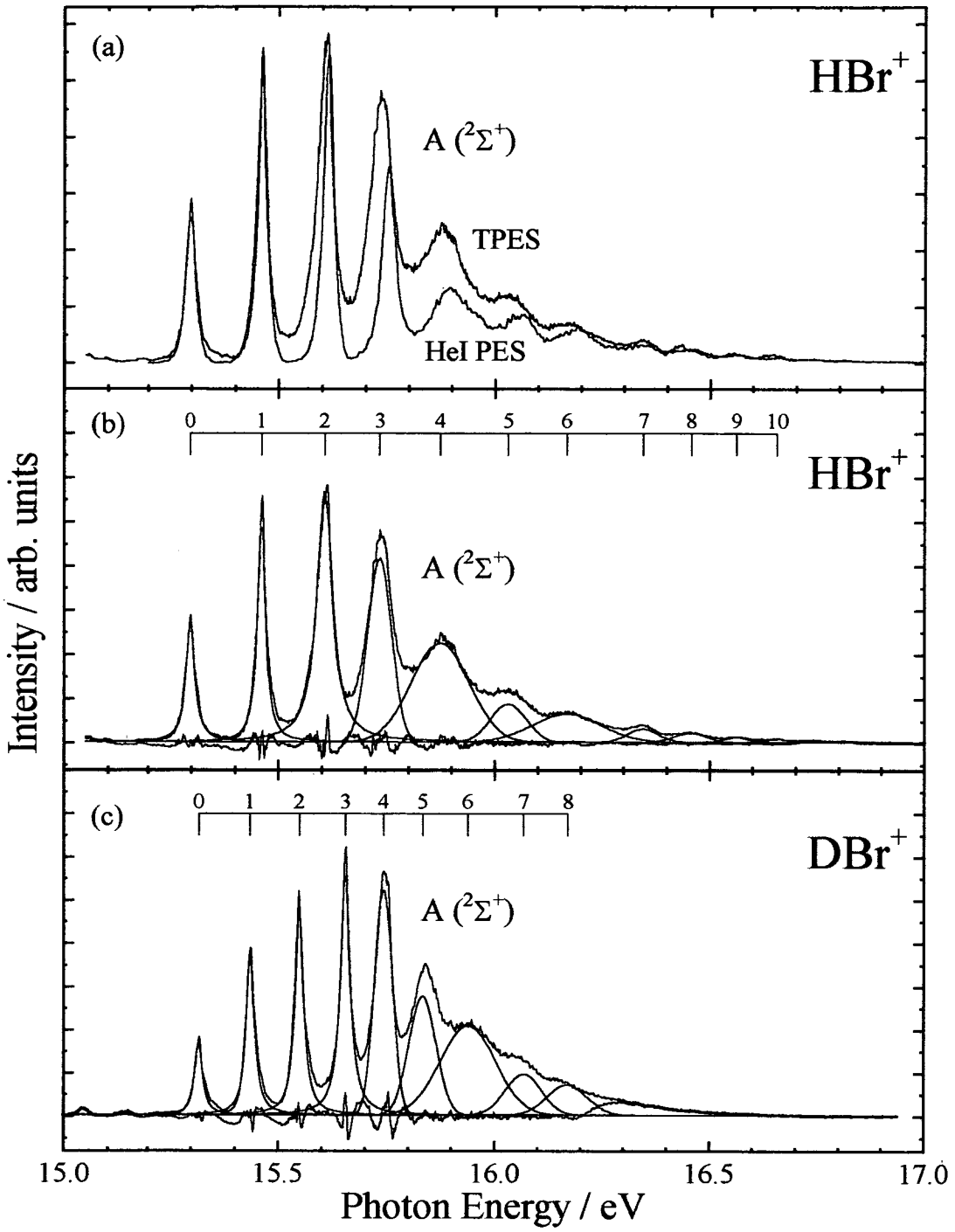

Figure 5-5 Threshold photoelectron spectra of the A ($^2\Sigma^+$) state of hydrogen and deuterium bromide. The HeI PES spectrum is reproduced with permission from Yencha *et al.* [131]. The spectra have been fitted using both Gaussian and Lorentzian functions as detailed in the text.

In both isotopomers the fit procedure has only been attempted for vibrational levels which are clearly identifiable in the spectra, so the fitted vibrational progression for DBr^+ stops at lower energy than for HBr^+. Clearly this is an effect due to the smaller vibronic frequency in the heavier isotope. Of special interest in Table 5-5 is the difference between the fitted positions in the HBr^+ HeI PES spectrum (Baltzer *et al.* [134]) and the present TPES work. The large deviations may be connected with the predissociative nature of the higher vibrational levels, however it is difficult to speculate on the ionisation mechanism which accounts for the discrepancy between the two techniques. Finally it is worth noting that although 15 or possibly 16 vibrational levels have been observed in the A ($^2\Sigma^+$) state of HBr^+ by Baltzer *et al.* [134] only 11 vibrational levels are identified here. This is most likely due to the slightly poorer signal to noise ratio in the TPES work.

5.3.2.*(b) The TPE spectrum of HBr and DBr from 11.6 to 12.05 eV*

Figure 5-6 shows the high resolution threshold photoelectron spectra of hydrogen and deuterium bromide for the region between the X ($^2\Pi_i$) ionisation thresholds. Details of the resolution of the spectra and the sub-spectra which comprise Figure 5-6 are as follows. (1) HBr: the sum of 5 spectra with 0.5 meV stepsize and 3 meV resolution from 11.5 to 11.8 eV catenated to the sum of 5 spectra with 0.5 meV stepsize and 3 meV resolution from 11.8 to 12.05 eV. (2) DBr: the sum of 3 spectra with 0.5 meV stepsize and 3 meV resolution from 11.55 to 11.82 eV, catenated to the sun of 4 spectra with 0.5 meV stepsize and 3 meV resolution from 11.82 to 12.03 eV. The resolution is quoted from measurements of the Ar ($^2P_{1/2}$) ion line at 15.937 eV in adjacent calibration scans. Intensity scaling and energy calibration was carried out using spectra recorded over the entire region of interest.

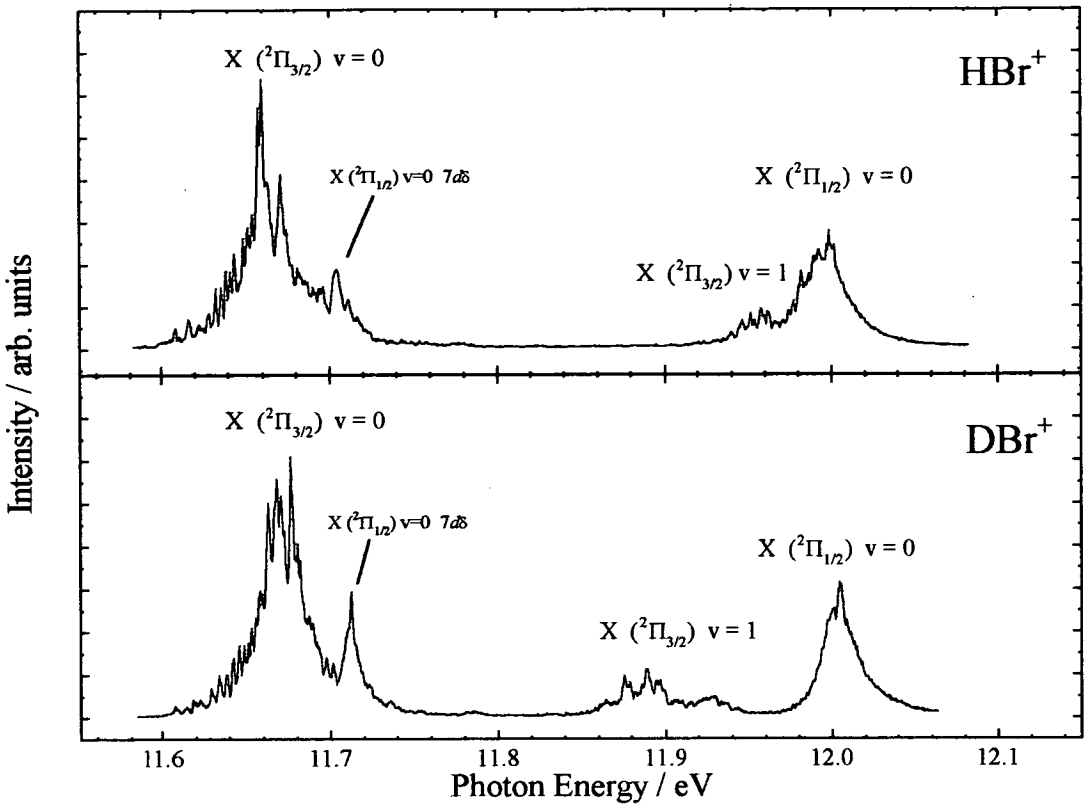

Figure 5-6 High resolution threshold photoelectron spectra of hydrogen and deuterium bromide for the X ($^2\Pi_i$) v^+=0 energy region. In both spectra the experimental resolution is < 3 meV as measured on the Ar ($^2P_{1/2}$) ionisation line at 15.937 eV.

Clearly the intensity of the different Ω components of the X ($^2\Pi_i$) state differ considerably, with a significant enhancement in the X ($^2\Pi_{3/2}$) spin-orbit component. This enhancement is probably due to a combination of spin-orbit, vibrational, and rotational autoionisation, the effect is common to all studies in this thesis. This spectrum was recorded with a view to understanding and modeling the dynamics of autoionisation and photoionisation into the various ionic levels shown in Figure 5-6, to compare the results with previous work on this region [140],[138],[139],[137]. However, the resolution of the spectrum is not high enough to assign the partially resolved rotational structure to specific final ion rotational levels. A higher resolution study of the spectrum from a beamline such as the Advanced Light Source in Berkeley, California, would be useful before a more in-depth study can be made. An autoionising Rydberg level that enhances the rotational envelope of the X ($^2\Pi_{3/2}$) state

has been assigned from the single photon ionisation work by Irrgang *et al.* [140] as the [X ($^2\Pi_{1/2}$) v^+=0] 7*dδ* Rydberg state with a quantum defect of 0.209 (n^*=6.791). However, further analysis of this region awaits a higher resolution spectrum.

5.3.3 Threshold photoelectron spectroscopy of the inner valence region of hydrogen and deuterium bromide

The threshold photoelectron spectra of hydrogen and deuterium bromide from 17 to 31.5 eV are shown in Figure 5-6. This Figure is an expanded view of Figure 5-3, which shows the full region of the present study. The XPS study of this energy region by Adam *et al.* [148] has been used to identify and assign the various ionic states in the region. Approximate positions for the electronic states are given in Table

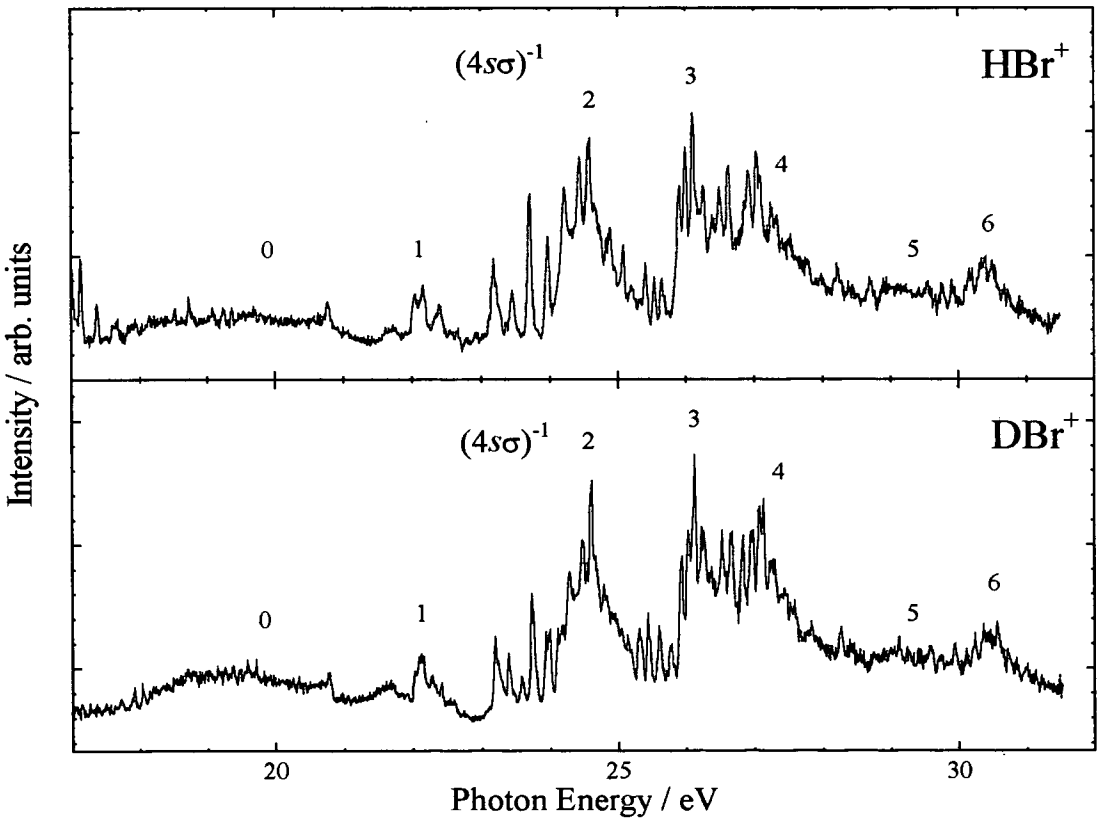

Figure 5-7 TPE spectrum of the inner valence ($(4s\sigma)^{-1}$) ionisation region of HBr and DBr. The resolution for this figure is the same as Figure 5-3. The various electronic states are labeled using the same notation as Adam *et al.* [148].

5-6 along with the positions determined by Adam *et al.* [148]. The TPE spectrum is at much higher resolution than that of Adam *et al.*, however, since the vibrational band contours in the TPE spectrum do not seem to show any features typical of a Franck-Condon distribution (i.e. an asymmetric Gaussian profile as in the XPS spectrum) it is difficult to determine the exact band position in the current work. The state labeled "0" in this work (at 19.5 eV) does not seem to be present in the XPS spectrum. As state "0" is so broad and structureless it seems likely that this feature is due to ionisation to either purely repulsive ion states, or the dissociative continuum of bound ion states that correlate to lower energy ionic dissociation limits. For instance, from Figure 5-2 the repulsive $^4\Sigma^-$,$^2\Sigma^-$, and $^4\Pi$ states that correlate to the [H + Br^+ (^3P_j)] asymptotes, which are involved in predissociation of the outer valence A ($^2\Sigma^+$) state, all enter the Franck-Condon window in this energy region. Further ion states are also accessible at this energy as can be seen from the potential energy diagram in the paper by Yencha *et al.* [131]. The region between 21 and 29 eV in Figure 5-7 is highly structured and is examined in more detail in the next section.

5.3.3. *(a) The TPE spectrum of hydrogen and deuterium bromide from 21-29 eV*

The highly structured portion of the inner valence ionisation of HBr and DBr is shown in Figure 5-8. Eight different vibrational progressions are tentatively assigned in this region. These assignments are based on the combined analysis of the HBr and DBr spectra using the isotope relations in Equation 4-1 (page 80). The spectroscopic constants for the X ($^1\Sigma^+$) state neutral were taken from Huber and Herzberg [177]. Also, since the ionisation processes in this region is nominally removal of a $4s\sigma$ non-bonding electron the vibrational frequencies of the various electronic states in the ion should be similar to that of the X ($^1\Sigma^+$) state of the neutral. Indeed, since the electron correlation effects tend to mix the $(4s\sigma)^{-1}$ ionisation with non-bonding $(4p\pi)^2$ $nl\lambda$ ionic Rydberg state configurations, many electronic states with vibrational frequencies close to that of the neutral would be expected [154]. The vibrational peak positions of the various electronic states are given in Table 5-8 and

the derived second order Dunham coefficients are included in Table 5-7 along with the contrasting X ($^1\Sigma^+$) state constants from Huber and Herzberg [177]. Table 5-7 shows that all states identified in Figure 5-8 have a harmonic frequency similar to the X ($^1\Sigma^+$) state of HBr, as is expected from the discussion of the expected electron configurations above. Spectral peaks marked with an asterisk are currently unassigned, however these peak positions are also tabulated in Table 5-8. The spectral features higher than 27 eV photon energy have a poor signal to noise ratio caused by the low photon flux from the McPherson monochromator (see Figure 2-1) and the assignment of spectral peaks above the K and L states has not been attempted for this reason. In both spectra there are 3 unassigned peaks interloping with the H state (26.0 - 26.3 eV). These peaks cannot arise from a single vibrational progression as the vibrational spacing increases. The relative spacing between the peaks for the different isotopomers also precludes the possibility that these peaks arise from different spin-orbit combinations in the molecular ion.

Currently there do not seem to be any detailed *ab initio* calculations in the literature from which vibrational frequencies can be obtained. The Greens function calculations by von Niessen *et al.* [194] only show three electronic states in the region 21 - 29 eV. The classification of the electronic states in this region must await more thorough calculations of the expected electronic structure in this region. A higher quality spectrum of this spectrally weak region (see Figure 5-3) would also be of use to confirm the vibrational assignments, especially in the congested region of the H, I, and J states.

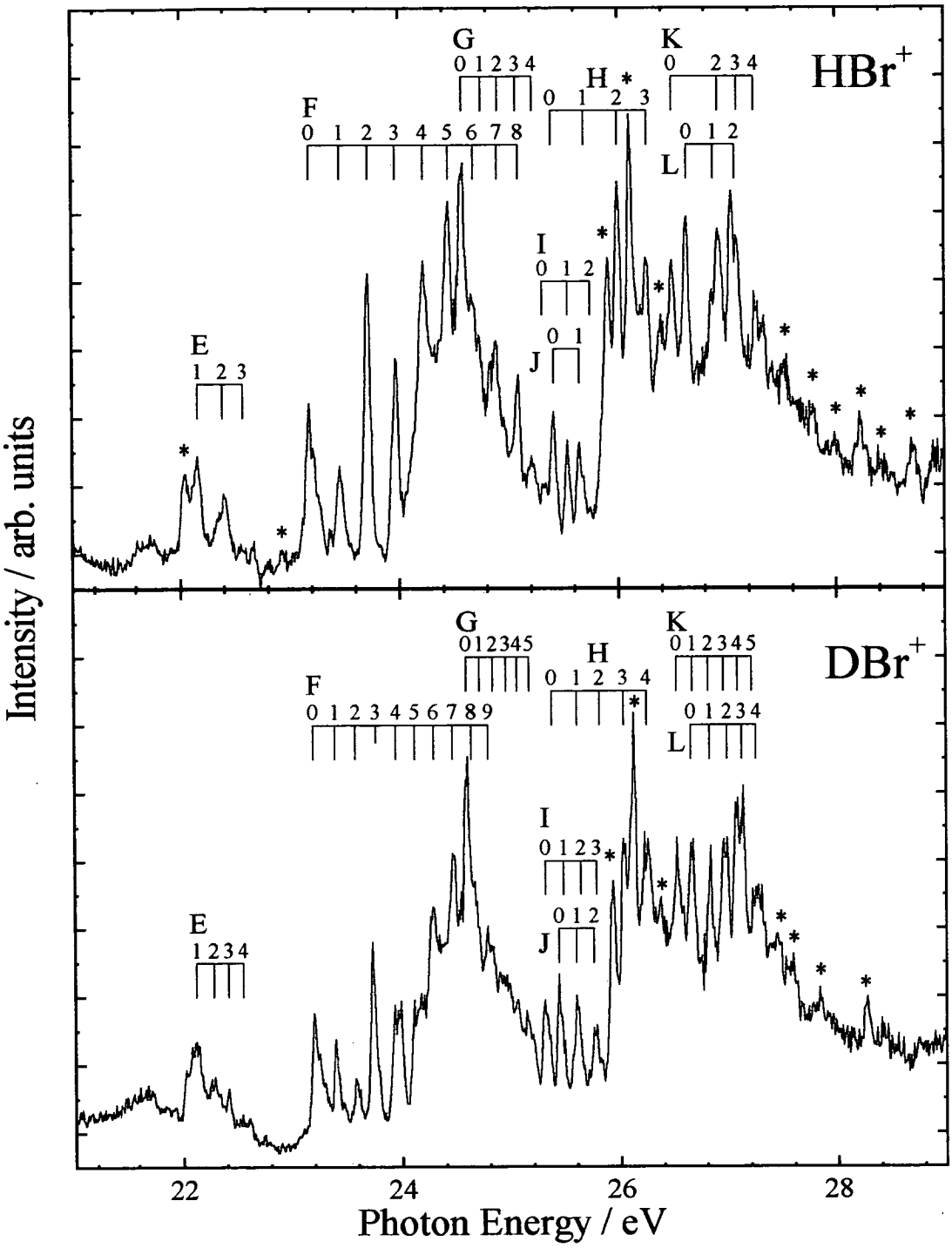

Figure 5-8 TPE spectrum of HBr and DBr from 21-29 eV. The resolution of the spectra is the same as Figure 5-3 (see Section 5.3.1). The peak assignments are based of the combined analysis of peak positions for both isotopes. Electronic states are labeled using the same labeling as the inner valence region of HCl and DCl (see section 0(a)). An * marks unassigned peaks.

5.4 Conclusions for the threshold photoelectron spectrum of hydrogen and deuterium bromide

The complete TPE spectra of HBr and DBr from the onset of ionisation up to 31.5 eV have been presented for the first time. The overall spectra show similar attributes to the related work on HCl, DCl, and HI (presented in this thesis). Namely, there is a rapid decrease in spectral intensity towards higher photon energy. The spectra are highly structured and are ripe with autoionising features.

Vibrational levels up to v^+=24 are seen for the X ($^2\Pi_{3/2}$) state of DBr^+, whereas the single photon Franck-Condon window only covers v^+ = 0 - 3. The extended vibrational structure is attributed to autoionisation of the A ($^2\Sigma^+$) *ns*σ $^1\Sigma$ Rydberg series into the X ($^2\Pi_i$) ion state. This assignment is based on careful consideration of the various Rydberg states available in the energy region for both hydrogen chloride and hydrogen bromide isotopomers. Comparison of the TPE spectra for the A ($^2\Sigma^+$) state with a previous HeI PES study shows that the ionisation dynamics of predissociated ionic levels are very different. In the TPES work (which is at higher resolution than the HeI PES) the predissociated vibrational levels are broadened and degraded to lower energy. It is possible that this broadening is due to a propensity for negative changes in total angular momentum, ΔN, for the threshold ionisation of predissociated vibrational levels, as is suggested for HCl and DCl (Chapter 4). However, currently there is no theoretical justification for this model or indeed any model which deals with the threshold predissociation/ionisation process. Also, from the differences in spectral intensity in the HeI PES and TPES studies it is clear that additional ionisation channels are accessible in the threshold ionisation of a predissociated vibrational level. Spectroscopic constants for the X ($^2\Pi_i$) and A ($^2\Sigma^+$) states have been determined and are tabulated for comparison with previous work, (predissociated levels of the A ($^2\Sigma^+$) state were not included for the reasons given above).

A high resolution (3 meV) spectrum of the X ($^2\Pi_i$) v^+=0 region of HBr and DBr shows significant rotational structure, however, the resolution is not high enough for the vibrational levels to be analysed at a rotational level. A higher resolution study using a third generation synchrotron such as the Molecular Dynamics beamline at the Advanced Light Source, Berkeley, California [127], would be useful in this regard.

The inner valence region of HBr and DBr is extremely weak in comparison to the outer valence region, however it is bounteous with vibrational structure. Eight electronic states have been (tentatively) identified in the region of study and spectroscopic constants for the states have been extracted. The electronic assignment of these states awaits more detailed *ab initio* calculations for this region.

In conclusion a great deal of new spectroscopic information has been obtained from the combined study of HBr and DBr and new observations of the threshold ionisation dynamics of predissociating vibrational levels are reported. Spectra with better signal to noise characteristics and higher spectral resolution are needed throughout the energy region to gain more information on the threshold ionisation processes, however, already much new information on the inner valence ion states of HBr and DBr has been gained.

5.5 Tables of results for hydrogen and deuterium bromide

Table 5-1 Observed and calculated vibrational band head positions (in eV) for the transitions: e + HBr^+ (X ($^2\Pi_i$), v′) ← HBr (X ($^1\Sigma^+$), v″=0)

	HBr^+ X ($^2\Pi_{3/2}$)		HBr^+ X ($^2\Pi_{1/2}$)	
v′	obs[a]	calc	obs[a]	calc
0	11.673	11.673	12.001	12.002
1	11.963	11.964	12.292	12.292
2	12.244	12.244	12.572	12.572
3	12.513	12.513	12.841	12.841
4	12.772	12.772	13.099	13.099
5	13.019	13.019	13.346	13.346
6	13.256	13.256	13.583	13.582
7	13.483	13.483	13.808	13.808
8	13.698	13.698	14.023	14.023
9	13.903	13.904	14.228	14.228
10	14.099	14.099	14.422	14.422
11	14.284	14.284	14.606	14.605
12	14.458	14.458	14.779	14.778
13	14.623	14.623	14.940	14.941
14	14.778	14.778	15.092	15.092
15	14.922	14.922	15.234	15.234
16	15.057	15.058		
17	15.183	15.183		

[a] ± 0.002 eV

Table 5-2 Observed and calculated vibrational band head positions (in eV) for the transitions: $e + DBr^+ (X\ ^2\Pi_i),\ v') \leftarrow DBr\ (X\ ^1\Sigma^+),\ v''=0)$

	$DBr^+\ X\ (^2\Pi_{3/2})$		$DBr^+\ X\ (^2\Pi_{1/2})$	
v′	obs[a]	calc	obs[a]	calc
0	11.677	11.676	12.005	12.005
1	11.886	11.886	12.214	12.214
2	12.089	12.090	12.418	12.418
3	12.289	12.288	12.616	12.616
4	12.481	12.481	12.808	12.808
5	12.668	12.668	12.995	12.995
6	12.850	12.850	13.177	13.177
7	13.026	13.026	13.353	13.353
8	13.197	13.197	13.523	13.523
9	13.363	13.363	13.688	13.689
10	13.523	13.523	13.848	13.848
11	13.677	13.677	14.002	14.003
12	13.827	13.827	14.152	14.152
13	13.971	13.971	14.296	14.295
14	14.111	14.110	14.434	14.434
15	14.244	14.244	14.567	14.567
16	14.373	14.373	14.694	14.694
17	14.497	14.497	14.816	14.817
18	14.615	14.615	14.933	14.934
19	14.728	14.728	15.045	15.045
20	14.837	14.837	15.152	15.152
21	14.940	14.940	15.253	15.253
22	15.039	15.039		
23	15.132	15.132		
24	15.222	15.221		

[a] ± 0.002 eV

Table 5-3 Observed and calculated vibrational band head positions (in eV) for the transitions: $e + HBr^+ (A\ ^2\Sigma^+,\ v') \leftarrow HBr (X\ ^1\Sigma^+,\ v''=0)$ and $e + DBr^+ (A\ ^2\Sigma^+,\ v') \leftarrow DBr (X\ ^1\Sigma^+,\ v''=0)$

	HBr^+ $A\ ^2\Sigma^+$		DBr^+ $A\ ^2\Sigma^+$	
v'	obs[a]	calc	obs[a]	calc
0	15.298 [b]	15.298 [b]	15.320 [b]	15.320 [b]
1	15.461 [b]	15.461 [b]	15.438 [b]	15.438 [b]
2	15.614 [b]	15.614 [b]	15.551 [b]	15.551 [b]
3		15.734(2) [c]	15.659 [b]	15.659 [b]
4		15.873(2) [c]		15.744(2) [c]
5		16.031(2) [c]		15.833(2) [c]
6		16.168(5) [c]		15.938(3) [c]
7		16.345(4) [c]		16.067(5) [c]
8		16.455(5) [c]		16.170(4) [c]
9		16.561 [d]		
10		16.655 [d]		

[a] ± 0.002 eV
[b] peaks used in Dunham fit
[c] position determined from fit to Gaussian functions (see Figure 5-5 and Table 5-5)
[d] position and width of peaks fixed for the fit procedure(see Figure 5-5 and Table 5-5)

Table 5-4 Summary of spectroscopic constants (in eV) derived from the analysis of the HBr and DBr TPES spectra for the outer valence region presented in this Chapter, and some relevant literature data for comparison.

State	ionisation energy	ω_e	$\omega_e x_e$ /10^{-3}	$\omega_e y_e$ /10^{-5}	Ref.
$HBr^+ X (^2\Pi_{3/2})$	11.673(2)	0.3024(1)	-5.60(1)	1.56(5)	this work [a]
	11.672				[131]
	11.672				[155]
	11.645				[151]
	11.6668				[138]
		0.30270	-5.877		[27]
$HBr^+ X (^2\Pi_{1/2})$	12.001(2)	0.30144(9)	-5.46(1)	0.58(5)	this work [a]
	11.979				[151]
		0.30270	-5.877		[27]
$HBr^+ A (^2\Sigma^+)$	15.298(2) [b]	0.1729(8)	-4.9(3)		this work [a]
	15.295				[131]
	15.296				[142]
	15.290 [c]				[134]
	15.288				[148]
	15.288				[151]
		0.1741	-4.674		[27]
$DBr^+ X (^2\Pi_{3/2})$	11.677(2)	0.21518(7)	-3.987(9)	1.11(3)	this work [a]
	11.673				[151]
		0.21502	-2.740		[27]
$DBr^+ X (^2\Pi_{1/2})$	12.005(2)	0.21447(6)	3.887(9)	0.42(4)	this work [a]
	12.002				[151]
		0.21502	-2.740		[27]
$DBr^+ A (^2\Sigma^+)$	15.320(2)	0.1231(6)	-3.5(2)		this work [a]
	15.284				[151]
		0.12388	-2.368		[27]

[a] vibrational constants determined from the combined analysis of HBr and DBr
[b] peak maximum (the peaks are degraded to lower energy)
[c] rotationally deconvoluted band origin

Table 5-5 Peak fitting results for the spectra shown in panels (b) and (c) of Figure 5-5. The fitted vibrational band maximum are for the transitions: e + HBr^+ ($A\ ^2\Sigma^+$, v′) ← HBr ($X\ ^1\Sigma^+$), v″=0) and e + DBr^+ ($A\ ^2\Sigma^+$), v′) ← DBr ($X\ ^1\Sigma^+$), v″=0). Data from Baltzer *et al.* [134] is used for comparison of the TPES and HeI PES vibrational positions.

v′	Function	Centre / eV [b]	ΔE / eV [c]	Relative area	Width / meV
			HBr^+ $A\ ^2\Sigma^+$		
0	Lorentzian	15.297(2)	+0.007	0.288(3)	0.0252(4)
1	Lorentzian	15.461(2)	+0.007	0.451(3)	0.0211(2)
2	Lorentzian	15.607(2)	-0.001	1.000(3)	0.0428(3)
3	Gaussian	15.734(2)	-0.010	0.750(6)	0.0645(4)
4	Gaussian	15.873(2)	-0.012	0.985(13)	0.157(3)
5	Gaussian	16.031(2)	-0.019	0.235(26)	0.097(5)
6	Gaussian	16.168(5)	-0.008	0.342(31)	0.192(18)
7	Gaussian	16.345(4)	+0.015	0.072(12)	0.085(11)
8	Gaussian	16.455(5)	+0.025	0.054(7)	0.090(12)
9	Gaussian	16.561 [a]	+0.017	0.024(3)	0.075 [a]
10	Gaussian	16.655 [a]	+0.006	0.017(3)	0.075 [a]
			DBr^+ $A\ ^2\Sigma^+$		
0	Lorentzian	15.317(2)		0.171(6)	0.0215(11)
1	Lorentzian	15.437(2)		0.399(6)	0.0225(5)
2	Lorentzian	15.549(2)		0.532(6)	0.0236(5)
3	Lorentzian	15.656(2)		0.723(7)	0.0272(4)
4	Gaussian	15.743(2)		0.805(7)	0.0481(5)
5	Gaussian	15.833(2)		0.645(55)	0.073(3)
6	Gaussian	15.938(3)		1.000(5)	0.150(14)
7	Gaussian	16.067(4)		0.305(30)	0.1 [a]
8	Gaussian	16.170 [a]		0.249(11)	0.1 [a]

[a] Parameters fixed in fit procedure.
[b] Where uncertainty = 0.002 eV the uncertainty is due to the spectral calibration.
[c] $\Delta E = E(v')_{(TPES)} - E(v')_{(HeI\ PES)}$, where $E(v')_{(HeI\ PES)}$ is taken from Baltzer *et al.* [134]

Table 5-6 Estimated electronic state energies (in eV) for the inner valence ionisation region of HBr and DBr.

	HBr^+		DBr^+
State label	Present work [a]	Adam *et al.* [148]	Present work [a]
0	19.5		19.5
1	22.2	22.1	22.2
2	24.59	24.58	24.60
3	26.1	26.2	26.1
4	27.1	27.5	27.1
5	29.2	29.5	29.2
6	30.4	30.8	30.4

[a] estimated peak maximum.

Table 5-7 Spectroscopic parameters (in eV) for the electronic states in the inner valence ($(4s\sigma)^{-1}$) ionisation region.

State	I.P. (HBr) [a]	I.P. (DBr) [a]	$\rho_i\omega_e$ [b]	$\rho_i^2\omega_e x_e$ [b]
X ($^1\Sigma^+$)			0.3284 [c]	-0.00561 [c]
E	22.163(20)	22.168(20)	0.227(19)	-0.0052(41)
F	23.181(30)	23.185(30)	0.2837(19)	-0.0050(4)
G	24.578(10)	24.575(10)	0.173(5)	-0.0028(11)
H	25.386(10)	25.377(10)	0.325(10)	-0.0069(26)
I	25.535(10)	25.529(10)	0.239(14)	-0.0066(47)
J	25.406(14)	25.414(14)	0.232(34)	-0.0009(160)
K	26.493(10)	26.499(10)	0.227(5)	-0.0076(11)
L	26.633(10)	26.638(10)	0.263(5)	-0.0146(16)

[a] If fit uncertainty < 0.01 eV : uncertainty = calibration uncertainty (±0.010 eV)

[b] $\rho_i = \sqrt{\mu(HBr)/\mu_i}$, μ_i is the reduced mass of HBr or DBr

[c] The vibrational constants for the X ($^1\Sigma^+$) state are from Huber and Herzberg [177].

Table 5-8 Table of measured and fitted vibrational peak positions (in eV) for the inner valence ($(4s\sigma)^{-1}$) ionisation region of hydrogen and deuterium bromide.

		HBr^+		DBr^+	
State	v'	exp [a]	fit	exp [a]	fit
E	0	22.163	22.168	22.124	22.122
	1	22.382	22.374	22.274	22.273
	2	22.572	22.569	22.414	22.419
	3			22.554	22.559
F	0	23.181	23.185	23.194	23.192
	1	23.461	23.459	23.394	23.389
	2	23.720	23.723	23.584	23.581
	3	23.969	23.977	23.734 [b]	23.768
	4	24.219	24.221	23.954	23.949
	5	24.448	24.454	24.124	24.126
	6	24.678	24.678	24.294	24.297
	7	24.897	24.891	24.463	24.463
	8	25.087	25.095	24.633	24.625
	9			24.788	24.781
G	0	24.578	24.575	24.593	24.597
	1	24.748	24.742	24.713	24.717
	2	24.907	24.905	24.833	24.835
	3	25.067	25.061	24.953	24.950
	4	25.217	25.212	25.053	25.062
	5			25.163	25.1701
H	0	25.386	25.377	25.373	25.378
	1	25.686	25.689	25.603	25.603
	2	25.995	25.987	25.813	25.820
	3	26.264	26.271	26.032	26.031
	4			26.242	26.235
I	0	25.535	25.529	25.313	25.315
	1	25.745	25.742	25.473	25.479
	2	25.306	25.302	25.633	25.636
	3			25.783	25.786
J	0	25.406	25.414	25.433	25.427
	1	25.646	25.644	25.593	25.591
	2			25.753	25.754

K	0	26.493	26.499	26.522	26.513
	1			26.662	26.667
	2	26.912	26.908	26.812	26.814
	3	27.092	27.089	26.952	26.953
	4	27.252	27.256	27.081	27.084
	5			27.211	27.207
L	0	26.633	26.638	26.652	26.648
	1	26.873	26.872	26.822	26.821
	2	27.073	27.077	26.982	26.979
	3			27.121	27.122
	4			27.251	27.250
Unassigned		22.043			
		22.932			
		25.905		25.932	
		26.105		26.122	
		26.393		26.372	
		27.551		27.441	
		27.791		27.581	
		27.990		27.831	
		28.229		28.270	
		28.418			
		28.708			

[a] ± 0.01 eV

[b] level not used in the vibrational fit procedure.

Chapter 6. Hydrogen iodide

6.1 Introduction

Hydrogen iodide has been the subject of much spectroscopic interest in the past, as is typical of all molecules in the hydrogen halide series. A simple molecular orbital diagram for the valence electronic structure of hydrogen iodide is given in Figure 6-1. From Figure 6-1 the valence electronic structure of HI should be $(5s\sigma)^2(5p\sigma)^2(5p\pi)^4(5p\sigma*)^0$, with only the $5p\sigma$ orbital involved in chemical bonding, so the ground state neutral molecule is labeled $^1\Sigma$. Removal of an electron from the $5p\pi$ orbital should result in a $^2\Pi$ state which will be strongly spin-orbit split. Removal of an electron from the bonding σ orbital should yield a $^2\Sigma^+$ state, and the same would be expected for removal of the inner valence non bonding σ orbital.

There have been numerous photoelectron experiments on hydrogen iodide [156],the most recent and relevant of which is the work by Adam *et al.* [157]. Adam

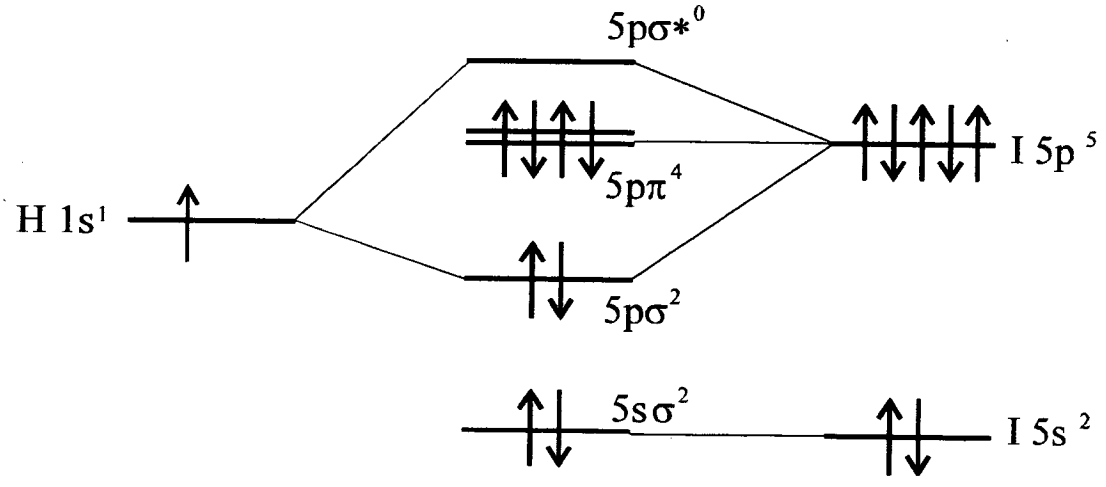

Figure 6-1 Molecular orbital diagram for the valence states of hydrogen iodide.

et al. report XPS [j], and UPS [k] results for the valence ionisation of hydrogen iodide. Three bands corresponding to $5p\pi^{-1}$, $5p\sigma^{-1}$, $5s\sigma^{-1}$ and are observed using XPS radiation. The X $^2\Pi_i$ $(5p\pi)^{-1}$ state is observed to be spin-orbit split as expected and the A $^2\Sigma^+$ $(5p\sigma)^{-1}$ state extends over a wider energy range than the X ($^2\Pi_i$) state as predicted from the molecular orbital diagram in Figure 6-1. The B $^2\Sigma^+$ state $(5s\sigma)^{-1}$ does not agree with the *one hole* picture of molecular ionisation [158],[159] and instead results in a series of 7 states from 19.0 to 28.0 eV.

When the outer valence (X and A) states were studied under higher resolution conditions using the UPS source and HeI radiation, Adam *et al.* [157] were able to resolve three vibrational levels in both spin-orbit components of the X state. They report the X $^2\Pi_{3/2}$ ionisation potential at 10.384 eV and the higher X $^2\Pi_{1/2}$ component at 11.048 eV, so the spin-orbit splitting is –0.664 eV. The vibrational frequency (ω_e) was calculated to be 263 meV. They also measured the relative intensity of the different vibrational levels and using a Franck-Condon fit of these intensities allowed them to predict an equilibrium bondlength for the X $^2\Pi_i$ state of ~1.64 Å.

Adam *et al.* [157] were also able to resolve for the first time two relatively sharp features in essentially continuum *structure* of the A state centred at ~14.3 eV. These two peaks (at 13.97 and 14.15 eV) were assigned to the first two vibrational levels in this state. It must be noted here that unlike the higher members of the hydrogen halide series there were previously no reports of observations of A $^2\Sigma^+ \rightarrow$X $^2\Pi_i$ fluorescence and it had always been assumed that the A state is entirely predissociated, showing no vibrational or rotational structure. This assumption was reinforced by the fact that previous photoelectron experiments had shown no structure in the A ($^2\Sigma^+$) state (see ref. [156]). Also, in their Photoionisation mass spectrometry study of hydrogen iodide, Eland and Berkowitz [160] report "the HI^+

---

[j] X-ray photoelectron Spectroscopy using Al Kα Radiation at hν = 1487 eV.

[k] Ultra-violet Photoelectron Spectroscopy using an electron cyclotron source giving high intensity HeI and HeII radiation with a 65 meV FWHM resolution on the He 1s photoelectron line.

yield curve is featureless and essentially flat from 600 to 950 Å" (13.05 to 20.66 eV) reinforcing the idea that the A state is entirely predissociated. Eland and Berkowitz also recorded the I^+ channel during this study and found a rising background starting at ~13.5 eV and peaking at 14.75 eV, again backing the predissociative model.

It is certainly not unexpected that the A state of HI should be predissociated as can be seen in comparison with hydrogen chloride and bromide. It has been reported that the A $^2\Sigma^+$ state of HCl is predissociated above $v^+=6$ (see Chapter 4), while the A $^2\Sigma^+$ state of HBr is predissociated above $v^+=2$ (see Chapter 5), so it seems reasonable to assume that predissociation in HI sets in at a lower vibrational level. The main cause of predissociation in HCl and HBr is calculated to be via the spin-orbit interaction of a repulsive $^4\Pi$ ionic state with the bound A $^2\Sigma^+$ ion state [186]. The $^4\Pi$ state correlates to the X ($^2\Pi_i$) state dissociation products. The spin-orbit interaction increases with increasing nuclear mass, so predissociation would be expected to be extensive in hydrogen iodide, reconciling the lack of previous observations of structure in the A ($^2\Sigma^+$) state. So it was quite a surprise to find evidence of vibrational structure in the A ($^2\Sigma^+$) state of HI^+ (Adam *et al.* [157]) and certainly warrants further investigation.

The energy region between the band origins of the X $^2\Pi_{3/2}$ and X $^2\Pi_{1/2}$ sub-states has also been the subject of many experimental and theoretical studies [160], [161],[162],[163],[164]. These are mainly centred on the spin-orbit autoionisation phenomenon as HI is an ideal case for this type of study, exhibiting a large spin-orbit splitting. The Rydberg structure lying between these two sub-state band origins is well characterised by laser photoionisation studies by Hart and Hepburn [164] and by Mank *et al.* [161]. The work by Hart and Hepburn [164] covered the entire energy between the two spin-orbit origins with a gas temperature of 300 K, with only a small part of this region recorded using a pulsed expansion cooled to ~10 K. However, 6 sets of Rydberg series converging to the X $^2\Pi_{1/2}$ state could be assigned to the autoionising structure. The work by Mank *et al.* [161] again covered the whole energy region between the two sub-state band origins with higher resolution than Hart

and Hepburn [164] using a gas temperature of ~13 K. This allowed Mank *et al.* [161] to assign 12 Rydberg series converging to the X ($^2\Pi_{1/2}$) ion core. Their results suggested that Rydberg states of increasingly high principal quantum number, n, converging on the X $^2\Pi_{1/2}$ ion core are gradually better described by an evolution from the Hund's case (c) to the Hund's case (e) coupling scheme (see Appendix C, Herzberg [165], and Lefebvre-Brion [166]).

The X $^2\Pi_{1/2}$ state band origin has also been the subject of a recent (rotationally resolved) ZEKE-PFI study by Pratt [167]. This paper confirms the rotational and Λ-doubling constants for HI^+ that were estimated in the work by Mank *et al.* [161]. Pratt also notes that the high-n Rydberg states involved in the ZEKE-PFI experiments can undergo the dissociative charge transfer reaction $HI^* + HI \rightarrow HI^+ + H + I^-$. This observation may prove useful in the analysis of the threshold photoelectron spectrum because, as mentioned in Chapter 2, the penetrating field electron spectrometer is not mass selective, and will detect threshold electrons and iodine anions equally well.

The energy region between $v^+=2$ in the X $^2\Pi_{1/2}$ state at 11.56 eV and the origin of the A $^2\Sigma^+$ state at 13.97 eV shows no vibrational structure in conventional photoelectron spectroscopy [157]. There are however, two previous reports of vibrational structure in this *Franck-Condon Gap* region. Böwering *et al.* [168] reported the combined use of conventional photoelectron spectroscopy [1] with synchrotron radiation. They irradiated hydrogen iodide with various different wavelengths of radiation from 112.5 nm to 90 nm (11.02 to 13.77 eV) and recorded photoelectron spectra for each wavelength at an experimental resolution of 80 meV. Using their data, with subsequent manipulations, they were able to report vibrational constants for the X $^2\Pi_i$ ion state, computed from data covering the X $^2\Pi_{3/2}$ $v^+=0$-4 and X $^2\Pi_{1/2}$ $v^+=0$-9 vibrational levels. A summary of their results is in Table 6-3 for comparison with the present work. Finally, it is worth noting that Böwering *et al.*

---

[1] i.e. the energy analysis of kinetic electrons

[168] found they could not obtain any photoelectron signals once the excitation photon was in the range 13.5 - 13.9 eV, showing that autoionisation processes producing kinetic electrons had ceased. They noted that the dissociation limit for the X $^2\Pi_i$ state also occurs at 13.5 eV (see later) which then suggested that autoionisation to bound ionic levels ($HI^* \rightarrow HI^+ + e^-$) could not compete with dissociative autoionisation ($HI^* \rightarrow H + I^+ + e^-$) resulting in the production of lower energy electrons.

Zietkiewicz *et al.* [169] have also reported the multiphoton ionisation of hydrogen iodide at 532 and 355 nm using a Nd:YAG laser. They operated a magnetic bottle spectrometer [170] in time of flight mode to detect energy dispersed photoelectrons formed in the multiphoton ionisation process. At 532 nm excitation the electron time of flight distribution showed the ionisation products were essentially I^+, suggesting the molecule dissociated before ionisation. However, with 355 nm radiation the electron time of flight was very structured, and they assigned the X ($^2\Pi_{3/2}$) and X ($^2\Pi_{1/2}$) vibrational progressions from v^+=0-10 and v^+=0-7 respectively. However, Zietkiewicz *et al.* [169] noted they could not assign the spectra unambiguously, producing two different sets of molecular parameters from their data.

The work by Böwering *et al.* [168] and Zietkiewicz *et al.* [169] warrants some further discussion as it is relevant to the results later in this chapter. Both experiments rely on the autoionisation of Rydberg levels converging to the A ($^2\Sigma^+$) ion core into the X $^2\Pi_i$ ion continuum. These processes can be considered as the combination of two Franck-Condon allowed processes. Firstly, the photoabsorption to the intermediate Rydberg state, and secondly, the autoionisation of the intermediate state to the final ion state. One of these intermediate Rydberg states has been observed in photoabsorption work by Terwilliger and Smith [171]. They observed only one peak between 1040 and 860 Å, centred at 1005 ± 10Å (12.33 eV) with a width of ~4500 cm^{-1} with no discernible structure. So it is reasonable to assume that the Rydberg state is fully predissociated like the A ($^2\Sigma^+$) state it converges to, and the autoionising

state populated by Böwering *et al.* [168] and Zietkiewicz *et al.* [169] would be expected to predissociate as well as autoionise.

The Penning ionisation electron spectrometry study of hydrogen iodide by Yencha *et al.* [172] also observed non-Franck-Condon vibrational levels of the X ($^2\Pi_i$) state for both spin orbit components. Vibrational levels from v^+=0-5 were observed. The experimenters commented that the extension of the vibrational structure could not be due to Rydberg levels converging on the A state as the Penning atom is at higher energy, and instead suggested it is due to an ionic contribution on the entrance channel to Penning ionisation (i.e. $He^* + HI^-$). This is reported to be typical for all the halogen acids [173],[174],[175]. Yencha *et al.* [172] also observed two vibrational levels in the broad continuum structure of the A ($^2\Sigma^+$) state, the spacing between the levels is in agreement with the spacing measured by Adam *et al.* [157] as discussed earlier.

The binary (e,2e) spectroscopy by Brion *et al.* [176] is at much lower resolution than much of the work previously discussed, however it does clearly demonstrate how a low resolution study can be used to gain information on (1) the symmetry of molecular orbitals, and (2) the extent to which electron correlation effects can be important in forming the final ionic states. In these binary electron experiments a high energy electron (1200 eV) is used to ionise the hydrogen iodide. Two emitted electrons are collected in coincidence, both at an angle of 45° to the incident electron. The out-of-plane azimuthal angle of the detectors can be varied and, by varying this angle, information of the symmetry of molecular orbitals can be obtained. Their work on HI clearly showed that the X ($^2\Pi_i$) and A ($^2\Sigma^+$) states are formed from the ionisation of an electron in a nodal orbital (i.e. p-type), whereas the B $(5s\sigma)^{-1}$ state was formed from removal of a non-nodal orbital (i.e. s-type), showing that the molecular orbital diagram in Figure 6-1 is essentially correct. However, the experiment also shows that ionisation from the $5s\sigma$ orbital results in the formation of many ion states, with similar structure to the observations by Adam *et al.* [157].

A potential energy diagram for ground state of HI and the outer valence states of HI^+ is shown in Figure 6-2. Morse curves simulate the various bound states and the Franck-Condon window is shown as the classical turning points of the X ($^1\Sigma^+$) v=0 wavefunction. The equilibrium bondlengths for the X ($^2\Pi_i$) ion states come from the Franck-Condon fits by Adam *et al.* [157] and the vibrational frequency of the A ($^2\Sigma^+$) state was taken to be the spacing between v^+=0 and 1 in the same work. The Rydberg level observed in absorption by Terwilliger and Smith [171] is indicated on the diagram (the state seems to be completely predissociated) and the $^4\Pi$ state correlating to the [H (^2S) + I^+ (^3P_j)] dissociation limit was created as an exponential decay, positioned to cut through the A ($^2\Sigma^+$) state near the bottom of the well. All other data came from Huber and Herzberg [177], Huffman et al. [183], and Moore [223].

There is no previous report of a threshold photoelectron study of hydrogen iodide in the literature. The threshold technique should allow access to autoionising levels at much higher resolution than the work by Böwering *et al.* [168] and Zeitkiewicz *et al.* [169]. This should differentiate between the two possible vibrational assignments of the X ($^2\Pi_i$) state and may also give more detail on the vibrational structure in the A ($^2\Sigma^+$) state. Finally, a threshold photoelectron study of the $5s\sigma^{-1}$ ionisation region may allow more information to be gleaned as to the electron configuration of the *2 hole - 1 particle* (2h-1p) final ion states in this region. With these ideas in mind a threshold photoelectron study of the valence states of hydrogen iodide was completed.

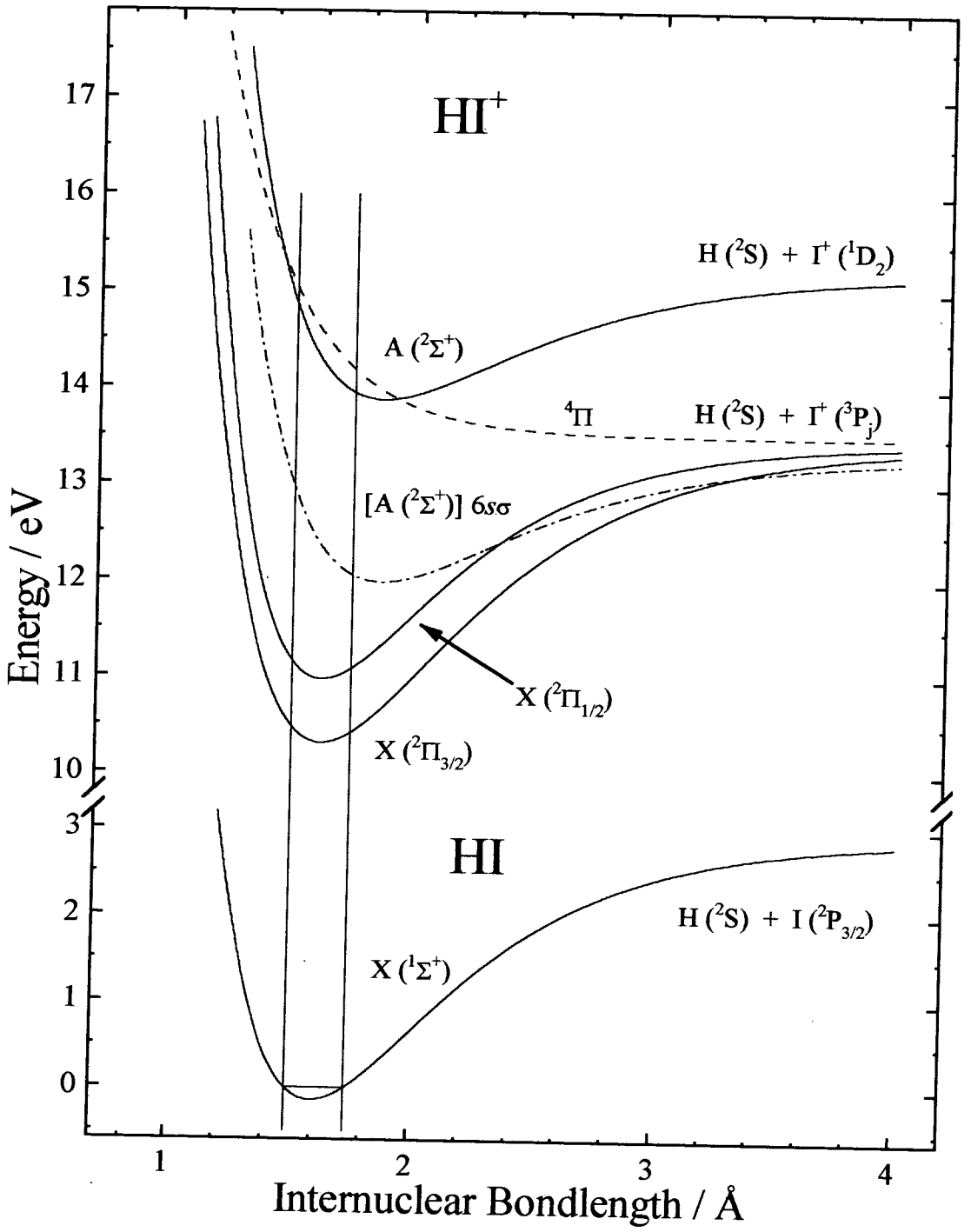

Figure 6-2 Potential energy diagram for the X ($^1\Sigma^+$), X ($^2\Pi_i$), and A ($^2\Sigma^+$) states of HI/HI$^+$. (for further details see text)

6.2 Special Experimental Details

Spectra recorded during the studies of hydrogen iodide were recorded with ~20% argon gas *in-situ*. Keeping argon in the spectra allowed for two internal calibration points (Ar^+ $^2P_{3/2}$, $^2P_{1/2}$), and also allowed efficient monitoring of the threshold performance of the penetrating field spectrometer between study scans. The total gas pressure in the chamber was 1.0×10^{-4} mBar, of which ~2.0×10^{-5} mBar was argon. Details of the gas sample preparation are given in section 2.5.5. Even using these thorough preparation methods a small amount of hydrogen was present between 15.4 and 15.6 eV in the final spectrum, however, this is of no consequence as HI does not have any spectral features in this energy region.

It should also be noted that addition of hydrogen iodide to the argon gas resulted in a ~70% drop in the photoelectron signal. This is normal for all study gases immediately after admission, and normally spectrometer tuning returns the signal to previous levels. However, in the case of hydrogen iodide it was impossible to regain the original signal levels. It may be that threshold electrons are being attached to neutral HI molecules, HI does have a large threshold electron attachment cross section [178],[179], and some electrons may be scavenged by the hydrogen iodide before they leave the interaction region. Hydrogen iodide undergoes dissociative attachment of threshold electrons (i.e. $HI + e^- \rightarrow H + I^-$) [180]. As the gas stream is thermalised the energy of the iodine anions formed by dissociative attachment will also be approximately thermalised. The detection efficiency of the spectrometer is constant for changing mass, so if dissociative attachment were occurring there would be a net loss of signal (the threshold electrons are changed into thermalised anions so many are not detected).

The data for the spectrum presented in Figure 6-3 was collected as follows. Four spectra covering small ranges were catenated to produce the full spectrum with suitable overlapping of spectral features. Between 10.2 and 13.076 eV a single spectrum was recorded with a stepsize of 2 meV and a count duration of 6 seconds per step. From 13.078 to 14.998 eV three spectra were recorded with a stepsize of 2

meV and a count duration of 2 seconds per step. Over the range 15.000 to 18.596 eV a single spectrum was recorded using 4 meV stepsize and 4 seconds per step, and from 18.600 to 31.000 eV four spectra were recorded with at 10 meV stepsize and 4 seconds duration. The spectra were summed (where appropriate) and catenated after normalisation for photon flux. The resolution of the spectrum varies over the different ranges. From 10.2 to 15.0 eV $\Delta E/E = 4.44\times10^{-4}$ (i.e., ΔE = 7 meV FWHM at the Ar^+ ($^2P_{3/2}$) line at 15.759 eV) and from 15.0 to 31.0 eV $\Delta E/E = 1.07\times10^{-3}$ (i.e., ΔE = 17 meV measured on the Ar^+ ($^2P_{1/2}$) line at 15.937 eV). The energy region from 10.2 to 15.0 eV is quoted at the Ar^+ ($^2P_{3/2}$) ion line. This line is normally broader than the Ar^+ ($^2P_{1/2}$) line due to the close lying 11s' Rydberg level (see Figure 1-4) and from previous spectra on argon at the same resolution this corresponds to an effective resolution of 6 meV at the Ar^+ ($^2P_{1/2}$) ion line. So the resolution of the 10.2 to 15.0 eV range is $\Delta E/E=3.76\times10^{-5}$.

6.3 Results and Discussion

6.3.1 Overview of the valence region

Figure 6-3 shows the threshold photoelectron spectrum of hydrogen iodide from 10.2 - 31 eV, the full region of study. All three band systems are present, denoted, in order of increasing energy, by $(5p\pi)^{-1}$, $(5p\sigma)^{-1}$, and $(5s\sigma)^{-1}$ electron transitions. Most of the threshold electron signal occurs in the ground state X ($^2\Pi_i$) band system. This is quite different to the He I photoelectron spectrum by Adam *et al.* [157] where the ratio of the X ($^2\Pi_i$) $v^+=0$ peaks to the A ($^2\Sigma^+$) band maximum is ~ 5:1, here if the X ($^2\Pi_{3/2}$) and X ($^2\Pi_{1/2}$) peak heights are averaged the same ratio is ~30:1. The phenomenon where the excited state bands in threshold photoelectron spectroscopy are weaker than expected from conventional photoelectron spectroscopy seems to be a common effect, observed by this group previously in threshold photoelectron studies on Cl_2 and Br_2 [181], and I_2 [182], and in the current results for HCl and HBr presented in Chapters 4 and 5. The effect is even more extreme when the B ($^2\Sigma^+$) ($(5s\sigma)^{-1}$) state is considered. From Figure 6-3 the ratio of

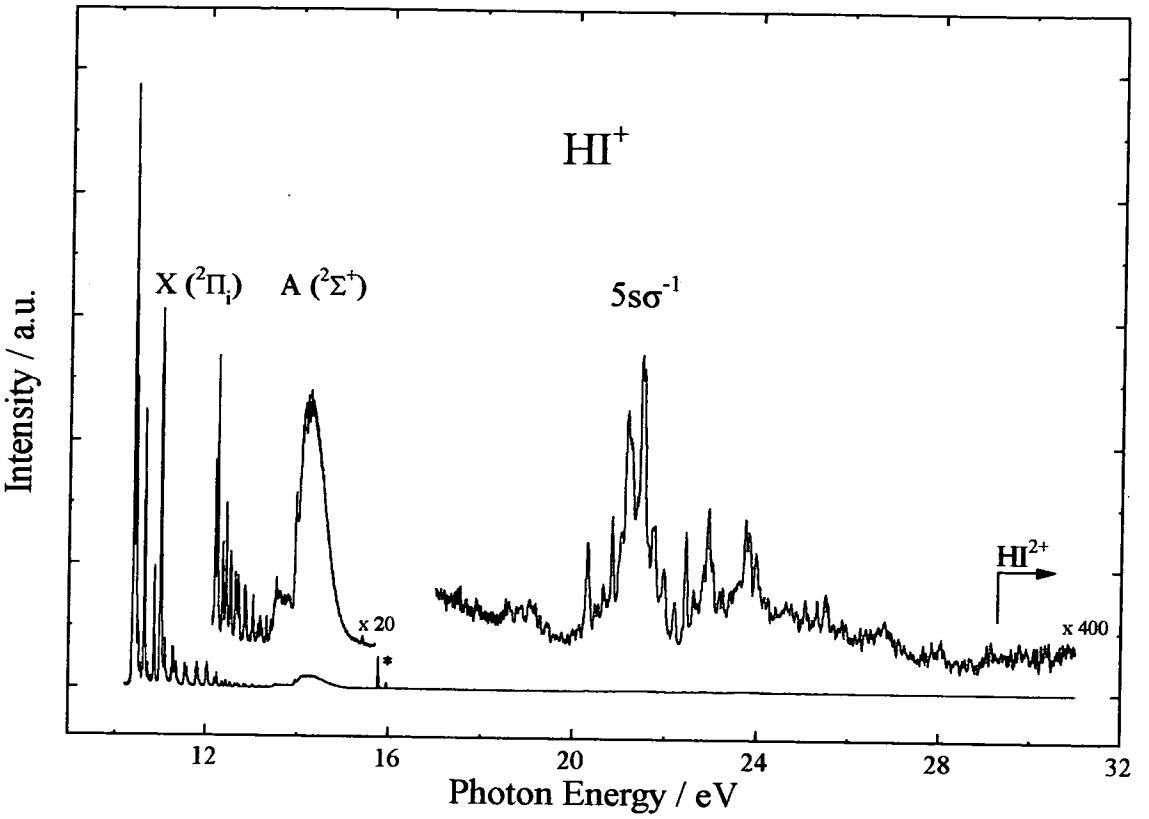

Figure 6-3 Threshold photoelectron spectrum of the valence states of hydrogen iodide showing the X ($^2\Pi_i$), A ($^2\Sigma^+$), and B ($^2\Sigma^+$) states of HI^+. The energy resolution of this spectrum ranges from ~4 meV at 10.2 eV to ~6 meV at 15.2 eV and ~19 meV at 17 eV to ~30 meV at 31 eV. (The asterisk in the lower trace marks the Ar^+ ^2P_i ionisation lines, used for calibration and spectrometer tuning)

the X ($^2\Pi_i$) $v^+=0$ levels to the highest band in the B ($^2\Sigma^+$) state is ~400:1, whereas in the XPS work by Adam *et al.* [157] this ratio is about 6:1.

A simple explanation for the decrease in relative intensity for higher band systems in threshold photoelectron spectroscopy is to simply surmise that the intensity of the lowest band system will be enhanced by electronic autoionisation from Rydberg levels associated with the higher ion states. In the case of inner valence ionisation $(5s\sigma)^{-1}$ it is quite probable that the very weak band intensities are a result of a small probability of producing a threshold electron in a correlated two electron process.

The in-depth analysis and discussion of the threshold photoelectron spectrum of HI is easier if separated into the outer valence $(5p\pi)^{-1}$, $(5p\sigma)^{-1}$ and inner valence $(5s\sigma)^{-1}$ ionisation regions, this recognises the breakdown of the *one hole* picture of molecular ionisation when dealing with inner valence electrons.

6.3.2 The outer valence ionisation region of hydrogen iodide

The threshold photoelectron spectrum of hydrogen iodide from 10.2-15.2 eV in Figure 6-4 shows the X ($^2\Pi_i$) and A ($^2\Sigma^+$) states formed by the removal of a $5p\pi$ and a $5p\sigma$ electron. The resolution of the spectrum is relatively high, ~ 4 meV at low energy to ~6 meV at high energy, as compared to ~30 meV resolution in the HeI photoelectron spectrum by Adam *et al.* [157]. The current spectrum also shows much more than the HeI photoelectron study.

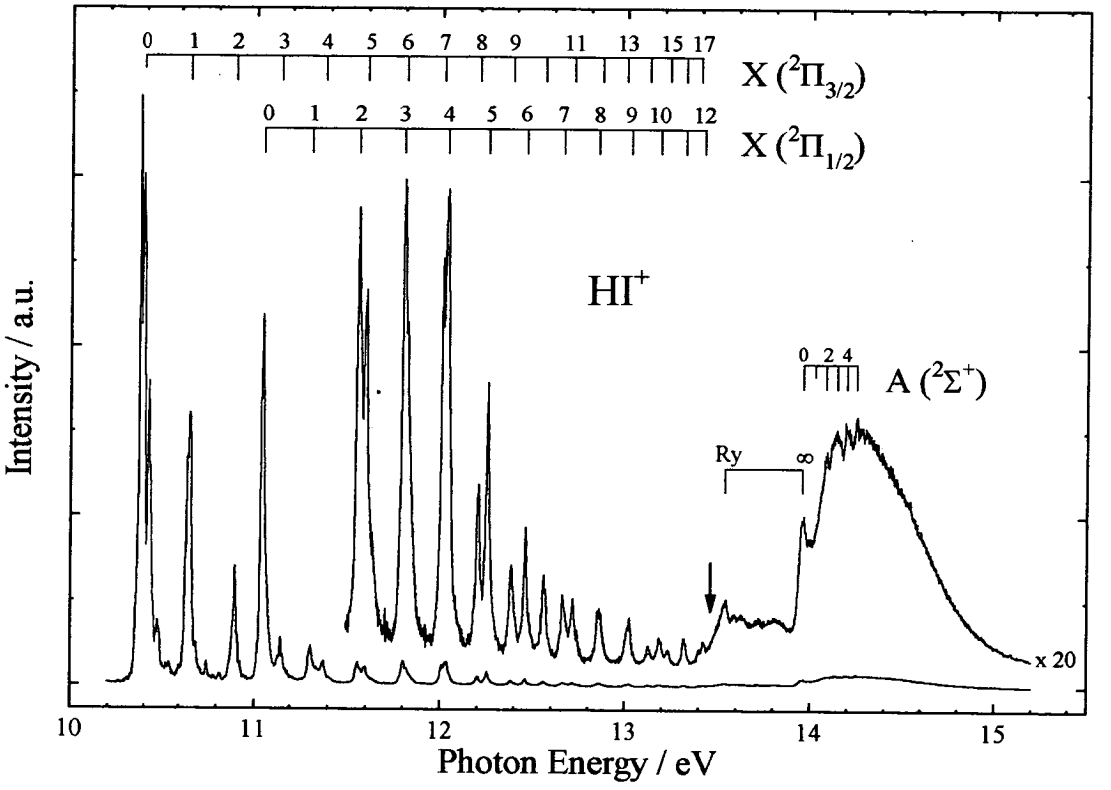

Figure 6-4 The threshold photoelectron spectrum of HI covering the X ($^2\Pi_i$) and A ($^2\Sigma^+$) states including assignment of the observed vibrational progressions. The vertical arrow at 13.464 eV shows the onset of dissociative ionisation (from Eland and Berkowitz [160]).

6.3.2.(a) *The energy region 10.2 to 13.5 eV*

Careful assignment of the structure in the region 10.2 eV to 13.5 eV allows the identification of 17 vibrational levels in the X ($^2\Pi_{3/2}$) sub-state and 13 vibrational levels in the X ($^2\Pi_{1/2}$)sub-state. The origin of the X ($^2\Pi_{3/2}$) sub-state in Figure 6-4 is masked by extensive autoionisation in this region, and is instead marked with a half length tick positioned from a fit to the rest of the vibrational progression. The positions of observed and fitted ion vibrational levels for the X ($^2\Pi_{3/2,1/2}$) states are given in Table 6-1. The vibrational levels were fitted to a fourth-order vibrational Dunham expression [165]. The fit parameters are given in Table 6-3 along with other work from the literature for comparison. It is worth noting that a fourth-order polynomial was needed to correctly fit the data over the full range. The fits generated from lower orders of polynomial tended to deviate from the measured data towards the ends of the fit region. The vibrational fitting procedure can be used to predict the number of vibrational levels the potential wells support before dissociation, the X ($^2\Pi_{3/2}$) supports up to v^+=20 and the X ($^2\Pi_{1/2}$) supports up to v^+=14.

The fit expressions for the two components of the X ($^2\Pi_i$) state were also used to determine the dissociation limit of each sub-state, the results are given at the bottom of Table 6-1. The appropriateness of the fitted expressions can be demonstrated by the accurate prediction of the dissociation limit of the HI X ($^1\Sigma^+$) state as follows: The extrapolated dissociation limits are (13.529 eV (3/2) and 13.543 eV (1/2)), so both correspond to the [H (^{2}S) + I^+ ($^3P_2$)] dissociation limit. Subtracting 0.026 eV for the contribution from thermal energy and 10.451 eV for IP(I) [I^+ ($^3P_2$) ← I ($^2P_{3/2}$)] [183] yields D_o (HI (X ($^1\Sigma^+$)) = 3.052 ± 0.004 eV (3/2) and 3.066 ± 0.004 eV (1/2), which compares well to 3.056 eV from Herzberg [165]

It is worth comparing the data generated here with the previous work on the HI X ($^2\Pi_i$) ion state. One sees the vibrational spectroscopic parameters are quite different, however, this is to be expected as the number of coefficients in the fit changes. It can be concluded that the assignments and/or energy positions of the

peaks assigned in the work by Böwering *et al.* [168] and Zietkiewicz *et al.* [169] do not agree with the present work, as seen by comparing the energy positions of the assigned peaks in the previous work with the present work. It must be concluded that the assignments and peak positions in the present work are more reliable than the others as they predict the dissociation energy of the X ($^1\Sigma^+$) state accurately.

The Rydberg states giving rise to the enhanced vibrational progression in the X ($^2\Pi_i$) ion state can be assigned from the threshold photoelectron work on HCl and HBr (see Chapters 4 and 5). The Rydberg states which lie in the correct energy region for HCl were found to be of [A ($^2\Sigma^+$)] *ns*σ $^1\Sigma$ symmetry. It is likely that Rydberg states of the same symmetry are also involved in threshold photoelectron production in HI. The expected energies for the *ns*σ Rydberg states can be calculated using a typical quantum defect of 4.00 for the *ns* Rydberg states of atomic iodine [172] and the ionisation potential of the A ($^2\Sigma^+$) state at 13.958 eV (see Table 6-2). Relevant energies are as follows: 6*s*σ = ~10.6 eV, 7*s*σ = ~ 12.5 eV, 8*s*σ = ~ 13.1 eV. These energies are in reasonable agreement with the enhanced vibrational levels in Figure 6-4, suggesting the Rydberg assignment is correct. So, the Rydberg states giving rise to the extended vibrational progression are assigned as [A ($^2\Sigma^+$)] *ns*σ $^1\Sigma$, where *n* ranges from 6 to 8 by comparison with the lighter members of the hydrogen halide series.

6.3.2.*(b)* *Discussion of the experimental results for the region 13.95 to 15.2 eV*

The energy range from 13.95 to 15.2 eV in Figure 6-4 shows some complicated structure. The vibrational peaks in this range are assigned to the A ($^2\Sigma^+$) state. The positions of the five peaks assigned to this state are given in Table 6-2, along with the results of a second-order vibrational Dunham fit expression. It should be noted that the fit is extremely good and the spectroscopic constants from the fit are included in Table 6-3 for comparison with other work. There are, however, problems with this simple assignment. The vibrational frequencies (ω_e) for the A ($^2\Sigma^+$) state of HCl and HBr are 0.191 eV and 0.174 eV [177]. Extrapolating linearly, one would

expect a vibrational frequency of 0.157 eV for HI. This is closer to the v^+=0-1 spacing observed by Adam *et al.* [157] (0.18 eV) than the spacing from the fit assignment in Table 6-3 (0.0682 eV). It is probable that the bands observed by Adam *et al.* [157] are assigned to v^+=0 and v^+=3 in the present assignment, these features are the most pronounced in the current spectrum and the spacing between each peak is the same to within 4 meV in both studies.

The difficulty with the new vibrational assignment is represented by the potential energy diagram in Figure 6-5. All the curves in Figure 6-5 except one marked with asterisks are identical to Figure 6-2. The asterisked curve has been simulated using the vibrational frequency associated with the assignments in this work, the dissociation energy to [H (^{2}S) + I^+ ($^1D_2$)] (from the IP(I) ($^1D_2$) [223] and D_o HI ($^1\Sigma^+$) [165]), and using an equilibrium bondlength of 1.86 Å. It is clear that this cannot be an accurate representation of the A ($^2\Sigma^+$) state as the Franck-Condon window does not cover a large enough energy range to generate the experimental results. The state could be shifted to a larger equilibrium bondlength to increase the Franck-Condon window, however, doing this would also require that the well was deepened considerably.

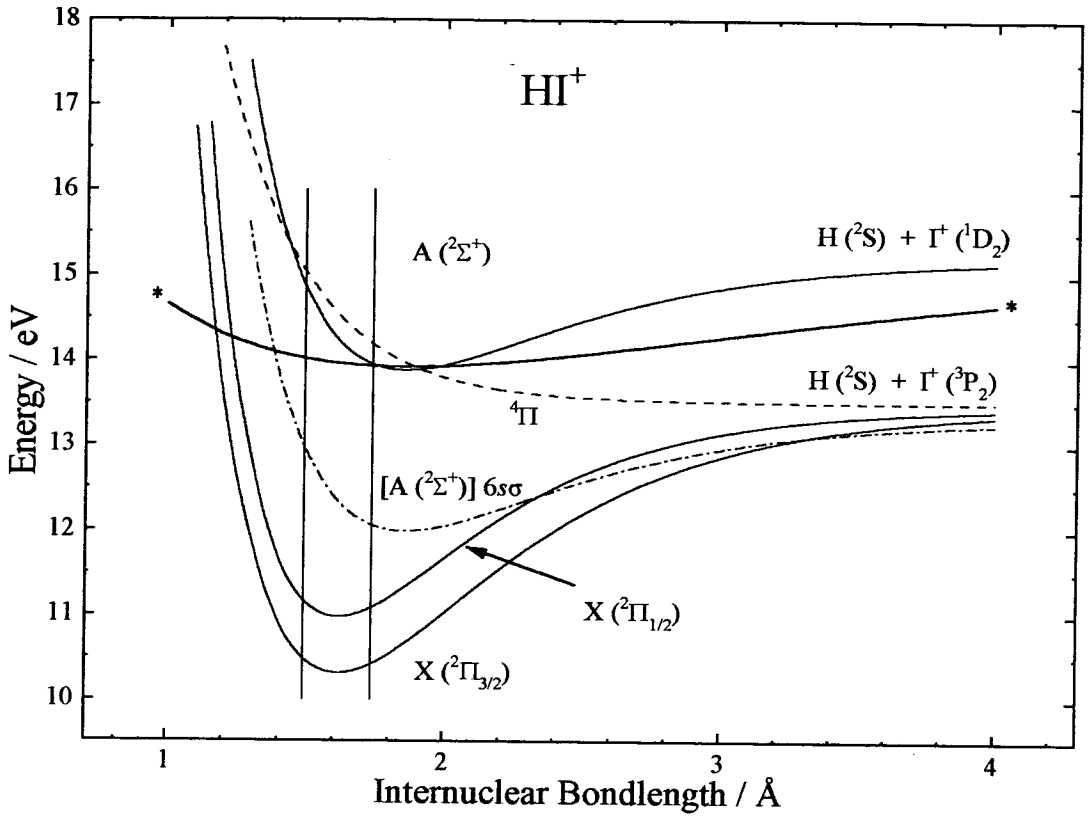

Figure 6-5 Potential energy diagram for HI^+. All states are identical to Figure 6-2 except for the one marked with asterisks. This is a Morse curve for the A ($^2\Sigma^+$) state using data derived from the A ($^2\Sigma^+$) vibrational levels in Figure 6-4. (The bondlength for the curve is 1.86 Å). The vertical lines denote the classical turning points of the X ($^1\Sigma^+$) v^+=0 vibrational wavefunction.

Recently Baltzer *et al.* [184] have recorded the A ($^2\Sigma^+$) state of HI using HeI radiation, showing it exhibits identical structure to the threshold photoelectron spectrum in Figure 6-4. This confirms that the TPE spectrum (Figure 6-4) has not been distorted by autoionising processes. It is worth considering possible explanations for the new closely spaced vibrational structure. Firstly, one notes that a doubling of the measured vibrational frequency (ω_e) for the A ($^2\Sigma^+$) state to 0.1364 eV would be quite close to the expected frequency of 0.157 eV as extrapolated from HCl and HBr. So, an obvious solution would be that there are two interloping (or nested) states which accidentally lie on one vibrational fit curve. The A ($^2\Sigma^+$) state cannot be spin-orbit split, and it seems extremely unlikely that two different states could fit to

one vibrational progression as closely as in Table 6-2, so two states are quite improbable.

Using the relationship [185]

$$D_e \approx \omega_e^2 / 4\omega_e x_e$$

Equation 6-1

the dissociation limit for the state would be predicted to be ~14.61 eV suggesting the structure in Figure 6-4 could be associated with a lower dissociation limit. A*b-initio* work by Banichevich *et al.* [186] on HBr^+ has investigated the electronic properties of the X ($^2\Pi_i$) and A ($^2\Sigma^+$) states. Of particular interest is the predissociation of the A ($^2\Sigma^+$) state correlating to [H(^{2}S) + I^+(^{1}D$_2$)] fragments by the dissociative $^4\Sigma^-$, $^2\Sigma^-$, and $^4\Pi$ states. These dissociative states correlate to the [H(^{2}S) + I^+(^{3}P$_j$) j=0,1,2] dissociation products. In HBr^+ the predissociation is due to a spin-orbit interaction between the repulsive states and the bound A ($^2\Sigma^+$) state, so it seems reasonable to assume the interaction would be stronger in HI^+. In HBr^+ the strongest interaction occurs between the A ($^2\Sigma^+$) and a $^4\Pi_{1/2}$ state. Two $^4\Pi_{1/2}$ states correlate to the I^+ (^{3}P$_{0,1}$) limits at large R. (the limit the predissociating state correlates to is not identified in ref. [186])

In the iodine ion there is a large (~0.8 eV) energy difference between the j=2 and the j=0,1 components of the I^+ (^{3}P$_j$) state [223]. The dissociation limits of HI^+ are [H (^{2}S) + I^+ (^{3}P$_0$)] = 14.307 eV, and [H (^{2}S) + I^+ (^{3}P$_1$)] = 14.387 eV. This is reasonably close to the predicted dissociation energy of the state (~14.61 eV) calculated using Equation 6-1 - certainly closer than dissociation to [H (^{2}S) + I^+ (^{1}D$_2$)] at 15.21 eV. It could be possible that the spin-orbit interaction of a diabatic $^4\Pi$ state with the expected (diabatic) A ($^2\Sigma^+$) state is strong enough to form an avoided crossing between the two states. This would lead to the formation of a new adiabatic A ($^2\Sigma^+$) state with a lower dissociation limit. This process has been simulated in Figure 6-6 where a Morse potential (A ($^2\Sigma^+$)) and a repulsive $^4\Pi_{1/2}$ ion state

correlating to I^+ ($^3P_0$) interact and form an avoided crossing. The energies of the new adiabatic states can be calculated from the simple perturbation of a two level system (see Atkins and Friedman [187]). From Atkins and Friedman [187] the energies of the two adiabatic curves formed by the avoided crossing of the diabatic ones are given as

$$E_{(1)\Omega,(2)\Omega} = \tfrac{1}{2}(E_{\Pi} + E_{\Sigma}) \pm \tfrac{1}{2}\left\{(E_{\Pi} - E_{\Sigma})^2 + 4H_{\Pi\Sigma}{}^2\right\}^{1/2}$$

Equation 6-2

where $E_{(1)\Omega,(2)\Omega}$ refers to the energy of the new lower ($E_{(1)\Omega}$) and upper ($E_{(2)\Omega}$) adiabatic states, E_{Π} and E_{Σ} are the energies of the upper and lower diabatic states, and

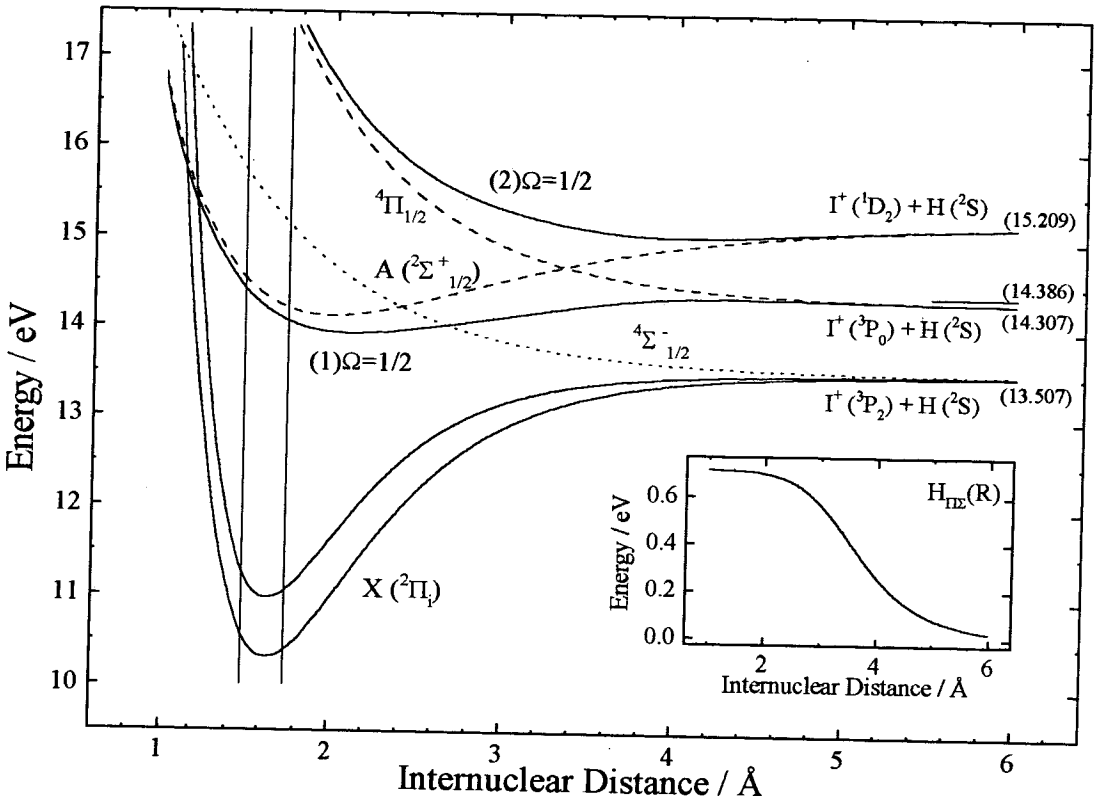

Figure 6-6 Simulated potential energy diagram for the outer valence ion states of HI^+. Four adiabatic ion states are shown as solid lines. The diabatic states forming the avoided crossing are shown as dashed lines, and the dotted line denotes a repulsive state which predissociates the new adiabatic ion state. The strength of coupling as a function of bondlength is shown in the insert. Further electronic states correlate with the I^+ ($^3P_{0,1}$) asymptotes [186]. However, they not been considered in this simple model.

$H_{\Pi\Sigma}$ is the magnitude of the perturbation between the two states (the off-diagonal matrix element). All variables in Equation 6-2 are functions of the internuclear bondlength and also the equation assumes that the diagonal matrix elements, H_{mm}, are zero. The calculations were performed in Microcal Origin [82] using the LabTalk script in Appendix B.

The adiabatic (1)Ω=1/2 state in Figure 6-6 was generated in an optimisation process involving adjusting: (a) the dissociation energy and vibrational frequency of the diabatic Morse potential; (b) the absolute magnitude of the coupling constant $H_{\Pi\Sigma}$, (c) how $H_{\Pi\Sigma}$ varies with internuclear distance, and (d) the "decay constant" and "amplitude" of the exponential decay function simulating the $^4\Pi_{1/2}$ diabatic curve. A Franck-Condon program [13] was used to calculate the vibrational eigenenergies and

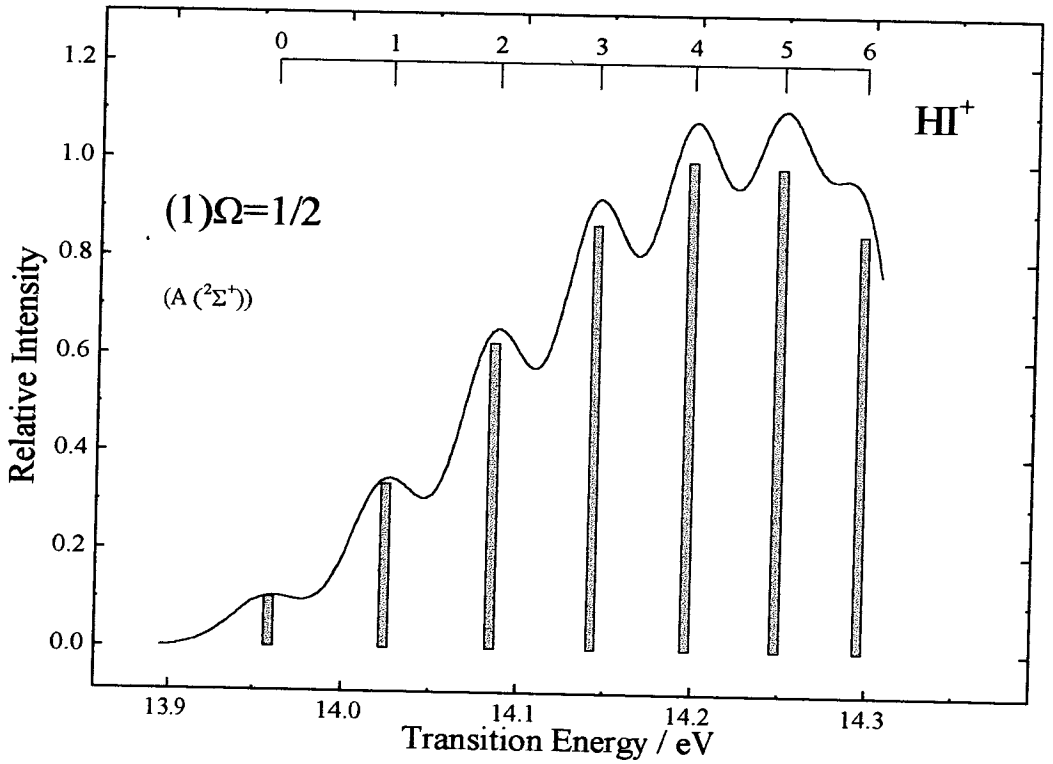

Figure 6-7 Franck-Condon simulation of the (1)Ω=1/2 (or A ($^2\Sigma^+$)) state of HI^+. The (1)Ω=1/2 state potential is taken from Figure 6-6. The bars represent the Franck-Condon factors for each vibrational level, as given in Table 6-4.

Franck-Condon intensities for the (1)Ω=1/2 ← X ($^1\Sigma^+$) transition.

With so many adjustable parameters generation of a suitable potential will have multiple solutions, however, the preferred solution is detailed in Appendix B. The equilibrium bondlength of the new state is 2.12 Å from the simulations. A Franck-Condon simulation of the new A (1)Ω=1/2 state in shown in Figure 6-7.

In conclusion, it seems perfectly feasible that the A (1)Ω=1/2 state of HI^+ adiabatically correlates with the I^+ ($^3P_0$) dissociation limit instead of I^+ ($^1D_2$). It is possible to simulate a suitable potential to explain the experimental results by invoking an avoided crossing between the $^4\Pi_{1/2}$ and A ($^2\Sigma^+_{1/2}$) diabatic states that gives realistic vibrational constants and Franck-Condon factors. However, the absence of v^+=1 and the increased intensity of v^+=0 in the experimental results in the A state (in Figure 6-4) are still not adequately explained. Banichevich *et al.* [186] calculate a $^4\Sigma^-_{1/2}$ state correlates to the lowest dissociation limit of HI^+ (I^+ ($^3P_2$)) and also participates in the spin-orbit predissociation of the A ($^2\Sigma^+$) state of HBr^+. A possible potential curve for this state is included as the dotted line in Figure 6-6, this curve has been drawn to cross the adiabatic A (1)Ω=1/2 state at ~14.02 eV, interacting very strongly with the v^+=1 ion vibrational level. A strong interaction would imply the v^+=1 level would be extensively predissociated and broadened, making it appear less intense in the spectrum. Predissociation of the higher vibrational levels would also be expected and this may explain why they are broader than the v^+=0 level. The same argument can be used to explain why the v^+=0 level is more intense than expected. The Franck-Condon simulation in Figure 6-7 is truncated at the dissociation limit of the new A (1)Ω=1/2 potential well, however the simulation shows that there will be a significant Franck-Condon factor for ionisation into the dissociative continuum of the adiabatic A (1)Ω=1/2 state in agreement with the spectrum in Figure 6-4.

6.3.2.*(c) The energy region 13.5 to 13.95 eV*

The relatively flat region between 13.5 and 13.9 eV in Figure 6-4 is still unexplained. Hydrogen iodide is unique within the hydrogen halide series as the dissociation energy of the X ($^2\Pi_i$) state is lower than the adiabatic ionisation energy of the A ($^2\Sigma^+$) state. Below the HI^+ [H (^2S) + I^+ ($^3P_2$)] dissociation limit, the extensive vibrational structure in the X ($^2\Pi_i$) state is associated with electronic autoionisation of Rydberg levels converging to the A ($^2\Sigma^+$) state, and this absorption would be expected to continue into the X ($^2\Pi_i$) state repulsive continuum. Böwering *et al.* [168] did not detect any kinetic electron signals in the 13.5 to 13.95 eV region showing that the Rydberg levels in this region do not autoionise to bound X ($^2\Pi_i$) ion state vibrational levels. These Rydberg levels are also unlikely to fluoresce as their lifetime will be very short due to predissociation. So it seems likely that Rydberg states within the dissociative continuum of the X ($^2\Pi_i$) state either (1) predissociate and fluoresce, or (2) predissociate and autoionise.

The vertical arrow at 13.464 eV in Figure 6-4 indicates the experimentally determined appearance potential of I^+ from mass resolved photoionisation spectroscopy [160]. This corresponds with a steep rise in the threshold photoelectron spectrum, culminating with a peak at 13.537 eV (marked Ry in Figure 6-4). It seems likely that this peak is associated with the lowest vibrational level of a Rydberg state in the region as it has similar shape to the A ($^2\Sigma^+$) v^+=0 peak. The effective principal quantum number (n^*) for this peak is 5.68, suggesting the peak belongs to the $d\pi$ series of Rydberg states. Assuming a quantum defect of 2.32, the peak is assigned to the [A ($^2\Sigma^+$)] 8$d\pi$ $^1\Pi$ Rydberg state (the quantum defects for various Rydberg states of HCl have been taken from [116] and were used for comparison). This assignment can be perplexing when considered in the context of the Rydberg assignments in Chapters 4 and 5. Those Chapters showed that the [A ($^2\Sigma^+$)] n$d\pi$ $^1\Pi$ Rydberg series do not produce threshold electrons even though they are easily observed in photoabsorption and photoionisation [28],[116]. So, it seems likely the [A ($^2\Sigma^+$)] n$d\pi$ $^1\Pi$ Rydberg states autoionise to produce kinetic electrons. However, Böwering *et al.*

[168] have shown that kinetic electrons are not produced in the range 13.5 eV to 13.9 eV. It seems extremely unlikely that there are no Rydberg states in this energy region, and these Rydberg states must somehow decay. A Rydberg state at 12.33 eV has been observed as a broad continuum [28], so it is unlikely that the Rydberg states will have time to fluoresce. More likely, the Rydberg state will by predissociated yielding electronically excited fragments. The predissociated state will cross the X ($^2\Pi_i$) state at some point and could autoionise into the ion continuum yielding a threshold electron.

It is worth considering other possibilities for the signal in the region 13.5 to 13.9 eV. There are numerous ion-pair dissociation limits in this energy region [H^- (^1S) + I^+ ($^3P_0$) = 13.556 eV], [H^+ (^1S) + I^- (^1S) = 13.593 eV], [H^- (^1S) + I^+ ($^3P_1$) = 13.556 eV] [188],[189]. The threshold electron spectrometer only differentiates charged particles from their initial energies, not their mass. This is in common with all electrostatic analysers, where the ion (or electron) trajectories of different mass but identical electric charge are identical in space, though not in time (the heavier ones take longer to complete the trajectory). When the excitation energy is only slightly above an ion-pair dissociation limit anions with only a small amount of kinetic energy could be formed and detected, and, as there is a very large mass difference between H and I the $H^{(+/-)}$ ion will remove almost all of any excess kinetic energy. This would suggest that, if the [$H^+ + I^-$ =13.593 eV] ion dissociation channel were active, a signal due to I^- could be detected over ~0.4 eV [190] above threshold, which could possibly explain the continuous signal between 13.5 and 13.9 eV. However, Yencha *et al.* [191] reported they were unable to detect any I^- formation in their photoabsorption ion yield study on HI in this energy region.

Detection of any H^- from the other two ion-pair dissociation limits given above would only occur at the dissociation limit as the H^- will carry away almost all the excess kinetic energy from the dissociation [192]. In conclusion, it seems unlikely that the detection of anions gives rise to the flat region between 13.5 and 13.9 eV and

the most likely origin of the signal is due to dissociative autoionisation of the Rydberg levels in this region.

6.3.2.*(d)* *The threshold photoelectron spectrum of HI from 10.2 to 11.5 eV*

Figure 6-8 shows the threshold photoelectron spectrum of hydrogen iodide between 10.2 and 11.5 eV. The line shapes of the X ($^2\Pi_{3/2}$) v^+=0,1,2 vibrational levels are distorted by autoionisation from Rydberg levels converging to the higher X ($^2\Pi_{1/2}$) ion limit. The final state ion vibrational levels are indicated at the top of Figure

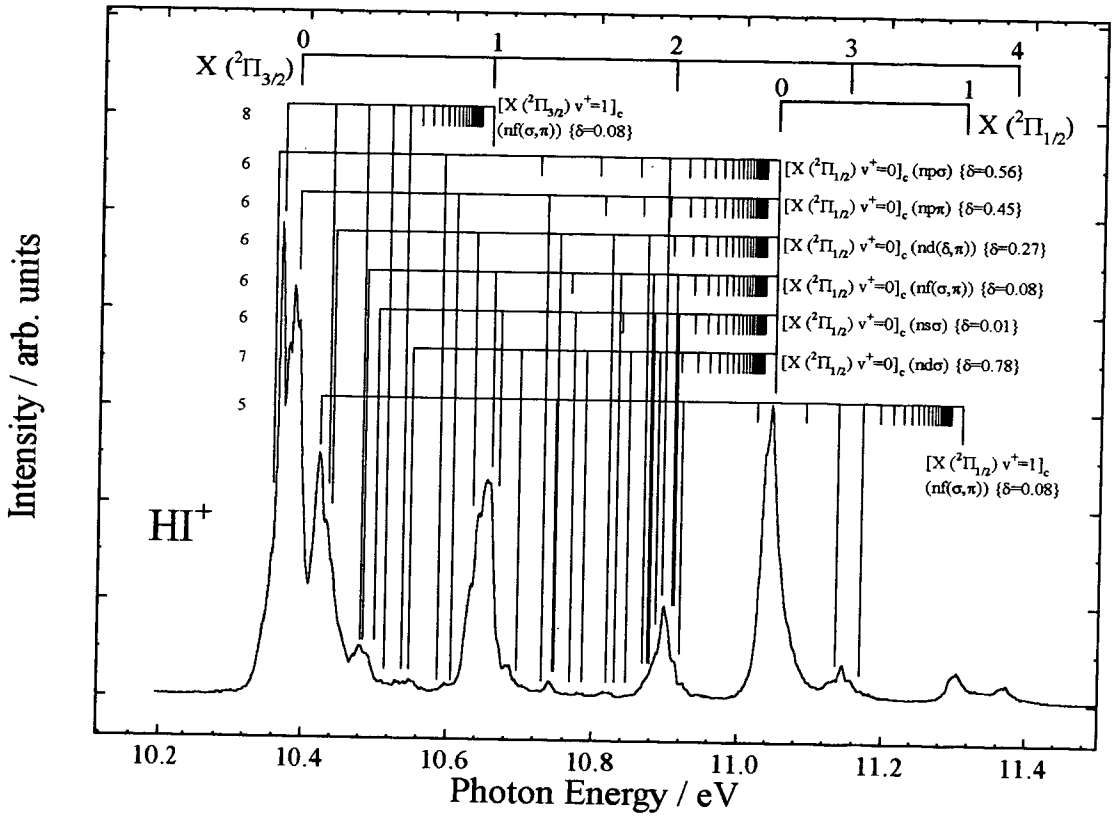

Figure 6-8 Threshold photoelectron spectrum of HI$^+$ between the X ($^2\Pi_{3/2}$) and X ($^2\Pi_{1/2}$) ionisation thresholds. The labels at the top of the figure indicate the final ion states, while the labels in the centre of the figure indicate the position of autoionising Rydberg levels. The quantum defects for the Rydberg series are taken from the work by Hart and Hepburn [164] and Mank *et al.* [161], and the numbers to the left of the Rydberg ladders correspond to the lowest quantum number of each Rydberg series plotted.

6-8 and the intermediate Rydberg series are plotted in the centre of the Figure. The quantum defects for the various Rydberg series are taken from the photoionisation studies by Hart and Hepburn [164] and Mank *et al.* [161], which are at much higher resolution than this present work.

It can easily be seen that all of the autoionising features present in the spectra can be assigned to intermediate Rydberg levels that autoionise to produce a near-threshold electron. It is possible that some of the autoionising Rydberg levels converge to higher levels than the X ($^2\Pi_{1/2}$) band origin. Two Rydberg series converging to the X ($^2\Pi_i$) v^+=1 levels are included in Figure 6-8 as they align well with spectral features not assigned to the six X ($^2\Pi_{1/2}$) v^+=0 series. However, the peak positions of autoionising levels in threshold photoelectron spectroscopy are not necessarily identical to those in photoionisation studies. In threshold photoelectron spectroscopy the extra criteria that the autoionisation process produces a threshold electron will in general distort the position of the autoionising Rydberg lines so the extra two series may be superfluous. As the resolution of the threshold spectrum is lower than the work by Hart and Hepburn [164], and Mank *et al.* [161] there is no real value in further analysing this part of the spectrum as it seems most of the features have been examined previously.

6.3.3 The inner valence ionisation region of hydrogen iodide

Figure 6-9 shows the threshold photoelectron spectrum of HI from 17 to 31 eV. The spectral features are very weak compared to the outer valence region as can be seen more clearly in Figure 6-3, this seems to be a common feature with the threshold photoelectron spectra (see HCl in Chapter 4, and HBr in Chapter 5). The resolution in the present spectrum (~22 meV at 21.0 eV) is somewhat better than the XPS (HeII) PES work by Adam *et al.* [157] though the signal to noise is lower here, however both spectra show similar features.

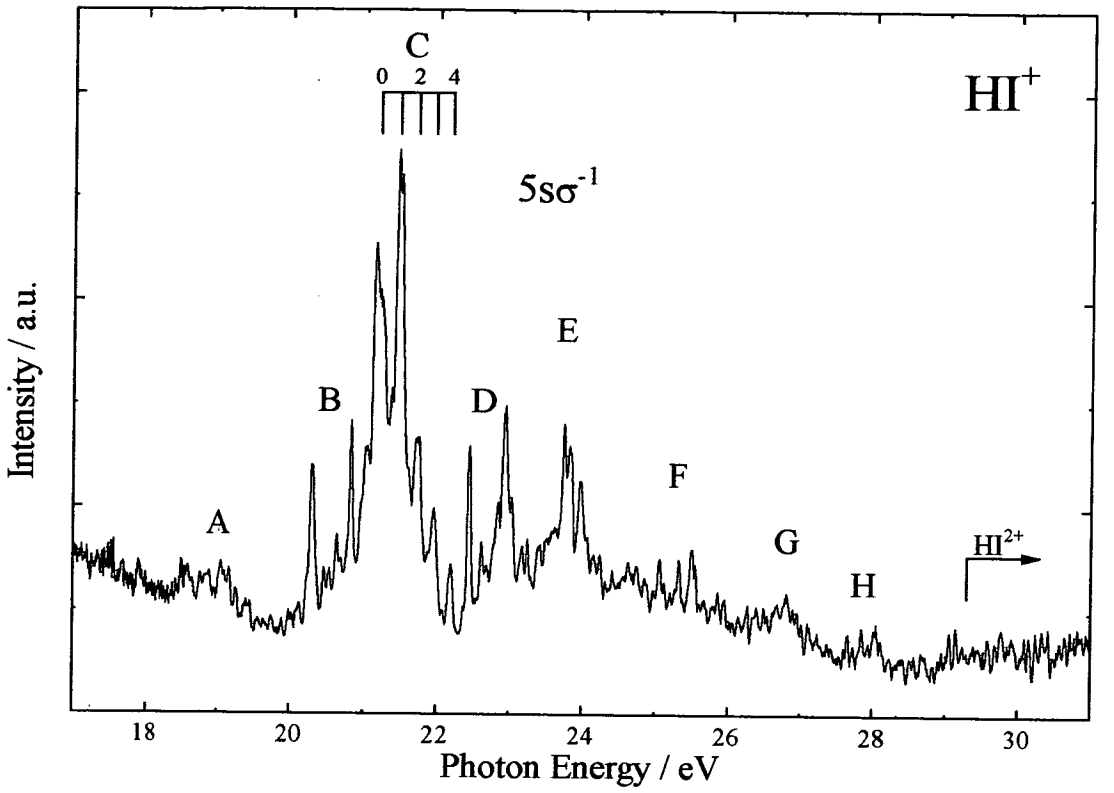

Figure 6-9 The threshold photoelectron spectrum of HI showing the $(5s\sigma)^{-1}$ ionisation region.

Eight distinct features are identified in Figure 6-9 below the double ionisation potential of HI at 29.29 eV [193], and are labeled A through H. Band systems A and F through H show no discernible peak structure. Band C is the most intense in the spectrum and is classified as the "main band" $(5s\sigma)^{-1}$ in common with the results of Adam *et al.* [157] and the Green's Function calculations Von Niessen *et al.* [194]. Five vibrational levels have been identified in Band C and are given in Table 6-5 along with the other peaks in the spectrum. A second order Dunham expression has been fitted to these five levels and the results are included in Table 6-3. Comparable results from Adam *et al.* [157] and Baltzer *et al.* [195] are also included. The new spectroscopic constants for the main band of the B ($^2\Sigma^+$) state are very similar to the X ($^2\Pi_i$) state as would be expected as both states involve the removal of an essentially non-bonding electron. Features A and B, and D through H are ascribed to various *two hole one particle* states $[(5s\sigma)^2,(5p\sigma)^2,(5p\pi)^2\ nl(\sigma,\pi)]$, however the poor signal

to noise characteristics of the spectrum are not conducive to further analysis of these regions. A clearer spectrum will be needed to identify the origin of the peaks.

6.4 Conclusions for the threshold photoelectron spectrum of hydrogen iodide

The threshold photoelectron spectrum of hydrogen iodide is still quite poorly understood even after this study. However, this work has produced a large amount of new data on the ion states of the molecule. Assignment of the spectra presented in this Chapter has led to the accurate prediction of the dissociation limits of the X ($^2\Pi_i$) states and vibrational levels have been observed over almost all of the potential well. This is also the first time that the X ($^2\Pi_i$) vibrational levels above v^+=2 have been unambiguously assigned.

The vibrational structure recorded in the A ($^2\Sigma^+$) state has a much smaller vibrational spacing than the previous work by Adam *et al.* [157]. Some simple perturbation calculations in this chapter suggest that the A ($^2\Sigma^+$) state dissociates to the [H (^{2}S) + I^+ ($^3P_0$)] dissociation limit instead of correlation to the [H (^{2}S) + I^+ ($^1D_2$)] dissociation products as in the case for HBr^+. A study of the same energy region in DI would help with the spectral analysis of the A ($^2\Sigma^+$) state and the inner valence region.

The continuous structure between the dissociation limit of the X ($^2\Pi_i$) state and the onset of the A ($^2\Sigma^+$) state is attributed to dissociative autoionisation of Rydberg levels converging to the A ($^2\Sigma^+$) state. These Rydberg states autoionise into the X ($^2\Pi_i$) state dissociative continuum. The sharp rise in the threshold electron signal at the X ($^2\Pi_i$) dissociation limit corresponds with the formation of I^+ at this energy as reported by Eland and Berkowitz [160], and the disappearance of any kinetic electron signal in the work by Böwering *et al.* [168]. One sharp peak in this structure has been assigned to the origin band of the autoionising [A ($^2\Sigma^+$)]8$d\pi$ $^1\Pi$

Rydberg state. Possible detection of anions as ion-pair dissociation products (H^-, I^-) is discounted as being responsible for the flat region between the two peaks.

Five vibrational levels have been identified in the B ($^2\Sigma^+$) ($(5s\sigma)^{-1}$) "main band" transition. A second order Dunham fit to these levels yields spectroscopic constants in good agreement with those for the X ($^2\Pi_i$) state. This is to be expected as both states are, to the first approximation, formed by the removal of a non-bonding electron. Further analysis of this spectral region must await results with better signal to noise characteristics.

From the results presented in this Chapter it seems possible that X ($^2\Pi_{1/2}$) ← A ($^2\Sigma^+$) fluorescence could be detected from the origin of the A ($^2\Sigma^+$) band. This may warrant a new study of the ion fluorescence in this energy region. These results also show the usefulness of threshold photoelectron spectroscopy in the examination of weak ionisation features. For instance, the absorption work by Terwilliger and Smith [171] between 1040 and 860 Å observed only one Rydberg level. In the threshold spectrum an entire series or Rydberg levels are seen (indirectly) converging to the A ($^2\Sigma^+$) state.

The results presented here show that there is still a lot to be understood about the valence ionisation of hydrogen iodide. In particular it seems a single photon XUV ZEKE study [196] over the entire outer valence region would be extremely worth while.

6.5 Tables of results for hydrogen iodide

Table 6-1 Observed and calculated vibrational band head positions (in eV) for the transitions: e + HI^+ ($X\ ^2\Pi_i$, v') ← HI ($X\ ^1\Sigma^+$, v''=0)

	$^2\Pi_{3/2}$, transition energy		$^2\Pi_{1/2}$, transition energy	
v'	obs[a]	calc	obs[a]	calc
0		10.388	11.047	11.045
1	10.652	10.651	11.307	11.310
2	10.901	10.903	11.561	11.562
3	11.145	11.145	11.803	11.801
4	11.375	11.377	12.032	12.031
5	11.601	11.599	12.252	12.251
6	11.815	11.811	12.460	12.461
7	12.012	12.013	12.660	12.661
8	12.202	12.204	12.848	12.850
9	12.384	12.386	13.024	13.024
10	12.556	12.556	13.181	13.181
11	12.716	12.716	13.319	13.316
12	12.864	12.864	13.423	13.425
13	13.000	12.999		
14	13.122	13.121		
16	13.319	13.323		
17	13.401	13.400		
Limit [b]		13.529		13.543

[a] Uncertainty ±0.004 eV.
[b] Determined by extrapolation of fit expressions.

Table 6-2 Observed and calculated band head positions (in eV) for the transitions: e + HI^+ ($A\ ^2\Sigma^+$, v') ← HI ($X\ ^1\Sigma^+$, v''=0)

	Transition Energy	
v'	obs [a]	fit
0	13.958	13.958
1		14.023
2	14.084	14.084
3	14.142	14.142
4	14.198	14.197
5	14.248	14.248

[a] Uncertainty ±0.004 eV.

Table 6-3 Summary of spectroscopic constants (in eV) derived from the analysis of the HI TPES data presented here and from literature data

State	Ionisation Energy [a]	ω_e	$\omega_e x_e$ /10^{-3}	$\omega_e y_e$ /10^{-5}	$\omega_e z_e$ /10^{-6}	Ref.
$HI^+ X (^2\Pi_{3/2})$	10.388[b]	0.2737	-5.61	8.31	-3.95	this work
	10.386[c]	0.2797	-7.27			[168]
	10.385(13)	0.2921	-12.1	39.1[d]		[169]
	10.384					[157]
	10.386(1)					[164]
	10.386(1)					[160]
$HI^+ X (^2\Pi_{1/2})$	11.045(4)	0.2833	-9.77	68.3	-3.4	this work
	11.05[c]	0.2789	-6.30			[168]
	11.046(19)	0.3047	-12.8			[169]
	11.048					[157]
	11.051(1)					[164]
	11.0495(10)					[160]
	11.0481(1)[e]					[167]
	11.04802[f]					[161]
$HI^+ A (^2\Sigma^+)$	13.958(4)	0.0682	-1.70			this work
	13.97					[157]
	14.00					[172]
$HI^+ B (^2\Sigma^+)$	21.20(1)	0.2781	-6.57			this work
("main" band)	21.23					[157]
("main" band)	21.23	0.188	~0.00			[195]

[a] Experimental (0-0) transition value unless otherwise noted.
[b] Determined from fitting procedure.
[c] Quoted in [169].
[d] Determined from third-order fit of published data.
[e] Rydberg convergence limit for $v^+=0$, $J^+=1/2$, f
[f] Rydberg convergence limit for $v^+=0$, $J^+=1/2$, e

Table 6-4 Franck-Condon calculations for the formation of the adiabatic A ($^2\Sigma^+$) state of HI^+ (see Figure 6-6 and Figure 6-7): e + HI^+ (A $^2\Sigma^+$, v') ← HI (X $^1\Sigma^+$, v''=0), also a second order Dunham fit to the energies.

Vib	Energy / eV	FC Intensity	Vib	Energy / eV	FC Intensity
0	13.95856	0.10257	5	14.24816	0.98753
1	14.02414	0.33686	6	14.29558	0.85326
2	14.08511	0.62684			
3	14.14245	0.86993	$\omega_e = 0.0682$ eV		
4	14.19683	1	$\omega_e x_e = -1.725\times10^{-3}$ eV		

Table 6-5 Band system maxima or band head positions of observed transitions (in eV) from HI X ($^1\Sigma^+$, v''=0) to states of HI^+ identified in Fig. 3 compared with states and binding energies (in eV) of HI^+ from the HeII PES and Al K_α XPS study of HI [157] in the same energy region as in Figure 6-9.

Band System	v^+	Transition Energy [a]	State [b]	v^+	Binding Energy
A		19.0	1		19.0
B		20.29	a		20.29
		20.83	b		20.85
			c		
C	0	21.20[c]	2	0	21.23
	1	21.47[c]		1	21.44
				(2)	21.64
	2	21.72[c]		(3)	21.73
	3	21.96[c]		(4)	21.87
	4	22.19[c]			
D		22.44	3a		22.47
			3b		22.65
		22.93	3c		22.88
			3d		23.05
E		23.53[d]	4a		23.60
		23.73	4b		23.77
		23.81	4c		23.88
		23.97	4d		24.01
F		25.3	5		25.7
G		26.9	6		27.0
H		28.0	7		28.0

[a] Uncertainty ±1 in the last digit.
[b] Combined HeII PES and Al K_α XPS results [157]
[c] Peak centroid.
[d] Shoulder.

Chapter 7. Fluorine

7.1 Introduction

As would be expected for a small and important molecule like fluorine it has been the subject of numerous experimental and theoretical studies in the past. So much so that the electronic states of fluorine and its cation have previously been studied by absorption spectroscopy [197],[198],[199], electron energy-loss spectroscopy [200[,[201],[202], photoionisation mass spectrometry [203],[204], [205], emission spectroscopy [206],[207], photoelectron spectroscopy [208],[209], [210], [211], [212], [213], threshold photoelectron spectroscopy [214], resonance-enhanced multi-photon ionization spectroscopy [215], and by theory [201],[211], [212],[216],[217]. However, in spite of all these experimental and theoretical studies, the electronic states of fluorine and its cation still are not well-understood by comparison with the heavier diatomic halogens. This is particularly true of the ion states of fluorine owing to experimental difficulties due to their high formation energies.

At present the most recent experimental report on the electronic states of F_2^+ is the high-resolution HeI photoelectron spectroscopic study of van Lonkhuyzen and de Lange [213]. van Lonkhuyzen and de Lange [213] observed, for the first time, vibrational structure in the A ($^2\Pi_{i,u}$) band system and resolved the spin-orbit split vibrational progressions. In this study they observed and assigned the adiabatic ionization energies of both the X ($^2\Pi_{i,g}$) and A ($^2\Pi_{i,u}$) states of F_2^+, confirming the vibrational numbering given by Tuckett *et al.* [207] in their jet cooled A ($^2\Pi_{i,u}$)→X ($^2\Pi_{i,g}$) emission study of F_2^+. The vibrational assignments given by Tuckett *et al.* [207] were based on Franck-Condon intensity fits to the experimentally measured

vibrational intensities and resulted in re-assignments of the vibrational numbering in the previous room temperature A→X emission study by Porter [206]. Although jet cooling of the molecular beam allowed for easier vibrational assignments, much of the rotational band structure was lost, so Tuckett *et al.* [207] combined their data with the room temperature spectrum by Porter [206]. The HeI PES study by van Lonkhuyzen and de Lange [213] also observed vibrational structure in the B ($^2\Sigma_g^+$) band system of F_2^+ for the first time. This allowed the calculation of the equilibrium distance of the B ($^2\Sigma_g^+$) state of F_2^+ using Franck-Condon fits to the experimental data.

Cartwright and Hay [217] have performed a detailed theoretical study of the potential energy curves of F_2 and F_2^+ using configuration interaction calculations and this has yielded further spectroscopic constants in good agreement with the A ($^2\Pi_{i,u}$) →X ($^2\Pi_{i,g}$) emission work by Tuckett *et al.* [207]. These calculations also predict the position of three weakly bound states of F_2^+ which are possibly seen in our TPE spectrum (see section 7.3.3) and also the geometry of the B ($^2\Sigma^+$) state which has so far only been determined by Franck-Condon simulations [213].

7.2 Special experimental details

Recent studies within this group on the TPES of the heavier members of the halogen series, Cl_2 and Br_2 [218], and I_2 [219], have been very successful and it is natural to extend the study to complete the homologous series. However, the risks involved in handing fluorine are much larger than those of the other halogens due to its extreme chemical reactivity and as such it is worth detailing the specific experimental methods for this study.

The fluorine source used was a recently developed self regulating electrochemical cell on hire from the BNFL Electrogas Business [220]. The cell electrolyzes a 1:2 mixture of molten potassium fluoride and hydrogen fluoride yielding greater than 99% purity fluorine at a pressure typically 10 mBar above ambient atmospheric pressure. Volatile hydrogen fluoride was removed from the fluorine

stream using a sodium fluoride trap, however a small amount of argon persists in all spectra as it was used to purge the cell during the initialization procedure. The hydrogen by-product was diluted with argon then vented to atmosphere. Once the cell is initialized, internal level probes regulate the electrolysis current ensuring the fluorine supply pressure does not vary significantly.

Care had to be taken to ensure the rate of fluorine production exceeded that of consumption by the experiment as the fluorine side of the cell is effectively connected to vacuum whilst the hydrogen side is open to atmosphere. Both waste and exhausted fluorine gas was scrubbed by a combination of activated alumina and activated charcoal filter elements. After about 24 hours continuous operation the cell begins to produce a impurity with a threshold photoelectron spectrum similar to CF_4 [221]. When impurities became apparent in the spectra the cell was purged and re-started, the impurities may have been a consequence of the low duty cycle of the cell during data collection.

7.3 Results and Discussion

7.3.1 General overview of the threshold photoelectron spectrum of molecular fluorine

The overall TPE spectrum of F_2 was generated by taking several single-scan spectra of a portion of the full energy range studied. After the normalization of each scan for the intensity of the light source, scans were summed and joined to other parts of the spectrum. The resolution of the overall TPE spectrum was determined to be $\Delta E/E = 7.53 \times 10^{-4}$ (i.e. ΔE = 12.0 meV at 15.937 eV) and was determined to be largely controlled by the bandwidth of the photon source, in this case the photon bandpass was fixed at 1.00 Å corresponding to an energy resolution of 10.0 meV at 15.937 eV. Higher resolution TPE spectra were recorded over a portion of the full energy range studied. The resolution of these spectra is shown in the relevant figure captions.

The overall TPE spectrum of F_2 covering the photon energy range of 15.6-21.9 eV is shown in Figure 7-1. It displays the three band systems of F_2^+ for the formation of the X ($^2\Pi_{i,g}$), (A $^2\Pi_{i,u}$), and B ($^2\Sigma_g^+$) states known from PES [213] resulting from the removal of a π_g, π_u^*, and σ_u electron. Figure 7-2 shows a potential energy diagram constructed from work by Colbourn *et al.* [198], Tuckett *et al.* [207], van Lonkhuyzen and de Lange [213], and this present work, which is useful in the following general discussion and the rest of this chapter. The classical turning points of the X $^1\Sigma_g^+$ v = 0 wavefunction are indicated in Figure 7-2 showing the Franck-Condon window into the three bound ionic states. Two representative Rydberg states are also included to illustrate the autoionisation processes discussed later in this chapter.

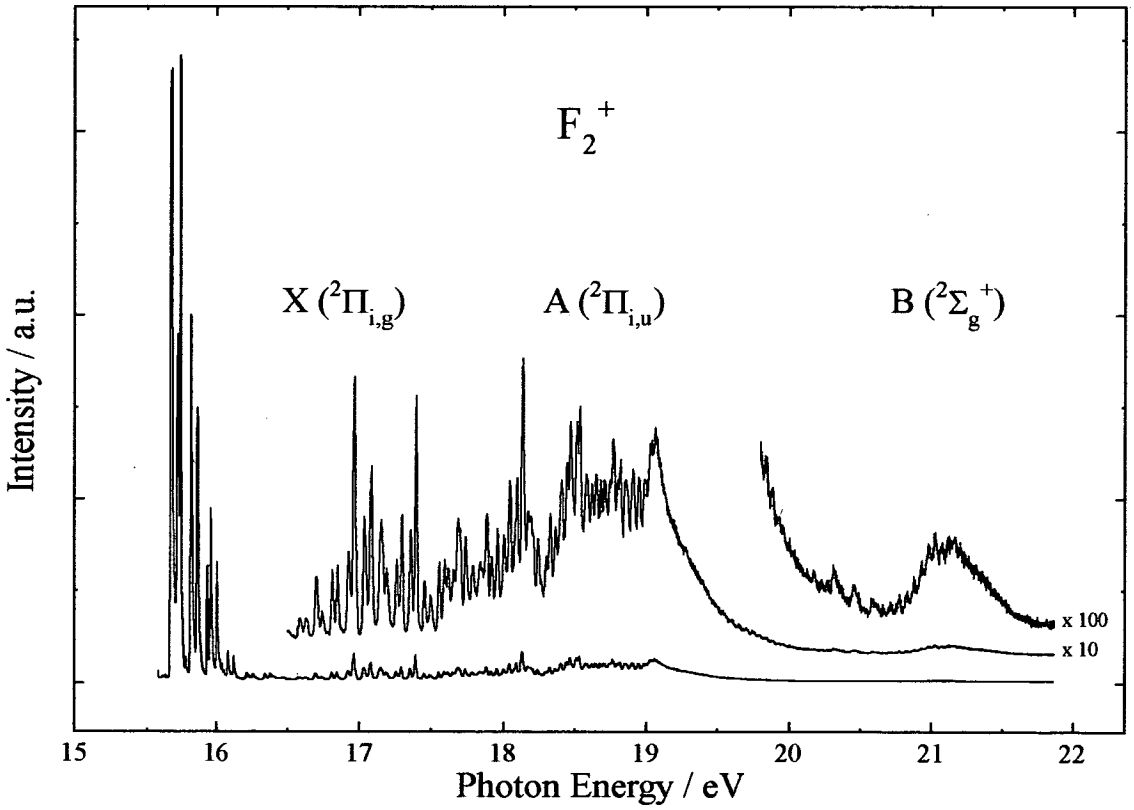

Figure 7-1 Overall threshold photoelectron spectrum of fluorine showing the bands due to formation of the X ($^2\Pi_{i,g}$), and A ($^2\Pi_{i,u}$) and B ($^2\Sigma_g^+$) states of F_2^+. The energy resolution of this spectrum is $\Delta E/E = 7.53 \times 10^{-4}$, i.e., ΔE = 12 meV at 15.937 eV (Ar ($^2P_{1/2}$)).

From Figure 7-1 two features of the spectra are clearly apparent. Firstly, nearly all the spectral intensity resides in the lower vibrational levels of the X ($^2\Pi_{i,g}$) state, as can be seen in the lowest trace in Figure 7-1. Secondly, there is extensive vibrational structure in the non-Franck-Condon regions of the X ($^2\Pi_{i,g}$) and A ($^2\Pi_{i,u}$) states. This is especially true in the non-Franck-Condon region of the X ($^2\Pi_{i,g}$) state. The high intensity of the lowest vibrational levels of the X ($^2\Pi_{i,g}$) state is due to efficient vibrational autoionisation of vibrationally excited Rydberg states into the ion continua of lower vibrational levels. This effect has been observed in photoionisation studies by Berkowitz *et al.* [205] in the region just above the onset of ionisation.

The extended vibrational structure between the X ($^2\Pi_{i,g}$) and A ($^2\Pi_{i,u}$) states is probably due to the resonance autoionisation from Rydberg states converging on the A ($^2\Pi_{i,u}$) state into vibrationally excited levels of the X ($^2\Pi_{i,g}$) state ion. The vibronic structure between the Franck-Condon regionsof the A ($^2\Pi_{i,u}$) and B ($^2\Sigma_g^+$) states is probably a result of initial excitation into a Rydberg level converging to the B ($^2\Sigma_g^+$) state followed by autoionisation into the purely repulsive parts of either the X ($^2\Pi_{i,g}$) or A ($^2\Pi_{i,u}$) states. The autoionisation process from a [B ($^2\Sigma_g^+$)] $nl\lambda$ Rydberg state into the X ($^2\Pi_{i,g}$) or A ($^2\Pi_{i,u}$) state ion may occur via a neutral repulsive intermediate as in the model by Guyon *et al.* [33]. However, information proving or disproving the Guyon model is not available in the current results.

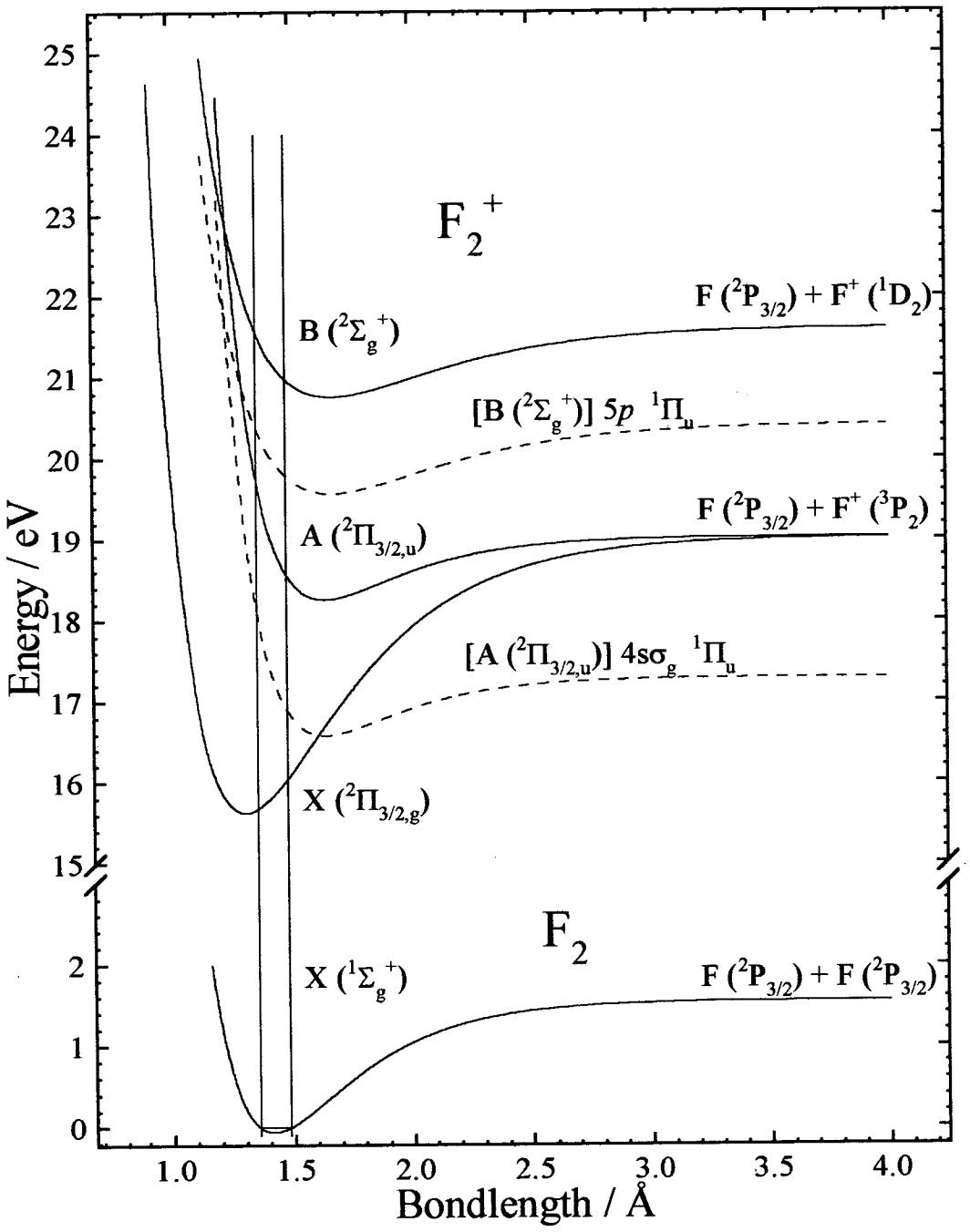

Figure 7-2 Potential energy diagram for the optically accessible states of F_2^+. Rydberg states converging on the A and B states are included as possible intermediate states for autoionisation processes. Spectroscopic data used to generate this diagram is taken from [198],[207],[213], and this work.

7.3.2 The high-resolution TPES of F_2 in the 15.68-15.95 eV range

Figure 7-3 shows a high-resolution (3.0 meV) threshold photoelectron spectrum of F_2 over the energy range covering the first two vibrational bands (v^+= 0,1) of both spin-orbit components (Ω = 3/2, 1/2) of the X ($^2\Pi_{i,g}$) band system of F_2^+. The positions of the ionic levels are indicated at the top of the figure. Also indicated are the Rydberg series converging to vibrationally excited levels of the X ($^2\Pi_{i,g}$) core. Rydberg states that are probably distorting the vibrational bands in the threshold photoelectron spectrum are indicated with long vertical lines. The quantum defect for each Rydberg series has been fitted using the vibrational peak positions in Table 7-1 for the Rydberg convergence limits and the quantum defect of each series was

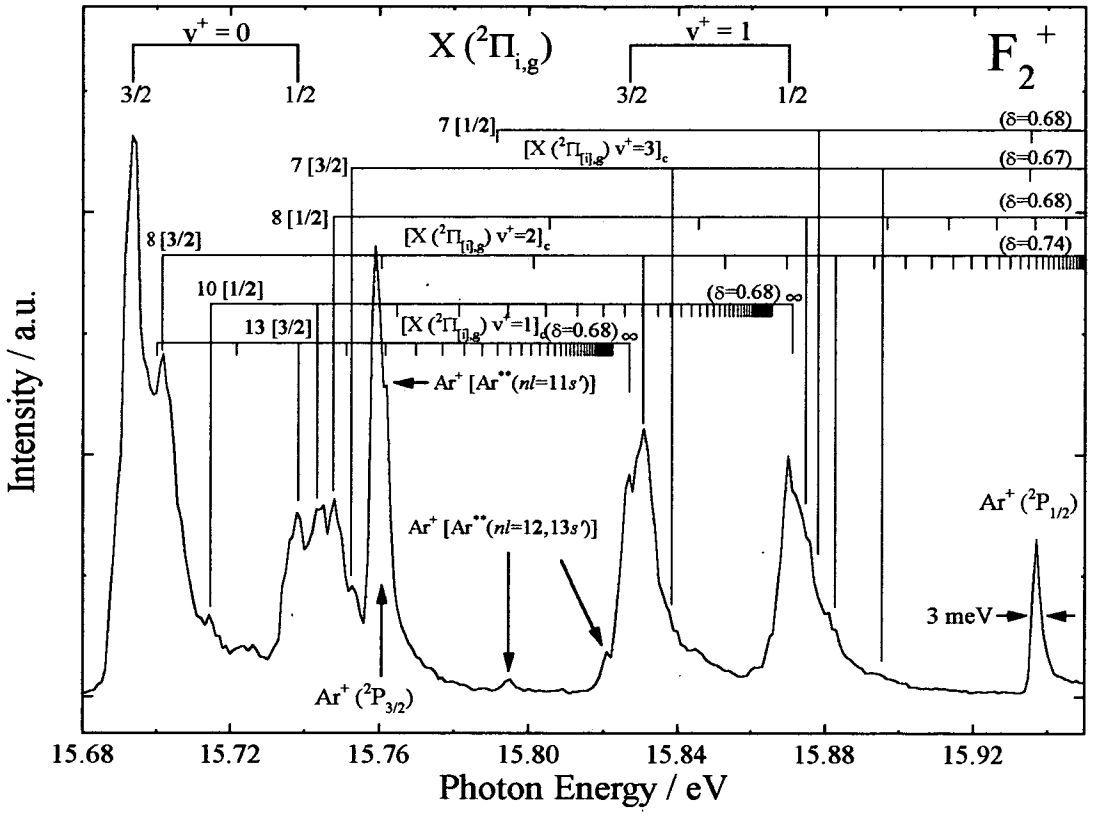

Figure 7-3 High resolution threshold photoelectron spectrum of the X ($^2\Pi_{i,g}$) v^+=0,1 bands of F_2^+. The true ion positions are shown at the top of the figure, whereas in the middle of the figure the position of autoionising Rydberg levels are identified. The resolution of the spectrum is 3 meV measured at the Ar ($^2P_{1/2}$) ionization line.

adjusted to fit the unassigned peaks in the spectrum.

The argon ($^2P_{1/2}$) ionization peak in Figure 7-3 establishes the effective resolution in the spectrum at 3.0 meV, exactly the photon resolution of the monochromator. This shows that the penetrating-field electron spectrometer has a negligible effect on the resolution of the spectrum. The observation of a high-energy shoulder on the main Ar^+ ($^2P_{3/2}$) line also establishes that the spectrometer is detecting electrons within ~3 meV of threshold (see Chapter 2). The adiabatic ionisation energy of fluorine is obtained from this spectrum as 15.693 ± 0.001 eV. This agrees well with the previous, lower resolution TPE result of 15.694 eV [214], which was obtained in a rather novel way (by dividing the threshold photoelectron signal by the total positive ion signal), and is only slightly below the PES finding of 15.697 eV [213]. The ionic data derived from the spectrum is presented in Table 7-1.

More thorough examination of Figure 7-3 shows that the 3/2 component is more intense than the 1/2 component for both vibrational levels. In non-resonant photoionisation a branching ratio of 1:1 is found between the two spin-orbit components [16]. The enhancement in the 3/2 component in the TPE spectrum is probably a result of spin-orbit autoionisation occurring between the two spin-orbit limits. Figure 7-4 shows a potential energy diagram for this energy region in F_2^+ to illustrate the autoionising effects seen in Figure 7-3. To the right of the two Morse curves in Figure 7-4 there are eight Rydberg series converging on various ionic cores of the X ($^2\Pi_{i,g}$) state. A quantum defect of 0.68 has been used to simulate these series up to n=50. If initially one only considers the two Rydberg series converging on the Ω=3/2,1/2 sub-states of the band origin, then many of the Rydberg levels converging to the higher energy spin-orbit sub-state have sufficient energy to autoionise into the lower sub-state ion continuum. This suggests the threshold signal associated with the lower Ω=3/2 level will be more intense than the higher energy Ω=1/2 if a Rydberg level converging on the Ω=1/2 spin substate is suitably isoenergetic with the Ω=3/2 ionization threshold. However, the Rydberg manifold converging to the 1/2 core is quite dense at the 3/2 core ionization potential (the

separation between successive Rydberg levels is ~5 meV at this point). So, if a rotational contour for each Rydberg level is also considered, the enhancements due to each specific Rydberg level would overlap in energy and give rise to a more intense 3/2 peak, but the enhanced peak would show no structure from the intermediate Rydberg states as the states are too closely spaced to be resolved.

When the Rydberg *ladders* converging on $v^+=1$ are included in this discussion it is easily seen that both spin-orbit and vibrational (and the two combined) autoionisation is energetically allowed. The observation from Figure 7-3 that the $v^+=0$ bands are stronger than the $v^+=1$ bands conflicts with the HeI PES work by van

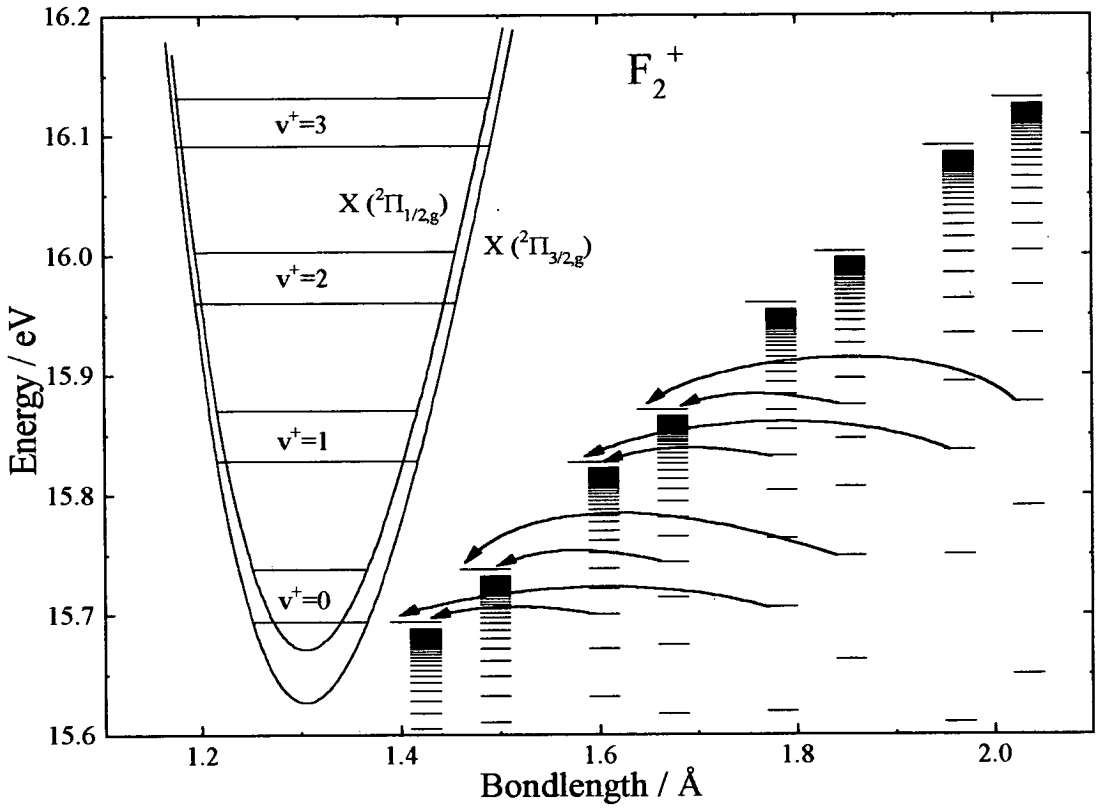

Figure 7-4 Potential energy diagram for the X $^2\Pi_{i,g}$ $v^+=0,1$ bands of F_2^+. The Morse curves are generated as in Figure 7-2. Rydberg series converging on the eight ionic limits are plotted ($\delta=0.68$) showing the differing autoionisation channels open to each Rydberg level converging to each ionization limit. The most dominant ionization channels in Figure 7-3 are indicated by the arrows.

Lonkhuyzen and de Lange [213] (which also includes Franck-Condon simulations) showing appreciable vibrational autoionisation occurs in the TPE spectrum. In fact the majority of the small peaks and shoulders in Figure 7-3 can be assigned to purely vibrationally autoionising Rydberg levels converging to vibrationally excited ion cores. The assignments in Figure 7-3 are based on the best fit of the Rydberg structure in this spectrum to the multiple Rydberg series (X $(^2\Pi_{3/2,1/2,g})$ v^+=0,1,2,3) using a constant quantum defect. These calculated quantum defects are in good agreement with the vacuum ultraviolet absorption work on F_2 by Cole and Margrave [199] ($\delta_{np\pi}$=0.74, $\delta_{np\sigma}$=0.66). From the Rydberg assignments is seems that the predominant autoionisation mechanism is purely vibrational, with a loss of 1 or 2 vibrational quanta, and occasionally a combination of both vibrational and spin-orbit autoionisation. The main autoionisation routes are indicated by the curved arrows in Figure 7-4. Close examination of the Rydberg levels using Figure 7-3 allows the observation that Rydberg levels and ion levels with the same Ω value tend to lie in closer proximity than Rydberg and ions with differing Ω values, so the detection efficiency of the autoionisation events which maintain Ω will be highest. (The autoionising peak positions and assignments are given in Table 7-5.)

The photoabsorption cross section of successive members of a Rydberg series scales as n^{*-3} [7] (where $n^* = n - \delta$), so lower principal quantum numbers will give rise to the highest photoabsorption cross sections. In the present case this would suggest that Rydberg series converging on higher excited vibrational levels would lead to even stronger autoionisation peaks in the threshold photoelectron spectrum - if they were suitably isoenergetic with a final ion level. However, the Franck-Condon factors for these higher vibrational levels are very small (see [213]), so there is little point in trying to assign the autoionising features as arising from higher vibrational quantum numbers.

7.3.3 The TPES of F_2 in the 15.6-19.4 eV range

Figure 7-5 shows part of the threshold photoelectron spectrum of F_2^+ covering the X ($^2\Pi_{i,g}$) and A ($^2\Pi_{i,u}$) states. The resolution of the spectrum is 12.0 meV, as measured on the *in-situ* Ar^+ ($^2P_{1/2}$) line at 15.937 eV (marked with an asterisk in Figure 7-5). Clearly, the spectrum shows extensive vibrational structure in non-Franck-Condon region. This extended vibrational structure is most probably due to resonance autoionisation of Rydberg states of F_2 present in this energy region, in common with the TPE spectra of the heavier halogens [218],[219].

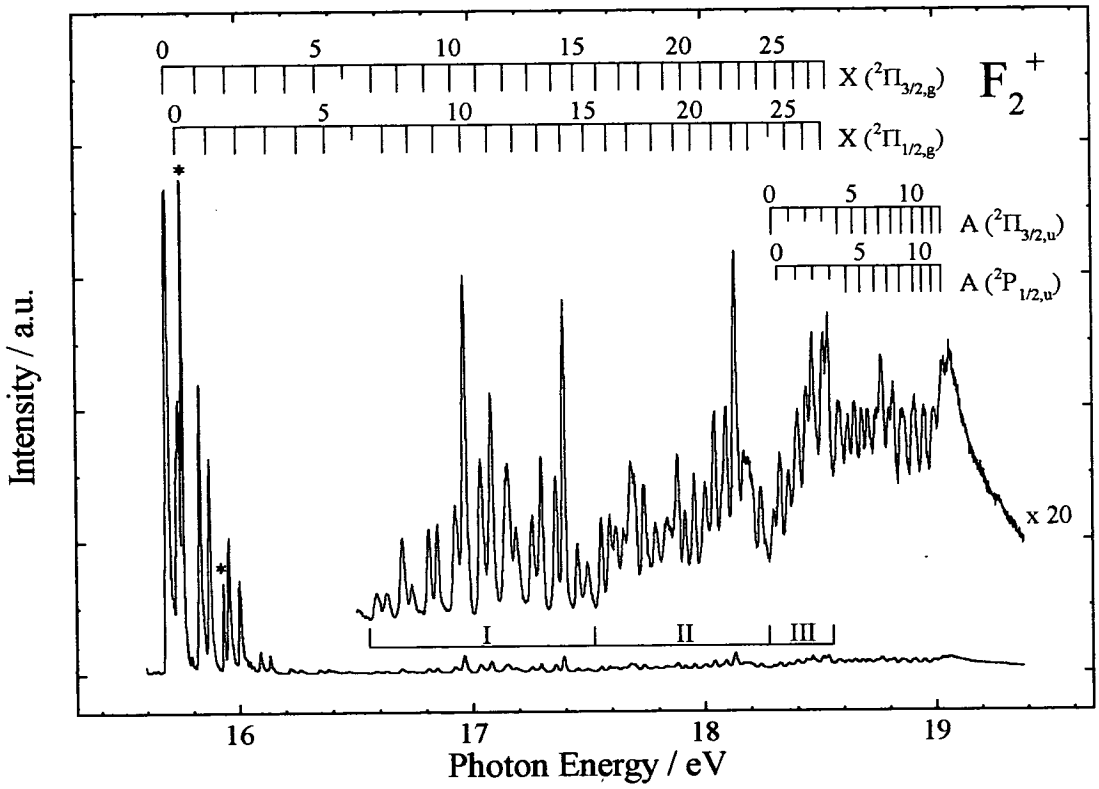

Figure 7-5 Broad view of the X ($^2\Pi_{i,g}$), and A ($^2\Pi_{i,u}$) threshold photoelectron band systems of F_2^+ with the assignment of the observed vibrational progressions. The peaks marked with the asterisks (*) are the argon ion doublet peaks at 15.759 eV ($^2P_{3/2}$) and 15.937 eV ($^2P_{1/2}$). The resolution of this spectrum is the same as in Figure 7-1 (e.g., ΔE = 12.0 meV at 15.937 eV).

Three distinct regions of intensity are marked below the upper curve of Figure 7-5. These regions probably reflect the autoionisation contribution of three or more Rydberg states lying in the energy region. System III appears to be prematurely terminated at the prominent onset of A ($^2\Pi_{i,u}$) ion-state formation by direct photoionisation. This energy range (~16.6-18.6 eV) shows extensive autoionisation structure in the photoionisation yield spectrum of F_2 (Berkowitz *et al.* [205]), and was similarly attributed to a Rydberg series converging on the A ($^2\Pi_{i,u}$) ion state. The quantum defect of the Rydberg series can be estimated from the apparent onset of system I at ~16.6 eV and the adiabatic ionization potential of the A ($^2\Pi_{3/2,u}$) state at 18.300 eV, yielding n^*=2.8 ($n^* = n-\delta$), suggesting δ=1.2 . This value is in agreement with previous results in the threshold photoelectron spectroscopy of Cl_2 [218], and is close to the calculated quantum defect for an s-type Rydberg series in atomic fluorine of ~1.3 [223]. So, the vibrational intensity distributions, I, II, and III, can be assigned (tentatively) to the Rydberg states $[(\sigma_g)^2(\pi_u)^3(\pi_g^*)^4]_i$ $ns\sigma_g$ $^1\Pi_u$, where n = 4, 5, and 6. Figure 7-2 includes a Rydberg state produced using the spectroscopic parameters for the A ($^2\Pi_{i,u}$) state with principal quantum number n=4 and quantum defect δ=2.

The vibrational structure in the X ($^2\Pi_{i,g}$) band system is shown in Figure 7-5. The half-length tick marks indicate no assigned peak due to low peak intensity. The measured peak positions are listed in Table 7-1 together with calculated peak positions based on a second order vibrational Dunham fit [1]. Similarly, the A ($^2\Pi_{i,u}$) band system has been assigned in Figure 7-5 and the experimental and calculated peak positions tabulated in Table 7-2. The spectroscopic constants for the X ($^2\Pi_{i,g}$) and A ($^2\Pi_{i,u}$) states of F_2^+ derived from the fitted data in Table 7-1 and Table 7-2 are given in Table 7-3 where they are compared with similar data taken from the literature. The agreement between the present results and those of the literature is quite good.

There is considerable spectral congestion above 17.55 eV in Figure 7-5 so a higher resolution threshold photoelectron spectrum (8.8 meV at 18.25 eV) was recorded from 17.5eV to19.2 eV. This spectrum is shown in Figure 7-6. The last two vibrational peak structures observed in Figure 7-6 occur at v^+=13 (19.03 eV) in the A ($^2\Pi_{3/2,u}$) subsystem and at v^+=12 (19.021 eV) in the A ($^2\Pi_{1/2,u}$) subsystem. They are followed by a rise in the spectrum at 19.056 eV corresponding to the point of complete break-off of vibrational structure. The vertical arrows in Fig. 3 indicate the thermodynamic dissociation limits for [F ($^2P_{3/2}$) + F^+ ($^3P_2$)] formation at 19.025 eV and for [F ($^2P_{1/2}$) + F^+ ($^3P_2$)] formation at 19.075 eV, calculated as follows: The dissociation energy of molecular fluorine (X ($^1\Sigma_g^+$)) was taken from the absorption work by Colbourn *et al.* [198] as D_o = 1.602 eV, the first ionization potential of atomic fluorine was taken from Huffman *et al.* [222] as F^+ $^3P_2$ = 17.423 eV, and the

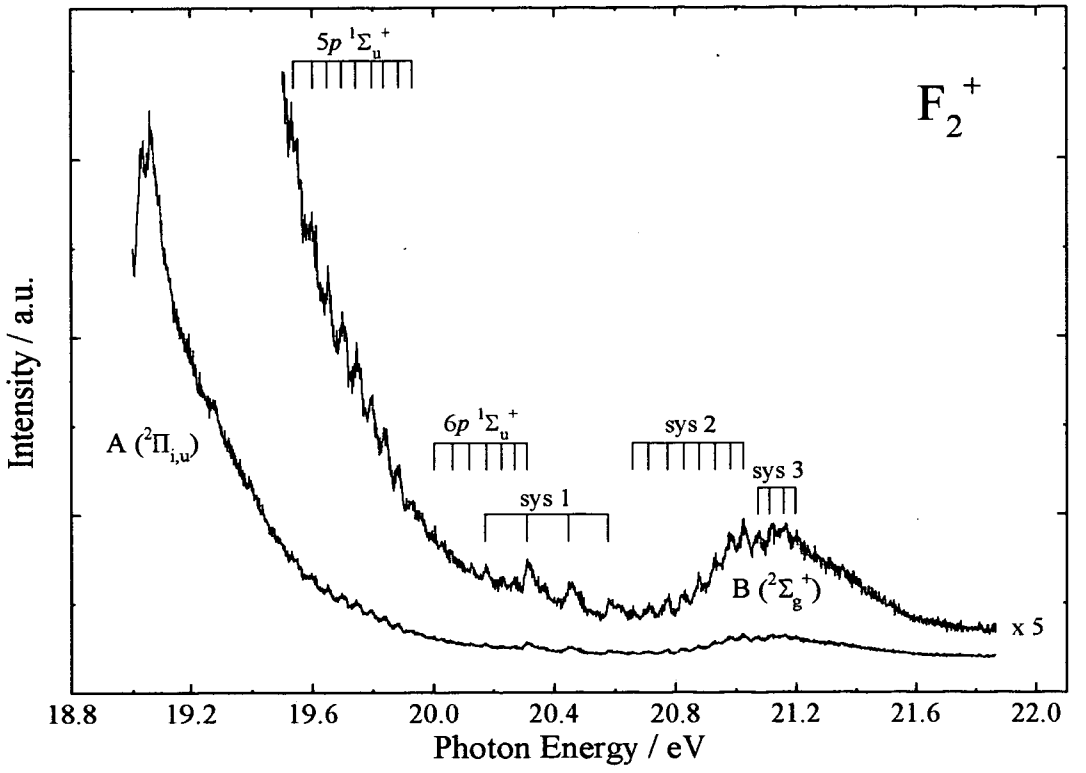

Figure 7-6 An expanded view of a portion of the X ($^2\Pi_{i,g}$) and A ($^2\Pi_{i,u}$) ion states of F_2^+ at a slightly higher resolution ($\Delta E/E = 4.82 \times 10^{-4}$, i.e., ΔE = 8.8 meV at 18.25 eV) than that shown in Figure 7-5.

spin orbit separation of the fluorine atom from Moore [223] as F ($^2P_{3/2}$) — F ($^2P_{1/2}$) = 0.050 eV.

A few of the peaks in Figure 7-6 are not identified as belonging to either the X ($^2\Pi_{i,g}$) or A ($^2\Pi_{i,u}$) band systems. These have been marked with asterisks. These peaks cannot be assigned to the normal impurities commonly found in fluorine [224] (e.g. N_2 [225], O_2 [226], HF (Chapter 3), OF_2 [227], and CF_4 [221]), so they may belong to fluorine. The potential energy curves of F_2^+ calculated in configuration interaction work by Cartwright and Hay [217] can be used to gain an insight into the electronic states of F_2^+. Cartwright and Hay [217] calculate there are three bound doublet states ($^2\Sigma_u^+$, $^2\Sigma_g^-$, and $^2\Delta_u$) in this energy region. Although photoionisation into these three bound states would be optically allowed from the ground state of F_2, it is unlikely that the bound portions of the states would lie in the Franck-Condon region due to their considerably larger equilibrium bondlengths. For example, the r_e values for these potentials have been calculated to be 1.80 Å ($^2\Sigma_u^+$) [217], 1.80 Å ($^2\Sigma_g^-$) [216], and 1.775 Å ($^2\Delta_u$) [217], respectively, while the r_e of the ground state of F_2 is 1.4118 Å [198]. However, it is possible that these states could be accessed via intermediate neutral Rydberg states lying in this energy range that could then autoionise and appear in the TPE spectrum. It is not possible to identify any regular vibrational features from the asterisked peaks in Figure 7-6 because of considerable spectral congestion. However, some of the peak separations do approximately correspond to the vibrational separations that might be expected based on the computed vibrational constants [216],[217]. The peak positions of these unidentified features are given in Table 7-4.

A further feature of interest in both Figure 7-5 and Figure 7-6 is the sharp cut-off in the X ($^2\Pi_{i,g}$) vibrational progression at ~ 18.5 eV, from this point onwards only the A ($^2\Pi_{i,u}$) state is observed. This system is the first threshold photoelectron study completed in this group where vibrational levels associated with the X state of a molecular ion are still accessed once the A state of the ion is energetically accessible. In fact, in the 18.3 - 18.5 eV energy region, there seems to be a propensity to

autoionise by electronic rearrangement of the ion core as opposed to purely vibrational or spin-orbit autoionisation. This autoionisation event seems to favour a $\sigma_g^2\pi_u^3\pi_g^{*4} \rightarrow \sigma_g^2\pi_u^4\pi_g^{*3}$ core electron rearrangement over maintaining the original $\sigma_g^2\pi_u^3\pi_g^{*4}$ configuration. So the ionization event must involve the correlated rearrangement of two electrons. Purely vibrational autoionisation would only require energy exchange between the ion core and the Rydberg electron and although spin-orbit autoionisation will also involve two electrons, only the vector coupling of the core electron orbital and spin angular momentum is modified, not the actual electron configuration.

It would be useful to explain why this propensity for electronic autoionisation seems to occur. The Franck-Condon simulations of the A ($^2\Pi_{i,u}$) state by van Lonkhuyzen and de Lange [213] show that there is appreciable oscillator intensity even in the dissociative continuum. So, the disappearance of the X ($^2\Pi_{i,g}$) state cannot be explained by lack of a curve crossing of the X ($^2\Pi_{i,g}$) state and a [A ($^2\Pi_{i,u}$)] $ns\sigma_g$ Rydberg level, because as n increases there will never be a situation where populated Rydberg levels do not cross the X ($^2\Pi_{i,g}$) state. Figure 7-7 shows a simulated photoabsorption spectrum for a series of Rydberg levels converging on the A ($^2\Pi_{i,u}$) state, and Franck-Condon representation of the absorption to the A ($^2\Pi_{i,u}$) state itself. The Morse potentials for the X ($^1\Sigma_g^+$) and A ($^2\Pi_{i,u}$) states have been used for a Franck-Condon simulation of the A ($^2\Pi_{i,u}$) $\leftarrow$ X ($^1\Sigma_g^+$) system. The intensity of each vibrational level in the Franck-Condon simulation was interpolated to produce a smooth envelope void of vibrational structure (equivalent to allowing the reduced mass of the molecular system to approach infinity). The Franck-Condon envelope for a Rydberg state converging to the A ($^2\Pi_{i,u}$) state should be very similar to the A ($^2\Pi_{i,u}$) state itself (neglecting absolute intensities). So the total photoabsorption cross section of a series of Rydberg states converging to the A ($^2\Pi_{i,u}$) state can be simulated by intensity and energy scaling of a set of curves similar to curve Y in Figure 7-7. The oscillator strength to a particular Rydberg state scales as n^{*-3} and the Rydberg formula was used to calculate the energy of each successive Rydberg state. Curve Z

in Figure 7-7 shows the result for a Rydberg series from n=4-50 with δ=1.2 (as observed in Figure 7-5). The relative intensity of curves Y and Z have been chosen so that the curves cross at ~18.5 eV, however unless the intensity of curve Y is significantly changed the crossing point will not vary by any appreciable amount, certainly for the purpose of this discussion.

Comparing Figure 7-5 and Figure 7-7, it is relatively clear that the main autoionising features in the X ($^2\Pi_{i,g}$) vibrational progression coincide with the [A ($^2\Pi_{i,u}$)] $ns\sigma_g$ $^1\Pi_u$, n=4-50 Rydberg series. The termination of the ion progression

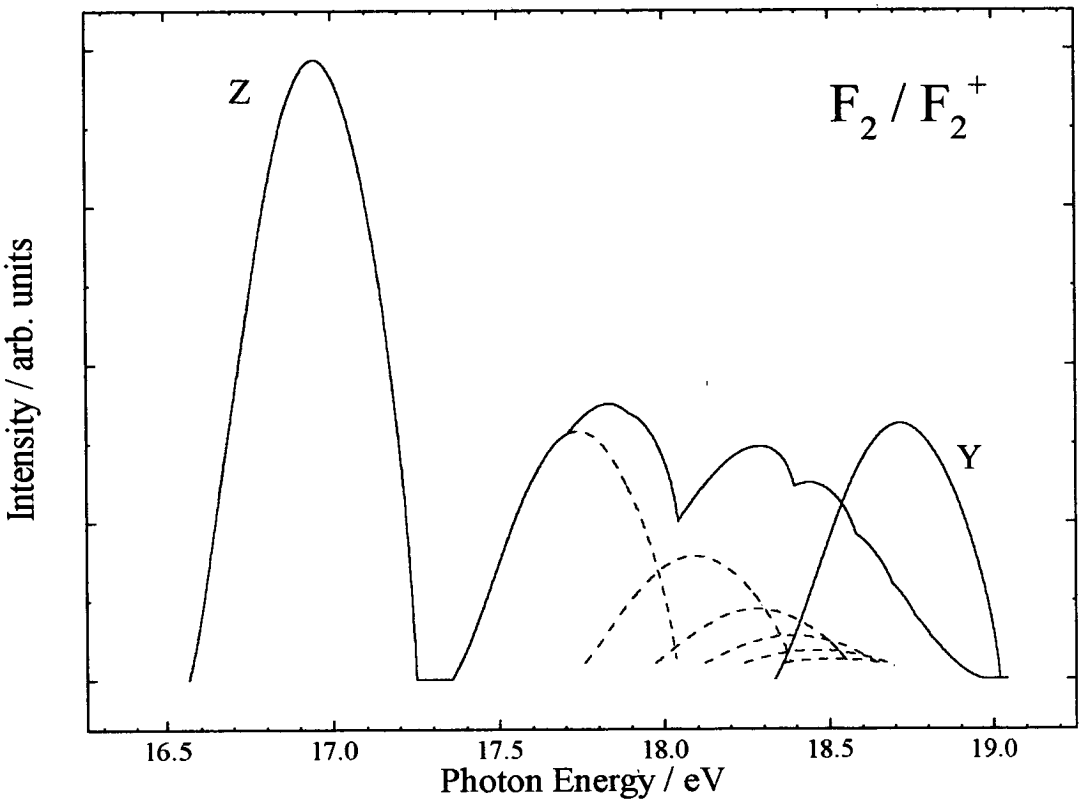

Figure 7-7 Simulated photoabsorption and photoionisation spectra for the A ($^2\Pi_{i,u}$) ion state and the $ns\sigma$ series Rydberg levels converging to it. Z is the summed simulated photoabsorption cross-section into the $[(\sigma_g)^2(\pi_u)^3(\pi_g^*)^4]_{3/2}$ $ns\sigma_g$ ($^1\Pi_u$) n=4-50 Rydberg series. Y is the Franck-Condon overlap for the A ($^2\Pi_{i,u}$) ← X ($^1\Sigma_g^+$) transition. The relative intensity of Z and Y is arbitrary. The dashed lines show the individual contributions of the $ns\sigma_g$ Rydberg states from n = 5 - 10.

coincides with a sharp drop in the Rydberg photoabsorption curve, and the steep rise in what amounts to the A ($^2\Pi_{i,u}$) photoionisation curve (curve Y). So, it can be concluded that the termination of the X ($^2\Pi_{i,g}$) state vibrational progression at ~18.5 eV is probably due to changes in the intensity of the photoabsorption and photoionisation cross-sections for the [A ($^2\Pi_{i,u}$)] *nsσ* $^1\Pi_u$ Rydberg and the A ($^2\Pi_{i,u}$) ion state.

Finally, it is worth attempting to explain the plateau region of the A ($^2\Pi_{i,u}$) state between 18.55 and 18.95 eV in Figure 7-6. A Franck-Condon simulation [13] for the A ($^2\Pi_{i,u}$) state of F_2^+ is shown in Figure 7-8 for direct comparison with Figure 7-6 (the simulated and experimental resolutions are identical). The rather abnormal distribution in the simulation is a result of the summation of the two spin-orbit sub-states of the A ($^2\Pi_{i,u}$) state. The spectroscopic data for the X ($^1\Sigma_g^+$) and A ($^2\Pi_{i,u}$)

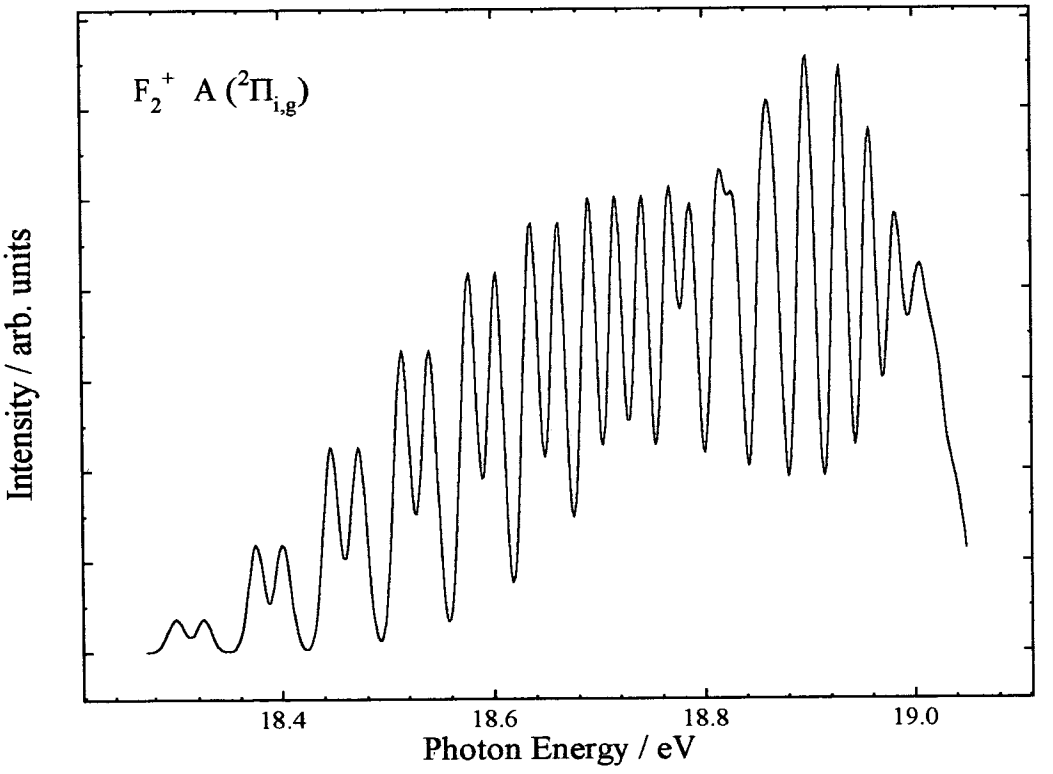

Figure 7-8 Franck-Condon simulation of the A ($^2\Pi_{i,u}$) state of F_2^+. The resolution of the simulation is the same as the experimental resolution in Figure 7-6.

states used for the Franck-Condon simulation was taken from refs. [198],[207],[213], [223], and Table 7-2. The A ($^2\Pi_{3/2,u}$) and A ($^2\Pi_{1/2,u}$) sub-states were simulated separately, then the two were added. Although the simulation does not match the experimental results perfectly it does give some indication why the region from 18.55-18.95 is quite flat in Figure 7-6, and also that the origin of the rise in intensity at ~19.0 eV is due to the spectral overlap of vibrational levels from the two sub-states.

7.3.4 The TPES of F_2 in the 19.0-21.9 eV range

Figure 7-9 shows a portion of the TPE spectrum of F_2 covering the dissociative continuum of the A ($^2\Pi_{i,u}$) band system and the entire B ($^2\Sigma_g^+$) band system. There is a considerable amount of vibrational structure superimposed on the continuum tail of the A $^2\Pi_{i,u}$ band system which extends up into the B ($^2\Sigma_g^+$) band system. Two vibronic bands have been identified as being due to the *np* Rydberg series for n = 5 and 6, converging on the B ($^2\Sigma_g^+$) state of F_2^+. Their quantum defects are 1.62 (n=5) and 1.69 (n=6) respectively. The vibrational spacings are very similar to the B ($^2\Sigma_g^+$) state spacings in the HeI PES work by van Lonkhuyzen and de Lange [213]. These Rydberg states probably undergo resonance autoionisation, finally populating the dissociative continuum of either the X ($^2\Pi_{i,g}$) or A ($^2\Pi_{i,u}$) states of F_2^+. It is possible that the autoionisation process proceeds via further intermediate neutral states as in the model by Guyon *et al.* [33], but since there are no theoretical calculations on the neutral states at present, it is impossible to decide whether there are further states involved in the ionization process, and, if there are indeed further states, what they might be.

The TPE spectrum in Figure 7-9 shows two regions with well-defined structure, labeled sys 1 and sys 2, with widely different spacings. The intensities of these systems appear anomalously high to belong to the same *np* Rydberg series as above. The vibrational structure on the low energy side of the B ($^2\Sigma_g^+$) band system (sys 2) does not correspond in energy position with the vibrational structure observed in the HeI PE spectrum of F_2 [16], although the spacings are similar. As the

calibration of the spectrum has been proven in the region of the X ($^2\Pi_{i,g}$) and A ($^2\Pi_{i,u}$) states, and we are unable to find any spectral impurities, it must be concluded that the structure is real. The three or possibly four features, labeled sys 3 in Figure 7-9, at the top of the B ($^2\Sigma_g^+$) band system of F_2^+ are probably the true vibrational structure for the B ($^2\Sigma_g^+$) state. The second peak in sys 3 would correspond to the vertical ionization potential of this state with a value of 21.112 ± 0.006 eV, in good agreement with the HeI PES result [213]. The energy positions of all the features identified in Figure 7-9 are listed in Table 7-4.

Currently there have been no detailed *ab initio* calculations on the electrically neutral molecular states in this energy region, however there have been some

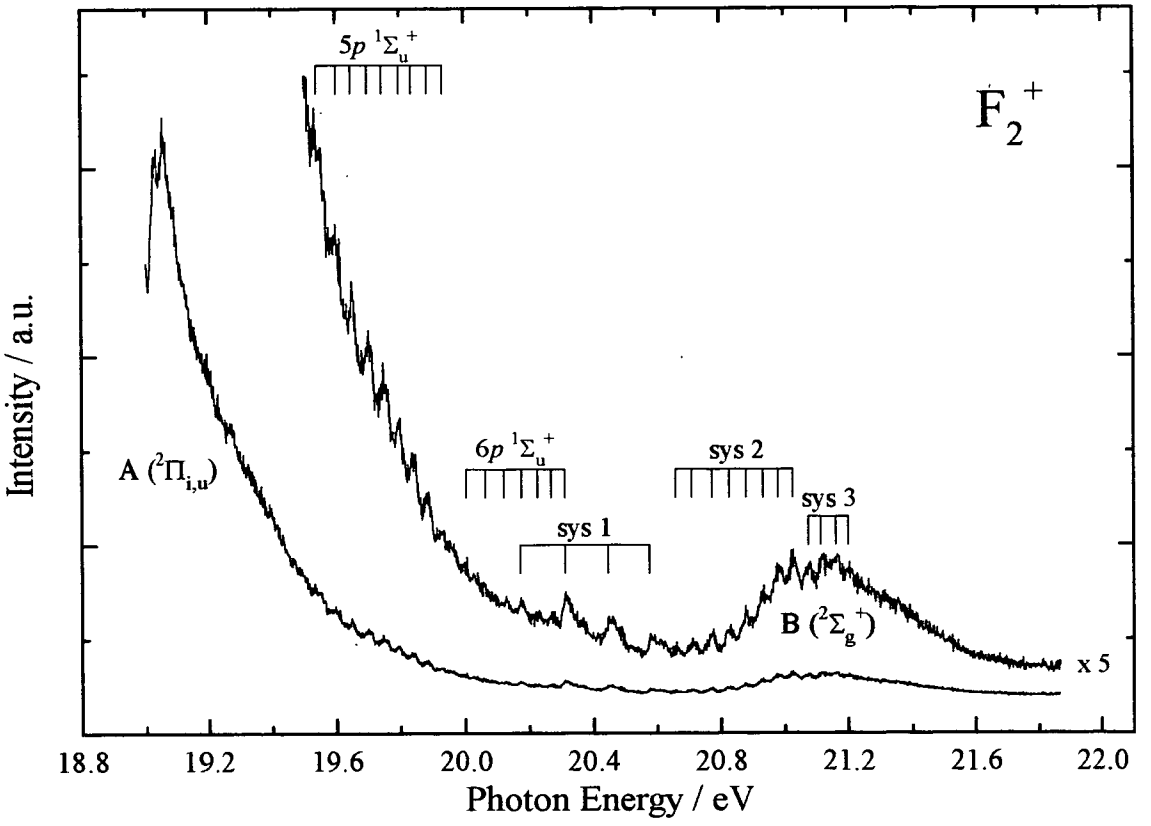

Figure 7-9 An expanded view of a portion of the threshold photoelectron spectrum of fluorine showing the high-energy tail of the A ($^2\Pi_{i,u}$) band system and the full B ($^2\Sigma^+$) band system of F_2^+. The Energy resolution of this portion of the threshold photoelectron spectrum is the same as in Figure 7-1, i.e., ΔE = 15.0 meV at 20.0 eV.

calculations on lower energy regions. These calculations show that many Rydberg states are heavily perturbed by avoided crossings with valence (ion-pair) states. It is not unreasonable to assume that these perturbations will occur in the region of sys 1 and sys 2 also. From the intensity and vibrational spacing of sys 1 and sys 2 it is possible to conclude that sys 1 should be formed from a rather narrow potential well because of the large observed vibrational spacings, while sys 2 could be formed from a much shallower well. Also, the equilibrium position of sys 1 is closer to the r_e of the X ($^1\Sigma_g^+$) state than for sys 2 (as sys 1 is more intense than sys 2). As already noted the vibrational spacing of sys 2 would be similar to that expected for an unperturbed Rydberg level converging to the B ($^2\Sigma_g^+$) state, and from the *ab initio* work by Cartwright and Hay [217] there will be ion-pair states in this region with vibrational frequencies similar to sys 2. Cartwright and Hay [217] have also calculated that the B ($^2\Sigma_g^+$) state is formed by the avoided crossing of two $^2\Sigma_g^+$ states, showing the electronic states in this region are strongly perturbed. One of the $^2\Sigma_g^+$ states is purely repulsive, originating from the [F (^{2}P) + F^+ (^{3}P)] asymptote and the other is a bound potential originating from the [F (^{2}P) + F^+ (^{1}D)] asymptote. It would be expected that Rydberg levels associated with the two ion asymptotes could also perturb each other, however the exact position of the perturbation will depend on any differences in the quantum defect of the two series. When the three ion-pair states with dissociation limits in this general energy region are also brought into this picture [228],[229], it becomes obvious more *ab initio* calculations are needed to interpret the threshold spectra more fully.

7.4 Summary and Conclusions

The threshold photoelectron spectrum of fluorine shows extensive structure in the X ($^2\Pi_{i,g}$), A ($^2\Pi_{i,u}$), and B ($^2\Sigma_g^+$) band systems. This structure can be assigned to extended vibrational progressions in the X ($^2\Pi_{i,g}$) and A ($^2\Pi_{i,u}$) states. The majority of the X ($^2\Pi_{i,g}$) state vibrational levels are in the Franck-Condon Gap region [213], so they must be accessed by indirect ionisation processes. The position of the spectral enhancements in the X ($^2\Pi_{i,g}$) state vibrational distribution has allowed the

intermediate Rydberg states to be assigned as the [A ($^2\Pi_{i,u}$)] $ns\sigma_g$ $^1\Pi$ Rydberg series, where n = 4 - 6. Also, the extended vibrational progression has been fitted to produce spectroscopic constants from a dataset covering ~90% of the well depth.

Some of the lowest vibrational levels of the A ($^2\Pi_{i,u}$) state are masked by high vibrational levels of the X ($^2\Pi_{i,g}$) state. This suggests that electronic autoionisation is favoured over vibrational autoionisation in this region. The A ($^2\Pi_{i,u}$) state vibrational levels have also been used to determine new spectroscopic constants. Ionisation into the dissociative continuum of the X ($^2\Pi_{i,g}$) and A ($^2\Pi_{i,u}$) states yields structure associated to Rydberg states with a B ($^2\Sigma_g^+$) ion core. These states must autoionise into the dissociative continuum of either the X ($^2\Pi_{i,g}$) or A ($^2\Pi_{i,u}$) states, and yield a threshold electron. The autoionisation dynamics cannot be derived from the spectra.

The B ($^2\Sigma_g^+$) state is quite weak in the threshold photoelectron spectrum and shows extensive features on the low energy side. *Ab initio* calculations on the electronic ion states in this region [217] shows the B ($^2\Sigma_g^+$) state is formed by an avoided crossing. It seems likely that Rydberg states in this region will also be perturbed, and, since ion-pair states reside in this energy region, it is quite possible that sys 1 and sys 2 in Figure 7-9 are due to the autoionisation of perturbed neutral states into the ion continuum. The structure of sys 1 and sys 2 would then reflect the intermediate neutral state and not the final ion state.

7.5 Tables of results for fluorine

Table 7-1 Observed and calculated vibrational band head positions (in eV) for the transitions: e + F_2^+ ($X\ ^2\Pi_{i,g}$, v') ← F_2 ($X\ ^1\Sigma_g^+$, v''=0)

	$^2\Pi_{3/2,g}$ transition energy		$^2\Pi_{1/2,g}$ transition energy	
v'	obs [a]	calc	obs [a]	calc
0	15.693 [b]	15.694	15.738 [b]	15.738
1	15.827 [b]	15.828	15.870 [b]	15.871
2	15.960	15.960	16.004	16.003
3	16.091	16.089	16.131	16.132
4	16.219	16.216	16.261	16.259
5	16.342	16.341	16.382	16.383
6		16.463		16.505
7	16.585	16.583	16.631	16.624
8	16.699	16.701	16.738	16.741
9	16.810	16.816	16.848	16.856
10	16.924	16.928	16.966	16.968
11	17.033	17.038	17.079	17.078
12	17.149	17.146	17.187	17.186
13	17.256	17.251	17.296	17.291
14	17.356	17.354	17.392	17.394
15	17.452	17.455	17.493	17.494
16	17.551	17.552	17.589	17.592
17	17.651	17.648	17.684	17.688
18	17.738	17.741	17.788	17.781
19	17.840	17.832	17.882	17.872
20	17.918	17.920	17.957	17.960
21	18.005	18.006	18.045	18.046
22	18.093	18.089	18.133	18.130
23	18.170	18.170	18.204	18.211
24	18.242	18.248		18.290
25	18.326	18.324	18.361	18.366
26	18.403	18.398	18.441	18.440
27	18.467	18.469	18.515	18.512
28	18.535	18.538		

[a] Uncertainty ±0.002 eV.

[b] Uncertainty ±0.001 eV, from Figure 7-3.

Table 7-2 Observed and calculated vibrational band head positions (in eV) for the transitions: e + F_2^+ ($A\ ^2\Pi_{i,u}$, v') ← F_2 ($X\ ^1\Sigma_g^+$, v''=0)

	$^2\Pi_{3/2,u}$ transition energy		$^2\Pi_{1/2,u}$ transition energy	
v'	obs [a]	calc	obs [a]	calc
0	18.300	18.300		18.333
1		18.375	18.410	18.409
2		18.448	18.481	18.481
3		18.517	18.549	18.551
4	18.581	18.583	18.617	18.617
5	18.647	18.646	18.679	18.679
6	18.706	18.706	18.737	18.738
7	18.762	18.762	18.792	18.794
8	18.816	18.815	18.850	18.847
9	18.864	18.865	18.896	18.896
10	18.912	18.911	18.942	18.941
11	18.956	18.954	18.984	18.984
12	18.993	18.994	19.021	19.023
13	19.030	19.031		

[a] Uncertainty ±0.002

Table 7-3 Summary of spectroscopic constants (in eV) derived from analyses of the F_2 TPES data presented here and from literature data

State	Ionization Energy	ω_e	$\omega_e x_e$ x 10^{-3}	SOS[b]	Ref.
F_2^+ X ($^2\Pi_{3/2,g}$)	15.693(1)	0.1369	-1.22	0.045	this work
	15.694	0.1380	-1.21	0.043	[214]
	15.697(3)	0.1354	-1.07	0.043	[213]
		0.1351	-1.11		[207]
F_2^+ X ($^2\Pi_{1/2,g}$)	15.738(1)	0.1363	-1.20		this work
	15.738				[214]
		0.1350	-1.11		[207]
F_2^+ A ($^2\Pi_{3/2,u}$)	18.300(2)	0.0793	-1.64	0.033	this work
	18.304(10)	0.0777	-1.59	0.035	[213]
		0.0798	-1.67		[207]
F_2^+ A ($^2\Pi_{1/2,u}$)	18.333[c]	0.0794	-1.69		this work
		0.0780	-1.71		[207]

[a] Experimental (0-0) transition value unless otherwise noted.
[b] Spin-orbit splitting between v=0 bands in sub-components.
[c] Determined from fitting procedure.

Table 7-4 Band head positions (in eV) for the unidentified vibrational features in Figure 7-6 (marked with asterisks) and the identified vibrational features in Figure 7-9.

System	Energy position [a]	System	Energy position [a]
unidentified	17.619	sys 1	20.171
	17.701		20.311
	17.850		20.446
	18.075		20.577
	18.186		
	18.262	sys 2	20.658
	18.568		20.710
			20.774
$5p\ ^1\Sigma_u^+$	19.541		20.827
	19.603		20.879
	19.649		20.932
	19.698		20.980
	19.744		21.024
	19.796		
	19.835	sys 3	20.073
	19.885		21.112
	19.931		21.159
			21.199
$6p\ ^1\Sigma_u^+$	20.002		
	20.063		
	20.121		
	20.175		
	20.227		
	20.269		
	20.310		

[a] Uncertainty ± 0.002 eV

Table 7-5 Positions and assignments of the autoionising Rydberg levels labeled in Figure 7-3.

Energy / eV	Rydberg assignment		Final ion state (v', Ω)	spin-orbit autoionisation ?
	configuration	Quantum defect, δ		
15.715	[X ($^2\Pi_{1/2,g}$) v^+=1] 10*pσ*	0.68	v^+=0 [3/2]	YES
15.744	[X ($^2\Pi_{1/2,g}$) v^+=1] 11*pσ*	0.68	v^+=0 [1/2]	NO
15.702	[X ($^2\Pi_{3/2,g}$) v^+=2] 8*pπ*	0.74	v^+=0 [3/2]	NO
15.831	[X ($^2\Pi_{3/2,g}$) v^+=2] 11*pπ*	0.74	v^+=1 [3/2]	NO
15.748	[X ($^2\Pi_{1/2,g}$) v^+=2] 8*pσ*	0.68	v^+=0 [1/2]	NO
15.875	[X ($^2\Pi_{1/2,g}$) v^+=2] 11*pσ*	0.67	v^+=1 [1/2]	NO
15.883	[X ($^2\Pi_{1/2,g}$) v^+=2] 14*pπ*	0.74	v^+=1 [1/2]	NO
15.753	[X ($^2\Pi_{3/2,g}$) v^+=3] 7*pσ*	0.67	v^+=0 [1/2]	YES
15.839	[X ($^2\Pi_{3/2,g}$) v^+=3] 8*pσ*	0.67	v^+=1 [3/2]	NO
15.878	[X ($^2\Pi_{1/2,g}$) v^+=3] 8*pσ*	0.68	v^+=1 [1/2]	NO
15.896	[X ($^2\Pi_{3/2,g}$) v^+=3] 9*pσ*	0.67	v^+=1 [1/2]	YES

[a] uncertainty ± 0.001 eV
[b] formula: $E_n = I.P. - R_y/(n-\delta)^2$
[c] based on closest ionization limit to lower energy
[d] based on Rydberg series limit and final ion assignment

Chapter 8. Experimental designs and future directions

8.1 Introduction

Chapter 2 describes the experimental apparatus used for data collection however, during the course of data collection for this thesis many modifications have been made to the existing apparatus. Also, a new experimental design is in the process of being built. As the new apparatus is currently incomplete (due to funding difficulties etc.) it seemed more appropriate to discuss its features in a separate Chapter. This also gives an opportunity to discuss the developments to the existing apparatus without complicating Chapter 2, and also provides an occasion to discuss possible future studies.

8.2 Modifications to existing apparatus

At the start of experimental work for this thesis the spectrometer functioned correctly, having already been used for studies on Cl_2 and Br_2 [59], I_2 [60], and CF_4 [61], however there were many niggling problems with the experimental design. The spectrometer itself was mounted on a single insulating post, giving problems with mechanical stability and alignment of the gas and photon beams. A further problem with the original design concerned the mu-metal magnetic shielding. If the experimental chamber had to be opened while the apparatus was on the beamline the whole apparatus had to be removed from the mirror box (see Figure 2-2 and Figure 2-3), This took a considerable amount of time and was also an extremely delicate operation. The operational problems with the mu-metal shielding have been solved by

modifying the shielding so that the chamber can be opened *in situ*, and the spectrometer mounting assembly has been redesigned to increase its rigidity.

Figure 8-1 shows the change in experimental design from the start (left) to the finish (right) of this thesis. The grayed components in the diagram represent the changes made to the spectrometer support assembly. The orientation of the mu-metal shielding has been changed. Previously both mu-metal shields were fixed to the top flange of the chamber, and, since the glass capillary (for the photons) passed through a hole in the mu-metal shields, it was impossible to remove the top from the chamber without first removing the chamber from the mirror box. This problem was solved by (1) inverting the outer mu-metal shield and fixing it to the bottom of the chamber and (2) inverting the inner mu-metal shield, fixing its lid to the top of the chamber, and cutting a slot in the side and bottom of the shield to allow the glass capillary to pass. The hashed area in Figure 8-1 shows the slot. Two linear bearing assemblies (not shown in Figure 8-1) were fitted to the outside of the chamber to guide the top flange

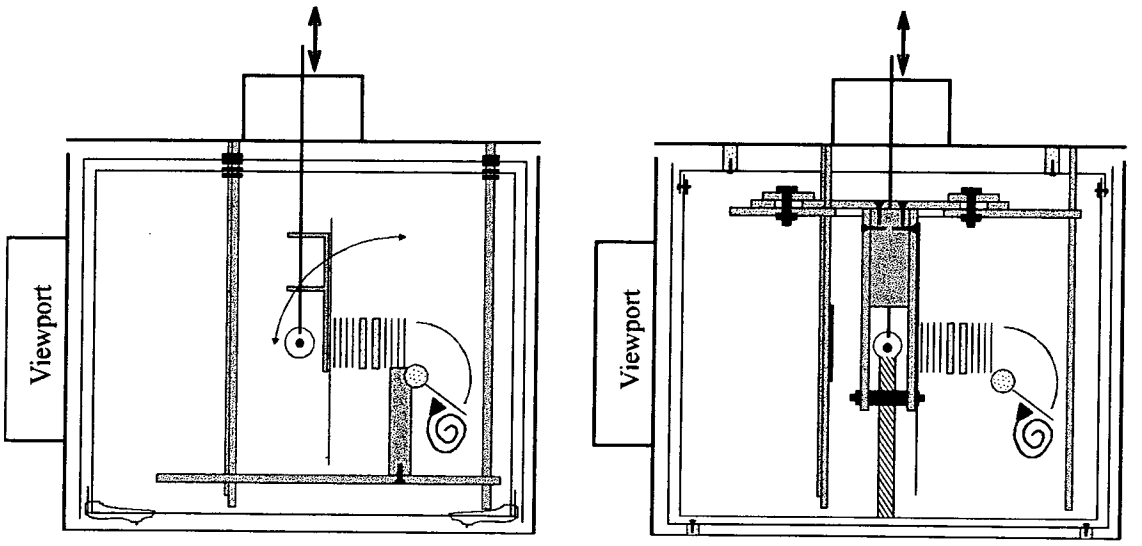

Figure 8-1 Schematic of the changes to the mounting of the threshold photoelectron spectrometer during the course of work for this thesis. The original design is on the left and the modified design on the right. The new design eliminates mechanical instability in the spectrometer mounting arrangement and also allows for the fitting of a photoion spectrometer opposite the photoelectron spectrometer for TPEPICO studies if desired.

as it mates with the chamber, this ensures the slot in the mu-metal shielding is aligned correctly with the glass capillary transmitting the photon beam. Fixing the lid of the inner shield to the top chamber flange also allows for easier spectrometer maintenance. Previously the spectrometer and its support plate had to be removed from inside the mu-metal shielding. However, the new arrangement of the mu-metal allows the inner shield to be removed giving access to the spectrometer while it is still mounted.

The mounting mechanism for the spectrometer was changed to overcome some mechanical instability. In the initial design the spectrometer was supported by a post underneath the cylindrical deflection analyser and guide brackets on the front end of the lens assembly. Unfortunately, adjusting the height of the platinum needle above the plane of the lens assembly and the photon beam tended to make the spectrometer tilt (as shown in Figure 8-1). This has been solved by mounting the spectrometer below an electrically isolated cradle. The cradle is designed to be positioned before the chamber is evacuated, and, so that the spectrometer can be removed and remounted to the cradle without any repositioning problems. The design also allows the introduction of a small time-of-flight photoion detection system for TPEPICO studies. Essentially all of the operational difficulties with the original design have been eliminated, however one small problem still remains. The top flange on the chamber has to be lifted off by a crane. This is not ideal for an experiment designed to operate 24 hours a day. A new chamber design was required to eliminate this problem, and a new threshold photoelectron apparatus has been under construction, however at present the chamber and support stand have been fabricated but the internal components have not. Having said this, it is worth detailing the general features and ideas behind the new design and the types of experiments the new apparatus would be useful for.

8.3 Design features of the new threshold photoelectron / threshold photoion coincidence experiment

Figure 8-2 shows the general design characteristics for the new instrument for threshold photoelectron and threshold photoelectron photoion coincidence (TPEPICO) experiments. The chamber is oriented so that it can be opened easily using a linear bearing assembly, allowing quick access to the spectrometer assemblies. The linear bearing trolley has a turntable fitted to allow the spectrometer and mu-metal shielding to be rotated to one side for easy inspection once the chamber has been opened. The design incorporates a differentially pumped ionisation region using an ADP 3000 l/s Cryostatic vacuum pump for the main gas load, while a Leybold 400 l/s Turbo pump ensures a higher vacuum at the ion and electron detectors. This differentially pumped ionisation region should reduce the counting time required in coincidence experiments.

The ionisation region will be redesigned considerably. Ionisation will take place in a aluminum cube with holes drilled through the six faces. The bottom schematic in Figure 8-2 shows the cube. The study gas enters the cube from the right and the photon axis is perpendicular to the plane of the paper. Non-ionised gas will preferentially travel towards the Cryostatic pump as this is the largest exit hole in the cube, whereas only a small gas load will escape through the other 4 holes in the cube. A large conical funnel forms a barrier between the "high pressure" and differentially pumped regions. The interaction region is designed specifically for true coincidence experiments, which as a rule, generally have poor coincidence count rates, so, increasing the gas density in the ionisation region should lead to shorter recording times and better signal to noise. A photoion and threshold photoelectron spectrometer are envisaged to be the most useful coincidence tools for experiments discussed later. The gas inlet system has not been currently designed, however, two arrangements are of interest. The effusive source, as used for the results in this thesis, would be an obvious source for initial testing of the performance of the apparatus, however a skimmed supersonic jet expansion could have possible advantages in some

experiments. For instance, the highly directional flow from a skimmed supersonic source should be ideal for increasing the gas density in the ionisation region while the near collision free conditions in the beam will remove any collision induced ionisation effects from the spectra [230],[231].

Another benefit of jet cooling is that is should increase the detection efficiency of the ion detector in TPEPICO experiments. The Boltzmann distribution for an effusive source at room temperature is 26 meV, but typically the penetrating field photoion spectrometer has better resolution. So, many of the ions will be discriminated against as they have too high initial kinetic energy even though all threshold electrons will be detected. A jet expansion source will narrow the velocity and kinetic energy distribution of the neutral species and this should increase the detection efficiency of the photoion detector. A typical supersonic jet expansion using argon as a carrier gas will have a velocity of 250 ms^{-1} [232]. This equates to 0.032 eV of translational energy for a molecule of 100 atomic mass units - so the ions would not be extracted from the ionisation volume using the conventional TPEPICO arrangement in Figure 8-2. However, there are too solutions: (1) Use the detection pulse from the threshold electron to apply a larger pulse across the interaction region to push the photoion towards the photoion detector, or (2) mount the photoion detector at an angle to the gas beam instead of perpendicular to it. Design (1) is ideal when the ratio of non-threshold photoelectron production to threshold photoelectron production is small, otherwise there may be difficulties in differentiating between ions formed during the two processes. Design (2) is more difficult to engineer but should, in principle, work for all ratios of non-TPE to TPE production. However design (2) may result in a reduction in the operating resolution of the threshold photoelectron spectrometer due to the modified electrostatic fields in the interaction region. Trial and error seems to be the best way to find a solution.

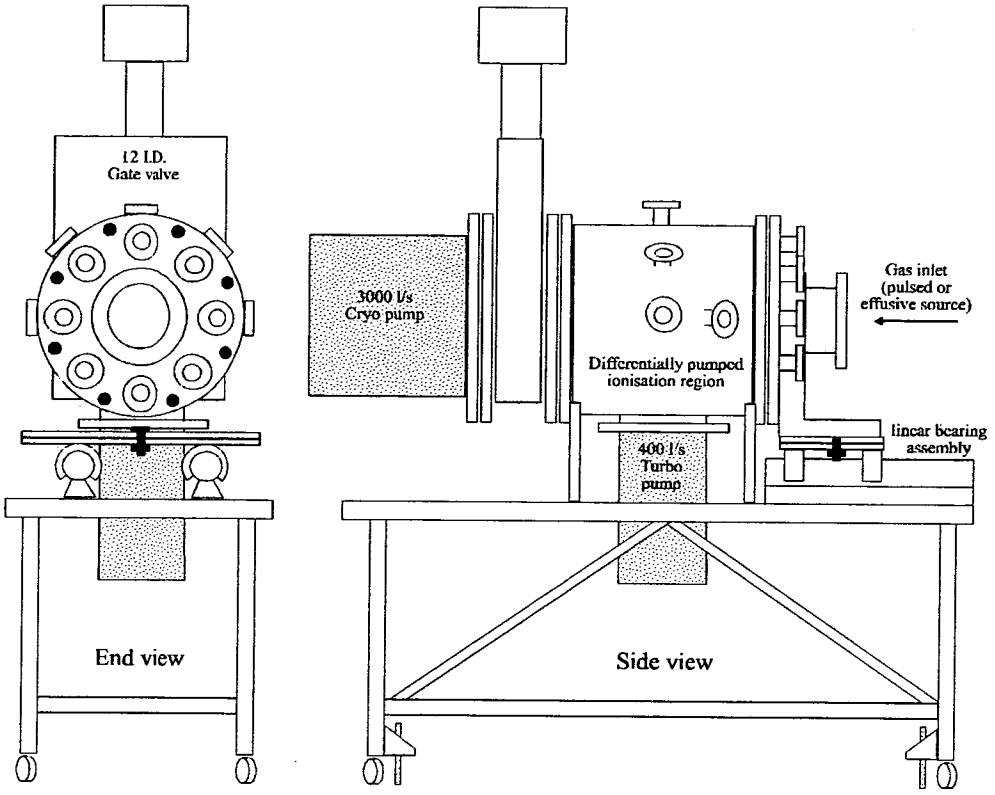

Cross section of ionisation chamber

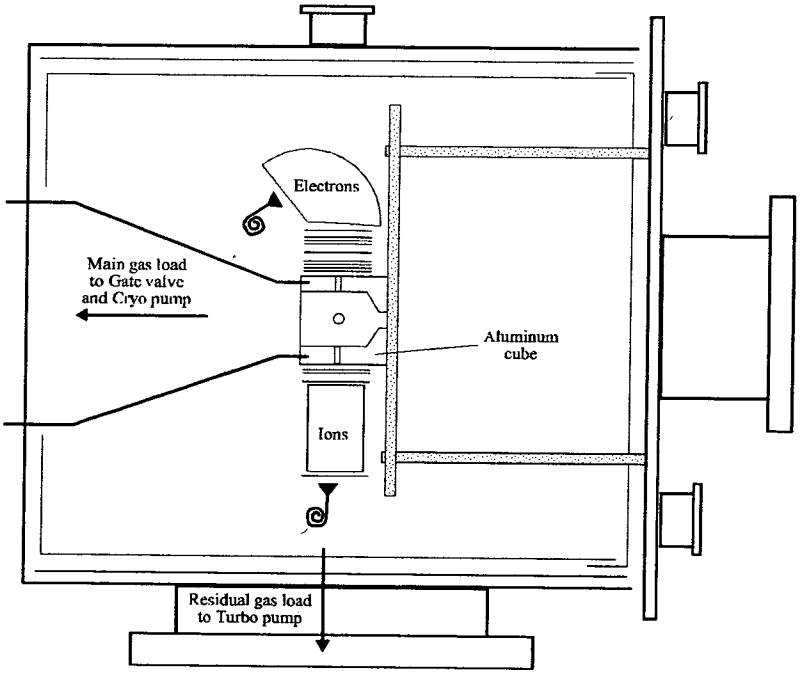

Figure 8-2 Schematic of the proposed new threshold photoelectron experiment. At the present the ionisation chamber and the stand have been built. Further funds are required to complete the design.

The rotational cooling in a supersonic expansion is not ideal for studies where rotationally resolved spectra are a major goal, for instance in the lowest and first excited vibrational levels in the X ($^2\Pi_i$) state of the hydrogen and deuterium halides. However, in heavier systems where rotational resolution is not achievable, the rotational cooling may sharpen up the vibrational lines and allow the determination of more accurate spectroscopic constants for the electronic states. An increase in spectral resolution combined with rotational cooling may also help the characterise the ionisation pathways in threshold photoelectron spectroscopy.

8.4 Future research areas for the new instrument

Molecular systems of interest with the new apparatus would be systems like the interhalogens XY. These species coexist in dynamic equilibrium with the homonuclear halogens X_2 and Y_2 so photoelectron studies are complicated by the spectra of all three molecules. It is possible to manipulate the $2XY \leftrightarrow X_2 + Y_2$ equilibrium in order to obtain the spectra of XY and X_2 without Y_2, however, the complexity of threshold photoelectron spectra would almost certainly preclude the unambiguous assignment of two similar species from a single spectrum. A more elegant way to differentiate between the spectra is by using the TPEPICO technique. Essentially the technique works as follows: The penetrating field spectrometer extracts a threshold electron from the ionisation volume and the electron is detected by standard electronics. The pulse signifying detection of an electron is used to start a time-to-amplitude converter (TAC) which continuously ramps a voltage with time. The detection of the corresponding photoion triggers a stop pulse for this increasing voltage, and the size of the voltage indicates the time duration between the start and stop pulses. Some knowledge of the flight times of various ions through the ion detector allows the ion time-of-flight to be converted into mass. A histogram of these TAC voltages gives the mass distribution of the ion fragments and this can be easily achieved using standard counting electronics. Normally TPEPICO is used to monitor dissociation pathways in the molecular ion by using the time-of-flight photoion detector to differentiate the masses of the ionic fragments. However, the technique

can also be used to differentiate between the ionisation of the interhalogens XY and X_2 as the masses of the two species differ. Once ion dissociation channels are accessible it may be difficult to differentiate between TPEPICO signals from XY and X_2 (if only X^+ is detected), however, the interesting extended vibrational progressions generally only occur in the X ($^2\Pi_{i,(g)}$) and A ($^2\Pi_{i,(u)}$) states of the ion, and since these states both correlate to the lowest atomic asymptotes [233] ion dissociation should not be a problem in the spectroscopically interesting energy regions. In summary, TPEPICO should be an ideal technique for the study of the interhalogens, and the technique should also be applicable to many equilibrium systems.

Another interesting experiment concerns the recent publication of the threshold photoelectron spectrum of SF_6 by Yencha *et al.* [234] where extensive vibrational structure was seen superimposed on the first 4 electronic states of SF_6^+. This structure is not seen in conventional photoelectron studies of SF_6 [235] and has been assigned to shape resonances in the electronic structure of SF_6 which are probed by the threshold photoelectron technique. However, it is well known that SF_6 has a very large capture cross section for low energy electrons and is also a good energy moderator of electrons, so it is possible that the threshold photoelectron spectrum by Yencha *et al.* [234] may consist of a contribution from SF_6^- (electrostatic energy analysers cannot discriminate the mass of charged particles without some form of time-of-flight electronics [236],[237]). TPEPICO would afford the opportunity to investigate whether these electron attachment processes are occurring in the ionisation region as they may effect the TPE spectrum. For instance two TAC's can be used to measure the time between arrivals of (1) N^- and SF_6^+, and (2) SF_6^+ and N^- (N^- represents either e^- or SF_6^- as without the TAC information the two cannot be differentiated). Information on the species detected could then be easily extracted from the TAC measurements. This use of TPEPICO is not restricted to SF_6, HI also has a large threshold electron attachment cross section [178],[179] and can also undergo dissociative charge transfer reactions [167] so the possible influences of these processes on the threshold photoelectron spectrum can also be studied.

Finally, it is worth pushing threshold photoelectron studies towards higher resolution. The current spectral resolution is effectively dependent on the smallest usable photon bandwidth from the VUV monochromator. Third generation synchrotrons such as the Advanced Light Source (ALS) at Berkeley, California represent a significant improvement in spectral resolution. The 6.5 metre monochromator on the Molecular Dynamics beamline at the ALS represents a significant improvement in spectral resolution over the McPherson monochromator at the Daresbury Laboratory so transferring either the current threshold photoelectron apparatus or the new apparatus still under construction should allow rotationally revolved TPE spectra of the hydrogen and deuterium halides to be recorded. The results already achieved in this thesis are promising in this regard.

In conclusion there are many new research avenues to explore, however time and effort need to be expended in ensuring the new threshold photoelectron experiment is brought to fruition.

Chapter 9. Discussion and conclusions

This Chapter is divided into three sections. The first section pinpoints the main features of the results. The following section expands these points and puts them into context. Finally, the last section contains some concluding remarks.

9.1 Highlights of the results and analysis

- There is a systematic decrease in the intensity of TPE spectra with increasing photon energy. This seems to be due to a combination of autoionisation and electron correlation effects.

- The X states of all study molecules show highly extended vibrational progressions due to the electronic autoionisation of Rydberg levels converging to the higher energy ion states. The threshold autoionisation process is very selective to the symmetry of the intermediate Rydberg state.

- The TPE spectra of the A ($^2\Sigma^+$) states of HCl and HBr are similar to the HeI PES spectra except for the predissociated vibrational levels. The predissociated levels in the TPE spectra are broadened towards lower energy and enhanced by additional ionisation processes. It is speculated that these processes are due to the rotational autoionisation of repulsive neutral states into repulsive ion states.

- The vibrational levels in the X ($^2\Pi_i$) state of HI are unambiguously assigned for the first time. Additionally, five vibrational levels of the A ($^2\Sigma^+$) state of HI have been observed for the first time. Analysis of the experimental data suggests that the A ($^2\Sigma^+$) state is well modeled by an avoided crossing between two diabatic states in Hund's case (c) coupling.

- High resolution (~ 3 meV) spectra over the first ionisation potential of the HX and DX systems show some rotational structure. However, the resolution of the spectra is not high enough to allow the rotational features to be assigned unambiguously. Further improvements in spectral resolution are needed before rotational assignments can be made.

- Structure primarily associated with intermediate Rydberg states is observed in HI and F_2. These Rydberg states must autoionise into the dissociative continuum of lower ion states, however, the Franck-Condon factors for direct autoionisation are likely to be very small.

- The TPE spectra for the inner valence regions of HX and DX are very weak, but they also show considerable structure. Many different electronic states are formed during ionisation due to electron correlation. The electronic configuration of these states cannot be derived from the TPE spectra but many vibrational progressions have been identified. Further classification of the states awaits more detailed *ab initio* calculations.

- The threshold electron spectrometer has been modified to make maintenance easier and to increase its resolution. The modified spectrometer assembly has been designed to allow TPEPICO studies in possible future work. A new TPE /TPEPICO apparatus has also been designed. The new design incorporates a differentially pumped ionisation region and the ability to use both effusive and supersonic jet sources.

9.2 General discussion

Possibly the most striking observation in this thesis concerns the intensity of the different electronic states in the threshold photoelectron spectrum. All molecules show a phenomenal disparity between the intensity of the lowest and highest ion states. For the HX and DX systems the X ($^2\Pi_i$) state is approximately 500 times more intense than ionisation from the inner valence $ns\sigma$ orbital. Non-resonant

ionisation using either high energy electrons or extreme ultra-violet radiation ($h\nu \cong 1500$ eV) shows that the relative intensity of these states is within a factor of 10. So, the threshold photoelectron results cannot be explained using the differing spectroscopic pole strengths. It is possible that the low intensity in the inner valence region arises from competing ionisation processes. For instance, if the ionisation occurs indirectly through a super-excited neutral state then there will probably be many competing de-excitation pathways from this state. Only some of these pathways will lead to a final ion state that is isoenergetic with the super-excited neutral state so it seems likely that the TPE signal will be weaker for ionisation to the inner valence region. In contrast, ionisation to a Rydberg state only slightly above the first adiabatic potential would be expected to yield a larger proportion of threshold electrons as the number of open decay channels for the Rydberg state will be much smaller.

It is also possible that the weak spectral features for the inner valence region could be explained in terms of correlated two electron ionisation. The ion states formed during inner valence ionisation generally differ from the initial electron configuration by more than one electron rearrangement. For two electron ionisation Wannier [238] predicted that the photodouble ionisation cross section ($M^{2+} \leftarrow M$) varies as $E^{1.056}$, where E is the excess energy. This formula fits well for the threshold photodouble ionisation of helium from the double ionisation potential to 1.5 eV above [239]. The reason for the low intensity at threshold could possibly be explained in terms of the electrostatic interaction between the two ejected electrons and the doubly changed ion core: Two electrons have to leave the molecule with the same kinetic energy (0 eV). The electrons see each other and the doubly positive core. Unless both electrons depart with the same energy at the same time the following scenario arises: the electron furthest away from the core will be shielded by the other electron, and so has a smaller potential barrier to escape. Conversely, the closer electron feels a stronger attraction to the core as it no longer gets any shielding from the other electron. The net effect is that the closer electron remains with the core with binding energy $-E_b$ and the further away electron is ionised with E_b energy above threshold. A

similar effect should also occur for inner valence ionisation. Two electrons will typically be excited, one is ejected at threshold and the other excited into an ionic Rydberg state. Unless the initial energy partitioning between the electrons is correct a threshold electron will never be produced. For example, a final electron configuration in an HCl^+ state could be written as $(3s\sigma)^2(3p\sigma)^2(3p\pi)^2\ nl\lambda$. This could be viewed as a two step process involving first ionisation then Rydberg excitation: HCl [X $(^1\Sigma^+)$] $\rightarrow$ HCl^+ [X $(^2\Pi_i)$] $\rightarrow$ HCl^+ [X $(^1\Sigma^+)]^{2+}$ $nl\lambda$. The energies for each step are easily calculable and could be apportioned to the two electrons involved (in a thought experiment). However, if two electrons were given these energies threshold ionisation is unlikely to occur as electron correlation would redistribute the energies during the ionisation event, and, from the arguments on double ionisation above, a kinetic electron would be produced. Concluding, it may be possible that the low spectral intensity for inner valence ionisation in the HX and DX systems is due to electron correlation effects during the threshold ionisation event.

One of the nicest parts of the consistent study of a set of similar molecules is that it can produce spectra which are readily comparable. Figure 9-1 shows the threshold photoelectron spectra of the hydrogen halides for the outer valance ionisation region and Figure 9-2 shows the equivalent spectra for the deuterium halides. All spectra show extended vibrational structure in the X $(^2\Pi_i)$ state. These vibrational levels can be used to refine the spectroscopic data for the ion states, however rotationally resolved A $(^2\Sigma^+) \rightarrow$ X $(^2\Pi_i)$ fluorescence has been recorded for all molecules except hydrogen iodide, so generally the vibrational spectroscopic constants are well known. The assignment of the autoionising Rydberg states responsible for the extended vibrational progressions has uncovered some interesting results. They have been assigned as having [A $(^2\Sigma^+)$] $ns\sigma$ $^1\Sigma$ symmetry, but the most intense Rydberg states in photoabsorption and photoionisation have [A $(^2\Sigma^+)$] $np\pi$, $nd\pi$ $^1\Pi$ symmetry. So the $^1\Pi$ states must produce kinetic electrons in the autoionisation event. The [A $(^2\Sigma^+)$] $ns\sigma$ $^1\Sigma$ (and [A $(^2\Sigma^+)$] $nd\sigma$ $^1\Sigma$) Rydberg states are not observed in photoabsorption or photoionisation as they are masked by the more

intense $^1\Pi$ states, but are observed by the fluorescence of neutral fragments. The threshold ionisation model by Guyon *et al.* [33] using neutral dissociative intermediate states seems to agree with the observed spectra, and suggests that threshold autoionisation and the fluorescence of atomic fragments are competing processes with the same initially excited Rydberg states. By the same token, the Franck-Condon model by Bardsley [14] and Smith [15],[16] doesn't seem to fit with the observed TPE spectra.

The TPE spectra of the A ($^2\Sigma^+$) states of the hydrogen halides are very similar to the HeI PES spectra except for the predissociated vibrational levels in HCl and HBr. The predissociated levels show two curious effects where the vibrational peakshape is broadened towards lower energy only, and the intensity of the strongly predissociated vibrational levels is increased. This suggests additional ionisation pathways are accessible for threshold ionisation to a predissociative ion state. In HCl, this broadening has been modeled as being due to a preference for negative changes in rotational angular momentum during the ionisation event. However, in DCl the model does not fit quite as well. Possibly the broadening to lower energy is due to the resonant autoionisation of repulsive neutral states into repulsive ion states. The potential energy curves for a rotationless Rydberg state and its rotationless parent ion state will not cross each other. But, the states can easily cross if the Rydberg state has more rotational angular momentum than the ion state, so, in this case the Franck-Condon factor for threshold ionisation may be appreciable. Therefore, a possible model for the increased intensity of predissociated ion levels is (1) initial photoabsorption to a vibrationally excited (bound) Rydberg state, followed by (2) predissociation of this Rydberg state by a dissociative Rydberg state, and finally (3) the autoionisation of the dissociative Rydberg state into the dissociative ion state (with a transfer of angular momentum to the ejected electron). Whatever the true ionisation scheme the conservation of total angular momentum during the ionisation event should apply. A more thorough study of the possible ionisation pathways is needed before further conclusions into the ionisation dynamics can be drawn.

The resolution that the threshold photoelectron spectrometer can routinely achieve has been improved from ~6 meV to ~3 meV during the course of the work for this thesis. This has allowed partially resolved rotational structure to be recorded in the X ($^2\Pi_i$) v^+=0,1 vibrational levels of the HX and DX systems. The spectra show evidence of spin-orbit, vibrational, and rotational autoionisation, but an increase in spectrometer resolution to ~1 meV or better will be needed before these spectral features can be assigned. Combining the threshold electron spectrometer with the high brightness of a third generation synchrotron light sources may achieve this resolution. A rotationally resolved TPE spectrum of the hydrogen halides will provide a useful comparison with ZEKE spectra. The spectra would be expected to be identical.

All of the threshold photoelectron spectra show autoionising structure which can be assigned to initial photoabsorption of intermediate Rydberg states. However, the TPE spectra of HI and F_2 have particularly interesting examples of this phenomenon. In both cases spectral features are assigned to the autoionisation of a bound Rydberg state into the dissociative continuum of a lower ion state, but the observed spectral features show the energetics of the Rydberg state. Normally the position of peaks in TPE spectra indicate the energy levels of the final ion state, however the HI and F_2 spectra clearly show examples where only the structure of the Rydberg state is seen. This is essentially due to the continuum nature of the ion state at the same energy, however, the dynamics of this autoionisation process are of interest. The Franck-Condon overlap between the Rydberg and ion states will be very small (especially at threshold) as the two states will not cross, so the autoionisation process is difficult to describe by Franck-Condon means. It seems more likely that the bound Rydberg states are predissociated by repulsive states, and that these repulsive states autoionise when they cross the ion state. The net effect is to produce a threshold electron.

Ionisation from the inner valence molecular orbital in HX and DX is very weak and the spectra are highly complex. Figure 9-3 shows the threshold

photoelectron spectrum of the hydrogen halides for the inner valence region and Figure 9-4 shows the equivalent region in deuterium halides. The spectra are characterised by sharp ionisation features consisting of "main band" and "satellite" ionisation. Many vibrational progressions have been tentatively identified in the spectra, however the electronic structure of the states giving rise to these progressions has not been assigned. More detailed *ab initio* calculations will be needed before the spectra can be assigned. Another feature of inner valence ionisation is the broad continuum to lower energy than the "main band" and "satellite" features. This is probably due to direct ionisation into lower energy dissociative ion states.

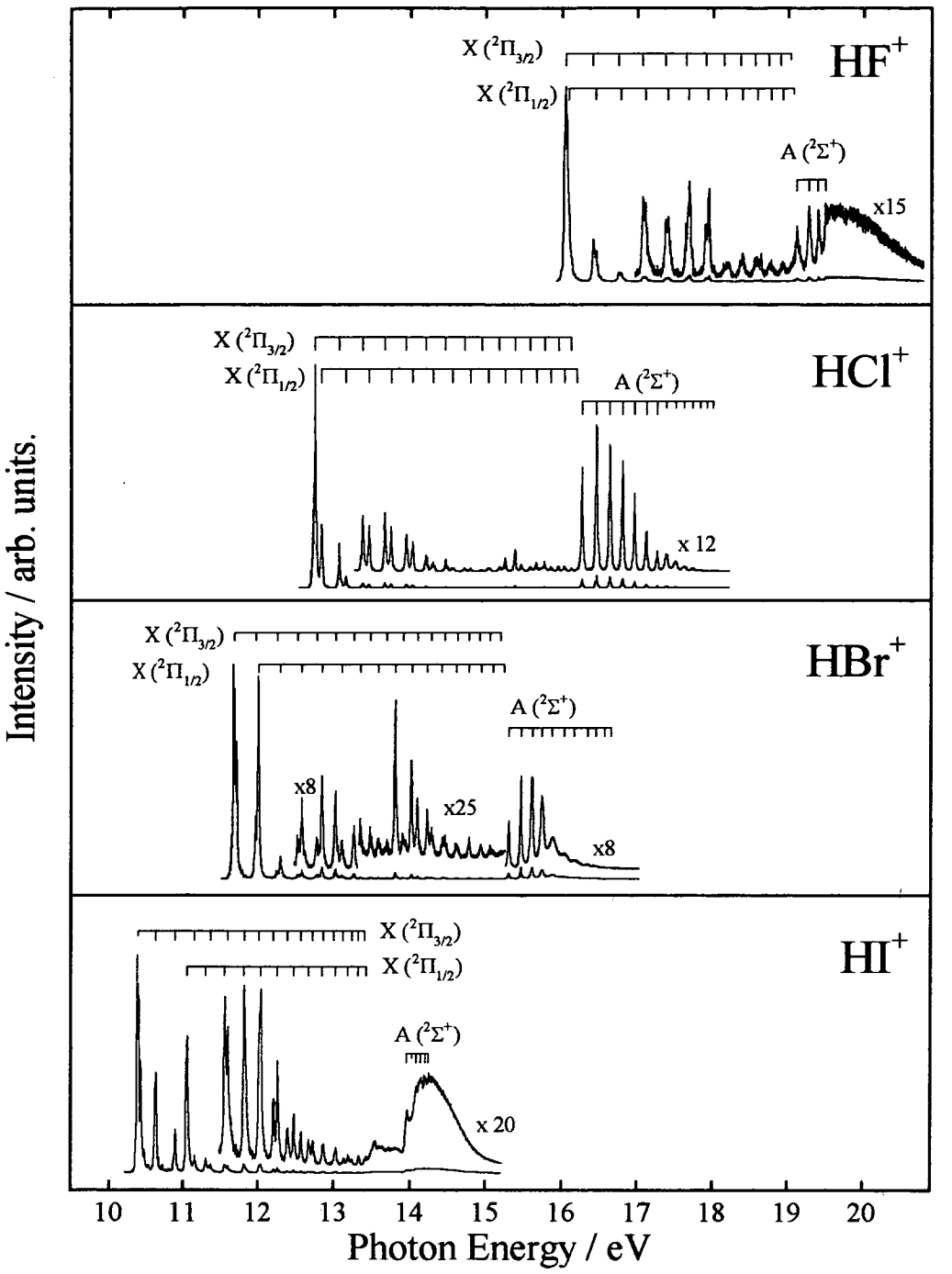

Figure 9-1 Threshold photoelectron spectra of the hydrogen halides for the outer valence ionisation region. The spectra are taken from relevant Figures in this thesis.

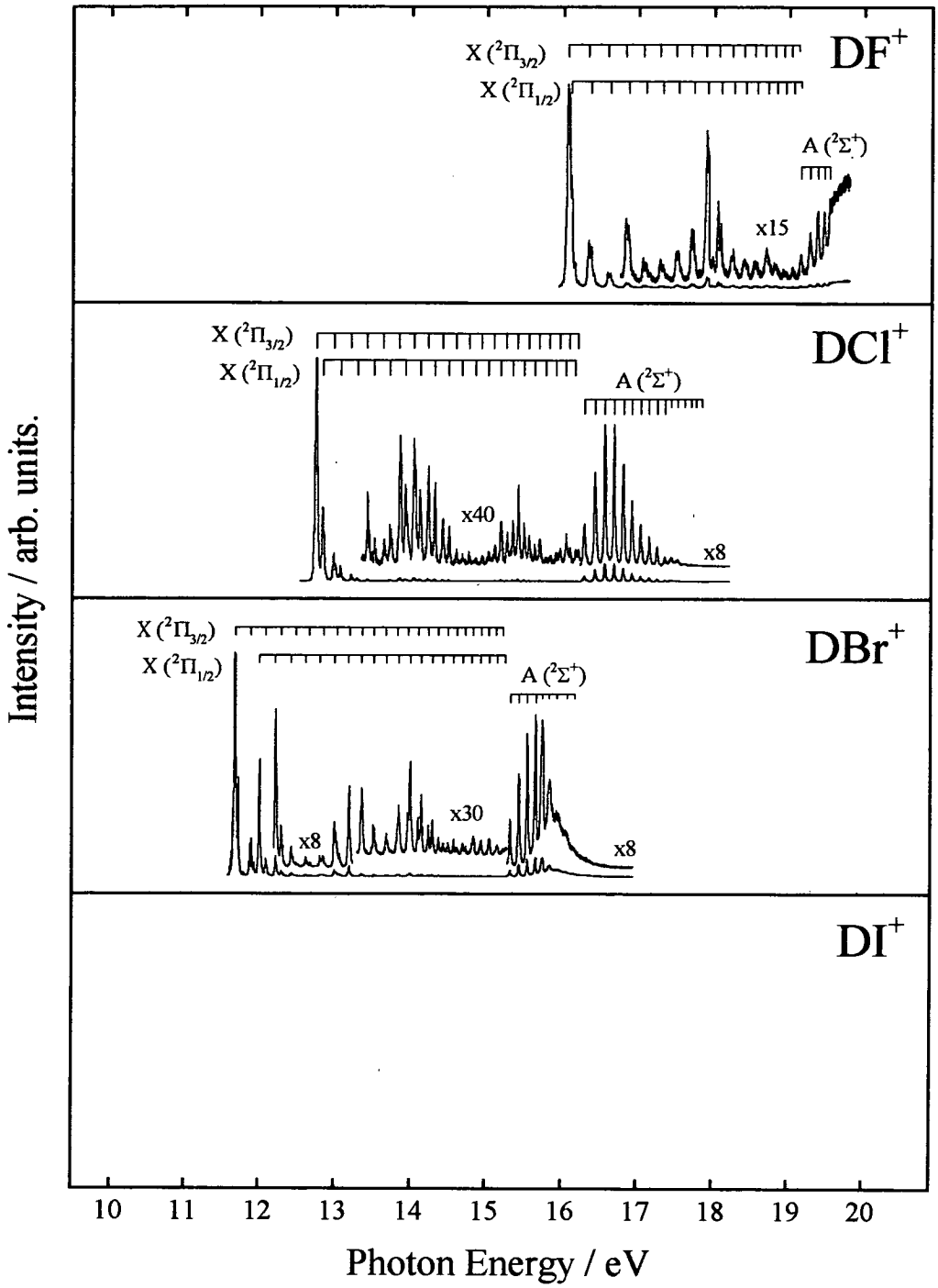

Figure 9-2 Threshold photoelectron spectra of the deuterium halides for the outer valence ionisation region. The spectra are taken from relevant Figures in this thesis. (At present, the spectrum of DI has not been studied)

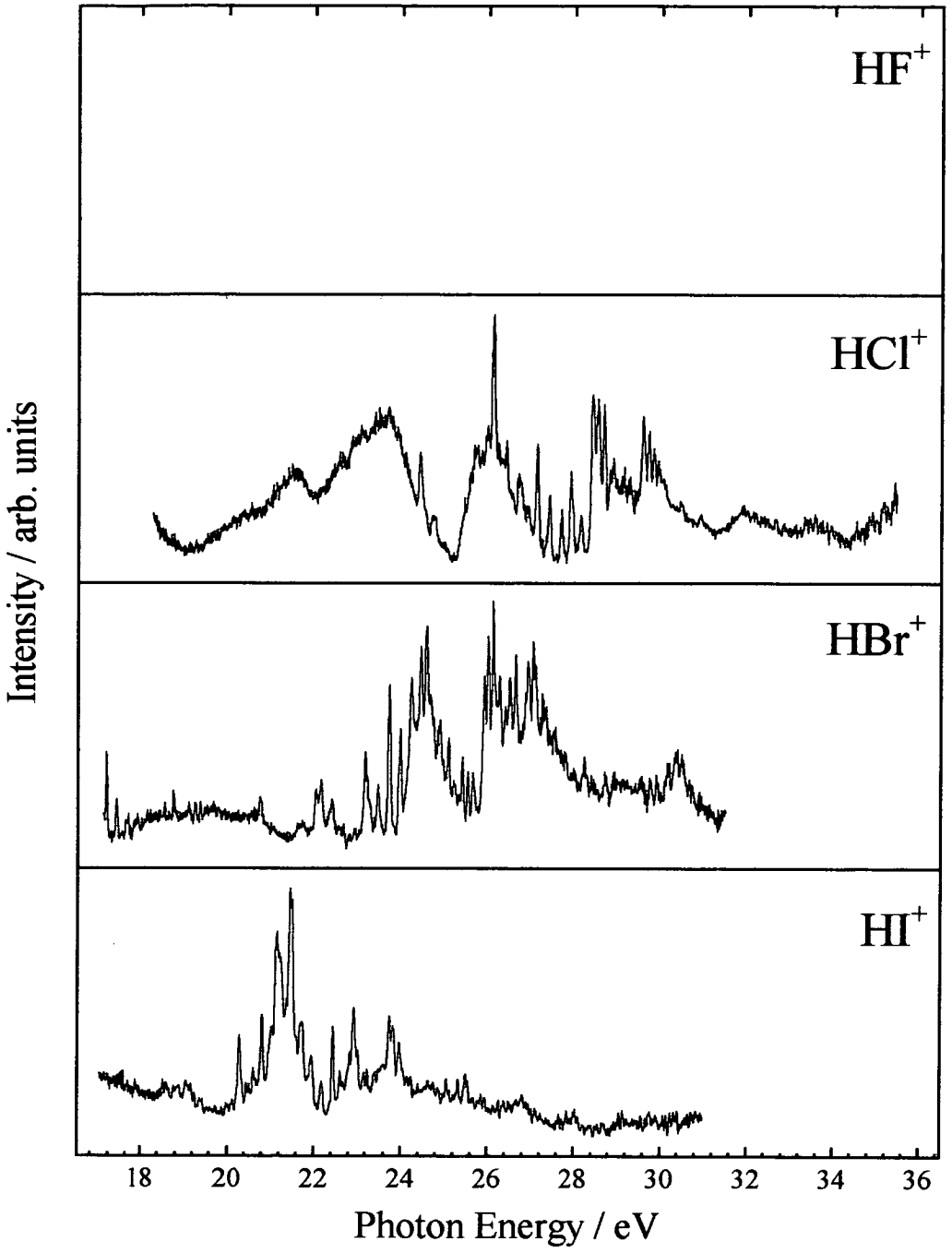

Figure 9-3 Threshold photoelectron spectra of the hydrogen halides for the inner valence ionisation region. The spectra are taken from relevant Figures in this thesis. (The inner valence ionisation region of HF is around 40 eV - too high for the present studies.)

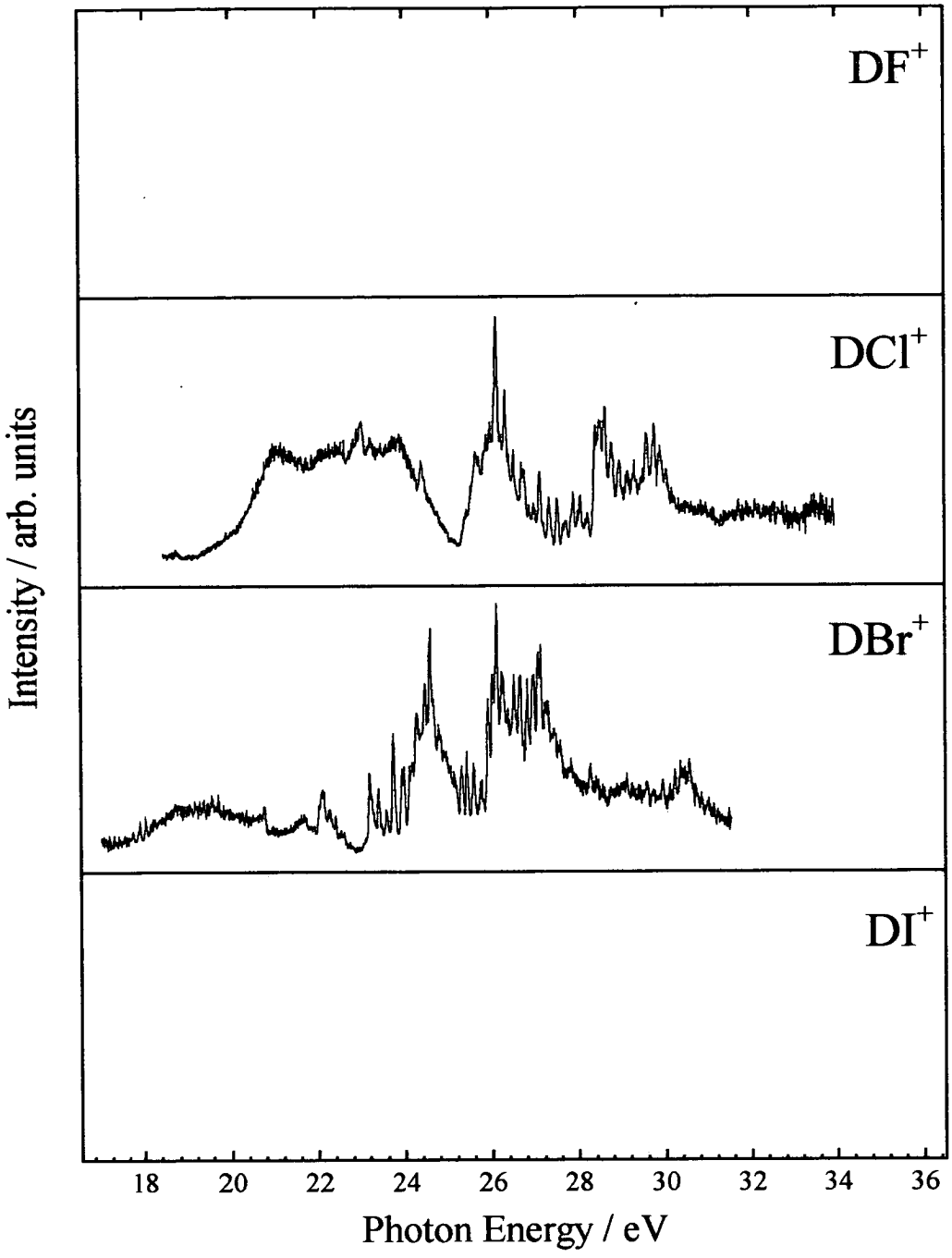

Figure 9-4 Threshold photoelectron spectra of the deuterium halides for the inner valence ionisation region. The spectra are taken from relevant Figures in this thesis. (The inner valence ionisation region of DF is around 40 eV - too high for the present studies, and the ionisation of DI has not been studied.)

9.3 Concluding remarks

Threshold photoelectron spectroscopy, like all ionisation techniques, has its good and bad features. TPES allows the energies of non-Franck-Condon vibrational levels to be measured, however the technique only gives indirect information on the dynamics of the ionisation event. Thus, the assignment of the "doorway" Rydberg states in TPES has a subjective element. If the electronic energy levels of the ion are of interest then this does not matter, however, when the decay dynamics of the intermediate Rydberg states are a main feature of the study the non-specificity of the technique is a hindrance. Ideally, the intermediate Rydberg state would be characterised by a combination of photoabsorption, mass resolved photoionisation, wavelength resolved fluorescence excitation, tunable conventional photoelectron spectroscopy, and threshold photoelectron spectroscopy; all at the same resolution and using the same excitation source. This body of work may then explain why Rydberg states of different symmetry are either present or absent in the threshold photoelectron spectrum, and at the same time would give a good insight into the various decay dynamics of different Rydberg states.

Threshold autoionisation only seems to be a significant ionisation process in the lowest ion state. This is probably because as more and more ionic states become energetically accessible, the number of decay channels open to the autoionising neutral states gets larger. There may also be a propensity to autoionise to the most stable ion state.

Spectra of both the HX and DX systems have proved very useful in the analysis of results. The assignment of the Rydberg states that autoionise into the X ($^2\Pi_i$) ion continuum has utilised both systems. The DCl spectrum was used to eliminate the [A ($^2\Sigma^+$)] $nd\pi$ $^1\Pi$ Rydberg series and the HCl spectrum eliminated the [A ($^2\Sigma^+$)] $np\pi$ $^1\Pi$ Rydberg series. Combining the data for both sets of isotopes has allowed the derivation of consistent vibrational constants for both HX and DX. This

combined analysis has also been particularly important in the assignment of vibrational progressions in the inner valence region as many electronic bands are overlapped.

Finally, one of the benefits of threshold photoelectron spectroscopy is that intensity corrected spectra over large energy ranges are easily obtained. The spectra are aesthetically pleasing and provide summaries of the differing spectroscopic properties of the HX and DX systems. The figures in Appendix F (Appendix F-1 to F-4) show the same data as Figures 9-1 to 9-4 in a different format. Some of the Figure panels in both sets of composite spectra are blank. It would be useful to record the spectra of the missing systems to complete a large section of work on the hydrogen and deuterium halides.

Appendices

Appendix A. Preparation of deuterium fluoride

The preparation of deuterium bromide was carried out by by D.R. Brown, (University of Oxford).

All work was carried out in a Monel/PTFE/FEP high vacuum line and starting materials handled in a nitrogen-purged glove box. Calcium fluoride (Aldrich, 99.9%) was dried by heating in a platinum crucible to 800°C followed by subsequent purging in a glove box until cool. This was taken into the box, ground up, and the process repeated until the solid remained free-flowing after heating. Sulphuric acid (Aldrich, 98% solution in D_2O, 99.5% isotopic purity) was used as supplied except for degassing. Antimony pentafluoride was loaded into a pre-passivated Kel-F ampoule inside a nitrogen purged glove bag.

A 750 cm^3 stainless steel can guarded by a stainless steel Whitey valve was passivated with fluorine gas (300 torr) for 3 hours and then loaded with 100g CaF_2 and 100g D_2SO_4. This was attached to the Monel vacuum line, and the line re-passivated to remove moisture. Production of DF began almost immediately without heating, and the volatiles were passed into a PTFE/FEP trap held at -196°C, and then transferred at room temperature into a Kel-F ampoule containing 0.5g SbF_5 drying agent. Heating the can to 180°C coupled with mild agitation completed the reaction. The DF was allowed to react with SbF_5 for 2 hours to ensure no D_2O was present, and the contents of the ampoule were transferred to a pre-passivated stainless steel storage ampoule guarded by a Whitey valve. Some DF was left in the Kel-F ampoule to ensure the SbF_5 remained involatile (being present as SbF_6^- and other oligomeric species) In a 50% overall yield, a total of 22g DF was collected.

Appendix B. LabTalk script for the two state problem

This LabTalk script was written to rapidly simulate a perturbation of a two level system. It was applied to the A ($^2\Sigma^+$) state of hydrogen iodide in Chapter 6. The script assumes that the diabatic potentials to be perturbed have already been simulated (the mathematical representations of the curves are given below). The off-diagonal $H_{\Pi\Sigma}$ (=$H_{\Sigma\Pi}$) term will be a function of the internuclear bondlength, R, and the dataset *andy_i* was used to control this change with R. *andy_i* was generated separately. The magnitude of H_{12} was set at a pop-up prompt, which in effect scales the dataset *andy_i*. The diabatic potentials were simulated from 1 to 5.999 Å in 0.001 steps.

```
andy_a = rep_a;
andy_d = rep_b;
andy_d = morse_b;
getnumber -s (magnitude / eV) pert (perturbation);
andy_f = 0.5*(andy_d + andy_e) - 0.5*sqrt(((andy_d - andy_e)^2)+4*(pert^2)*andy_i);
andy_g = 0.5*(andy_d + andy_e) + 0.5*sqrt(((andy_d - andy_e)^2)+4*(pert^2)*andy_i);
andy_h = andy_f*8065.541;
type -b;
```

The script was interfaced to the Franck-Condon program via a script in Appendix D.

The various functions for the diabatic states used in the scripts were:

(a) Morse Potential. (generated using the LabTalk in Appendix D):
D_e=8800 cm^{-1} ω_e=550 cm^{-1} r_e=2.00 Å μ=0.992 a.m.u. T_e=112315 cm^{-1}
Rmin = 1.00 Å Rmax = 5.99 Å step = 0.001 Å

(b) the magnitude of $H_{\Pi\Sigma}$ (input in the origin script above):
pert = 0.716 eV

(c) the switching function for H_{12}:

```
andy_a[i] = 1+(i-1)/1000;
for (i=1;i<5001;i+=1) {
1/2 * (1-tanh ((andy_i[i] - 3.215)* 1.2));
};
```

(d) diabatic $^4\Pi_{1/2}$ curve:

```
andy_a[i] = 1+(i-1)/1000
(i=1;i<5001;i+=1) {
andy_d[i] = (116043 +70000*exp(-i/48))/8065.541;
};
```

Appendix C. The Hund's coupling cases

In Hund's case (a) the interaction of electronic motion with nuclear motion is considered weak but the electronic motion is strongly coupled to the internuclear axis. The orbital angular momentum of the electrons in the molecule are coupled to give a total orbital angular momentum $\boldsymbol{L}$ and the electron spin angular momenta are coupled to produce a resultant $\boldsymbol{S}$. Spin-orbit coupling between $\boldsymbol{L}$ and $\boldsymbol{S}$ is quite weak so that

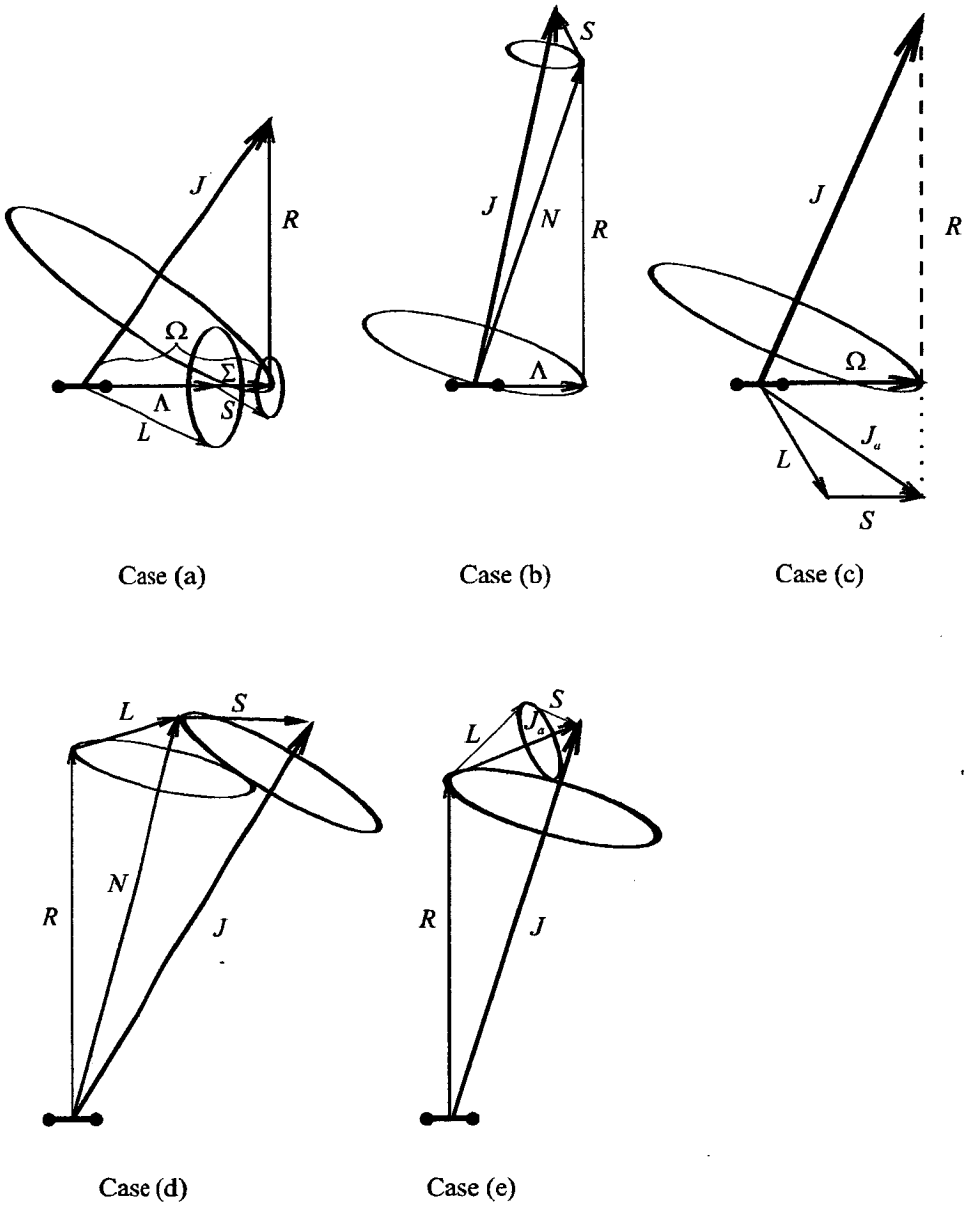

Appendix C-1 The five Hund's angular momentum coupling cases.

both $\boldsymbol{L}$ and $\boldsymbol{S}$ precess around the internuclear axis. The projections of $\boldsymbol{L}$ and $\boldsymbol{S}$ onto the internuclear axis, Λ and Σ, are combined to give the total projection Ω, where $\Omega=|\Lambda+\Sigma|$. The angular momentum due to nuclear rotation, $\boldsymbol{R}$, is coupled to Ω giving the total angular momentum $\boldsymbol{J}$ which is fixed in space. Whenever Ω, and hence Λor Σ, is non-zero this means that the axis of rotation of the entire molecule is not perpendicular to the nuclear axis. The good quantum numbers for Hund's case (a) are $\boldsymbol{S}$, Σ, Λ, Ω, and $\boldsymbol{J}$. (However as Ω is related to Σ and Λ it is redundant). The Hund's case (a) scheme generally describes first and second row diatomic systems.

In Hund's case (b) the electronic spin angular momentum is decoupled from the internuclear axis and the projection of the orbital angular momentum, Λ, is coupled to the nuclear angular momentum $\boldsymbol{R}$ to give a resultant angular momentum $\boldsymbol{N}$. The spin angular momentum $\boldsymbol{S}$ then couples to $\boldsymbol{N}$ to produce the total angular momentum $\boldsymbol{J}$. Good quantum numbers in Hund's case (b) are $\boldsymbol{J}$, $\boldsymbol{S}$, $\boldsymbol{N}$, and Λ. Hund's case (b) can also be used to describe light systems however generally these systems have large rotational constants.

In Hund's case (c) the orbital angular momentum $\boldsymbol{L}$ and spin angular momentum $\boldsymbol{S}$ are strongly coupled giving the resultant electronic angular momentum $\boldsymbol{J_a}$. The projection of $\boldsymbol{J_a}$ onto the internuclear axis, $\eta\Omega$, is coupled to the nuclear angular momentum $\boldsymbol{R}$ giving the total molecular angular momentum $\boldsymbol{J}$. Good quantum numbers in Hund's case (c) are Ω and $\boldsymbol{J}$. Hund's case (c) is important for systems with a larger spin-orbit coupling such as third row systems and iodine containing compounds.

In Hund's case (d) both the orbital and spin angular momenta are decoupled from the molecular axis and instead the orbital angular momentum of the Rydberg electron $\boldsymbol{L}$ is coupled to the rotational angular momentum of the core $\boldsymbol{R}$ giving the total angular momentum exclusive of spin $\boldsymbol{N}$. The spin angular momentum $\boldsymbol{S}$ then couples to $\boldsymbol{N}$ to give the total angular momentum $\boldsymbol{J}$. Good quantum numbers in Hund's case (d) are $\boldsymbol{J}$, $\boldsymbol{S}$, $\boldsymbol{N}$, and $\boldsymbol{R}$. Hund's case (d) is a useful limiting model for

high-n Rydberg states where l, the orbital angular momentum of the Rydberg electron, is non-zero (l is not strictly a good quantum number in a molecule).

In Hund's case (e) the orbital and spin angular momenta of the Rydberg electron ($\boldsymbol{L}$ and $\boldsymbol{S}$) are strongly coupled giving the resultant $\boldsymbol{J}_a$. The nuclear angular momentum $\boldsymbol{R}$ is then coupled to $\boldsymbol{J}_a$ giving the total angular momentum $\boldsymbol{J}$. Good quantum numbers are $\boldsymbol{R}$, $\boldsymbol{J}_a$, and $\boldsymbol{J}$. Until recently examples of Hund's case (e) coupling had not been observed, however work on HI by Mank *et al.* [240] shows evidence of Hund's case (e) coupling in high-n Rydberg states converging to the X ($^2\Pi_i$) ions.

Appendix D. LabTalk scripts used for data preparation

The following LabTalk scripts were written as analysis and data manipulation tools for this thesis, however they should be useful to many Origin users. The LabTalk scripting manuals have few examples so the following scripts are included as an introduction to the scripting language. The scripts are not commented to any great extent, however, they are short and should be easily decipherable using the LabTalk manual.

```
menu -plot /* make sure plot window menu */
menu 10 &Scripts
# ------------------------------------------------------------------
Menu "1. pi&ck points from plot" {
# script gathers user selected points from plot into worksheet POINTS
i=1;
%l = %h;
getNamedWKS POINTS; get %(points,1) -e endpt; test=(endpt>0)?1:0;
window -z %l;
switch(test){
case 1:
        %n =PREVIOUS DATA GATHERED - use RESTART if you wish to discard it;
case 0:
        %n=WORKSHEET EMPTY - it doesn't matter which;
}
%m = "append restart";
type -q either choose append or re-start, then use the data reader or screen reader;
getnumber (which ?) i:m (%n);
switch(i) {
        case 1:
                break;
        case 2:
                ClearWorksheet POINTS; break;
}
window -a %l;
integer = 0;
type -q ------- use mouse or cursor keys, double click or hit return to select point --------; sec -w 1;
def PointProc {
        if (integer == 0) {get POINTS_a -e numb;};
        integer+=1;
        newind = integer + numb;
        POINTS_a[newind] = x;
        POINTS_b[newind] = y;
        type -q use mouse or cursor keys, double click or hit return to select point - number stored = $(newind);
};
}
#------------------------------------------------------------------
Menu "2. ma&rk peaks with X coordinate" {
# the positions in the worksheet POINTS are added to the active plot
%l = %h;
if (exist(NUMBERS)==2) {window -c NUMBERS;}
create NUMBERS -w 30 a b c;
worksheet -f 3 2;
numbers_a = %(points,1);
numbers_b = %(points,2);
get col(1) -e endpos;
for (i=1;i<endpos+1;i+=1) {
        %(numbers,3,i) = %(numbers,1,i);
};
worksheet -t 3 6;
window -a %l;
layer -i numbers_c;
```

```
set numbers_c -tr 90;
set numbers_c -ty 50;
}
#-------------------------------------------------------
Menu "&add current file info. onto plot" {
# adds filename, path, date, and window name onto active plot - checks to see filename is not untitled.org
if (%g=="Untitled") {type -b filename is still "%g.ORG"  - save file under a new name then run script again; break 1;}
test= (exist(mylabel.fsize)==4)?1:0;
%n = "Path : ";
for(i=1;i<20;i+=1) {
if (%[%x,#i,\]!="") {%n= %n%[%x,#i,\]\\;} else {break;}
};
label -s -sa -n myLabel  ( file : %g.ORG \r\n %n \r\n Date : $(@D,D8) \r\n Window : %h);
if (test==0) {mylabel.fsize=6; mylabel.left=0; mylabel.top=0;};
}
#-------------------------------------------------------
Menu "simulate a Rydberg ladder" {
# script which can be useful for Rydberg series fitting
# type -b (rydberg fitting program by A.J.C);
%l=%h;
getNamedWKS RYDBERGFIT;
checkvar ip 8065.541;
checkvar delta 1.3;
checkvar nmin 3;
checkvar nmax 30;
checkvar spike 0;
checkvar back 10;
getnumber (ion potential (cm-1)) ip (quantum defect) delta (lowest quantum no.) nmin (highest quantum no.) nmax (ladder "baseline") back (ladder "ticks") spike (input for Rydberg ladder  simulation);
ClearWorksheet RYDBERGFIT;
ryd = 1.09737e5;   // the rydberg constant in cm-1
i=1;        // initiates i - the row number
for (n=nmin;n<=nmax;n+=1,i+=1){
  rydbergfit_a[(i-1)*3 + 1] = ip -  (ryd / ( n - delta)^2);
  rydbergfit_a[(i-1)*3 + 2] = ip -  (ryd / ( n - delta)^2);
  rydbergfit_a[(i-1)*3 + 3] = ip -  (ryd / ( n - delta)^2);
  rydbergfit_b[(i-1)*3 + 1] = back;
  rydbergfit_b[(i-1)*3 + 2] = spike;
  rydbergfit_b[(i-1)*3 + 3] = back;
};
rydbergfit_a/=8065.541;
window -a %l;
type -a;
ip=;
delta=;
nmin=;
nmax=;
spike=;
back=;
null=;
}
#-------------------------------------------------------
Menu "Go to X position in worksheet" {
# shortcut to plotted worksheet - select the data reader, move to position, and hit return
/* origin script to automatically go to the correct position in a worksheet */
type -q use data reader to find point of interest;
/* origin script to automatically go to the correct position in a worksheet */
dotoolbox -q;
dotoolbox -b 2;
# type -b now use the data reader to select the position in worksheet.      (The screen reader tool is blocked) ;
def PointProc {
            %k=%[%c,'_'];
            window -a %k;
            window -z;
            y1=index-1;
            dotoolbox -u 2;
            };
}
#-------------------------------------------------------
Menu "Unblock the screen reader tool" {dotoolbox -u;} # useful if the "go to X position in worksheet" script is not completed
}
#-------------------------------------------------------
```

```
# ************************************************************************
menu -worksheet
menu 10 &Scripts
#-----------------------------------------------
Menu "make a ladder from the highlighted column" {
# makes a ladder - useful for labelling points on a spectrum - use "pick points" to get the positions ?
TestColSel;
%l=%c;%o=%h;
get %c -e endpos;
%m=ladder;
rep 10 {
type -q accept "%m" to create or replace the worksheet "%m", or type a new worksheet name;
if (exist(%m)==2) {%n = worksheet "%m" exists !;} else {%n = worksheet "%m" is new;}
getstring (choose name for worksheet      use only alpha-numeric characters  - previous data is overwritten - click OK to accept) %m
(%n);
%n = %b;
if (%m =="%n") { break;} else {%m = %n;}
}
if (%n=="%h") {type -b command not allowed - both input and output worksheets are "%n"; break 1;}
checkvar back 100;
checkvar peak 0;
getnumber (height of ladder) back (height of peak) peak (ladder routine by A.J.C.);
getNamedWKS %n; ClearWorksheet %n;
for (i=1;i<endpos+1;i+=1) {
            %n_a[i*3 - 2] = %l[i];
            %n_a[i*3 - 1] = %l[i];
            %n_a[i*3 - 0] = %l[i];
            %n_b[i*3 - 2] = back;
            %n_b[i*3 - 1] = peak;
            %n_b[i*3 - 0] = back;
            type -q "i=$(i)" of $(endpos);
};
}
#-----------------------------------------------
Menu "change the Y values for the ladder" {
# on the fly ladder changer, useful when the ladder is in the wrong position
%l=%h;
get %(%l,1) -e endpos;
back = %(%l,2,1);
peak = %(%l,2,2);
test = %(%l,2,3);
if (back != test) {type -b;type -b this isn't a standard ladder;break;} else {
getnumber (Y value of backbone) back (Y value of spike) peak (changing the Y values of the ladder);
for (i=1;i<endpos/3+1;i+=1) {
            %(%l,2,(i*3 - 2)) = back;
            %(%l,2,(i*3 - 1)) = peak;
            %(%l,2,(i*3 - 0)) = back;
            type -q "i=$(i)" of $(endpos);}
};
}
#-----------------------------------------------
Menu "recover the points from a ladder" {
# highlight the column to be recovered - points will be put in worksheet RECOVERED
TestColSel;
get %c -e endpt; %l=%c;
if ((%l[1] == %l[3]) && (%l[1] == %l[2])) {
            GetNamedWKS RECOVERED; ClearWorksheet RECOVERED;
            for (i=3;i<=endpt;i+=3) {%(RECOVERED,2,(i/3)) = %l[i];}
} else {type -b; type -b this is not the standard ladder format - command aborted;}
}
#-----------------------------------------------
Menu "make a vertical ladder from the 1st column" {
# script was written to generate Rydberg levels convering to an ion limit
%l=%h;
get %(%l,1) -e endpos;

checkvar back 100;
checkvar peak 0;
if (exist(null)==4) {del null;};
getnumber (x minimum) back (x maximum) peak (ladder routine by A.J.C.);
getNamedWKS LADDER;
```

```
for (i=1;i<endpos+1;i+=1) {
        ladder_b[i*3 - 2] = %(%l,1,i);
        ladder_b[i*3 - 1] = %(%l,1,i);
        ladder_b[i*3 - 0] =null;
        ladder_a[i*3 - 2] = back;
        ladder_a[i*3 - 1] = peak;
        ladder_a[i*3 - 0] =null;
};
set ladder -e endpos*3;
}
#-------------------------------------------------------------
Menu "goto X position in worksheet" {
# moves to the closest worksheet row - works on highlighted column
testcolsel;
sum(%c);  /* use the sum command to get maximum and minimum the getnumber commamd */
checkvar pos $(sum.mean);
getnumber (X coordinate) pos [active dataset extends from $(sum.min) to $(sum.max)];
get %c -e numpts;
low=1; high=numpts;
# simple loop which gradually finds the "root" of the function by Bisection of the rows in the dataset
for (i=1;i<=30;i+=1) {
bottom= %c[low] - pos; top= %c[high] - pos;
middle=int((low+high)/2); halfway = %c[middle] - pos;          /* taking integer part as row position */
if (middle == high || middle == low) {break;};                 /* this is the normal exit point for the loop */
if (top*halfway > bottom*halfway) {high = middle;} else {low = middle;};
};
y1=middle-1; /* sets the row for display */
if (i == 30) {type -b non-standard exit from loop - move to X position manually;};
# bisection to the point of interest shouldn't take more than 20 times (2^20 = 1048576 rows)
# so if the loop completes all possible repitions something is wrong
}
#-------------------------------------------------------------
Menu "make a morse potential" {
# generate a morse potential using normal spectroscopic constants
getNamedWKS MORSE;
clearworksheet MORSE;
checkvar de 20000;
checkvar we 200;
checkvar re 1.9;
checkvar mu 20;
checkvar te 4;
checkvar rmin 1;
checkvar rmax 6;
checkvar step 0.002;
checkvar choice 1;
%l = "eV wavenumbers";
getnumber (dissociation limit "De") de (harmonic freq. "We") we (equil_m bondlength) re (reduced mass) mu (term energy "Te") te
(output in eV or cm-1 ?) choice:l (energies in cm-1 - length in A);
getnumber (start point) rmin (stop point) rmax (stepsize) step (over what range ? "A");
morse_a = data(rmin,rmax,step);
if (choice==1) {multip = 1; break;} else {multip = 8065.541;};
# define the a constant in the expression
const = 1.3559e-3 * we * sqrt(mu/(de/8065.541));
morse_b = (((de/8065.541) * (1 - exp(-const*(morse_a - re)))^2) + (te/8065.451))*multip;
type -a;
de=;
we=;
re=;
mu=;
te=;
}
#-------------------------------------------------------------
Menu "convolute col(2) in active wks (col(1) is X)" {
# gaussian convolution routine with active plotting - hack script to change function
%l=%h; if (%l=="conv" || %l=="convlast") {
type -b the active worksheet is already the result of a convolution - script will be aborted;
break 1;
}
type -h;
%m=%(%l,1);
sum(%m);
checkvar stop $(sum.max);
```

```
checkvar start $(sum.min);
checkvar step 1;
checkvar sigma 4;
getnumber (start) start (stop) stop (step) step (FWHM) sigma (limits on the convolution);
if (exist(convlast)==2) {clearWorksheet convlast;} else {GetNamedWKS convlast;}
if (exist(conv)==2) {%(convlast,1) = %(conv,1); %(convlast,2) = %(conv,2);del %(conv,2);del %(conv,1); win -c conv;}
getNamedWKS conv;
sec -e time;
conv_a=data(start,stop,step);
get %(conv,1) -e steps;
set %(conv,2) -e steps;
%(conv,2) = 0.0;
getNamedPlot convolution line; graph %(conv,2); graph %(convlast,2); set %(convlast,2) -c 10; layer -all;
get %(%l,1) -e numb;
break -be convoluting worksheet "%l";
break -r 1 numb;
for (i=1;i<=numb;i+=1) {
        type -q now working on peak $(i);
                break -p i;
                area = %(%l,2,i)*sigma*sqrt(pi/2)*0.849;
                FWHM = sigma * 0.849;
                conv_b += gauss(%(conv,1),0,%(%l,1,i),FWHM,area);
                # layer -all; sec -p 1; del -a;
                del -a;
};
break -end;
layer -all;
sec -e time;
type -a;
type gaussian convolution on worksheet %l;
stop=;
start=;
step=;
steps=;
sigma=;
type script took $(time) seconds;
type -b;
type -q  FINISHED !!!;
}
#-------------------------------------------------------------------
Menu "calculate n* for an ion and Rydberg pair" {
# calculates the n* for a Rydberg state when supplied with the ionisation limit and the Rydberg position
# origin script to calculate n*'s
# supply I.P and energy of Rydberg level
# returns Nstar
checkvar ip 1000;
checkvar ryd 900;
checkvar choice 1;
%l = "eV wavenumber";
getnumber (ionisation potential) ip (Rydberg energy) ryd (eV or cm-1 ?) choice:1 (enter energies and select energy units);
if (choice==1) {rydconst = 13.605; break;} else {rydconst = 1.097373e5;};
Nstar = sqrt(rydconst / (ip-ryd));
type -a;
ip=; ryd=; rydconst=; Nstar=;
}
#-------------------------------------------------------------------
Menu "import multiple files into 1 worksheet" {
# the filenames and column names are catenated into the worksheet column names
getfile -m *.dat;                                                    # clearWorksheet ABCDE;
getNamedWKS ABCDE;cols = %(ABCDE,@#); rep cols {del %(%h,1)};
totcol = 0;
for(i = 1; i <= count; i+=1) {
getfile -g i;
win -t data; cols = %(%h,@#); rep cols {del %(%h,1)};
open -w %A;
cols = %(%h,@#);
%l = %h;
win -a ABCDE;
wo -a cols;
for(j = 1; j <= cols; j+=1) {
%(ABCDE,(j+totcol)) = %(%l,j);
%m = %(%l,j); %n = %[%m,'_']; %o = %[%m,>'_']; %p = %n.%o;
```

```
wo -n $(j+totcol) %p;
}
for(j = 1; j <= cols; j+=1) {
del %(%l,1);
}
totcol+=cols;
win -c %l;
};
}
#-------------------------------------------------------
Menu "run the Franck-Condon program" {
# you should already prepare potentials called "lower.dat" and "upper.dat"
getNamedWKS fcctrl; clearWorksheet fcctrl;
open -w c:\temp\fcctrl.dat;
%m = "absorption fluorescence";
a=%(%h,1,1); b=%(%h,1,2); c=%(%h,1,3); d=%(%h,1,5); e=%(%h,1,6); f=%(%h,1,7);
g=%(%h,1,8); h=%(%h,1,9); k=%(%h,1,10); i=%(%h,1,4)+1;
l=%(%h,1,11); o=%(%h,1,12); n=%(%h,1,13);
# a=;b=;c=;d=;e=;f=;g=;h=;i=;k=;
getnumber [reduced mass (a.m.u)] a [sep-n of states] b [energy of 1st level] c [abs-n or fluores] i:m [attenuation factor] d
(information on the states - energies in cm-1);
getnumber [start] e [finish] f [FWHM] g [stepsize] h [Gaussian threshold] k (information on the spectral region of interest);
getnumber [start] l [stop] o [step] n (information on the potential energy curves);
# a=;b=;c=;d=;e=;f=;g=;h=;i=;k=;
%(%h,1,1)=a; %(%h,1,2)=b; %(%h,1,3)=c; %(%h,1,5)=d; %(%h,1,6)=e; %(%h,1,7)=f;
%(%h,1,8)=g; %(%h,1,9)=h; %(%h,1,10)=k; %(%h,1,4)=i-1;
%(%h,1,11)=l; %(%h,1,12)=o; %(%h,1,13)=n; i=0;
wks.export.cntrl=3; wks.export.separator="\t";
save -w fcctrl c:\temp\fcctrl.dat; sec -p 1;
run -e c:\temp\fcprog.pif;
type -b wait until program finished before pressing ok;
getNamedWKS peaks; clearWorksheet peaks; open -w c:\temp\peaks.dat; peaks_b/=8065.541;
getNamedWKS specout; clearWorksheet specout; open -w c:\temp\specout.dat; specout_a/=8065.541; GetnamedPlot spectrum;
graph specout_b; layer -a;
}
```

Appendix E. LabTalk script for rotational band contour fitting in Chapter 4

The script calculates the transition energy and rotational intensity for various rotational branches in the ionisation of HCl and DCl. The rotational constants for the various vibrational levels of HCl come from Edvardsson *et al.* [100]. In the case of DCl the rotational constants were derived from the HCl data using the change in reduced mass and a polynomial fit of B_E V's E, where B_E is the rotational constant at energy E. The LabTalk script prompts for the (rotationless) term energy of the transition, the rotational constant of the ion vibronic level, and the branching ratio of the various branches. The script assumes that all the worksheets have been previously with the correct column headings. A little trick has been used to simplify the coding of the calculations. For instance, consider an o branch transition ($\Delta N=-2$). If the rotational quantum numbers for the neutral run from 0 to 50 then the N branch rotational quantum numbers can be previously set to run from -2 to 48 (-2 and -1 have no physical significance, however their inclusion makes coding easier). The script assumes this has already been done and then uses column math's to speed up the calculation. The negative rotational quantum numbers are removed in the script at line 52. Finally, the script runs the Gaussian convolution script in Appendix D to produce a simulated spectrum. See the LabTalk manual for specific programming syntax [82].

```
1.  getnumber [term energy] te [rotational constant] bv [branch start] brs [branch finish]
    brf (energies in eV - branch numbering  - l=1, u=10);
2.  getnumber [l] bl [m] bm [n] bn [o] bo [p] bp (ratio of branches);
3.  getnumber [q] bq [r] br [s] bs [t] bt [u] bu (ratio of branches);
4.  type -a;separator 2;te=;bv=;brs=;brf=;c=;bl=;bm=;bn=;bo=;bp=;bq=;br=;bs=;bt=;bu=;
5.  l_ej = te + bv*l_j*(l_j+1) - g_ej;          {l,m,n,... represent the rotational branch of the
6.  m_ej = te + bv*m_j*(m_j+1) - g_ej;          ion + threshold electron}
7.  n_ej = te + bv*n_j*(n_j+1) - g_ej;          {ej is the energy of the rotational level j}
8.  o_ej = te + bv*o_j*(o_j+1) - g_ej;          {bv is the rotational constant for level v}
9.  p_ej = te + bv*p_j*(p_j+1) - g_ej;          {g is the worksheet storing the information
10. q_ej = te + bv*q_j*(q_j+1) - g_ej;          on the grond state of the molecule}
11. r_ej = te + bv*r_j*(r_j+1) - g_ej;          {the rotational quantum numbers stored in
12. s_ej = te + bv*s_j*(s_j+1) - g_ej;          l_j, m_j, n_j,... have previously been adjusted
13. t_ej = te + bv*t_j*(t_j+1) - g_ej;          to account for the change in rotational
14. u_ej = te + bv*u_j*(u_j+1) - g_ej;          angular momentum in the transition}
```

```
15.  l_intj = g_intj * bl;                  {intj is the intensity of the rotational level j}
16.  m_intj = g_intj * bm;                  {bl, bm, bn,... rotational branching ratios for
17.  n_intj = g_intj * bn;                  the different rotational branches}
18.  o_intj = g_intj * bo;
19.  p_intj = g_intj * bp;
20.  q_intj = g_intj * bq;
21.  r_intj = g_intj * br;
22.  s_intj = g_intj * bs;
23.  t_intj = g_intj * bt;
24.  u_intj = g_intj * bu;
25.  clearWorksheet spect;
26.  for(work=brs;work<=brf;work+=1) {     {allows the range of branches to be chosen}
27.  switch(work)
28.  {
29.  case 1:
30.  %l = l; break;                        {simply assigns a different letter to the string
31.  case 2:                                variable for each case. This letter is the name
32.  %l = m; break;                        of a worksheet}
33.  case 3:
34.  %l = n; break;
35.  case 4:
36.  %l = o; break;
37.  case 5:
38.  %l = p; break;
39.  case 6:
40.  %l = q; break;
41.  case 7:
42.  %l = r; break;
43.  case 8:
44.  %l = s; break;
45.  case 9:
46.  %l = t; break;
47.  case 10:
48.  %l = u; break;
49.  }

50.  for(i=1;i<=50;i+=1) {                 {for each worksheet defined by the case switch above
51.  get spect_ej -e endpt;                 copy the transition energy and intensity of the transition
52.  if (%l_j[i] >= 0) {                    into the worksheet spect if the final rotational quantum
53.  spect_ej[endpt+1] = %l_ej[i];          number is greater than zero}
54.  spect_intj[endpt+1] = %l_intj[i];
55.  };
56.  };
57.  ;
58.  };
59.  win -a spect;
60.  menu -e 3120;                          {runs the Gaussian convolution script on worksheet
61.  win -a convolution;                    spect (see Appendix D)}
62.  layer -i finish_sum;
```

Appendix F. Composite spectra - the HX and DX systems

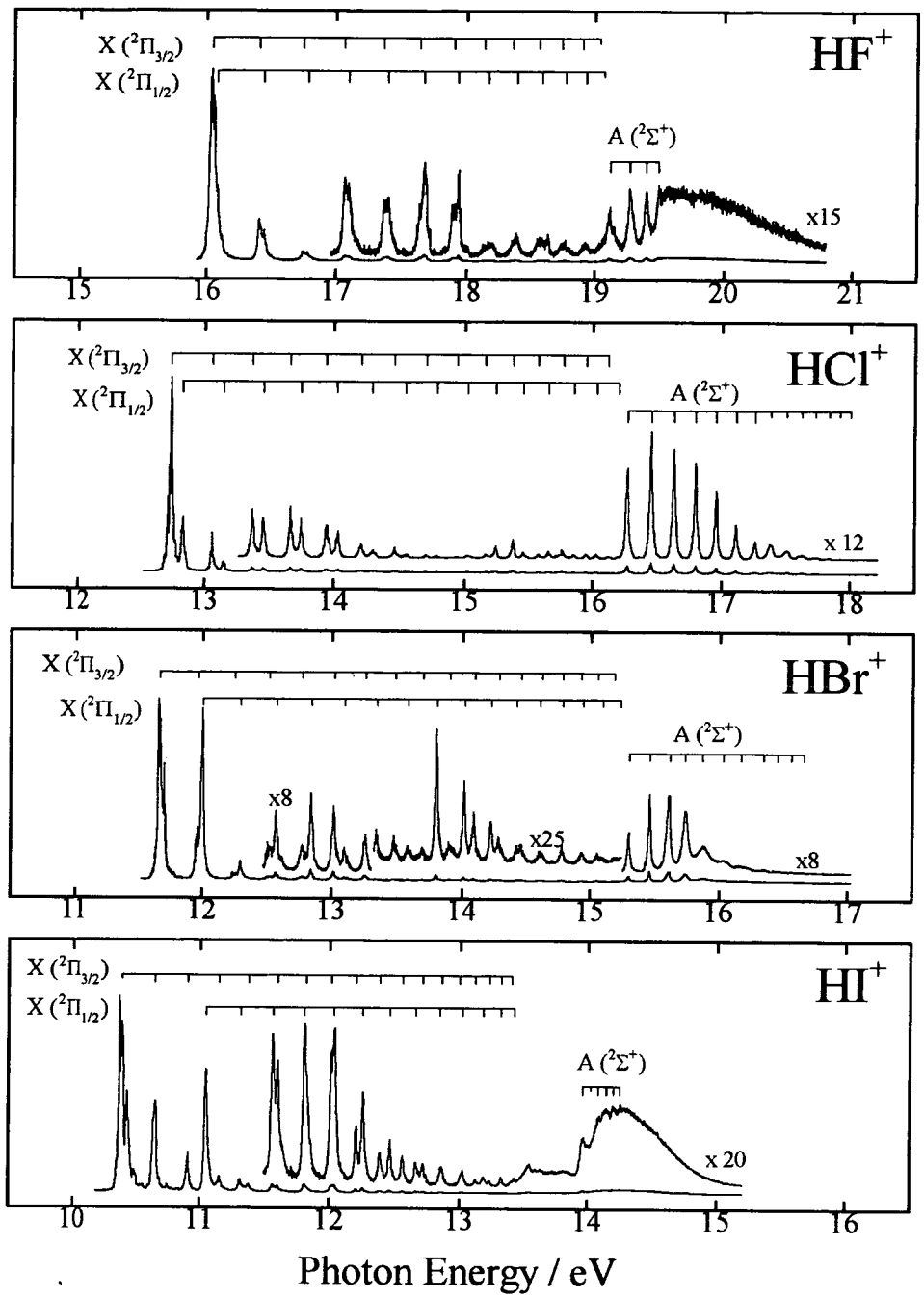

Appendix F-1 Composite threshold photoelectron spectra of the HX systems for the outer valence region.

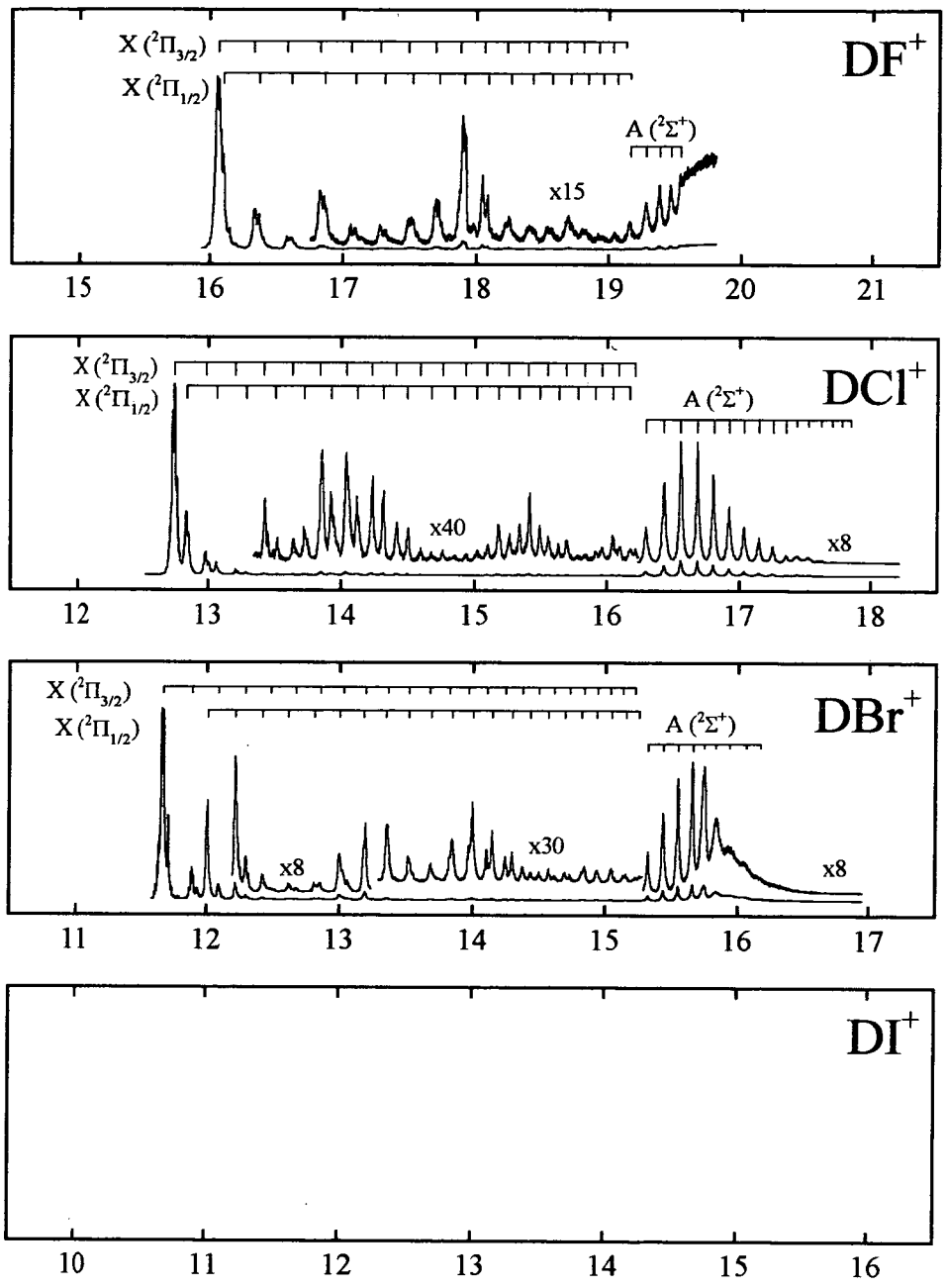

Appendix F-2 Composite threshold photoelectron spectra of the DX systems for the outer valence region.

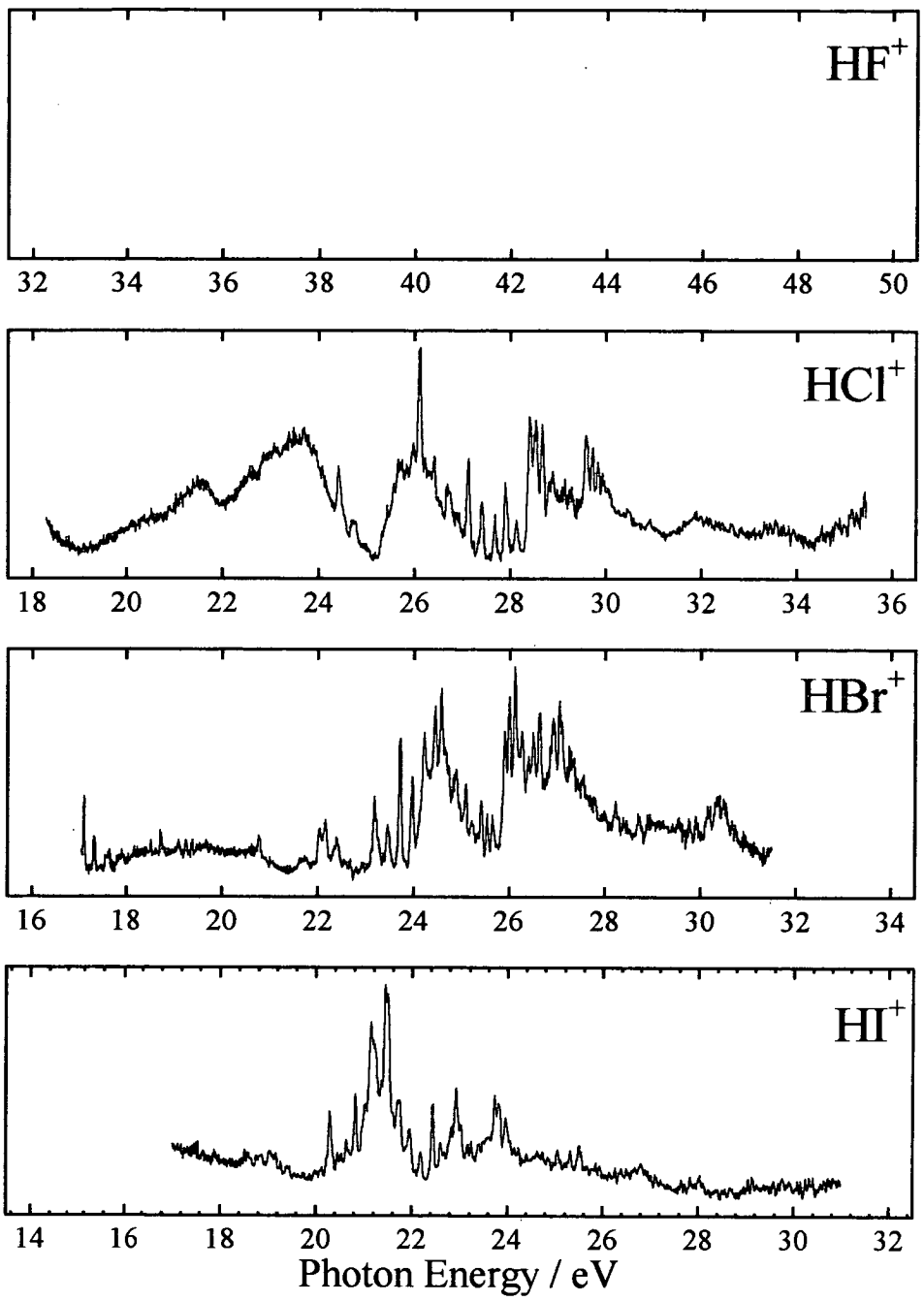

Appendix F-3 Composite threshold photoelectron spectra of the HX systems for the inner valence region

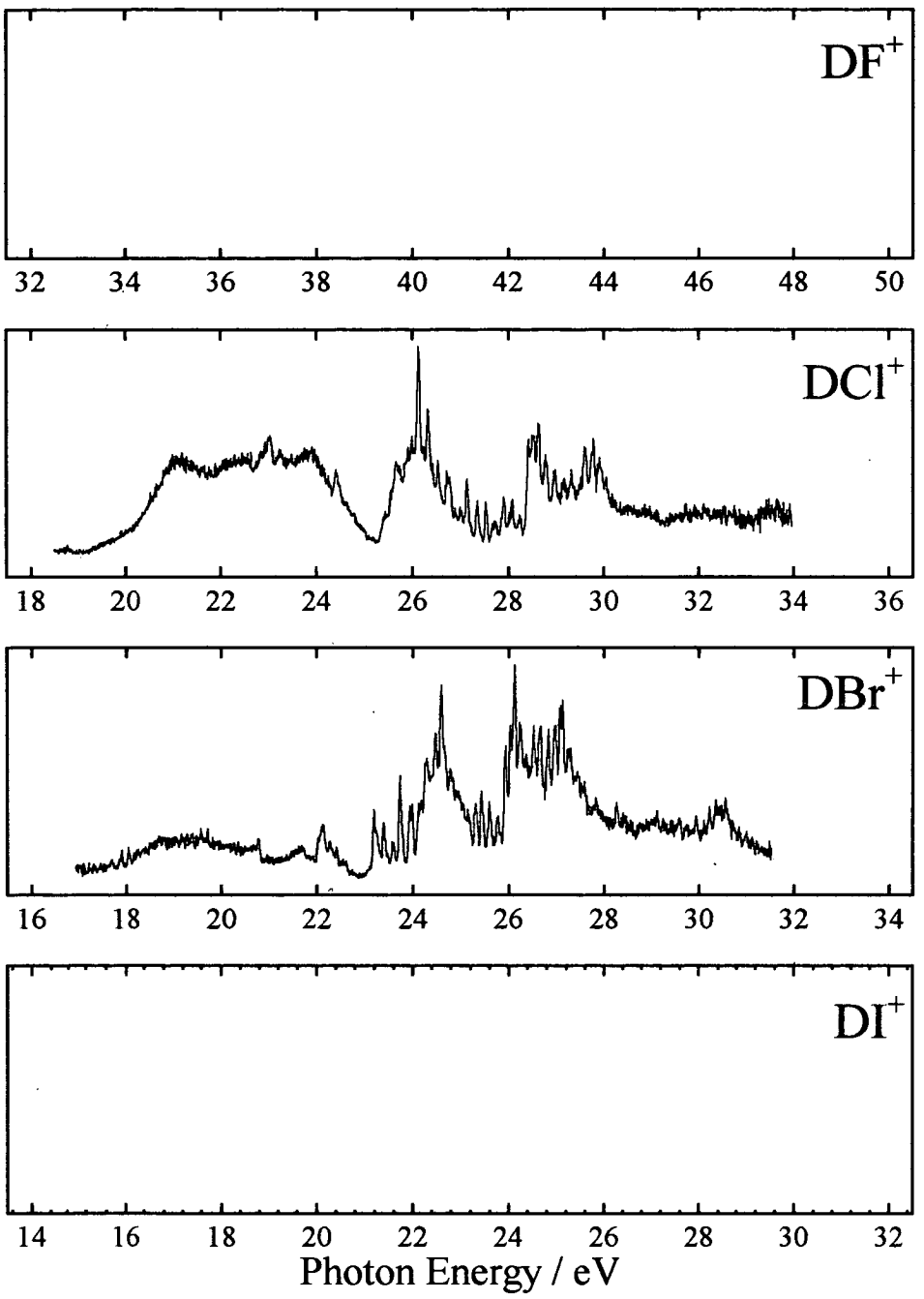

Appendix F-4 Composite threshold photoelectron spectra of the DX systems for the inner valence region

List of figures

List of tables

References

[1] Molecular Spectra and Molecular Structure. Vol. 1. 2nd Ed. G. Herzberg. Krieger Publishing Company, Malabar, Florida. (1989).

[2] Perturbations in the Spectra of Diatomic Molecules. H. Lefebvre-Brion and R.W. Field. Academic Presss Inc. London. (1986).

[3] Molecular Quantum mechanics. P.W. Atkins and R.S. Friedman. 3rd Ed. Oxford University Press (1997) ISBN 0 19 855947 X

[4] H. Lefebvre-Brion in High Resolution Laser Photoionisation and Photoelectron Studies. Edited by I. Powis, T. Baer, and C.Y. Ng. John Wiley and Sons. Chichester. (1995) ISBN 0-471-94158-1

[5] R.E. Huffman, Y. Tanaka, and J.C. Larrabee. Applied Optics. 2 (1963) 617

[6] Synchrotron Radiation Research. H. Winick and S. Doniach (eds), Plenum Press, New York. (1980). ISBN 0-306-40363-3

[7] Rydberg Atoms. T.F. Gallagher. Cambridge University Press. (1994). ISBN 0-521-38531-8

[8] E.E. Eyler in High Resolution Laser Photoionisation and Photoelectron Studies. Edited by I. Powis, T. Baer, and C.Y. Ng. John Wiley and Sons. Chichester. (1995) ISBN 0-471-94158-1

[9] Atomic Spectra and Atomic Structure. G. Herzberg. Dover Publications. New York. (1944) ISBN 0-486-60115-3

[10] Theoretical Atomic Physics. Harald Friedrich. Springer-Verlag. New York. (1991) ISBN 0-387-54179-9

[11] P.M. Guyon and J. Berkowitz. J. Chem. Phys. 54 (1971) 1814

[12] J. Berkowitz, G.B. Ellison, and D. Gutman. J. Phys. Chem. 98 (1994) 2744

[13] Written by M. MacDonald and K.P. Lawley, later additions and refinements by K.P. Lawley. The program has been interfaced into Microcal Origin using a Labtalk script in Appendix E.

[14] J.N. Bardsley. Chem. Phys. Lett. 2 (1986) 329

[15] A.L. Smith. Phil. Trans. Roy. Soc. Lond. A. 268 (1970) 169

[16] A.L. Smith. J. Quant. Spectrosc. Radiat. Transfer. 10 (1970) 1129

[17] U. Fano. Phys. Rev. 124 (1961) 1866

[18] F. Mies. Phys. Rev. 175 (1968) 164

[19] A.J. Blake, J.L. Bahr, J.H. Carver, and V. Kumar. Phil. Trans. Roy. Soc. Lond. A 268 (1970) 159

[20] N. Martensson, P. Baltzer, P.A. Bruhwiler, J.-O. Forsell, A. Nilsson, A. Stenborg, and B. Wannberg. J. Electron Spectrosc. Rel. Phenom. 70 (1994) 117

[21] G.C. King. Private communication. (The supplied plot was digitised using a LabTalk script in Appendix E)

[22] R. Spohr, P.M. Guyon, W.A. Chupka, and J. Berkowitz. Rev. Sci. Instrum. 42 (1971) 1872

[23] P.M. Guyon, R. Spohr, W.A. Chupka, and J. Berkowitz. J. Chem. Phys. 65 (1976) 1650

[24] A.J. Yencha, M.-W. Ruf, and H. Hotop. Z. Phys. D. 27 (1993) 131

[25] H. van Lonkhuyzen and C.A. DeLange. Chemical Physics. 89 (1984) 313

[26] D. Edvardsson, P. Baltzer, L. Karlsson, M. Lundqvist, and B. Wannberg. J. Elect. Spectrsc. Rel. Phemon. 73 (1995) 105

[27] K.P. Huber and G. Herzberg. Molecular Spectra and Molecular Structure, Vol 4. Constants of Diatomic Molecules Van Nostrand, Princeton. (1979)

[28] D.T. Terwilliger, A.L. Smith. J. Chem. Phys. 63 (1975) 1008

[29] H. Lefebvre-Brion and F. Keller. J. Chem. Phys. 90 (1989) 7176

[30] J. Raftery, and W.G. Richards. J. Phys. B. 6 (1973) 1301

[31] D.W. Turner, C. Baker, A.D. Baker, and C.R. Brundle. Molecular Photoelectron Spectroscopy. Wiley Interscience, London. (1970)

[32] T. Baer, P.M. Guyon, I. Nenner, A. Tabche-Fouhaille, R. Botter, L.F.A. Ferreira, and T.R. Govers. J. Chem. Phys. 70 (1979) 1585

[33] P.M. Guyon, T. Baer, and I. Nenner. J. Chem. Phys. 78 (1983) 3665

[34] T. Baer and P.M. Guyon. in High Resolution Laser Photoionisation and Photoelectron Studies. edited by I. Powis, T. Baer, and C.Y. Ng. J. Wiley and Sons. Chichester, England. (1995) ISBN 0-471-94158-1

[35] P.M. Guyon, T. Baer, L.F.A. Ferreira, I. Nenner, A. Tabche-Foulaile, R. Botter, and T.R. Govers. J. Phys. B. 11 (1978) L141

[36] T. Baer, P.M. Guyon, I. Nenner, A. Tabche-Fouhaille, R. Botter, L.F.A. Ferriera, and T.R. Govers. J. Chem. Phys. 70 (1979) 1585

[37] R.G. Tonkyn, R.T. Wiedmann, and M.G. White. J. Chem. Phys. 96 (1992) 3696

[38] see for instance: Synchrotron Radiation Research. H. Winick and S. Doniach (eds), Plenum Press, New York. (1980) ISBN 0-306-40363-3

[39] S. Cvejanovic and F.H. Read. J. Phys. B. 7 (1994) 1180

[40] G.C. King, M. Zubek, P.M. Rutter, and F.H. Read. J. Phys. E. 20 (1987) 440

[41] R.I. Hall, A. McConkey, K. Ellis, G. Dawber, L. Avaldi, M.A. MacDonald, and G.C. King. Meas. Sci. Technology. 3 (1992) 316

[42] Y. Lu, Y. Morioki, T. Tanaka, H. Yoshii, R.I. Hall, T. Hayaishi, and K. Ito. J. Chem. Phys. 102 (1995) 1553

[43] K. Muller-Dethlefs, M. Sander, and E.W. Schlag. Chem. Phys. Lett. 112 (1984) 291

[44] K. Muller-Dethlefs in High Resolution Laser Photoionisation and Photoelectron Studies. edited by I. Powis, T. Baer, and C.Y. Ng. J. Wiley and Sons. Chichester, England. (1995) ISBN 0-471-94158-1

[45] D. Th. Biernacki, S.D. Colson, and E.E. Eyler. J. Chem. Phys. 88 (1988) 2099

[46] W.A. Chupka. J. Chem. Phys. 98 (1993) 4520

[47] M.J.J. Vrakking and Y.T. Lee. Phys. Rev. A. (Rapid Communications.) 51 (1995) R894

[48] M.J.J. Vrakking and Y.T. Lee. J. Chem. Phys. 102 (1995) 8818

[49] E. Waterstradt, R. Jung, H-J. Dietrich, and K. Muller-Dethlefs. Rev. Sci. Instrum. 64 (1993) 3104

[50] M.C.R. Cockett, J.G. Goode, K.P. Lawley, and R.J. Donovan. J. Chem. Phys. 102 (1995) 5226

[51] F. Merkt and P.M. Guyon. J. Chem. Phys. 99 (1993) 3400

[52] I. Cacelli. Chem. Phys. Lett. 158 (1989) 199

[53] L.S. Cederbaum, W. Domcke, J. Schirmer, and W. von Niessen. Adv. Chem. Phys. LXV (1986) 115

[54] S. Svensson, L. Karlsson, P. Baltzer, B. Wannberg, U. Gelius, and M.Y. Adam. J. Chem. Phys. 89 (1988) 7193

[55] M.Y. Adam, M.P. Keane, A. Naves de Brito, N. Correia, P. Baltzer, B. Wannberg, L. Karlsson, and S. Svensson. J. Electron. Spectrosc. Rel. Phenom. 58 (1992) 185

[56] M.Y. Adam, M.P. Keane, A. Naves de Brito, B. Wannberg, P. Baltzer, L. Karlsson, and S. Svensson. Chemical Physics. 164 (1992) 123

[57] F. Carnovale, R. Tseng, and C.E. Brion. J. Phys. B. 14 (1981) 4771

[58] W. von Niessen, L.S. Cederbaum, W. Domcke, and G.H.F. Diercksen. Chemical Physics. 56 (1981) 43

[59] A.J. Yencha, A. Hopkirk, A. Hiraya, R.J. Donovan, J.G. Goode, R.R.J. Maier, G.C. King and A. Kvaran. J. Phys. Chem. 99 (1995) 7231

[60] A.J. Yencha, M.C.R. Cockett, J.G. Goode, R.J. Donovan, A. Hopkirk and G.C. King, Chem. Phys. Lett. 229 (1994) 347

[61] A.J. Yencha, A. Hopkirk, A. Hiraya, G. Dujardin, A. Kvaran, L. Hellner, M.J. Besnard-Ramage, R.J. Donovan, J.G. Goode, R.R.J. Maier, G.C. King, and S. Spyrou. J. Electron Spectrosc. Relat. Phenom. 70 (1994) 29

[62] Synchrotron Radiation Research. H. Winick and S. Doniach (eds), Plenum Press, New York. (1980) ISBN 0-306-40363-3

[63] The Feynman Lectures In Physics. R.P. Feynman, R.B. Leighton, and M. Sands. Addison - Wesley Publishing Company. Reading, Massachusetts.

[64] Electromagnetism (2nd ed). I.S. Grant and W.R. Phillips. John Wiley & Sons. Chichester, England. (1990) ISBN 0-471-92711-2

[65] D.M.P. Holland, J.B. West, A.A. MacDowell, I.H. Munro, and A.G. Beckett. Nucl. Instrum. Meth. in Phys. Res. B. 44 (1989) 233

[66] Swagelok Co., Solon, Ohio. U.S.A. 44139. Scottish distributor: South Scotland Valve and Fitting. 9/11 MacAdam Place, South Newmoor Industrial Estate, Irvine, Strathclyde U.K. KA11 4HP

[67] Hiden Analytical Ltd. Gemini Business Park, Warrington, England.

[68] Leybold Ltd. Waterside Way, Plough Lane, London. U.K. SW17 7AB

[69] G.C. King, M. Zubek, P.M. Rutter, and F.H. Read, J. Phys. E 20 (1987) 440.

[70] R.I. Hall, A. McConkey, K. Ellis, G. Dawber, A. Avaldi, M.A. McDonald and G.C. King, Meas. Sci. Technol. 3 (1992) 316.

[71] A.L. Hughes and V. Rojansky. Phys. Rev. 34 (1929) 284.

[72] A.L. Hughes and J.H. McMillen. Phys. Rev. 34 (1929) 291.

[73] P. Baltzer, L. Karlsson, M. Lundqvist, and B. Wannberg. Rev. Sci. Instrum. 64 (1993) 2179

[74] A.C. Gallagher and G. York. Rev. Sci. Instrum. 45 (1974) 663

[75] S.J. Osborne, A. Ausmees, J.O. Forsell, B. Wannberg, G. Bray, L.B. Dantas, and S. Svensson. Synchrotron Radiation News. 7 (1994) 25

[76] SIMION by D.A. Dahl. Idaho National Engineering Laboratory. Idaho Falls. USA.

[77] Mathematical Methods for Physicists. G. Arfken. Academic Press Inc, London. 3rd Edition. (1985)

[78] Pyhsics of Atoms and Molecules. B.H. Bransden and C.J. Joachain. Longman Scientific & Technical, Harlow, England. (1992) ISBN 0-470-20424-9

[79] Experiments in Physical Chemistry. D.P. Shoemaker and C.W. Garland. McGraw-Hill Book Company Inc. (1962) p314

[80] Argo International Limited, Unit 1, Ilford Trading Estate, Paycocke Road, Basildon, Essex SS14 3DR.

[81] Linde Gas UK. Ltd. New Field Industrial Estate, Tunstall, Stoke on Trent. ST6 5PD

[82] Microcal Software, Inc. One Roundhouse Plaza, Northampton. MA 01060 USA

[83] C.E. Brion, I.E. McCarthy, I.H. Suzuki, and E. Weigold. Chem. Phys. Lett. 67 (1979) 115

[84] D. Edvardsson, P. Baltzer, L. Karlsson, M. Lundqvist, and B. Wannberg. J. Electron Spectrosc. Rel. Phenom. 73 (1995) 105

[85] K. Wang, V. McKoy, M.-W. Ruf. A.J. Yencha, and H. Hotop. J. Electron, Spectrosc. Rel. Phenom. 63 (1993) 11

[86] A. Mank, D. Rogers, and J.W. Hepburn. Chem. Phys. Lett. 219 (1994) 169

[87] S. Gewurtz, H. Lew, and P. Flainek. Can. J. Phys. 53 (1975) 1097

[88] W.G. Richards and R.C. Wilson. Trans. Faraday Soc. 64 (1968) 1729

[89] P.S. Julienne, M. Krauss, and A.C. Wahl Chem. Phys. Lett. 11 (1971) 16

[90] J. Raftery and W.G. Richards J. Phys. B. 5 (1972) 425

[91] P.M. Guyon, R. Spohr, W.A. Chupka, and J. Berkowitz. J. Chem. Phys. 65 (1976) 1650

[92] J. Berkowitz, W.A. Chupka, P.M. Guyon, J.H. Holloway, and R. Spohr. J. Chem. Phys. 54 (1971) 5165

[93] W.T. Zemke, W.C. Stwalley, J.A. Coxon, and P.G. Hajigeorgiou. Chem. Phys. Lett. 177 (1991) 412

[94] A.J. Yencha, A. Hopkirk, J.R. Grover, B. Cheng, H. Lefebvre-Brion, and F. Keller. J. Chem. Phys. 103 (1995) 2882

[95] R.E. Lenga. The Sigma Aldrich, Library of Chemical Safety Data. 2nd Ed. (1988). Sigma Aldrich Corporation. PO Box 355 Milwaukee, Wisconsin. 53201 USA

[96] Martin Hearne, British Nuclear Fuels Ltd. Personal communication.

[97] A.J. Yencha, M.-W. Ruf, and H. Hotop. Z. Phys. D. 27 (1993) 131

[98] P.C. Cosby, H. Helm, and M. Larzilliere. J. Chem. Phys. 94 (1991) 92

[99] I. Cacelli. Chem. Phys. Lett. 158 (1989) 199

[100] D. Edvardsson, P. Baltzer, L. Karlsson, M. Lundqvist, and B. Wannberg. J. Electron Spectrosc. Rel. Phenom. 73 (1995) 105

[101] J. Raftery and W.G. Richards. J. Phys. B. 6 (1973) 1301

[102] A.D. Pradhan, K.P. Kirby, and A. Dalgarno. J. Chem. Phys. 95 (1991) 9009

[103] A.J. Yencha, A.G. McConkey, G. Dawber, L. Avaldi, M.A. MacDonald, G.C. King, and R.I. Hall. J. Electron. Spectrosc. Rel. Phenom. 73 (1995) 217

[104] A.G. McConkey, K. Ellis, G. Dawber, A. Avaldi, M.A. MacDonald, and G.C. King. J. Phys. B. 27 (1994) 271

[105] H. Hotop, G. Hübler, and L. Kaufhold. Int. J. Mass. Spectrom. Ion Phys. 17 (1975) 163

[106] S. Svensson, L. Karlsson, P. Baltzer, B. Wannberg, U. Gelius, and M.Y. Adam. J. Chem. Phys. 89 (1988) 7193

[107] K. Kimura, S. Katsumata, Y. Achiba, T. Yamazaki, and S. Iwata. Handbook of HeI photoelectron Spectra of Fundamental Organic Molecules. Halsted Press. New York. (1981)

[108] H. Frohlich, P.M. Guyon, and M. Glass-Maujean. Physical Review A. 44 (1991) 1791

[109] S. Svensson, L. Karlsson, P. Baltzer, B. Wannberg, U. Gelius, and M.Y. Adam. J. Chem. Phys. 89 (1988) 7193

[110] M.Y. Adam. Physica Scripta. 35 (1987) 477

[111] P. Natalis, P. Pennetreau. L. Longton, and J.E. Collin. Chem. Phys. 73 (1982) 191

[112] A.L. Smith. Phil. Trans. Roy. Soc. A268 (1970) 169

[113] H. Frohlich, P.M. Guyon, and M. Glass-Maujean. J. Chem. Phys. 94 (1991) 1102

[114] R.G. Tonkyn, R.T. Wiedmann, and M.G. White. J. Chem. Phys. 96 (1992) 3696

[115] W.D. Sheasley and C.W. Mathews. J. Mol. Spectrosc. 47 (1973) 420

[116] H. Lefebvre-Brion, P.M. Dehmer, and W.A. Chupka. J. Chem. Phys. 88 (1988) 811

[117] H. Lefebvre-Brion and F. Keller. J. Chem. Phys. 90 (1989) 7176

[118] H. Frohlich and M. Glass-Maujean. Physical Review A. 42 (1990) 1396

[119] M.S.N. Al-Kahali, R.J. Donovan, K.P. Lawley, T.Ridley, and A.J. Yarwood. J. Phys. Chem. 99 (1995) 3978

[120] J.L. Dunham. Physical Review. 41 (1932) 721

[121] D.T. Terwilliger and A.L. Smith. J. Mol. Spectrosc. 45 (1973) 366; ibid, 50 (1974) 30; D.T. Terwilliger and A.L. Smith. J. Chem. Phys. 63 (1975) 1008

[122] D.T. Terwilliger and A.L. Smith. J. Mol. Spectrosc. 45 (1973) 366

[123] P. Baltzer. Private communication to A.J. Yencha. (Reproduced with permission)

[124] M.Y. Adam. Chem. Phys. Lett. 128 (1986) 280

[125] A.A. Wills, D. Cubric, M. Ukai, F. Currell, B.J. Goodwin, T. Reddish, and J. Comer. J. Phys. B. 26 (1993) 2601

[126] W. von Niessen, P. Tomasello, J. Schirmer, L.S. Cederbaum, R. Cambi, F. Tarantelli, and A. Sgamellotti. J. Chem. Phys. 92 (1990) 4331

[127] A.G. Suits, X.M. Yang, C.W. Hsu, P. Heimann C.Y. Ng, A.M. Wodtke, and Y.T. Lee. Abstracts of papers of the American Chemical Society. 210 (1995) 26

[128] C.W. Hsu, K.T. Lu, M. Evans, Y.J. Chen, C.Y. Ng, and P. Heimann. J. Chem. Phys. 105 (1996) 3950

[129] K.L. Saenger, R.N. Zare, and C.W. Mathews. J. Mol. Spectrosc. 61 (1976) 216

[130] H.J. Lempka, T.R. Passmore, and W.C. Price. Proc. Roy. Soc. A. 304 (1968) 53

[131] A.J. Yencha, M.-W. Ruf, and H. Hotop. Z. Phys. D. 21 (1991) 113

[132] M.J. Haugh and K.D. Bayes. J. Phys. Chem. 75 (1971) 1472

[133] R.F. Barrow and A.D. Caunt. Proc. Roy. Soc. A. 66 (1953) 617

[134] P. Baltzer, M. Larsson, L. Karlsson, M. Lundqvist, and B. Wannberg. Phys. Rev. A. 49 (1994) 737

[135] A. Mank, T. Nguyen, J.D.D. Martin, and J.W. Hepburn. Phys. Rev. A. 51 (1995) R1 (Rapid communications)

[136] H. Lefebvre-Brion, P.M. Dehmer, and W.A. Chupka. J. Chem. Phys. 85 (1986) 45

[137] B. Ruscic and J. Berkowitz. J. Chem. Phys. 93 (1990) 1747

[138] N.P.L. Wales, W.J. Buma, C.A. de Lange, H. Lefebvre-Brion, K. Wang, and V McKoy. J. Chem. Phys. 104 (1996) 4911

[139] R. Irrgang, M. Drescher, F. Gierschner, M. Spieweck, and U. Heinzmann. J. Electron Spectrom. Rel. Phenom. 80 (1996) 5

[140] R. Irrgang, N. Böwering, M. Drescher, M. Spieweck, and U. Heinzmann. J. Chem. Phys. 22 (1996) 8966

[141] H. Lefebvre-Brion. J. Chem. Phys. 93 (1990) 5898

[142] D.T. Terwilliger and A.L. Smith. J. Mol. Spectrosc. 50 (1974) 30

[143] D.T. Terwilliger and A.L. Smith. J. Chem. Phys. 63 (1975) 1008

[144] P.M. Dehmer and W.A. Chupka. Argonne National Laboratory Report ANL-78-65, part 1, pp13-18

[145] H. Lefebvre-Brion, M. Salzmann, H.-W. Klausing, M. Müller, N. Böwering, and U. Heinzmann. J. Phys. B. 22 (1989) 3891

[146] M. Salzmann, N. Böwering, H.-W. Klausing, R. Kuntze, and U. Heinzmann. J. Phys. B. 27 (1994) 1981

[147] K. England, T. Reddish, and J. Comer. J. Phys. B. 23 (1990) 2151

[148] M.Y. Adam, M.P. Keane, A. Naves de Brito, N. Correia, P. Baltzer, B. Wannberg, L. Karlsson, and S. Svensson. J. Electron Spectrosc. Rel. Phenom. 58 (1992) 185

[149] C.E. Brion, Y. Iida, F. Carnovale, and J.P. Thompson. Chemical Physics. 98 (1985) 327

[150] B. Wannberg, S. Svensson, M.P. Keane, L. Karlsson, and P. Baltzer. Chemical Physics. 133 (1989) 281

[151] J. Delwiche, P. Natalis, J. Momigny, and J.E. Collin. J. Electron Spectrosc. Rel. Phenom. 1 (1972/73) 219

[152] A.J. Yencha, D. Kaur, R.J. Donovan, A. Kvaran, A. Hopkirk, H. Lefebvre-Brion, and F. Keller. J. Chem. Phys. 99 (1993) 4986

[153] P.M. Guyon, T. Baer, and I. Nenner. J. Chem. Phys. 78 (1983) 3665

[154] L.S. Cederbaum, W. Domcke, J. Schirmer, and W. von Neissen. Adv. Chem. Phys. LXV (1986) 115

[155] F. Norling. Z. Phys. 95 (1935) 179

[156] see for instance : (a) D.C Frost, C.A. McDowell and D.A. Vroom. J. Chem. Phys. 46 (1967) 4255 (b) H.J. Lempka, T.R. Passmore and W.C. Price. Proc. Roy. Soc. Lond. A304 (1968) 53. (c) D.W. Turner, C. Baker, A.D. Baker, and C.R. Brundle. "Molecular Photoelectron spectrocopy" Wiley, New York. 1970 p.40. (d) C.E. Brion and P. Crowley. J. Electron. Spectrosc. Rel. Phenom. 11 (1977) 399. (e) K. Kimura, S. Katsumata, Y. Achiba, T. Yamayaki, and S. Iwata. "Handbook of HeI Photoelectron spectra of Fundamental Organic Molecules" Halsted Press, New York 1981 p.30 (f) T.A. Carlsom, P. Gerard, M.O. Krause, G. von Wald, J.W. Taylor, and F.A. Grimm. J. Chem. Phys. 84 (1986) 4755 (g) L. Karksson, S Svensson, P. Baltzer, M. Carlsson-Göthe, M.P. Kean, A. Naves de Brito, N. Correia, and B wannberg. J. Phys. B. 22 (1989)) 3001 (h) N. Böwering, M. Saltzmann, M. Müller, H.-W. Klausing, and U. Heinzmann. Phys. Rev. A 45 (1992) R11. (i) A. Mank, M. Drescher, T. Huth-Fehre, G. Schnhense, N. Böwering, and U. Heinzmann. J. Electron Spectrosc. Rel. Phenom. 52 (1990) 661. (j) N. Böwering, H.-W. Kluasing, M. Müller, M. Saltzmann, and U. Heinzmann, Chem. Phys. Letters. 189 (1992) 467. (k) M.Y. Adam, M.P. Keane, A. Naves de Brito, N. Correia, B. Wannberg, P. Baltzer, L. Karlsson, and S. Svensson. Chem. Phys. 164 (1992) 123. (l) C.J. Zeitkiewicz, Y.-Y. Gu, A.M. Farkas, and J.G. Eden. J. Chem. Phys. 101 (1994) 86.

[157] M.Y. Adam, M.P. Keane, A. Naves de Brito, N. Correia, B. Wannberg, P. Baltzer, L. Karlsson, and S. Svensson. Chem. Phys. 164 (1992) 123.

[158] see for example the introduction to: L.S. Cederbaum, W. Domcke, J. Schirmer, and W. von Niessen. Adv. Chem. Phys. LXV (1986) 115

[159] W. von Neissen P. Tomasello, J. Schirmer, L.S. Cederbaum, R. Cambi, F. Tarantelli, and A. Sgamellotti. J. Chem. Phys. 92 (1990) 4331

[160] J.H.D. Eland and J. Berkowitz. J. Chem. Phys. 67 (1977) 5034

[161] A. Mank, M. Drescher, T. Huth-Fehre, N Böwering, and U. Heinzmann. J. Chem. Phys. 95 (1991) 1676.

[162] T.A. Carlson, P. Gerard, M.O. Krause, G. von Wald, J.W. Taylor and F.A. Grimm. J. Chem. Phys. 84 (1986) 4755

[163] H. Lefebvre-Brion, A. Giusti-Suzor and G. Raseev. J. Chem. Phys. 83 (1985) 1557.

[164] D. Hart and J.W. Hepburn. Chemical Physics. 129 (1989) 51

[165] G. Herzberg. Molecular Spectra and Molecular Structure. Vol 1. Spectra of Diatomic Molecules. Krieger Publishing Company, Florida. (1989) ISBN 0-89464-268-5

[166] H. Lefebvre-Brion. J. Chem. Phys 93 (1990) 5898

[167] S.T. Pratt. J. Chem. Phys. 101 (1994) 8302

[168] N. Böwering, H.-W. Klausing, M. Müller, M. Salzmann, and U. Heinzmann. Chem. Phys. Lett. 189 (1992) 467

[169] C.J. Zietkiewicz, Y.-Y. Gu, A.M. Farkas, and J.G. Eden. J. Chem. Phys. 101 (1994) 86

[170] P. Kruit and F.H. Read. J. Phys. E. 16 (1983) 313

[171] D.T. Terwilliger and A.L. Smith. J. Chem. Phys. 63 (1975) 1008

[172] A.J. Yencha, M.-W. Ruf. and H. Hotop. Z. Phys. D. 29 (1994) 163

[173] A.J. Yencha, J. Ganz, M.-W. Ruf, and H. Hotop. Z. Phys. D. 14 (1989) 57

[174] A.J. Yencha, M.-W. Ruf, and H. Hotop. Z. Phys. D. 21 (1991) 113

[175] A.J. Yencha, M.-W. Ruf, and H. Hotop. Z. Phys. D. 27 (1993) 131

[176] C.E. Brion, I.E. McCarthy, I.H. Suzuki, and E. Weigold. J. Electron Spectrosc. Rel. Phenom. 27 (1982) 83

[177] K.P. Huber and G. Herzberg. Molecular Spectra and Molecular Structure, Vol 4. Constants of Diatomic Molecules (Van Nostrand, Princeton. 1979)

[178] S.H. Alajajian and A. Chutjian. Phys. Rev. A. 37 (1988) 3680

[179] A. Chutjian, S.H. Alajajian, and K.-F. Man. Phys. Rev. A. (1990) 1311

[180] H.S. Carman, Jr., C.E. Klots, and R. N. Compton. J. Chem. Phys. 99 (1993) 1734

[181] A.J. Yencha, A. Hopkirk, A. Hiraya, R.J. Donovan, J.G. Goode, R.R.J. Maier, G.C. King, and A. Kvaran. J. Phys. chem. 99 (1995) 7231

[182] A.J. Yencha, M.C.R. Cockett, J.G. Goode, R.J. Donovan, A. Hopkirk, and G.C. King. Chem. Phys. Letters. 229 (1994) 347

[183] R.E. Huffman, J.C. Larrabee, and Y. Tanaka. J. Chem. Phys. 47 (1967) 856

[184] P. Baltzer. Private communication. (Dec 1994)

[185] B.H. Bransden and C.J. Joachan. Physics of Atoms and Molecules. Longmaan Scientific and Technical. Essex. England. (1983) ISBN 0-470-20424-9

[186] A. Banichevich, R. Klotz, and S.D. Peyerimhoff, Molecular Physics. 75 (1992) 173

[187] P.W. Atkins and R.S. Friedman. Molecular Quantum mechanics. 3rd Ed. Oxford University Press (1997) ISBN 0 19 855947 X

[188] Calculated from the dissociation energy of HI [165], the various ionisation potentials of H and I [223], and the electron affinities of H and I [189]

[189] R.C. Weast. CRC Handbook of Chemistry and Physics. 55th Ed. CRC Press, Cleveland, Ohio. 1975 ISBN 087819-454-1

[190] Using the equations of classical mechanics : P_H=-P_I (where P is the momentum of either H or I), $E_H = P_H^2/2m_H$, (E_H is the kinetic energy of the hydrogen, m_H is the mass, with a similar equation for I). Equating and rearranging, $E_H = m_I E_I/m_H$, E_I = 0.003 eV to allow detection, E_H = 0.381 eV, thus the total energy release is $E_H + E_I$ = 0.384 eV

[191] A.J. Yencha, K. Kela, A. Hopkirk, A. Kvaran, and R.J. Donovan. Proceedings of the 17th International Conference on the Physics of Electronic and Atomic Collisions, Brisbane, 1991, eds. I.E. McCarthy, W.R. MacGuillivray, and M.C. Standage, abstract of contributed papers p. 62.

[192] Using the same arguments as [190] it is clear that >99% of the released kinetic energy goes to the H ion.

[193] L. Karlsson, S. Svensson, P. Baltzer, M.C. Göthe, M.P. Keane, A. Naves de Brito, N. Correia, and B. Wannberg. J. Phys. B. 22 (1989) 3001

[194] W. Von Niessen, L.S. Cederbaum, W. Domcke, and G.H.F. Diercksen. Chem. Phys. 56 (1981) 43

[195] P. Baltzer, L. Karlsson, S. Svensson, and B. Wannberg. J. Phys. B. 23 (1990) 1537

[196] see for example: A. Mank, T. Nguyen, J.D.D. Martin, and J.W. Hepburn. Phys. Rev. A. 51 (1995) R1 (Rapid communications) and A. Mank, D. Rogers, and J.W. Hepburn. Chem. Phys. Letters. 219 (1994) 169

[197] R.P. Iczkowski and J.L. Margrave. J. Chem. Phys. 30 (1959) 403.

[198] E.A. Colbourn, M. Dagenais, A.E. Douglas and J.W. Raymonda. Can. J. Phys. 54 (1976) 1343

[199] J.L. Gole and J.L. Margrave. J. Mol. Spectrosc. 43 (1972) 65

[200] H. Nishimura, D.C. Cartwright and S. Trajmar. J. Chem. Phys. 71 (1979) 5039

[201] A.P. Hitchcock, C.E. Brion, G.R.J. Williams and P.W. Langhoff. Chem. Phys. 66 (1982) 435

[202] R.-G. Wang, Z.-W. Wang, M.A. Dillon and D. Spence. J. Chem. Phys. 71 (1979) 5039

[203] V.H. Dibeler, J.A. Walker and K.E. McCulloh. J. Chem. Phys. 50 (1969) 4592

[204] V.H. Dibeler, J.A. Walker and K.E. McCulloh. J. Chem. Phys. 51 (1969) 4230

[205] J. Berkowitz, W.A. Chupka, P.M. Guyon, J.H. Holloway and R. Spohr. J. Chem. Phys. (1971) 5165

[206] T.I. Porter. J.Chem. Phys. 48 (1968) 2071

[207] R.P. Tuckett, A.R. Dale, D.M. Jaffey, P.S. Jarrett and T. Kelly. Mol. Phys. 49 (1983) 475

[208] D.C. Frost, C.A. Mcdowell, and D.A. Vroom. J. Chem. Phys. 46 (1967) 4255

[209] A.B. Cornford, D.C. Frost, C.A. McDowell, J.L. Ragle, and I.A. Stenhouse. J. Chem. Phys. 54 (1971) 2651

[210] A.W. Potts and W.C. Price. Trans. Faraday Soc. (1971) 1242

[211] G. Bieri, A. Schmelzer, L. Åsbrink and M. Jonsson. Chem. Phys. 49 (1980) 213

[212] G. Bieri, L. Åsbrink and W. Von Niessen. J. Electon Spectrosc. Rel. Phenom. 23 (1981) 281

[213] H. van Lonkhuyzen and C.A. de Lange. Chem. Phys. 89 (1984) 313

[214] P.M. Guyon, R. Spohr, W.A. Chupka and J. Berkowitz. J. Chem. Phys. 65 (1976) 1650

[215] P.F. Levelt, K.S.E. Eikema, S. Stolte, W. Hogervorst and W. Ubachs. Chem. Phys. Letters. 210 (1993) 307

[216] G.G. Balint-Kurti. Mol. Phys. 22 (1971) 681

[217] D.C. Cartwright and P.J. Hay. Chem. Phys. 114 (1987) 305

[218] A.J. Yencha, A. Hopkirk, A. Hiraya, R.J. Donovan, J.G. Goode, R.R.J. Maier, G.C. King and A. Kvaran. J. Phys. Chem. 99 (1995) 7231

[219] A.J. Yencha, M.C.R. Cockett, J.G. Goode, R.J. Donovan, A. Hopkirk and G.C. King. Chem. Phys. Letters 229 (1994) 347

[220] Fluorodec 30 generator BNFL Electrogas Business, Springfields, Preston, Lancashire PR4 0XJ

[221] A.J. Yencha, A. Hopkirk, A. Hiraya, G. Dujardin, A Kvaran, L. Hellner, M.J. Besnard-Ramage, R.J. Donovan, J.G. Goode, R.R.J. Maier, G.C. King, and S. Spyrou. J. Electron Spectrosc. Relat. Phenom. 70 (1994) 29

[222] R.E. Huffman, J.C. Larrabee, and Y. Tanaka. J. Chem. Phys. 47 (1967) 856

[223] C.E. Moore, "Atomic Energy Levels". Natl, Bur, Std. (U.S.) 35/V.I (1971)

[224] Encyclopedia of Chemical Technology. Ed. Kirk-Othmer Vol. 10 (3rd Ed.) Wiley Interscience

[225] K. Ellis, R.I. Hall, L. Avaldi, G. Dawber, A. McConkey, L, Andric, and G.C. King. J. Phys. B. 27 (1994) 3415

[226] P. Hammond, G.C. King, J. Jureta, and F.H. Read. J. Phys. B. 20 (1987) 4255

[227] A.B. Cornford, D.C. Frost, F.G. Herring, and C.A. McDowell. J. Chem. Phys. 55 (1971) 2820

[228] $[F^+ (^3P_2) + F^- (^1S_0)] = 15.624$ eV, $[F^+ (^1D_2) + F^- (^1S_0)] = 18.212$ eV, and $[F^+ (^1S_0) + F^- (^1S_0)] = 21.194$ eV, From $D_o(F_2) = 1.602$ eV [198], EA(F) = 3.401190 eV [229], IP(F) = 17.423 eV ($F^+ {}^3P_2$)[222], = 20.011 eV ($F^+ {}^1D_2$) [223], = 22.993 eV ($F^+ {}^1S_o$) [223].

[229] C. Blondel, P. Cacciani, C Delsart, and R. Trainham. Phys. Rev. A. 40 (1989) 3698

[230] K. Radler and J. Berkowitz. J. Chem. Phys. 70 (1979) 221

[231] K. Radler and J. Berkowitz. J. Chem. Phys. 70 (1979) 216

[232] R.R.J. Maier. Private communication

[233] A.W. Potts and W.C. Price. Trans. Farad. Soc. 67 (1971) 1242

[234] A.J. Yencha, D.B. Thompson, A.J. Cormack, D.R. Cooper, M. Zubek, and P. Bolognesi. Chemical Physics. 216 (1997) 227

[235] P. Baltzer, B. Wannberg, M. Lundqvist, L. Karlsson, D.M.P. Holland, M.A. MacDonald, M.A. Hayes, P. Tamasello, and W. von Niessen. Chemical Physics. 202 (1996) 185

[236] G.C. King. Private communication. (Lecture notes from a postgraduate lecture course on ion optics at Manchester University)

[237] Miklos Szilagyi. Electron and ion optics. Plenum Press, New York. (1988) ISBN 0-306-42717-6

[238] G.H. Wannier. Phys. Rev. 90 (1953) 817

[239] G.C. King. Nuclear Inst. Meth. Phys. Res. B79 (1993) 150

[240] A. Mank, M. Drescher, T. Huth-Fehre, N. Bowering, U. Heinzmann, and H. Lefebvre-Brion. J. Chem. Phys. 93 (1991) 1676

Publications arising from Ph.D. work

i. "High-resolution threshold photoelectron spectroscopy of molecular fluorine"
A.J. Cormack, A.J. Yencha, R.J. Donovan, K.P. Lawley, A. Hopkirk, and G.C. King.
Chemical Physics, 1996, Vol.213, pp.439-448

ii. "High-resolution threshold photoelectron spectroscopy of hydrogen iodide"
A.J. Cormack, A.J. Yencha, R.J. Donovan, K.P. Lawley, A. Hopkirk, and G.C. King.
Chemical Physics, 1997, Vol. 221, pp. 175-188

iii. "Threshold photoelectron spectroscopy of SF_6"
A.J. Yencha, D.B. Thompson, A.J. Cormack, D.R. Cooper, M. Zubek, P. Bolognesi, and G.C. King. Chemical Physics, 1997, Vol.216, pp.227-241

iv. "Threshold photoelectron spectroscopy of hydrogen and deuterium chloride"
A.J. Yencha, A.J. Cormack, A. Hopkirk, R.J. Donovan, and G.C. King. *submitted to Chemical Physics*

v. "Theshold photoelectron spectroscopy of hydrogen and deuterium bromide"
A.J. Yencha, A.J. Cormack, A. Hopkirk, R.J. Donovan, and G.C. King. *in preparation*

vi. "Threshold photoelectron spectroscopy of hydrogen and deuterium fluoride"
A.J. Yencha, A.J. Cormack, A. Hopkirk, R.J. Donovan, and G.C. King. *in preparation*

vii. "Threshold photoelectron spectroscopy of the halogen acids"
A.J. Cormack, R.J. Donovan, A.J. Yencha, A. Hopkirk, and G.C. King. Daresbury Laboratory Synchrotron Radiation Department Scientific Reports 1994-95 Vol. 1 pp. 332-333

viii. "Threshold photoelectron spectroscopy of fluorine in the region 15.6 to 21.8 eV"
A.J. Cormack, R.J. Donovan, K.P. Lawley, A.J. Yencha, A. Hopkirk, and G.C. King.
Daresbury Laboratory Synchrotron Radiation Department Scientific Reports 1995-96 Vol. 1 pp.421-422

ix. "Threshold photoelectron spectroscopy of iodine in the region 9-14 eV"
A.J. Cormack, M.C.R. Cockett, J.G. Goode, R.J. Donovan, A.J. Yencha, A. Hopkirk, and G.C. King. Daresbury Laboratory Synchrotron Radiation Department Scientific Reports 1994-95 Vol. 1 pp. 330-331

Conferences attended

i. Ames symposium, University of Edinburgh, April 1994.

ii. Spectroscopy Group meeting, Newcastle University, August 1994, oral presentation.

iii. Daresbury Laboratory annual user meeting, September 1994, presented one poster.

iv. Faraday Division. Dynamics of Electronically Excited States. University of Manchester. March 1995.

v. European Conference on Atomic and Molecular Physics, University of Edinburgh, April 1995.

vi. Annual Chemical Congress. Heriot-Watt University. April 1995.

vii. Spectroscopy Group meeting, Sheffield University, August 1995, oral presentation.

viii. Daresbury Laboratory annual user meeting, September 1995, presented two posters.

ix. European Science Foundation conference on "Very high resolution spectroscopy with photoelectrons - radicals clusters and excited states", Lenggries, Germany, September 1995, presented two posters

x. Spectroscopy Group meeting, Strathclyde University, August 1996, oral presentation.

xi. Daresbury Laboratory annual user meeting, September 1996, presented one poster.

xii. University of Edinburgh, Department of Chemistry Physical discussion meetings from 1993 to 1997.

University courses attended

i. *Infra-red Spectroscopy: Practice and theory*, Prof. D.C. McKean and Dr. C.R. Pulham, University of Edinburgh.

ii. *Numerical data handling*, Prof. Jim Scrivens, ICI Wilton Research Centre

iii. *MaxEnt: An introduction to probabilistic data handling.*

iv. *Physical section Colloquia*, 1993-1997

v. *Introduction to UNIX*, Edinburgh University Computer Service.

vi. *Introduction to Microsoft Word*, Edinburgh University Computer Service.

vii. *C programming*, Edinburgh University Computer Service.